

University of St Andrews



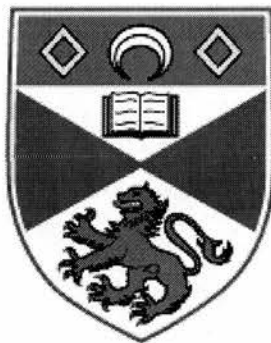
Full metadata for this thesis is available in
St Andrews Research Repository
at:

<http://research-repository.st-andrews.ac.uk/>

This thesis is protected by original copyright

Studies of Low-Dimensional Magnetic Systems

Shannon G. Brown



Thesis Submitted for the Degree of Doctor of Philosophy of
the University of St. Andrews on August 19, 2002



TL E370.

Studies Of Low-Dimensional Magnetic Systems

ABSTRACT

Low-dimensionality in magnetic and superconducting systems has been an area of intense experimental and theoretical study for a number of years now. This thesis reports experimental investigations of three different systems, namely; (1) artificial superconductor/ferromagnet multilayers, (2) ramsdellite LiTi_2O_4 and (3) the $\text{YBa}_2(\text{Cu}_{1-x}\text{M}_x)_3\text{O}_{7-\delta}$ cuprate. A brief account of the main physical properties and the relevant theories is presented in Chapter 1 with a more indepth review being provided at the introduction of each chapter of experimental results.

In this thesis the muon spin relaxation (μSR) and nuclear magnetic resonance (NMR) methods are the most complex experimental techniques. These are both covered in detail in Chapter 2. Similarly the sample preparation and characterisation techniques; including structural, chemical and magnetic analysis methods are discussed in Chapter 3.

In Chapters 4 and 5, complimentary studies of artificial multilayers are discussed.

The interplay between the competing magnetic and superconducting order parameters results in a variety of phenomena including a non-monotonic variation of the critical temperature with magnetic layer thickness and, under the correct conditions, a dimensional crossover.

Chapter 6 presents the results of an investigation of the magnetic and structural properties of LiTi_2O_4 ramsdellite. Low temperature diffraction have revealed a subtle transformation. SQUID and muon studies suggest a complex magnetic state combining Pauli paramagnetism and a second ordered state. At low temperatures additional magnetic ordering exists.

In Chapter 7, characterisation and preliminary ^{89}Y NMR results are reported. It was found that magic angle spinning (MAS) does indeed provide sufficient resolution to allow observation of induced satellite resonances.

Concluding remarks and a summary are given in the last chapter, Chapter 8.

*To my mother
Anne Brown
who waited so long for this.*

*And to the memory of my grandmother
Agnes Connor.*

*Discovery consists in seeing what everyone else has seen
and thinking what no one else has thought.*

Albert Szent-Gyorgi

Acknowledgements

Without the help and support of a number of people, this thesis would never have been completed or perhaps even started. The list that is provided below is not meant to be all-inclusive but only reflects my attempts to acknowledge the wide range of people who have had influence or a helping hand in the work described herein. My apologies to anyone who has been omitted.

As with all modern scientific research this thesis was not a purely an individual effort but is the result of a team effort. Firstly I want to thank both my supervisors for many discussions and much guidance during my time at St Andrews.

Much of the sample preparation was performed outside the University of St Andrews along with a range of experimental and characterisation techniques. To that end I would like to thank the following people for their help, expert advice and time: Chris Marrows and Mannan Ali of the University of Leeds; Andrew Harrison and Satish of Edinburgh University; Richard Gover of the University of Durham; Martin Smith of the University of St Andrews for both the sets of beam time.

Within the University of St Andrews, there are a number of people I wish to mention. Firstly, my thanks go to everyone who works at the School of Physics and Astronomy for providing an extremely friendly place to work, even if this was sometimes to the detriment of actually achieving any real work excluding checking email and surfing the web. Secondly I must thank the following people for their advice, help, time and patience: all the technical staff of the Physics department, in particular Fritz (glass blower), Bob Mitchell and Reg Gavine for their help with all things cryogenic; Julian Tolchard, of the Chemistry department, for many evenings spent making and characterising too many samples of ramsdellite; Martin Smith, also of the Chemistry department, for his efforts in preparing lithium doped YBCO samples without the co-operation of the lithium.

Lastly I must thank all my friends, both near and far, flatmates and office colleagues for their support and help throughout the past four years.

Declaration

I, Shannon G Brown, hereby certify that this thesis, which is approximately 35,000 words in length, has been written by me, that it is the record of work carried out by me and that it has not been submitted in any previous application for a higher degree.

date 02/04/2003 signature of candidate .

I was admitted as a research student in October 1998 and as a candidate for the degree of PhD in October 1999; the higher study for which this is a record was carried out in the University of St. Andrews between October 1998 and August 2002.

date 02/04/2003 signature of candidate .

I hereby certify that the candidate has fulfilled the conditions of the Resolution and Regulations appropriate for the degree of PhD in the University of St. Andrews and that the candidate is qualified to submit this thesis in application for that degree.

date 2/4/03 signature of supervisor ..

date 03/04/03 signature of supervisor ..

In submitting this thesis to the University of St. Andrews I understand that I am giving permission for it to be made available for use in accordance with the regulations of the University Library for the time being in force, subject to any copyright vested in the work not being affected thereby. I also understand that the title and abstract will be published, and that a copy of the work may be made and supplied to any bona fide library or research worker.

date 02/04/2003 signature of candidate

Contents

1	Superconductivity	1
1.1	Historical Review	1
1.2	Physical Properties	2
1.2.1	Meissner-Oschenfeld Effect	2
1.2.2	Type II superconductors	4
1.2.3	Josephson Effects	4
1.3	BCS Theory	5
1.4	Ginzburg-Landau Theory	5
1.5	Thin Films	8
1.5.1	The 3D anisotropic Ginzburg-Landau model	8
1.5.2	Lawrence-Doniach Theory	9
1.5.3	Tinkham Theory	9
1.6	Bean Model	11
2	Resonance Theory	13
2.1	Introduction	13
2.2	Nuclear Magnetic Resonance (NMR)	13
2.2.1	Classical Treatment	13
2.2.2	The Bloch Equations	15
2.2.3	Pulsed NMR	16
2.2.4	Nuclear spin interactions	19
2.2.5	The Magnetic Shift	21
2.2.6	Magic Angle Spinning (MAS)	23
2.2.7	NMR Instrumentation	25
2.3	Muon Spin Relaxation (μ SR)	29
2.3.1	Properties of the Muon	29

2.3.2	The μ SR Experiment	30
2.3.3	Muon Depolarisation Functions	32
2.3.4	Instrumentation	36
3	Sample Preparation and Characterisation Techniques	38
3.1	Introduction	38
3.2	Synthesis of YBCO-123 samples	38
3.2.1	Introduction	38
3.2.2	Zn doped YBCO	39
3.2.3	Li doped YBCO	40
3.3	Synthesis of Lithium ramsdellite	40
3.3.1	Introduction	40
3.4	Preparation of multilayers	41
3.4.1	Introduction	41
3.4.2	Sputtering Facilities	42
3.5	Structural characterisation	43
3.5.1	Diffraction Theory	43
3.5.2	Time of flight neutron diffraction	44
3.5.3	Rietveld Refinement of Powder Diffraction Data	45
3.5.4	Low angle scans	46
3.6	Chemical Analysis	48
3.6.1	Thermogravimetric Analysis	48
3.7	Magnetic Characterisation	48
3.7.1	Introduction	48
4	Investigation of T_c Suppression in Artificial Multilayers	52
4.1	Introduction	52
4.2	Theoretical Review	52
4.2.1	Previous Work	56
4.3	Characterisation	57
4.4	Experimental	61
4.5	Results	63
4.5.1	Nb-based multilayers	63
4.5.2	Pb-based multilayers	74
4.6	Conclusions and Further Work	80

5	Vortex Behaviour in Superconductor/Ferromagnet Multilayers	84
5.1	Introduction	84
5.2	Review	84
5.3	Characterisation	88
5.4	Experimental	88
5.5	Results	89
5.5.1	sc02 series	89
5.5.2	sc13 series	104
5.5.3	Magnetisation	108
5.5.4	Flux Flow	109
5.6	Conclusions and Further Work	112
6	Studies on the LiTi_2O_4 ramsdellite	116
6.1	Introduction	116
6.2	Previous Work	116
6.3	Characterisation	120
6.4	^7Li MAS NMR Study	122
6.4.1	Experimental	122
6.4.2	Results	122
6.5	Low Temperature Diffraction	131
6.5.1	Introduction	131
6.5.2	Neutron Diffraction	131
6.5.3	X-ray Diffraction	134
6.6	Magnetic Characterisation	137
6.6.1	dc magnetisation	137
6.6.2	Muon Spin Relaxation	142
6.7	Conclusions and Further Work	148
7	$\text{YBa}_2(\text{Cu}_{1-x}\text{M}_x)_3\text{O}_{7-\delta}$	152
7.1	High temperature Superconductivity (HTSC)	152
7.1.1	Structure of YBCO	152
7.1.2	Superconducting YBCO	156
7.2	Review of Doping experiments	158
7.3	Characterisation	161
7.3.1	Structural Analysis	161

7.3.2	T_c measurements	166
7.3.3	Thermogravimetric Analysis	168
7.3.4	Discussion	169
7.4	^{89}Y MAS NMR study	170
7.4.1	Experimental	170
7.4.2	Results	170
7.5	Conclusions and Further Work	175
8	Summary and Conclusions	179
8.1	Summary	179
8.2	Superconductor/Ferromagnet Multilayers	179
8.2.1	T_c Oscillations	180
8.2.2	Vortex Behaviour	180
8.3	LiTi_2O_4 Ramsdellite	181
8.4	$\text{YBa}_2(\text{Cu}_{1-x}\text{M}_x)_3\text{O}_{7-\delta}$	182
A	^7Li NMR Spectra of LiTi_2O_4	183

Chapter 1

Superconductivity

1.1 Historical Review

The phenomenon of superconductivity was first observed by Kamerlingh-Onnes in 1911[1]. At this time solid state physics was in its infancy and there was great interest in the temperature dependence of the electrical resistivity of metals. This led to Onnes' study of mercury and the discovery that its electrical resistivity drops abruptly to zero below 4.2K. This temperature is known as the critical or transition temperature.

Little advancement of this field followed until W. Meissner and R. Oschenfeld (1933)[2] discovered that upon cooling in an external field H_{ext} smaller than a critical value magnetic flux is completely expelled. In 1973 JR Gavaler found that sputtered films of Nb_3Ge began to superconduct at 22.3K [3]. This was soon increased to 23.2K by alteration of sputtering conditions by L.R. Testardi et al.[4]

Research in the superconducting field was revitalised in 1986 with the announcement of superconductivity in a compound at 35K[5]. The resultant frenzy of research that followed was rewarded with $\text{YBa}_2\text{Cu}_3\text{O}_{7-\delta}$ (YBCO) with a T_c of 92K[6]. Continued research has lead to the discovery of many other compounds with even higher critical temperatures. The highest to date belongs to the mercury based compound, $\text{HgBa}_2\text{Ca}_2\text{Cu}_3\text{O}_{8+\delta}$, displaying a transition above 150K when cooled under pressure[7].

The most recent addition to the superconductor family is MgB_2 [8] which had previously been overlooked. Unlike other diboride compounds MgB_2 boasts a transition temperature around 35K just beyond the reach of conventional theory. Its

discovery has renewed interest in the topic and the search to fully understand these fascinating materials.

1.2 Physical Properties

1.2.1 Meissner-Oschenfeld Effect

After zero resistance, the Meissner effect (as it has become known) is the second fundamental characteristic of a superconductor. The combination of these two properties results in a clear distinction between a superconductor and a *perfect conductor*; this difference is illustrated in Figure 1.1.

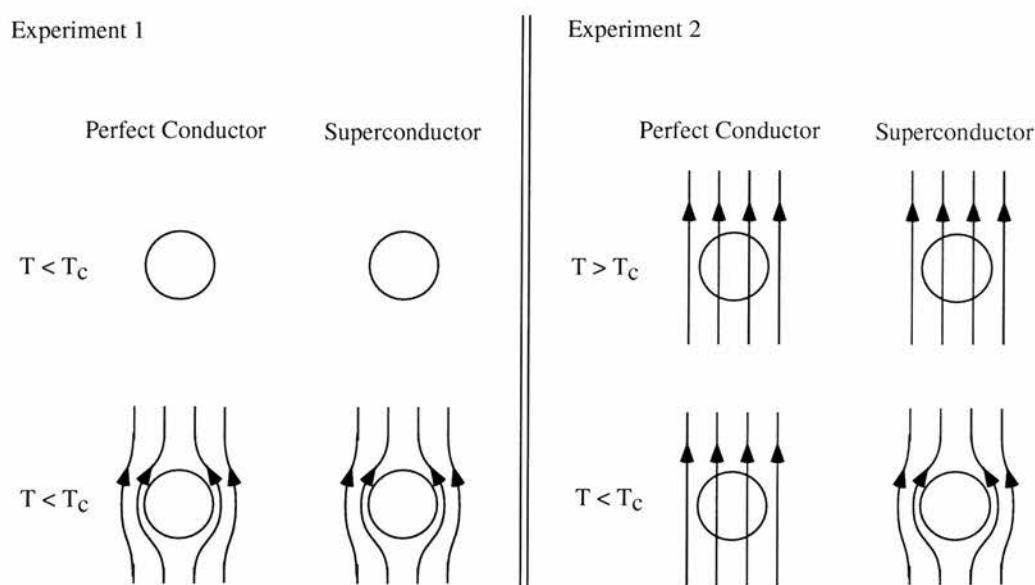


Figure 1.1: Experiments showing the difference between a superconductor and a perfect conductor. Experiment 1: sample cooled in zero field after which a field is applied; experiment 2: sample cooled in an applied field.

When an external field is applied after cooling through T_c both the superconductor and the perfect conductor induced currents would act to exclude the field. Application of the field before cooling will result in differing behaviour; the superconductor excludes the flux; the perfect conductor would remain fully permeated by the field. The final state of the superconductor does not depend on its history.

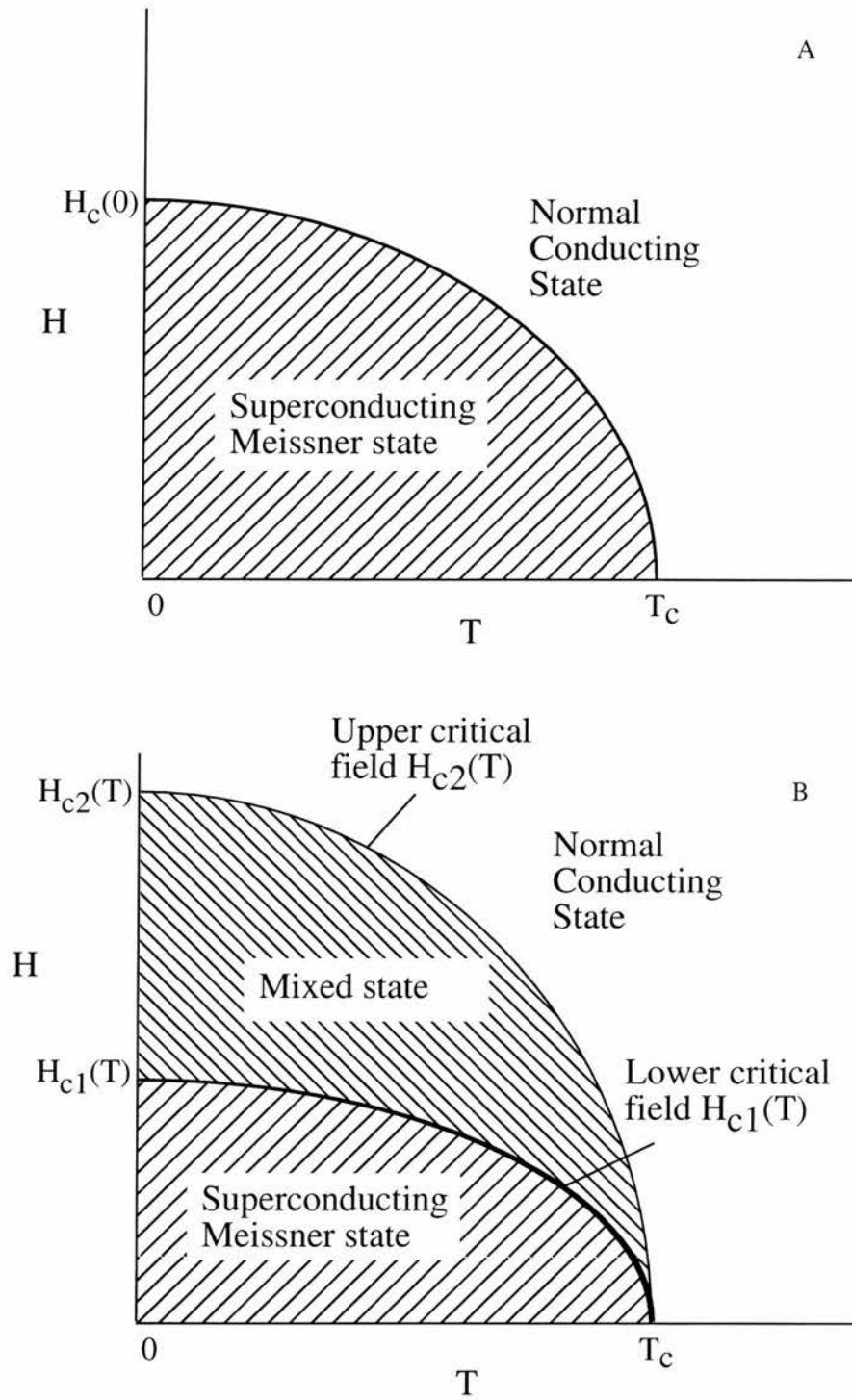


Figure 1.2: (A) The magnetic phase diagram of a type-I superconductor. (B) The magnetic phase diagram of a type-II superconductor.

In both situations screening currents flow in the superconductor resulting in perfect diamagnetic behaviour. These must have a finite depth implying that the external field penetrates the surface. The field has been shown to decay exponentially in an analogous manner to a penetration depth on metals.

Superconductivity does not persist to arbitrary magnetic fields. For each temperature there is a well-defined critical field $H_c(T)$ at which superconductivity disappears (see Figure 1.2A).

1.2.2 Type II superconductors

Type I materials exhibit the Meissner effect, expelling all magnetic flux, up to the critical field $H_c(T)$. Type II superconductors also exhibit the Meissner effect but only up to a lower critical field. Above this, magnetic flux can penetrate in the form fluxons. The superconductor forms a lattice of vortices, which channel the magnetic flux through the sample.

Upon increasing the external magnetic field the flux density increases until the upper critical field $H_{c2}(T)$ is reached, when the cores of the flux-lines overlap and the sample becomes normal. This behaviour is illustrated in Figure 1.2B.

1.2.3 Josephson Effects

In 1962, Josephson predicted that a zero voltage supercurrent

$$I = I_c \sin \Delta\varphi \quad (1.1)$$

should flow between two superconducting electrodes separated by a thin insulating barrier. Here $\Delta\varphi$ is the difference in the phase of the wavefunction in the two superconductors and I_c , the critical current, is the maximum supercurrent that the junction can support.

It was further predicted that if a voltage difference were maintained across the junction, the phase difference $\Delta\varphi$ would evolve according to

$$\frac{d(\Delta\varphi)}{dt} = \frac{2eV}{\hbar} \quad (1.2)$$

so that the current would be an alternating current of amplitude, I_c . The quantum energy $h\nu$ equals the energy change of the Cooper pair transferred across the junction. These predicted properties are known as the dc and ac Josephson effects.

1.3 BCS Theory

The first theory offering a complete microscopic description of superconductivity was provided by Bardeen, Cooper and Schrieffer (1957)[9] (BCS theory). In this model electrons bind into pairs and act as bosons, called Cooper pairs after Cooper[10] who calculated that even a weak interaction can bind electrons into pairs. The mechanism for this interaction was provided by Fröhlich who suggested that the interaction between electrons and lattice vibrations could lead to an effective interaction between the electrons themselves [11].

The basic concept of BCS theory can be understood by visualising the journey of an electron through a charged lattice, see Figure 1.3. This electron will leave a positive wake in its trail. A second electron is then attracted to this wake and is consequently bound to the first.

The bound electron pair form a ground state of lower energy than normal electrons. The energy gap that separates the two states is temperature dependent, vanishing at the transition temperature. It is related to the transition temperature by the simple expression

$$\Delta(0) = 1.76k_B T_c. \quad (1.3)$$

This phononic pairing mechanism is weak resulting in an upper transition temperature limit of approximately 30K, well below that observed in the cuprates.

1.4 Ginzburg-Landau Theory

In 1950, 7 years before BCS, Ginzburg and Landau introduced this description of the superconducting state [12]. It is based on Landau's theory of second-order phase transitions which can be characterised by a single order parameter. Initially it was thought to be purely phenomenological until Gorkov [13] (1957) showed it to be a limiting form of the microscopic BCS theory, being valid close to T_c . Landau's theory relies on a complex order parameter, ψ . When sufficiently close to the transition temperature the free energy F can then be expanded as a power series in this single parameter.

In the case of superconductivity this wavefunction is related to the density of superconducting electrons

$$n_s = |\psi|^2. \quad (1.4)$$

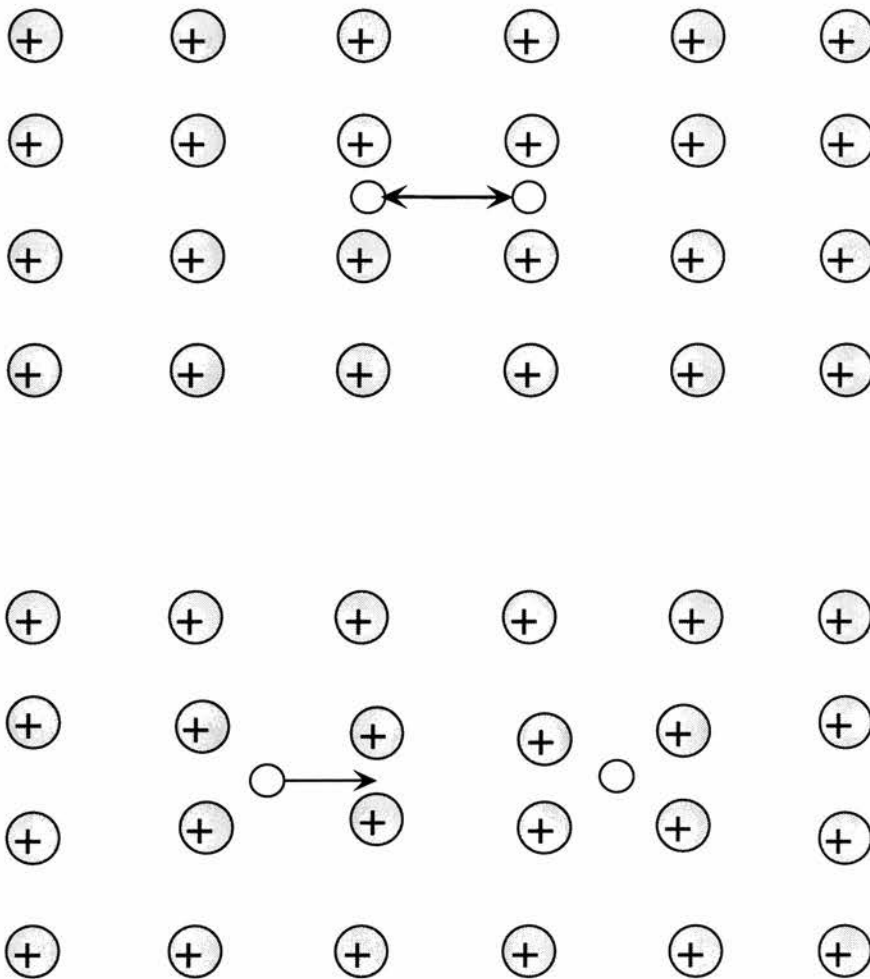


Figure 1.3: A schematic of the Cooper pair. In the top diagram the two electrons always repel each other due to the repulsive electrostatic interaction. In Fröhlich's scheme the first electron distorts the lattice producing a positive wake which attracts the second electron.

The postulated form for the dependence of the free energy is

$$F_s = F_n + \alpha|\psi(r)|^2 + \frac{1}{2}\beta|\psi(r)|^4 + \frac{\hbar^2}{2m}|\nabla\psi(r)|^2 + \frac{\hbar^2}{8\pi} \quad (1.5)$$

where F_n is the Helmholtz free energy in the normal state. The fourth term in this equation is a 'kinetic energy' contribution as a consequence of ψ being a function of position. The coefficients can be obtained by examining the free energy in the absence of fields and gradients

$$F_s - F_n = \alpha|\psi(r)|^2 + \frac{1}{2}\beta|\psi(r)|^4. \quad (1.6)$$

This is the condensation energy of the superconducting state. By inspection it can be seen that as $|\psi|^2$ tends to zero the condensation energy also tends to zero. In order to obtain a minimum in the condensation energy β must be positive, with α being either positive or negative. If α is positive, the minimum free energy occurs at $|\psi|^2=0$, corresponding to the normal state. On the other hand, if $\alpha < 0$, the minimum occurs when

$$|\psi|^2 = |\psi_\infty|^2 = -\frac{\alpha}{\beta} \quad (1.7)$$

where ψ_∞ is the value of the wavefunction within the bulk of the superconductor. The coefficient β is temperature independent and α obeys the following relationship

$$\alpha \propto (T - T_c) \quad (1.8)$$

There are two typical length scales in a superconductor determinable from the G-L theory. The first of these is the coherence length,

$$\xi^2(T) = \frac{\hbar^2}{2m|\alpha|} \propto \frac{1}{1-t} \quad (1.9)$$

where $t=T/T_c$ is the reduced temperature, which characterises the distance over which $\psi(r)$ can vary without undue energy increase. This gives an estimate of the Cooper pair size.

Also of importance is the penetration depth

$$\lambda = \left(\frac{m\beta}{4e^2|\alpha|} \right)^{1/2} \propto (1-t)^{-1/2} \quad (1.10)$$

which describes the penetration of magnetic fields into the superconductor.

These length scales give rise to the GL parameter

$$\kappa = \frac{\lambda(T)}{\xi(T)}. \quad (1.11)$$

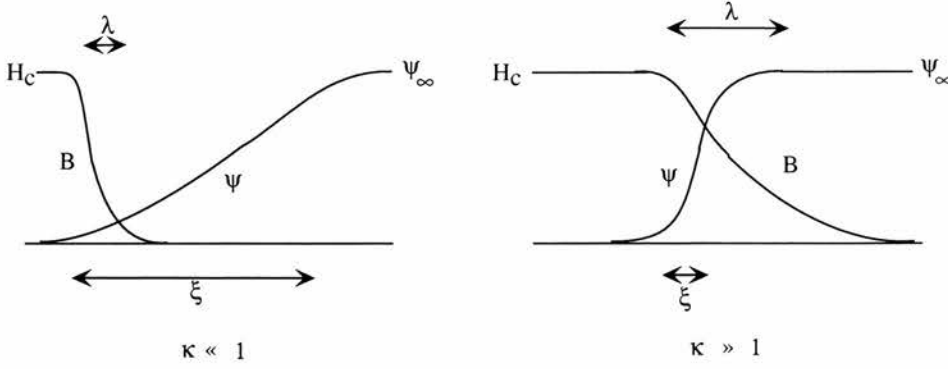


Figure 1.4: Schematic of cross-section in a domain wall. The case $\kappa \ll 1$ refers to a type I superconductor.

It is dimensionless and, since λ and ξ have similar temperature dependences, is temperature independent.

From G-L equations it is possible to derive an expression for H_{c2} , the upper critical field

$$H_{c2}(T) = \frac{\Phi_0}{2\pi\xi^2(T)} \quad (1.12)$$

where Φ_0 is the flux quantum. At this critical field value, the normal cores of the vortices effectively overlap and drive the sample normal.

1.5 Thin Films

1.5.1 The 3D anisotropic Ginzburg-Landau model

Anisotropy may be incorporated in the phenomenological G-L theory simply by the introduction of an effective-mass tensor m^* . For a system which may be regarded as uniaxial, the effective-mass tensor may be written as

$$[m^*]_{ij} = \begin{bmatrix} m_{xy} & 0 & 0 \\ 0 & m_{xy} & 0 \\ 0 & 0 & m_z \end{bmatrix} \quad (1.13)$$

where the z axis is the direction of symmetry. A natural result of this model are separate expressions for the critical fields parallel and perpendicular to the symmetry plane of the material

$$H_{c2\perp}(T) = \frac{\Phi_0}{2\pi\xi_{xy}^2(T)} = \frac{\Phi_0}{2\pi\xi_{\parallel}^2(T)} \quad (1.14)$$

$$H_{c2\parallel}(T) = \frac{\Phi_0}{2\pi\xi_{xy}(T)\xi_z(T)} = \frac{\Phi_0}{2\pi\xi_{\parallel}(T)\xi_{\perp}(T)}. \quad (1.15)$$

For an applied magnetic field making arbitrary angle θ with respect to the z-axis, the upper critical field $H_{c2}(\theta, T)$ can be expressed as follows

$$\left(\frac{H_{c2}(\theta)\cos(\theta)}{H_{c2\perp}}\right)^2 + \left(\frac{H_{c2}(\theta)\sin(\theta)}{H_{c2\parallel}}\right)^2 = 1. \quad (1.16)$$

1.5.2 Lawrence-Doniach Theory

In the Josephson-coupled model introduced by Lawrence and Doniach (LD) [14], layered compounds are pictured as a stacked array of two-dimensional superconducting layers which are weakly coupled via Josephson tunneling between adjacent layers. Taking the z direction as parallel to the c-axis, with D as the interlayer distance and x,y as coordinates in the planes, the free energy can be written

$$F = \sum_n \int \alpha|\psi_n|^2 + \frac{1}{2}\beta|\psi_n|^4 + \frac{\hbar^2}{2m_{xy}} \left(\left| \frac{\partial\psi_n}{\partial x} \right|^2 + \left| \frac{\partial\psi_n}{\partial y} \right|^2 \right) + \frac{\hbar^2}{2m_z D^2} |\psi_n - \psi_{n-1}|^2 dA \quad (1.17)$$

where the sum runs over the layers and the integral is over the area of each layer.

As $T \rightarrow T_c$ the superconducting order parameter varies slowly on the scale of the layer repeat distance and the theory reduces to the anisotropic Ginzburg-Landau theory. In this regime all the superconducting properties of layered compounds are expected to be three-dimensional in nature.

For all field orientations except near parallel, the critical fields are essentially those predicted from the anisotropic GL model. For low temperatures it predicts a divergence of $H_{c2\parallel}(T)$ at a temperature T^* defined by the relation

$$\xi_z(T^*) = D/\sqrt{2}. \quad (1.18)$$

Below this temperature the vortex cores fit between the layers, allowing individual layers to remain superconducting in much larger fields than would be possible for bulk superconductor with the same coherence length. According to the L-D model in this region $H_{c2\parallel}(T)$ is infinite reflecting the limitations of this primitive approach. T^* actually corresponds to a dimensional crossover for the critical field.

1.5.3 Tinkham Theory

Tinkham developed a theory to describe the transition to normal state of a 2D superconducting film in the presence of a magnetic field using a simple argument

based on fluxoid quantisation [15]. Figure 1.5 illustrates the contrast in the vortex behaviour in the two possible orientations. When the magnetic field is parallel to the film surface, the current loop is constricted by the film thickness and the energy increases as H^2 . In the perpendicular orientation, an increase in the field, H , results in a decrease in the loop diameter and the energy has a linear dependence on H .

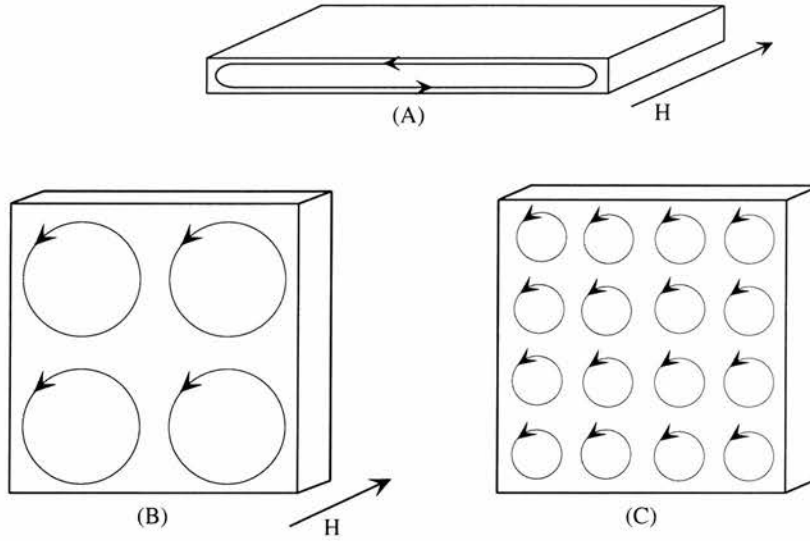


Figure 1.5: Schematic diagram of current configuration in parallel and perpendicular fields. In parallel geometry (A), the width of the loop is limited by the film thickness. In perpendicular geometry, (B) and (C), the size of vortex can adjust depending on the field strength so as to minimise energy.

With this in mind Tinkham obtained the following implicit relationship to describe the angular variation of the upper critical field in a thin film of thickness D

$$\left| \frac{H_{c2}(\theta) \sin(\theta)}{H_{c2\perp}} \right| + \left(\frac{H_{c2}(\theta) \cos(\theta)}{H_{c2\parallel}} \right)^2 = 1 \quad (1.19)$$

where the upper critical fields parallel and perpendicular to the film surface are defined thus

$$H_{c2\parallel}(T) = \frac{\sqrt{12}\phi_0}{2\pi\xi_{\parallel}(T)D} \quad (1.20)$$

$$H_{c2\perp}(T) = \frac{\phi_0}{2\pi\xi_{\parallel}^2(T)} \quad (1.21)$$

At large angles $H_{c2}(\theta)$ displays similar behaviour to that predicted in the anisotropic G-L theory. However, near $\theta=0^\circ$ there is a qualitative difference with the 2D film

having a pronounced cusp compared to the smoothly varying bell shape in the 3D case.

1.6 Bean Model

The Bean model is a useful tool for describing the magnetic properties of nonideal type-II superconductors and the flux distribution within the body when variable fields are applied. The effect of pinning centres is to hold the flux lines back near the surface; there is a gradient of flux density from the applied field value at the surface to zero some way inside. The field penetration profile in the superconductor is determined by the Maxwell equation

$$\nabla \times \mathbf{B} = \mu_0 \mathbf{J}. \quad (1.22)$$

The field gradient implies a current flowing at right angles to the field. This arises since when there is a variation on the flux-line density the currents from neighbouring rows do not cancel. In the Bean model, the flux-density profiles are simply straight lines, which simplifies qualitative description.

Figure 1.6 illustrates the profiles for flux penetrating into a thick slab of thickness D as the external field is increased and then decreased back to zero. With increasing field the flux penetrates from the edges into the centre until B_p is reached at which point flux has penetrated all the way through the sample. Upon decreasing the field a portion of the screening reverses and even at zero field there is trapped flux in the sample.

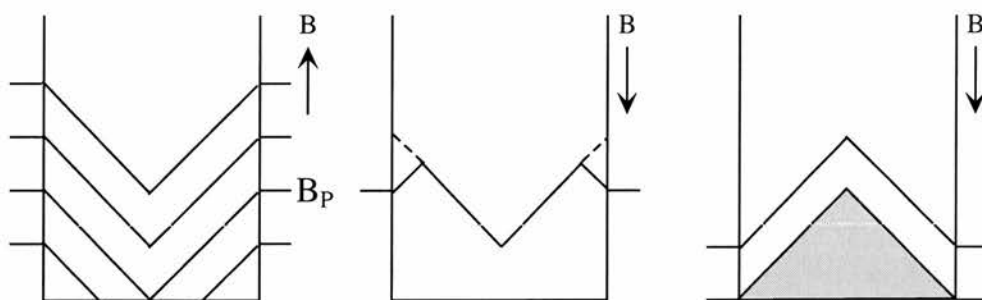


Figure 1.6: Schematic of the magnetic field penetration profiles at various stages of the applied field after cooling in zero-field.

References

- [1] H. K. Onnes, Akad. van Wetenschappen **14**, 818 (1911).
- [2] W. Meissner and R. Oschenfeld, Naturwissenschaften **21**, 787 (1933).
- [3] J. R. Gavaler, Appl. Phys. Lett. **23**, 480 (1973).
- [4] L. R. Testardi, J. H. Wernick, and W. A. Royer, Solid State Comm. **15**, 1 (1974).
- [5] J. G. Bednorz and K. A. Muller, Z. Phys. B **64**, 189 (1986).
- [6] M. K. Wu and C. W. Chu, Physical Review Letters **58**, 908 (1987).
- [7] A. Schilling, M. Cantoni, J. D. Guo, and H. R. Ott, Nature **363**, 6424 (1993).
- [8] J. Nagamatsu *et al.*, Nature **410**, 6824 (2001).
- [9] J. Bardeen, L. N. Cooper, and J. R. Schrieffer, Phys. Rev. **106**, 162 (1950).
- [10] L. N. Cooper, Phys. Rev. **104**, 1189 (1956).
- [11] H. Frolich, Phys. Rev **79**, 845 (1950).
- [12] V. L. Ginzburg and L. D. Landau, Zh. Eksperim. i. Teor. Fiz. **20**, 1064 (1950).
- [13] L. P. Gorkov, Zh. Ezsperim. i Tero Fiz. **36**, 1918 (1959).
- [14] W. E. Lawrence and S. Doniach, in *Proceedings of the 12th International Conference on Low-Temperature Physics* (Academic Press, Kyoto, 1971), p. 361.
- [15] M. Tinkham, Physical Review **129**, 2413 (1963).

Chapter 2

Resonance Theory

2.1 Introduction

Nuclear magnetic resonance (NMR) and μ SR represent two ways of performing the same experiment. Both techniques use magnetic species, providing information about the local environment of the probe. NMR relies on magnetic nuclei that are natural components of the sample whereas muons can be implanted into any structure. Also since muons are initially polarised a high magnetic field is not required, enabling μ SR experiments to be performed in zero field. These techniques and associated theoretical background as well as instrumentation are discussed below.

2.2 Nuclear Magnetic Resonance (NMR)

This technique manipulates the equilibrium nuclear magnetisation of a material using radio frequency fields. The resultant information gained from the response of the system is used to understand the atomic environment of the material. An outline of the underlying physical principles that are important in NMR is described using a semi-classical approach. A more in-depth understanding of the area can be obtained from Slichter [1], Abragam [2] and Harris [3].

2.2.1 Classical Treatment

In the semi-classical description of NMR, the nucleus is treated as a magnetic moment which precesses about a magnetic field \mathbf{B}_0 that is conventionally taken to be in

the z-direction. From quantum mechanics this is related to the angular momentum of the nucleus $\mathbf{I}\hbar$ by the equation

$$\boldsymbol{\mu} = \gamma\hbar\mathbf{I} = g\mu_N\mathbf{I} \quad (2.1)$$

where γ is the gyromagnetic ratio, specific to each nuclei. The unit of the nuclear magnetic moment is the nuclear magneton

$$\mu_N = \frac{e\hbar}{2m_p} \approx 5.05 \times 10^{-27} J.T^{-1}. \quad (2.2)$$

The equation of motion for this spin can be written

$$\frac{d(\mathbf{I}\hbar)}{dt} = \boldsymbol{\mu} \times \mathbf{B}_0 \quad (2.3)$$

and therefore

$$\frac{d\boldsymbol{\mu}}{dt} = \boldsymbol{\mu} \times \gamma\mathbf{B}_0. \quad (2.4)$$

In the situation where \mathbf{B} is constant with time, $\boldsymbol{\mu}$ precesses about \mathbf{B} , with the angle separating them remaining constant.

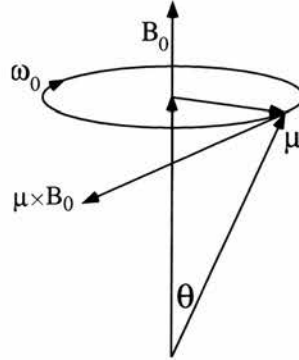


Figure 2.1: Larmor precession of $\boldsymbol{\mu}$ round \mathbf{B}_0 due to torque $\boldsymbol{\mu} \times \mathbf{B}_0$.

A useful technique in NMR is the transformation from the static laboratory frame (x,y,z) to a rotating reference frame (x',y',z') where z' is coincident with z . The field experienced by the moment in the frame rotating with angular frequency ω' is,

$$\mathbf{B}_{rot} = \left(B_0 - \frac{\omega'}{\gamma} \right) \hat{z}' \quad (2.5)$$

When

$$\omega' = \omega_0 = \gamma B_0 \quad (2.6)$$

the moment does not experience an effective field and is fixed along one direction in the rotating frame. Transforming back into the laboratory frame, the angular frequency of precession of the moment about \mathbf{B} is

$$\omega_0 = -\gamma B_0. \quad (2.7)$$

2.2.2 The Bloch Equations

The quantisation of the angular momentum restricts I to integer and half integer values. In the presence of a field there is an interaction energy, which is described by the Zeeman Hamiltonian

$$\mathcal{H}_Z = -\gamma \hbar B_0 I_Z \quad (2.8)$$

where I_z goes in integer steps from $-I$ to $+I$.

The high temperature limit can always be taken in conventional NMR so, from elementary statistical mechanics, the nuclear magnetisation is given by

$$M = \frac{n \gamma_n^2 \hbar^2 I(I+1)}{3k_B T} B_0 \quad (2.9)$$

and the static susceptibility is defined as

$$\chi_0 = \frac{M}{H} = \frac{\mu_0 M}{B_0}. \quad (2.10)$$

The above described equilibrium magnetisation is not obtained instantly upon the application of an external field. If at $t=0$ an unmagnetised specimen is placed in a magnetic field then the magnetisation will increase from the initial value $M=0$ to a final value $M=M_z$.

A phenomenological approach to the time dependence of the macroscopic nuclear magnetisation was first proposed by Bloch[4]. For a spin-1/2 system the relaxation back to equilibrium can be expressed

$$\frac{dn}{dt} = \frac{n_0 - n}{T_1} \quad (2.11)$$

n_0 is the thermal equilibrium population, n is the instantaneous population and T_1 is the time constant

$$\frac{dM_z}{dt} = \frac{M_0 - M_z}{T_1}. \quad (2.12)$$

Taking into account the effect of the rotating magnetic field which appears as the z -component of a torque on the magnetisation

$$\frac{dM_z}{dt} = \frac{M_0 - M_z}{T_1} + \gamma(\mathbf{M} \times \mathbf{H})_z. \quad (2.13)$$

In thermal equilibrium in a static field the magnetisation is parallel to that field with vanishing components along the other axes;

$$\frac{dM_x}{dt} = \gamma(\mathbf{M} \times \mathbf{H})_x - \frac{M_x}{T_2} \quad (2.14)$$

$$\frac{dM_y}{dt} = \gamma(\mathbf{M} \times \mathbf{H})_y - \frac{M_y}{T_2}. \quad (2.15)$$

A new relaxation time is introduced, T_2 , which is different from T_1 .

2.2.3 Pulsed NMR

In conventional NMR the probe radiation is employed continuously and either the field or frequency tuned until the resonance condition is satisfied. The pulse technique however, uses short bursts of radiation at a fixed magnetic field. The frequency associated with a pulse is called the carrier frequency and this is chosen to be close to resonance for the nucleus of interest.

Linear and circular polarisation of rf fields

Experimentally the rf field is produced by an alternating current in a solenoid and is linearly polarised along the axis of the solenoid. This field can be represented as two counter rotating fields of the same angular frequency but each with half the total amplitude

$$2B_1 \cos(\omega_{RF}t) = B_1(e^{i\omega_{RF}t} + e^{-i\omega_{RF}t}). \quad (2.16)$$

This is applied perpendicular to the static field. Transforming to a rotating reference frame it is evident that one sense of rotation is fixed in the x' - y' plane whilst the other rotates at 2ω . Conventionally the direction along which the static component lies is chosen to be the x' -axis. Only one sense of the rotation can interact strongly with the nuclear moments and the effective field in the rotating frame can be written

$$\mathbf{B}_{eff} = \left((B_0 - \frac{\omega_{RF}}{\gamma})\hat{z}' + B_1\hat{x}' \right). \quad (2.17)$$

At the resonance frequency, the effective field experienced by the system is simply \mathbf{B}_1 , the rotating magnetic field. If applied to a system in equilibrium with its magnetisation vector parallel to \mathbf{B}_0 , then the vector will precess about the effective field, or rf field, in the rotating frame. After a time τ , the pulse length, the magnetisation will have rotated by an angle

$$\theta = \gamma B_1 \tau. \quad (2.18)$$

The duration can be selected to be any value allowing the experimenter to place the magnetisation along any chosen direction. Two cases deserve attention, firstly $\theta = \pi/2$, the 90° pulse after which the moments lie along the y' direction. For $\theta = \pi$, the 180° pulse, this simply inverts the magnetisation vector.

Free Induction Decay

Application of a 90° pulse to a system of spins in thermal equilibrium results in the magnetisation vector lying along the y' -axis. In the laboratory frame this is precessing at ω_0 . Consequently a signal will be observed which is attenuated as transverse, spin-spin, relaxation occurs. The simplest form of transverse relaxation is

$$A(t) = A(0)e^{-t/T_2} \quad (2.19)$$

where T_2 is the transverse relaxation time, a measure of how quickly the spins de-phase. The plot of intensity against time is referred to as a free induction decay or FID. Generally a FID decays faster than expected from spin-spin relaxation. This is due to field inhomogeneities and the time constant associated with such effects is T_2^* . An example is given in Figure 2.2.

Fourier Transforms

Fourier transforms allow representations in the time domain to be transformed to equivalent representations in the frequency domain and vice versa. The Fourier transforms are given below

$$A(t) = \frac{1}{2\pi} \int_{-\infty}^{\infty} A(\omega) \exp(i\omega t) d\omega \quad (2.20)$$

$$A(\omega) = \int_{-\infty}^{\infty} A(t) \exp(-i\omega t) dt. \quad (2.21)$$

This technique is used to convert the free induction decay in the time domain, into a peak in the frequency domain. A typical FID and its Fourier transform are shown in the Figure 2.2.

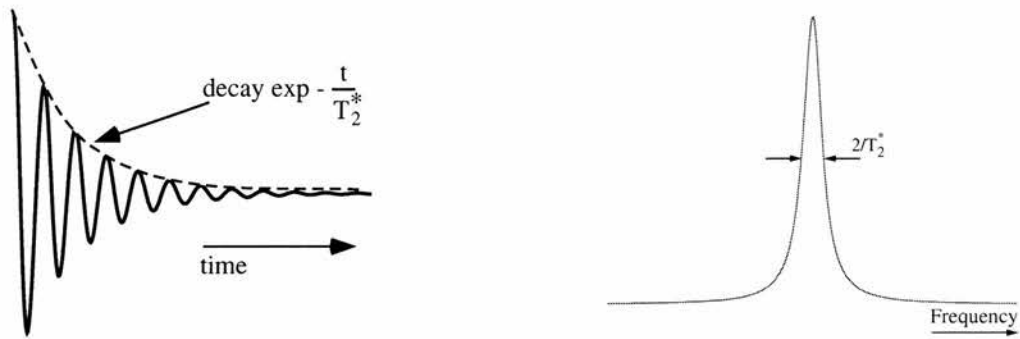


Figure 2.2: A typical FID and its Fourier Transform.

Spin echoes

A 90° - τ - 180° pulse sequence, referred to a spin or Hahn[5] echo sequence, leads to the formation of echoes. An example is shown in Figure 2.3

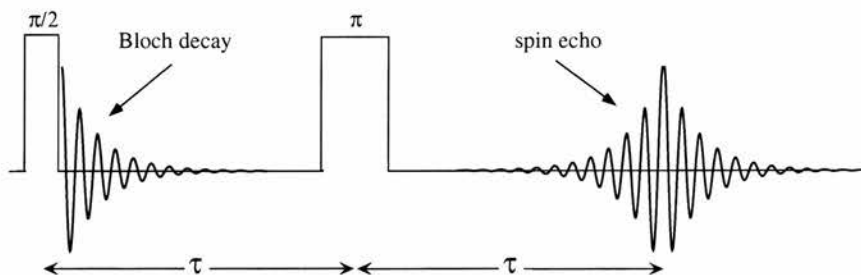


Figure 2.3: Hahn spin-echo sequence

After the initial pulse, the spread of magnetic field inhomogeneity causes de-phasing of the spins. The second pulse is applied after a further time τ . This results in a change of sign of the phase of the precession differences, so that spins that are precessing at faster rates are now behind in phase compared to those precessing at slower rates. At a time $t=\tau$ after the π pulse the bulk magnetisation reforms as the spins rephase. The process is shown below in Figure 2.4

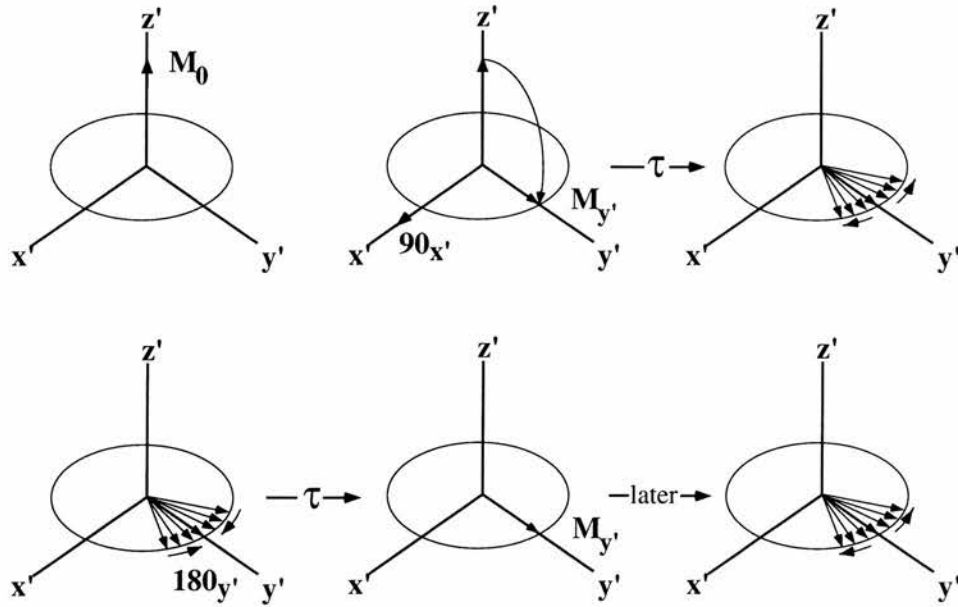


Figure 2.4: The spin echo sequence, as observed in the rotating frame, showing initial dephasing and the refocussing pulse

2.2.4 Nuclear spin interactions

The total energy associated with a nucleus of non-zero spin ($I_Z \neq 0$) can be expressed by the following Hamiltonian

$$\mathcal{H} = \mathcal{H}_Z + \mathcal{H}_1 + \mathcal{H}_D + \mathcal{H}_Q + \mathcal{H}_K + \mathcal{H}_\sigma + \dots \tag{2.22}$$

where the Zeeman term is normally dominant. Perturbation theory can be applied to expand this Hamiltonian, the Zeeman component being the zeroth-order term. The other contributions, including the rotating magnetic field, may be considered as a first order perturbation, although for strong quadrupolar splitting a second order term is often required.

Zeeman Interaction

The Zeeman interaction describes the splitting of energy levels into components associated with different quantised orientations of magnetic moments, with respect to a strong magnetic field. The Hamiltonian describing this interaction \mathcal{H}_Z , for a static magnetic field \mathbf{H}_0 in the z -direction, is that shown in equation 2.23, where

I_z is the z-component of the nuclear spin and γ is the gyromagnetic ratio, which is specific to each nuclei

$$\mathcal{H}_Z = -\gamma\hbar I_z H_0. \quad (2.23)$$

The Larmor frequency for transition between adjacent states is given by

$$\nu_L = \frac{-\gamma H_0}{2\pi}. \quad (2.24)$$

\mathcal{H}_1 represents the interaction between the spin and the rotating magnetic field. This can be expressed in terms of the raising and lowering operators

$$I^+ = I_x + iI_y \quad (2.25)$$

$$I^- = I_x - iI_y \quad (2.26)$$

by

$$\mathcal{H}_1 = -\frac{\gamma\hbar H_1}{2} (I^+ e^{-i\omega t} + I^- e^{i\omega t}) \quad (2.27)$$

where I^+ is characteristic of absorptive transitions, increasing m , the magnetic quantum number, by 1, and I^- of radiative transitions, decreasing m by 1.

Nuclear dipole-dipole interaction

Nuclei can interact directly via their magnetic moments. For two spins $\mathbf{I}_{j,k}$ separated by a distance \mathbf{r} this can be written

$$\mathcal{H}_D = \frac{-\gamma_j \gamma_k \hbar^2}{r^3} (3(\mathbf{I}_j \cdot \mathbf{r})(\mathbf{I}_k \cdot \mathbf{r}) - \mathbf{I}_j \cdot \mathbf{I}_k). \quad (2.28)$$

The presence of a strong external magnetic field allows the separation of the Hamiltonian into secular (stationary) and non-secular (time-dependent) parts. For the case of homonuclear interaction this gives

$$\mathcal{H}_D^t = \gamma^2 \hbar^2 \frac{(3 \cos^2 \beta_{jk} - 1)}{2r^3} (\mathbf{I}_j \cdot \mathbf{I}_k - 3I_{z,j} I_{z,k}). \quad (2.29)$$

The superscript 't' indicated 'truncated' Hamiltonian with the non-secular terms dropped. The physical origin of the line broadening due to the dipole-dipole interaction is a local field at the site of the nucleus due to each of the neighbouring nuclei, which will cause the Zeeman energy levels to shift slightly, corresponding to a slight shift in the NMR frequency. Local field variations throughout the sample occur as more, or fewer, neighbouring nuclei are spin up or spin down.

Electrical Quadrupolar Interaction

Nuclear resonance is not a purely magnetic effect but is also a sensitive probe of electric effects in molecules and solids. Nuclei that have asymmetric charge distributions, $I > 1/2$, have a nuclear quadrupole moment eQ , which interacts with the electric field gradient (efg) at the nuclear site. The classical equation interaction energy of a nuclear charge distribution with an external electric potential

$$E = \int \rho(r)V(r)d\tau. \quad (2.30)$$

A Taylor expansion of the potential V gives

$$E = V(0) \int \rho(r)d\tau + \sum V_{\alpha}(0) \int \alpha\rho(r)d\tau + \sum \frac{V_{\alpha\beta}}{2} \int \alpha\beta\rho(r)d\tau + \dots \quad (2.31)$$

where $\alpha, \beta = x, y, z$. Of these terms only the third has an orientation dependence and therefore any influence on nuclear resonance. This interaction is described by a tensor and it is possible to choose a set of axes for the efg such that only the main diagonal values are non-zero. This is the principal axis system (PAS).

The Hamiltonian describing the quadrupolar interaction

$$\mathcal{H}_Q = \frac{e^2qQ}{4I(2I-1)} [3I_z^2 - I(I-1) + 1/2\eta_q(I_+^2 + I_-^2)] \quad (2.32)$$

where η is the asymmetry parameter

$$\eta = \frac{V_{XX} - V_{YY}}{V_{ZZ}}. \quad (2.33)$$

As a first order perturbation the presence of a nuclear electric quadrupole interaction shifts the Zeeman levels. In polycrystalline samples the variation of orientation to the external field from crystallite to crystallite leads to a spreading of resonances and therefore broadening of the resonance. This is demonstrated in Figure 2.5.

2.2.5 The Magnetic Shift

Experimentally, the resonance line is displaced from the position expected for the bare nucleus. This is known as the magnetic shift (ΔK) and results from magnetic fields that the nucleus experiences in addition to the applied field B_0 . The total magnetic shift can be separated into two contributions, the chemical shift and the Knight shift

$$\Delta K = \frac{\Delta B}{B_0} = \sigma + K. \quad (2.34)$$

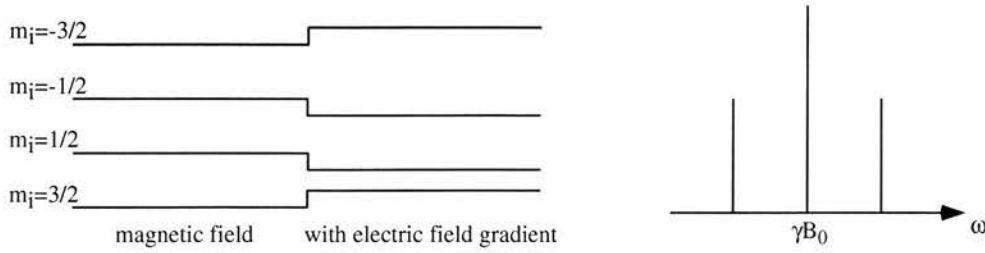


Figure 2.5: Splitting of the m_I degeneracy by quadrupolar effects and the corresponding frequencies. To first order, each level is shifted by the same energy with the central transition energy difference remaining unaffected.

In practice the total magnetic shift of a sample has to be compared to that of a known material, temperature independent.

The Chemical Shift

This interaction arises from the motion of electrons in the neighbourhood of the nucleus. Under the influence of an external magnetic field current will be induced. These will in turn produce an induced magnetic field modifying that which is experienced at the nucleus. This induced field is proportional to the applied field. The Hamiltonian shown in the equation below illustrates this effect,

$$\mathcal{H} = \gamma \mathbf{I} \cdot \sigma \cdot \mathbf{B}_0 \quad (2.35)$$

where σ is the shielding tensor. Chemical shifts generally have an isotropic component σ and an anisotropic component, referred to as the CSA (chemical shift anisotropy).

The Knight Shift

The unpaired electrons in a metal produce shifts which are many times larger than the ordinary shifts observed in diamagnetic materials. This Knight shift[6], arises from the polarisation of the conduction electrons which contribute an extra magnetic field at the nucleus. Since these electrons are not localised, each nuclear spin experiences the field from all electrons at the same time. The shift resulting from the Fermi contact interaction, s-wave metal, is given below

$$K = \frac{\Delta\nu}{\nu_0} = \frac{8\pi}{3} \langle |\psi_k(0)|^2 \rangle \chi_p M_0 \quad (2.36)$$

where χ_p is the Pauli susceptibility. This interaction can be written as the following Hamiltonian

$$\mathcal{H}_K = -\gamma\hbar\mathbf{I} \cdot \hat{\mathbf{K}} \cdot \mathbf{B}_0 \quad (2.37)$$

where $\hat{\mathbf{K}}$ is the Knight shift tensor. The interaction can be written in its principal axis system as follows

$$K = K_{iso} + \frac{1}{2}\Delta_K(3\cos^2\beta - 1 + \eta_K \sin^2\beta \cos 2\alpha) \quad (2.38)$$

where α and β are angles that describe the PAS with respect to the applied magnetic field.

For simple metals, the Knight shift can be described by the contact interaction. Korringa[7] derived the relationship between the spin-lattice relaxation time (T_1) and the Knight shift (K) when both are dominated by the contact interaction

$$T_1TK^2 = \left(\frac{\hbar}{4\pi k_B}\right) \frac{\gamma_e^2}{\gamma_n^2} \quad (2.39)$$

2.2.6 Magic Angle Spinning (MAS)

The absorption lines of solid samples have typical linewidths of tens of kilohertz, owing largely to the variation in local magnetic field due to the dipole-dipole interaction between nuclei and contributions from the anisotropy of the Knight shift. In liquids, rapid and random molecular motion averages these effects to zero giving linewidths several orders of magnitude narrower than in solids.

Mechanical rotation of a solid sample about an axis making an angle θ with respect to the static field direction can result in dramatic narrowing of the linewidth. This technique was originally employed by Andrew et al.[8] to remove the effects of dipolar broadening of the resonance spectra of solids. The rotation of a sample in a magnetic field is shown in Figure 2.6.

The angle β was used earlier in the description of the various interactions (eg equations 2.29 and 2.38) and can be expanded in terms of two other angles and the rotation angle $\omega_r t$ to give the following equation[9]

$$\begin{aligned} 3\cos^2\beta - 1 &= \frac{1}{2}(3\cos^2\theta - 1)(3\cos^2\alpha - 1) \\ &\quad + \frac{3}{2}\sin 2\theta \sin 2\alpha \cos \omega_r t \\ &\quad + \frac{3}{2}\sin^2\theta \sin^2\alpha \cos 2\omega_r t. \end{aligned} \quad (2.40)$$

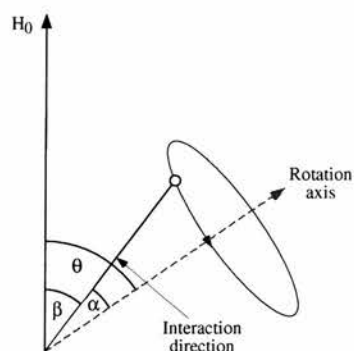


Figure 2.6: Geometry of Magic Angle Spinning. The rotation of a sample in a magnetic field can be described by a set of angles.

The parameter θ is controllable experimentally, the first term goes to zero when $\theta=54.7^\circ$, the magic angle. The main result is the disappearance of Dipolar broadening. Similarly the CSA averaged to zero and spin-spin interaction to its scalar and antisymmetric terms. This technique thus leads to a greatly reduced linewidth of solid samples. Unfortunately, with greater accuracy of the resonance frequency comes the loss of information about the anisotropic interactions.

Magic angle spinning significantly narrows the NMR resonance and concentrates its intensity into a smaller frequency range. The time dependent terms in equation 2.40 produce resonances at $\omega_r \pm n\omega_r$ relative to the main resonance (where n is an integer) and whose intensities are related to the static spectrum near that frequency.

2.2.7 NMR Instrumentation

Basic Spectrometer Design

A schematic of the main components involved in a pulsed NMR spectrometer is presented in Figure 2.7. The sample is contained within the RF coil inside the static magnetic field B_0 , this defining the z-axis. In essence the NMR probe is an LC circuit tuned to the Larmor frequency of interest. In standard NMR spectrometers this coil is used as both the transmitter and receiver.

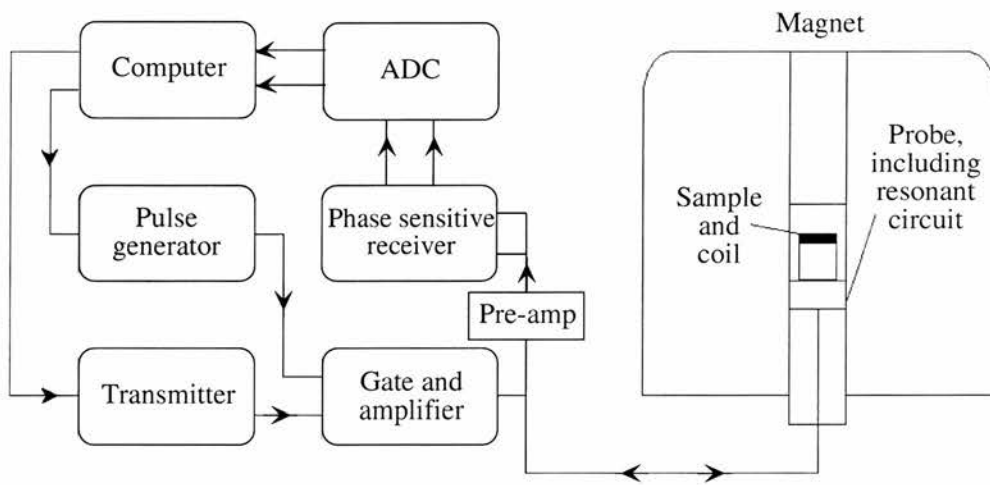


Figure 2.7: Schematic of typical NMR spectrometer

An RF frequency generator is used in continuous operation and pulses of power released through a gate controlled by a pulse generator. This signal is then amplified before being transmitted to the coil. The resultant sinusoidal RF current in the coil generates a magnetic field which effects the sample magnetisation, H_1 . These changes are sensed by the receiver coil and then amplified before being processed.

Unsurprisingly this is not a perfect system. A particular problem arises from the double use of the RF coil, there is always leakage of the pulse into the receiver amplifier. A finite time is required for the RF pulse to decay, known as ringdown. This results in a delay before the signal can be measured, called deadtime. Clever use of pulses can overcome this problem.

The Bruker MSL 500 Spectrometer

All NMR measurements were performed using the Bruker MSL 500 spectrometer described herein. An Oxford Instruments superconducting cryomagnet provides the static field of 11.74T. This has a bore of 89mm into which the probes are inserted. A continuous frequency range from 17 to 215MHz is available with a low frequency transmitter and another allowing work with protons at 500MHz.

Pulse Programs

The Bruker specific programming language allows a variety of complex pulse sequences with many variable parameters. Three basic types of pulse sequences were used to obtain data. The simplest of these is the standard QUADCYCL.PC single pulse program that is illustrated below

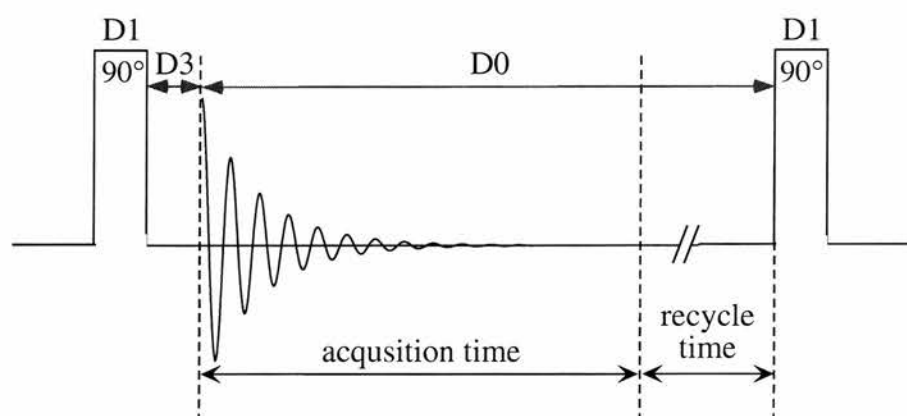


Figure 2.8: Schematic representation of a 'single pulse' pulse program

This pulse sequence consists of a single 90° pulse and a phase cycle that is 8 acquisitions in length, repeating each phase twice. The sequence begins with the transmitter gating, producing a pulse of duration D1 (pulse width). Ringing in the resonant circuit prevents the signal being detected immediately. A small delay D3 is encountered before the receiver is switched on and acquisition begins. The duration of acquisition is dependent on the frequency sweep width and the number of data points to be collected. Finally a delay occurs before changing the phase of the applied rotating field and repeating the sequence.

Another pulse sequence that was used was SAM1ECHO.PC which is a Hahn echo technique, as described earlier. Two pulses used with the second twice the duration of the first. This is useful when the deadtime is a significant fraction of the FID. When used with MAS it is preferable for the delay between pulses to be equal to an integral number of rotor periods. Studies of many materials using Fourier transform NMR, which have broad resonances, would be impossible without echo techniques.

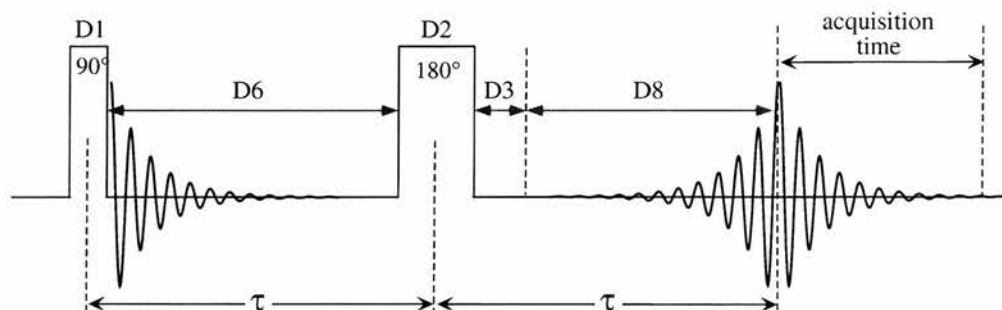


Figure 2.9: Schematic representation of a spin-echo sequence

The third sequence is the saturation recovery technique used to measure T_1 relaxation, and is shown in Figure 2.10.

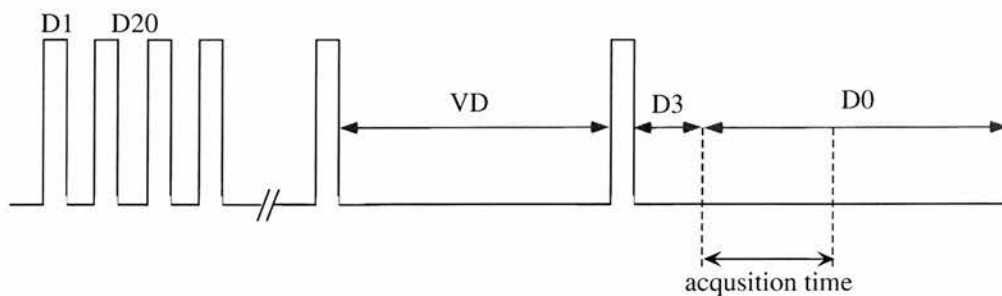


Figure 2.10: Schematic of saturation recovery pulse sequence

The sequence begins with a 'comb' of 90° pulses. This sets the magnetisation to zero and the recovery is sampled after a delay by application of another 90° pulse. The number of pulses in the comb is dependent upon how close each pulse is to 90° . A comb of 20 pulses was sufficient for all measurements presented here. The magnetisation recovery is given by

$$M_\tau = M_0(1 - \exp(-\tau/T_1)) \quad (2.41)$$

where M_0 is the magnetisation at equilibrium and τ the time delay until the recovery is sampled.

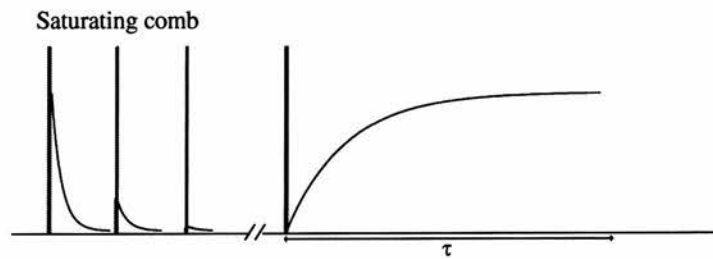


Figure 2.11: The time dependence of the nuclear magnetisation in a saturation recovery experiment

2.3 Muon Spin Relaxation (μ SR)

In contrast to NMR, in which specific target nuclei are required, μ SR is universally applicable as muons can be implanted in any material. The acronym μ SR refers to a number of techniques namely muon spin rotation, resonance or relaxation. It is the latter of these three that is used in this thesis and is discussed below.

2.3.1 Properties of the Muon

Positive muons are unstable particles which decay with a half-life of $\tau = 2.2\mu\text{s}$ into a positron, a μ -neutrino and a μ -antineutrino as shown below.



The physical properties of the positive muon are summarised in following table.

Table 2.1: The fundamental properties of the positive muon

Mass m_μ	$206.8 \times m_e$
Spin I_μ	$1/2$
Charge Q_μ	$+e$
Magnetic moment μ_μ	$3.183\mu_N$
Gyromagnetic ratio $\gamma_\mu/2\pi$	$135.5\text{MHz}\cdot\text{T}^{-1}$
Lifetime τ_μ	$2.197\mu\text{s}$

The spin and magnetic moment of the positive muon are parallel although they are anti-parallel to the muon momentum direction. In the decay process, parity violation causes the positrons to be emitted preferentially along the direction of the muon spin. The probability of detecting a positron as a function of the angle between the muon spin polarisation and the positron detector is given by:

$$P(\theta) = 1 + a_0 \cos \theta \quad (2.43)$$

The initial asymmetry parameter, a_0 , is strongly dependent on the energy of the positron emitted, ranging between a value of unity for the highest energy down to $1/3$. The angular probability distributions for these two extremes are shown in Figure 2.12.

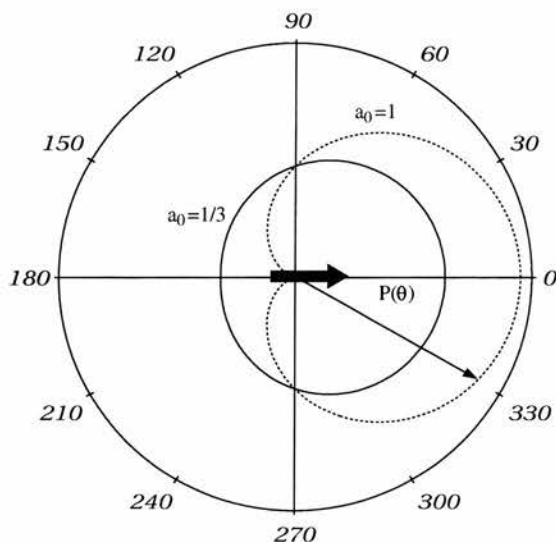


Figure 2.12: Polar plot of the angular probability distribution $P(\theta)$ for positron emission from muon decay. $a_0=1$ is shown as the dashed line and $a_0=1/3$ is the solid line.

2.3.2 The μ SR Experiment

Upon implantation into a sample, the muon loses kinetic energy by ionising outer-shell electrons, finally stopping at an interstitial site. Since no magnetic interactions are involved in this process the initial spin polarisation is preserved. The local internal magnetic field at a muon site originates from dipolar interaction with surrounding nuclear or electronic spins, as well as contact hyperfine fields from the spin density at the muon site. This means that there is a decay of the muon polarisation.

This depolarisation is monitored by measuring the positron decay product by detectors positioned front and back of the sample. A schematic of the experimental geometry for longitudinal field μ SR is shown in Figure 2.13. The number of positrons counted in the forward and backward detectors is given by

$$N_{F,B}(t) = N_{F,B}(0) \exp\left(-\frac{t}{\tau_\mu}\right) [1 \pm G_z(t)] + b \quad (2.44)$$

On a pulsed muon source, for which the beam-borne background is negligible, the depolarisation function is extracted from the measured count rates by taking the

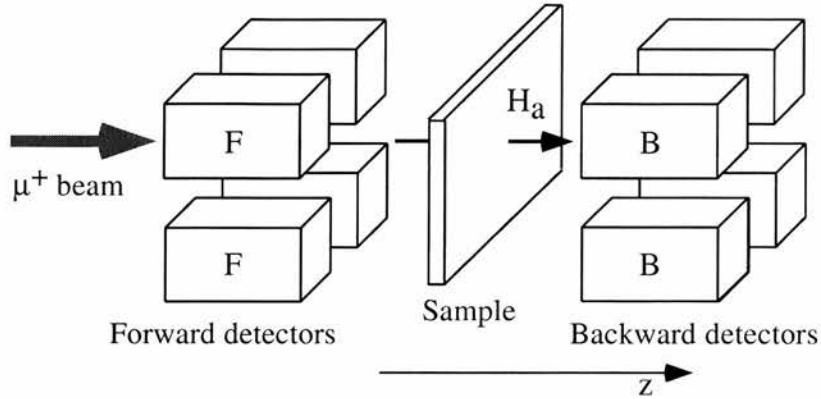


Figure 2.13: Schematic of the experimental arrangement for a muon spin relaxation experiment. H_a shows the direction of the longitudinal field, which is turned off in a zero-field experiment.

ratio

$$A(t) = \frac{N_F(t) - \alpha N_B(t)}{N_F(t) + \alpha N_B(t)} = a_0 G_z(t) \tag{2.45}$$

α is obtained from a fit to transverse field data measured in a field of 2-4mT. This calibration constant corrects for detector efficiency and path differences experienced by positrons due to sample thickness and so must be determined for each new sample.

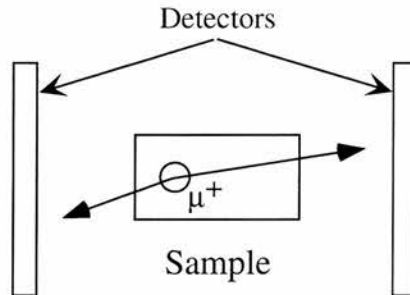


Figure 2.14: Schematic of possible differences in the path lengths positrons may travel to reach the detector banks. Those travelling to the right have more mass to travel through and further to traverse resulting in a reduction in the number of positrons detected.

The appropriate α is found when the transverse field spectrum calculated with this expression oscillates symmetrically about the time axis. For typical μ SR experiments a_0 will take a value of between 0.2 and 0.27[10].

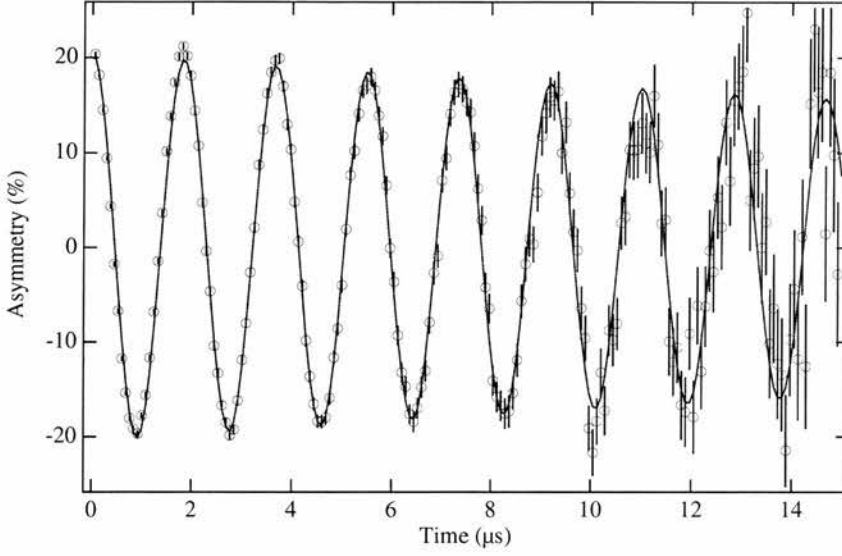


Figure 2.15: Muon spin rotation spectra of LiTi_2O_4 at 290K in a transverse magnetic field of 4mT obtained on the ARGUS spectrometer, used to obtain the calibration factor α , which was found to be 1.108 for this measurement.

2.3.3 Muon Depolarisation Functions

Static fields and muons

For a system of concentrated nuclear moments which are randomly oriented and static on the timescale of the muon lifetime, the local field distribution can be represented by a Gaussian function. Assuming that the random local fields are also isotropic, then each orthogonal component can be described by,

$$P^G(H_i) = \frac{\gamma_\mu}{\Delta\sqrt{2\pi}} \exp\left(-\frac{\gamma_\mu H_i^2}{2\Delta^2}\right) \quad (i = x, y, z) \quad (2.46)$$

where Δ is the Gaussian field distribution width. After implantation, assuming spins initially aligned along the z-axis, the time evolution of the muon spin m_z is given by,

$$m_z = \cos^2\theta + \sin^2\theta \cos(\gamma_\mu Bt) \quad (2.47)$$

where B is the magnitude of the field experienced and θ the angle between the B and z-axis.

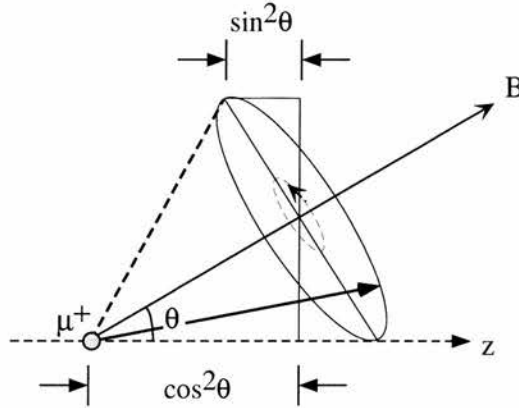


Figure 2.16: Muon spin precession around the internal magnetic field B.

The depolarisation function, or *zero field static Gaussian Kubo-Toyabe function*[11], is given by the statistical average of m_z ,

$$G_z^{GKT}(t) = \frac{1}{3} + \frac{2}{3}(1 - \sigma^2 t^2) \exp\left(-\frac{\sigma^2 t^2}{2}\right) \quad (2.48)$$

the nuclear depolarisation rate, σ , being related to the second moment of the field distribution by,

$$\sigma^2 = \gamma_\mu^2 M_2 = \gamma_\mu^2 \Delta^2. \quad (2.49)$$

Application of an external field parallel to the direction of initial muon spin alters the form of the depolarisation function producing the *applied field static Kubo-Toyabe function*[11]

$$G_z^{GKT}(t, \omega_L) = 1 - \frac{2\sigma^2}{\omega_L^2} \left(-\exp\left(-\frac{\sigma^2 t^2}{2}\right) \cos(\omega_L t) \right) + \frac{2\sigma^4}{\omega_L^3} \int_0^t \exp\left(-\frac{\sigma^2 \tau^2}{2}\right) \sin \omega_L \tau d\tau \quad (2.50)$$

where ω_L is the muon precession frequency about the external field. With increasing field the depolarisation becomes dominated by the contribution from the external field. In this way the muon spin can be decoupled from the random internal fields.

Similar expressions exist for a system of dilute static moments. In this case a Lorentzian field distribution of the following form is appropriate

$$P(H_i) = \frac{\gamma_\mu}{\pi} \frac{\Lambda}{(\Lambda^2 + \gamma^2 H_i^2)} \quad (2.51)$$

where Λ again describes the field width distribution. The depolarisation function obtained is the *zero-field static Lorentzian Kubo-Toyabe function*[12], given below.

$$G_z^{LKT}(t) = \frac{1}{3} + \frac{2}{3}(1 - \Lambda t) e^{-\Lambda t} \quad (2.52)$$

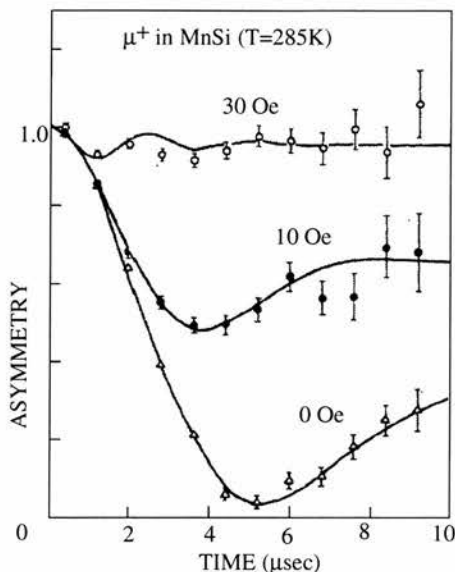


Figure 2.17: ZF- and LF- μ SR spectra observed in MnSi at RT. The muon spins are depolarised by nuclear dipolar fields, whilst this depolarisation is severely reduced in a longitudinal field of 30Oe.

Muon diffusion

A muon jumps between sites with a mean hopping frequency ν . In the strong collision model the muon experiences a sudden change in the local field and there is no correlation between the fields before and after the jump. In this model, the evolution of the polarisation of the muon following a jump is described by the static Kubo-Toyabe function with an initial amplitude determined by the polarisation immediately before the jump. The total polarisation at time t is a superposition of the polarisation of each muon at that time. The probability that a muon has not experienced a jump is given by $e^{-\nu t}$, providing a contribution to the total polarisation described by:

$$G_z^{(0)}(t) = G_z^{GKT}(t)e^{-\nu t} \quad (2.53)$$

The total polarisation is given by the dynamic Kubo-Toyabe. This equation is the sum of the contributions from those muons that have not jumped and those that have jumped n times.

$$G_z^{DKT}(t) = G_z^{(0)}(t) + \nu \int_0^t G_z^{DKT}(t-t')G_z^{(0)}(t')dt' \quad (2.54)$$

This is a complicated function for which an analytical approximation exists. The analytical approximation in zero longitudinal field is,

$$G_z^{DKT}(t) = \exp\left(-\frac{2\sigma^2}{\nu^2}(e^{-\nu t} - 1 + \nu t)\right) \quad (2.55)$$

Dynamic spin systems

If the magnetic field at the muon site is fluctuating, the muon will experience a time average of the total field distribution, effectively reducing the total distribution width. In the case of fluctuating atomic spins, the modulation cannot be assumed to be sudden and uncorrelated, as in the strong collision model. For dynamic spin systems, the autocorrelation function is a better description of the field fluctuations at the muon site,

$$\frac{\langle H(0)H(t) \rangle}{\langle H(0)^2 \rangle} = q_H(t) = \exp(-\nu t) \quad (2.56)$$

In a conventional paramagnet, there is no spin-spin correlation and therefore a unique spin relaxation time at a particular temperature, τ , is obtained. This results in a simple exponential function, where ν is the inverse of the spin relaxation time. This then leads to a muon depolarisation function due to fluctuating atomic spins in the fast fluctuation limit which is given by,

$$G_z(t) = \exp(-\lambda t) \quad (2.57)$$

where λ is the atomic contribution to the muon depolarisation rate. This is related to the atomic field distribution width Δ and the characteristic spin fluctuation time τ_c by

$$\lambda = \frac{\gamma_\mu^2 \Delta^2 \tau_c}{(1 + \omega_0^2 \tau_c^2)} \quad (2.58)$$

where ω_0 is the muon precession frequency due to the external longitudinal field. In a magnetic transition a characteristic divergence in λ is observed, resulting from an increase in internal field and a slowing of dynamic fluctuations.

2.3.4 Instrumentation

Our μ SR measurements were carried out on the ARGUS spectrometer at the ISIS pulsed muon and neutron facility at the Rutherford Appleton Laboratory, UK. High intensity pulses of spin polarised muons are produced, having width of 70ns, FWHM, at a repetition rate of 50Hz. A diagram of the ARGUS spectrometer is shown in Figure 2.18.

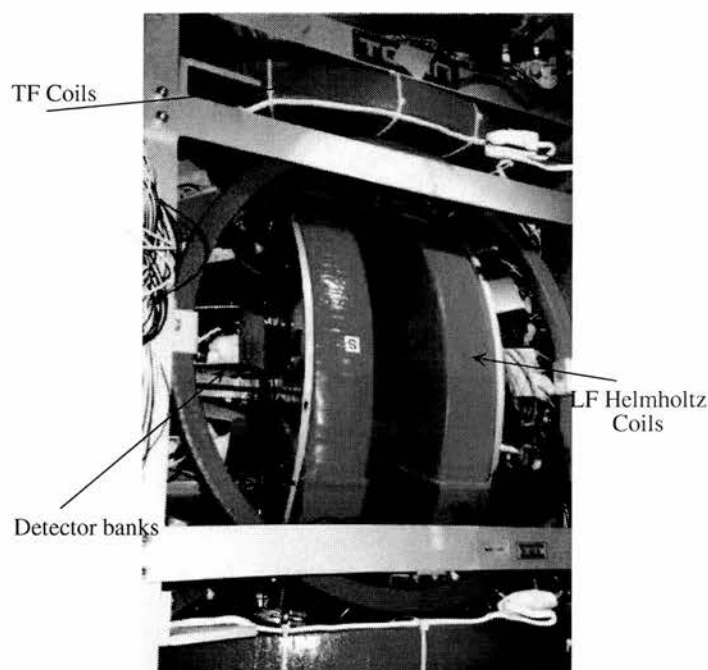


Figure 2.18: The ARGUS spectrometer located on the RIKEN-RAL muon facility at the Rutherford Appleton Laboratory.

The ARGUS spectrometer consists of 192 forward and backward detector banks. Each is a positron scintillator counter which captures positrons resulting from muon decay. Photons are produced, directed and amplified before being transmitted to the data acquisition electronics. Longitudinal fields of up to 0.39T are possible. A set of 3 orthogonal Helmholtz coils at the sample position is used to cancel the magnetic field of the earth for precise zero-field μ SR experiments.

References

- [1] C. P. Slichter, *Principles of Magnetic Resonance Second Edition* (Springer-Verlag, New York, 1978).
- [2] A. Abragam, *Principles of Nuclear Magnetic Resonance* (Oxford Science Publications, Hong Kong, 1996).
- [3] R. K. Harris, *Nuclear Magnetic Resonance Spectroscopy* (Longman Scientific and Technical, London, 1987).
- [4] F. Bloch, *Physical Review* **70**, 460 (1946).
- [5] E. L. Hahn, *Physical Review* **80**, 580 (1950).
- [6] C. H. Townes, C. Herring, and W. D. Knight, *Physical Review* **77**, 852 (1950).
- [7] J. Korringa, *Physica* **16**, 601 (1950).
- [8] A. R. Andrew, *Nature* **183**, 1659 (1958).
- [9] I. J. Lowe, *Physical Review Letters* **2**, 285 (1959).
- [10] J. H. Brewer and R. Cywinski, in *Muon Science* (IOP, Bristol, 1998).
- [11] R. S. Hayano *et al.*, *Physical Review B* **20**, 850 (1979).
- [12] R. Kubo, *Hyperfine Interactions* **8**, 731 (1981).

Chapter 3

Sample Preparation and Characterisation Techniques

3.1 Introduction

The samples studied in this thesis were prepared at the University of St Andrews, with the exception of the thin films which were made in the Department of Physics and Astronomy, University of Leeds. Varying methods were used in the manufacture of the powder samples. Multilayer thin films were prepared by DC magnetron sputtering. Once made, the structural purity was checked using X-ray diffraction and in some cases it was beneficial to use neutron diffraction. These methods and associated theory are discussed herein.

3.2 Synthesis of YBCO-123 samples

3.2.1 Introduction

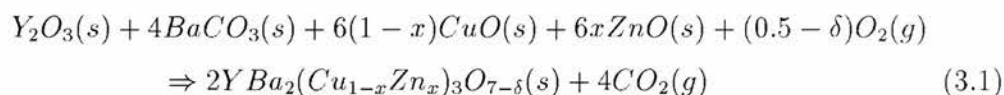
A series of doped $\text{YBa}_2(\text{Cu}_{1-x}\text{M}_x)_3\text{O}_{7-\delta}$ (YBCO) samples were prepared, where M=zinc or lithium. X-ray diffraction was used to confirm sample purity and structure. Oxygen content was determined by thermogravimetric analysis and was also inferred through lattice parameters from XRD studies.

Since the interest in these materials is primarily with the influence of doped impurities, knowledge of the site occupied and exact concentration is paramount. To this end a number of techniques were applied including, time of flight neutron

diffraction and atomic absorption spectroscopy.

3.2.2 Zn doped YBCO

All samples described herein were made in house using a horizontal tube furnace. The standard solid state sintering route was used, the reaction being described by the following equation



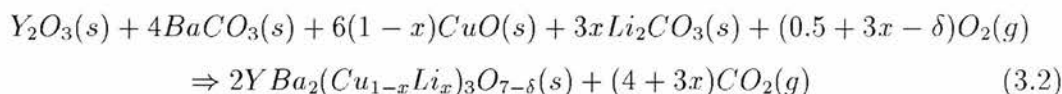
Starting materials were initially dried in a muffle furnace to remove unwanted moisture and then stored in a desiccator until required. Samples were synthesised with nominal compositions of $x = 0.00, 0.005, 0.01, 0.02$ and 0.03 . Appropriate molar amounts of the starting materials were weighed using a Sartorius Handy H51 four figure balance with an accuracy of $\pm 0.1\text{mg}$. These were thoroughly mixed and ground together in an agate mortar and pestle: agate has a smooth, non-porous surface which minimises contamination. The resultant fine grey powder was then cold pressed in a uni-axial die under a pressure of 2 kbar for approximately 10 minutes.

The pellets were placed in a quartz crucible and sintered overnight until black, then removed and reground. A further three days of high temperature sintering with intermediate grindings every 24 hours completed the reaction. This mixture was pelletised again and annealed at 925°C in a flowing oxygen environment for 14 hours. The temperature was reduced to 400°C in 7 hours, remaining there for a further 24 hours before slow cooling to room temperature. In the doped samples this final oxidation process was lengthened to 7 days to ensure oxygen homogeneity. Once cooled, the samples were immediately stored in a desiccator to preserve the oxygen content and prevent absorption of contaminants from the air.

The long reaction times and high temperatures are required due to the slow decomposition of $BaCO_3$ [1]. During sintering $BaCuO_2$ forms prior to the 123 phase which promotes the decomposition of $BaCO_3$. However the presence of this precursor at the grain boundary inhibits the diffusion of CO_2 . Consequently the regrinding and reheating sequence is required to expose new surfaces to each other and to eliminate the CO_2 completely. This also helps to ensure homogeneity of the reaction.

3.2.3 Li doped YBCO

The lithium doped samples were prepared by Martin Smith, department of chemistry, using a similar solid state technique as for the Zn doped, the reaction being described



These however, required more care due to the volatile nature of the dopant. To minimise Li loss, an overnight firing at 650°C was used to start the reaction without melting the lithium carbonate. The temperature was then raised to 860°C for two days to complete most of the calcination. The pellets were then cooled, reground and re-pelletised prior to a final firing at 960°C under air. Pellets were then cooled to 500°C in a muffle furnace under air and held at this temperature for 3-4 days to allow optimal oxygen uptake.

3.3 Synthesis of Lithium ramsdellite

3.3.1 Introduction

The $LiTi_2O_4$ samples for this work were prepared by Julian Tolchard, department of chemistry, University of St Andrews. The desired ramsdellite phase is a high temperature polymorph of the well known spinel structure. Starting materials were initially dried to remove unwanted moisture, except for the Ti metal as this would cause undesired oxidation.

The spinel form is produced in a 2 stage process. Firstly a precursor is prepared.



This is then reacted to create the desired $LiTi_2O_4$



Once prepared its purity is verified. It is then heated to above 925°C and held there for 36 hours before cooled quickly to preserve this phase whilst preventing the creation of spinel. Samples are normally wrapped in copper during this last

sintering. In our case samples were carbon wrapped to get higher temperature so that more ramsdellite was formed. A more extensive discussion of the preparation process can be found in Julian Tolchard's thesis[2].

3.4 Preparation of multilayers

3.4.1 Introduction

Sputtering is a well-established technique, discovered in the 1850's[3], and with the advent of modern vacuum technology it is now possible to deposit films of extremely high quality. Essentially it is the process of removing material from a target by the impact of energetic particles. This material is directed towards a surface where it will nucleate into islands and then grow into a film. Appropriate choice of target material allows deposition of a film of that material.

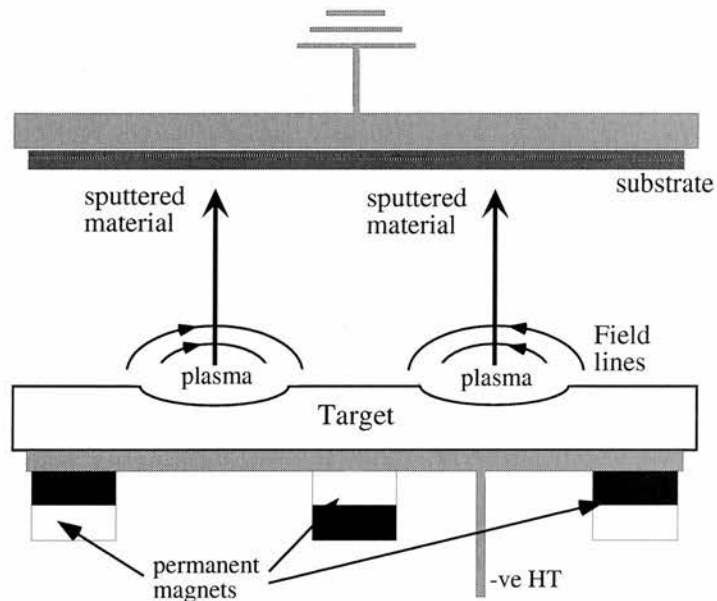


Figure 3.1: A magnetic cathode. The discharge is confined closely above the target by the magnetic field. Most target bombardment occurs below the racetrack, resulting in non-uniform target erosion.

The simplest way of striking up a discharge is to have a pair of electrodes in a low pressure gas and to apply a large voltage across them. An inert but heavy gas is required to provide enough impact on the target surface. This is normally argon.

This diode method produces poor quality samples. Improvements in the deposition quality can be achieved by the use of magnetic fields to provide confinement of the discharge plasma. A schematic of a dc magnetron is shown in Figure 3.1.

In this configuration the target is surrounded by permanent magnets creating a toroidal confinement field above the target. Trapped particles follow helical paths, resulting in a high density of impacts in this region, which is known as the ‘racetrack’.

3.4.2 Sputtering Facilities

The Superconducting/Ferromagnetic multilayer films were grown using the dc magnetron sputterer at the University of Leeds, under the supervision of Dr Chris Marrows. A picture of this sputterer is given in Figure 3.2.

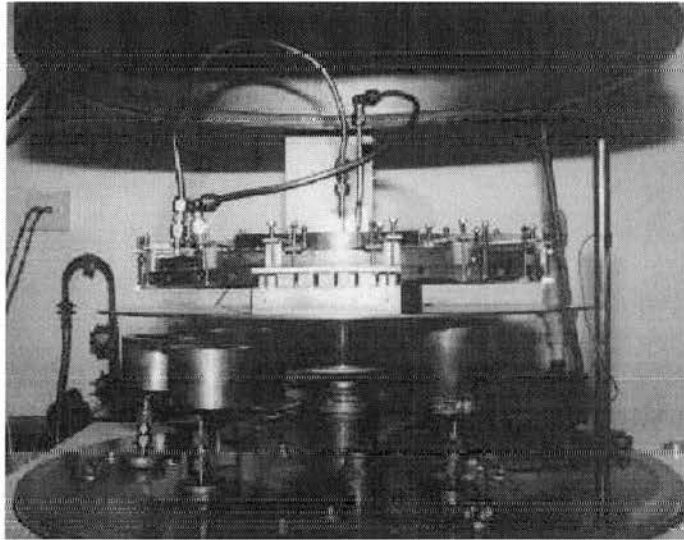


Figure 3.2: Inside view of the sputterer at the University of Leeds. The deposition sources are around the bottom, firing upwards.

In each vacuum cycle a total of 15 samples can be prepared. These are suspended from the large copper wheel immediately above a shutter. There are permanent magnets above the shutter hole, ensuring a uniform field in the plane of the sample. At the bottom of the system are the 6 magnetron sources. The substrate table and shutter are rotated with stepper motors allowing each to move separately.

A PC interface controls the sample table allowing any series of layers to be deposited. The deposition time over the gun is controlled in the same manner.

When a new target is used, a thin calibration sample of a known deposition time is prepared.

3.5 Structural characterisation

Diffraction is a non-destructive structural characterisation technique. It is well suited to both the identification of crystalline phases and compounds as well as analysis of thin-films and multilayers.

3.5.1 Diffraction Theory

In 1912 the German physicist Max von Laue realised that the regular array of atoms in a crystal could act as a natural 3-D diffraction grating for e-m radiation with wavelength comparable to atomic spacings[4]. These can be visualised as being arranged in planes with interspacing d , leading to the simple geometrical relation, Bragg's law[5]

$$n\lambda = 2d \sin \theta \quad (3.5)$$

When this law is satisfied diffracted beams are in phase and constructively interfere.

The diffraction phenomenon is a result of scattering. In the case of X-rays this is described by the interaction of the photons with the extra-nuclear electrons (Thompson scattering) whereas neutrons scatter primarily from the interaction between the neutron and the atom nucleus.

Incident particles with wavevector \mathbf{k}_i are scattered into a state with wavevector \mathbf{k}_f , with the wavevector (momentum) transferred by the neutron to the sample defined as

$$\mathbf{Q} = \mathbf{k}_i - \mathbf{k}_f \quad (3.6)$$

Bragg's law is satisfied when $\mathbf{Q} = \mathbf{G}_{hkl}$, the reciprocal lattice vector. The diffraction pattern of any crystal can be calculated by the structure factor

$$F_{hkl} = \sum_{r=1}^N f_r \exp(2\pi i(hx_r + ky_r + lz_r)) \quad (3.7)$$

where f_r is the form factor for atom type r . The intensity of scattered neutrons, or X-rays is given by

$$I \propto |F(\mathbf{G}_{hkl})|^2 \quad (3.8)$$

Powder diffraction experiments

In powder diffraction experiments, a collimated beam is incident upon a sample, all crystal planes being presented to the beam simultaneously. For a given wavelength, neutrons (x-rays) which satisfy the Bragg condition will be diffracted through an angle 2θ and will be located on the surface of a Debye-Scherrer cone.

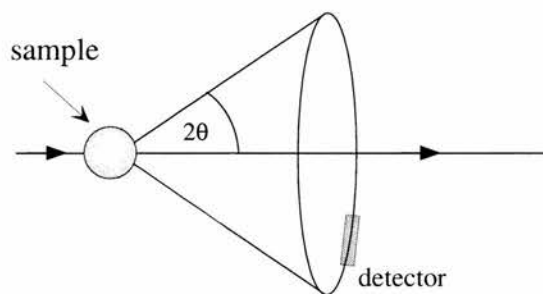


Figure 3.3: A Debye-Scherrer cone in a powder diffraction experiment

Typically the source is static while the sample and detector are rotated to satisfy the Bragg condition and keep the detector on the cone. In this way the detector rotates an angle 2θ and the sample by θ . A Philips PW3810 reflectance diffractometer, using Cu-K α radiation was used to collect data for this work.

3.5.2 Time of flight neutron diffraction

In time of flight neutron diffraction a pulse of neutrons with a distribution of wavelength λ , $n(\lambda)$, rather than a monochromatic beam, is incident on the sample. The pulses are diffracted by the sample and neutrons counted using a static detector of known position to the sample and neutron beam. The neutron wavelength and speed are related by the deBroglie equation

$$\lambda = \frac{h}{mv} \quad (3.9)$$

The speed, and therefore wavelength, at the sample is determined by the ratio of the time of flight (t) and the length of path traversed (L) to the detector

$$\lambda = \frac{ht}{mL} \quad \lambda(\text{\AA}) = 3.956 \frac{t(\text{ms})}{L(\text{m})} \quad (3.10)$$

The Bragg condition for time of flight

$$\frac{4\pi \sin(\theta)mL}{ht} = G_{hkl} = \frac{2\pi}{d_{hkl}} \quad (3.11)$$

The time of flight of the neutron can then be converted into d-spacing.

$$d_{hkl} = \frac{ht}{2mL \sin(\theta)} \quad (3.12)$$

All the neutron diffraction data for this work were obtained using this technique.

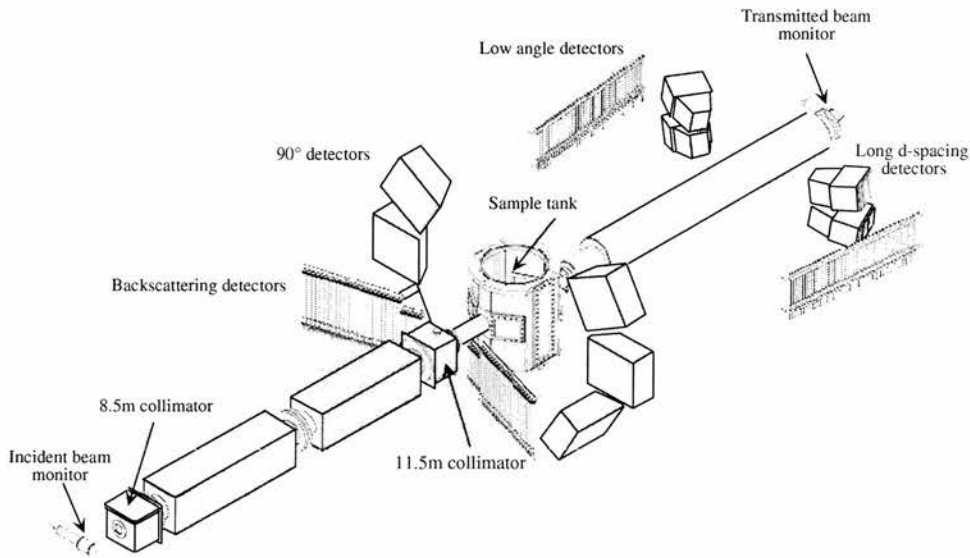


Figure 3.4: Schematic of a Time of Flight instrument (POLARIS, ISIS)

Time of flight data was collected on POLARIS and OSIRIS at ISIS, and VEGA at KEK Japan.

3.5.3 Rietveld Refinement of Powder Diffraction Data

The Rietveld[6] method is a technique for structure solution and refinement of diffraction data from polycrystalline samples. A structural model of the crystal is assumed and the expected pattern intensities are calculated. The model is iteratively adjusted and the calculated powder pattern compared with the measured pattern using a least-squares refinement procedure.

Although the difference profile is a good way of following and guiding the refinement, the accuracy of the fit is provided mathematically in terms of R factors (residual factors). The weighted-profile R value, R_{wp} is defined as

$$R_{wp} = \left(\frac{\sum w_i [y_i(obs) - y_i(calc)]^2}{\sum w_i y_i(obs)} \right)^{1/2} \quad (3.13)$$

where $y_i(\text{obs})$ is the observed intensity at step i , $y_i(\text{calc})$ the calculated intensity, and w_i the weight. Ideally this should approach the statistically expected R value, R_{exp} ,

$$R_{exp} = \left(\frac{N - P + C}{\sum w_i y_i(\text{obs})} \right)^{1/2} \quad (3.14)$$

where N is the number of observations, P the number of parameters and C the number of constraints in the model. The standard measure of the *goodness-of-fit* is defined

$$\chi^2 = \left(\frac{R_{wp}}{R_{exp}} \right). \quad (3.15)$$

For an ideal refinement the weighted and expected R factors should be identical, giving $\chi^2=1$.

Several pieces of software, capable of processing both x-ray and neutron diffraction data are readily available. In this work, the GSAS[7] and Rietan[8] packages were used to analyse neutron data, and FULLPROF[9] for the in-house x-ray diffraction data.

3.5.4 Low angle scans

Low angle scans are those where 2θ is varied between 1° and 10° . Total reflection of X-rays is observed for glancing angles of incidence less than the critical angle. A schematic of the experimental arrangement is given in Figure 3.5.

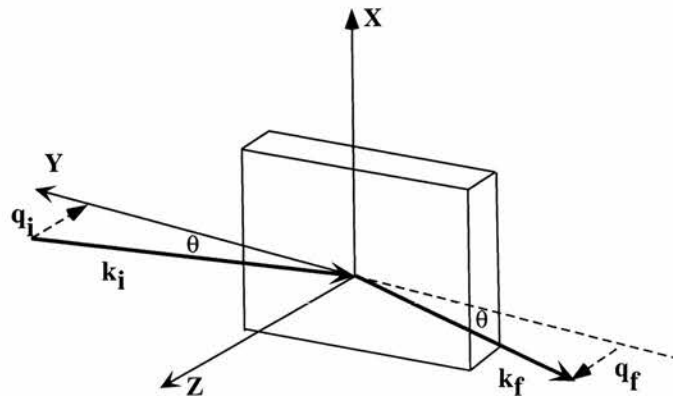


Figure 3.5: The geometry for reflectivity from a single interface

Just above the critical angle large intensity specular reflections are still observed.

The scattering vector is perpendicular to the film surface, and so information is obtained about the structure in this direction. Specular reflections from the buried surface can interfere with this reflected beam producing fringes, Kiessig fringes[10].

The simplest case of a single thick film of several hundred Å, and a single interface, will produce strong reflections, as shown in Figure 3.6.

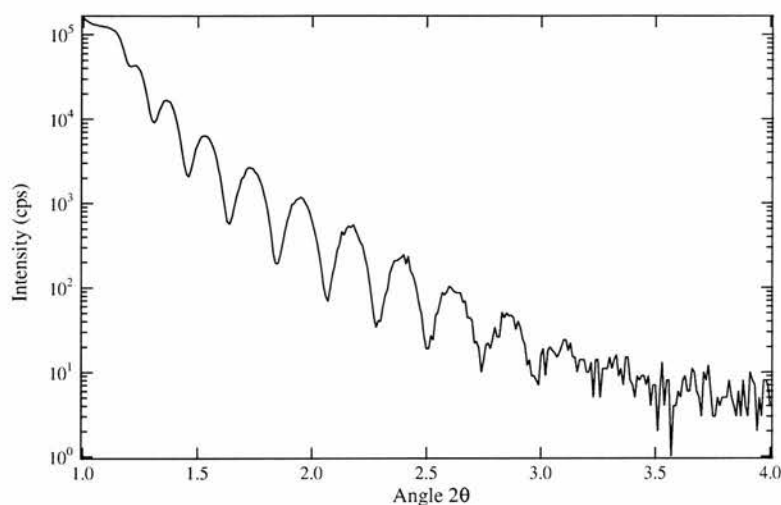


Figure 3.6: Kiessig thin film interference fringe from a pure Nb sample

These reflection fringes are related to the periodicity of the film and allow a method of measuring the film thickness. In the case of a single film

$$\delta^2 = \delta_0^2 + \frac{\lambda^2}{4t^2}m \quad (3.16)$$

where δ is the difference between successive maxima or minima, m is the fringe order and t is the film thickness. For a film of known deposition time, we only require λ to determine the thickness, and therefore the deposition rate. This calibration method is applied to every new sample.

These measurements were performed at the University of Leeds. The X-ray diffractometer is arranged in the Bragg-Brentano geometry. This system has a copper target producing Cu-K $_{\alpha}$ radiation with wavelength $\lambda=1.54\text{\AA}$.

3.6 Chemical Analysis

3.6.1 Thermogravimetric Analysis

Thermogravimetric analysis (TGA) is a technique in which the mass of the sample is monitored against its temperature, for a specified temperature program. The rate of heating/cooling can be varied, and the temperature held constant for a specified length of time, if desired. TGA is thus commonly used to study decomposition, dehydration and oxidation.

A simultaneous TA Instrument SDT2960 analyser was used to obtain results for both TGA. An accurate mass of sample powder was placed in an alumina crucible on the thermobalance unit. High purity calcined alumina powder was used as a reference material in a second crucible. This is used as an internal calibration of the sample environment. Thermal cycles were conducted in a flowing nitrogen atmosphere. The temperature was raised to 950°C at a rate of 10°C.min⁻¹ and held there for 30 minutes. The samples was then cooled at the same rate. Temperatures were measured by a Pt:Rh:Pt thermocouple.

3.7 Magnetic Characterisation

3.7.1 Introduction

The methods described herein were used to characterise the magnetic properties as well as to define transition temperatures. A variety of different techniques have been applied here although the majority of work involved SQUID and VSM magnetometers.

Vibrating Sample Magnetometer (VSM)

The vibrating sample magnetometer is a commercial instrument produced by Oxford Instruments. A temperature range of 3.8-330K and field range of ± 12 Tesla were available for experiments. A diagram of the set-up is given below.

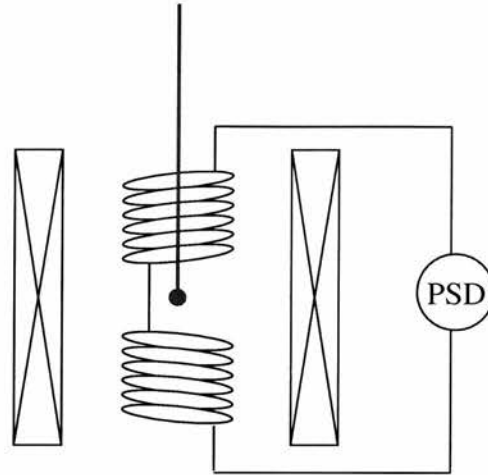


Figure 3.7: Schematic layout of the vibrating sample magnetometer

The sample is mounted in a delrin holder attached to a carbon fibre rod. This arrangement is inserted into a Helium cryostat which is mounted in the bore of a 12 Tesla superconducting magnet. The sample is vibrated along the vertical axis of the uniform field with typical amplitude of 1.5mm. Two detector coils, positioned as displayed above, pick up an induced emf from this motion. This is proportional to the rate of change of magnetic flux through the coils, defined by Faraday's induction law

$$V_s = -\frac{d\Phi}{dt} \propto \frac{d\mu}{dt}, \quad (3.17)$$

where μ is the magnetic moment. A vibration frequency of 66Hz is used since it avoids interference from mains supply noise and a large frequency can result in unwanted eddy currents. Within the cryostat the rod has 20mm of travel which is used to centre the vibration on the exact centre of the sense coil arrangement. The sample position is measurable with an accuracy of $10\mu\text{m}$. Both field strength and temperature are controllable. The voltage induced by the vibrating magnetic moment is calibrated against that obtained from a nickel sphere of known mass. The induced voltage, V_s , is related to the magnetic moment, μ , by the equation

$$V_s = A\mu f \sin(2\pi ft) \quad (3.18)$$

where f is the frequency of vibration and A the calibration factor obtained from knowledge of the nickel sphere response. And hence the moment of the sample can be calculated.

SQUID

A superconducting quantum interference device (SQUID) is essentially a flux to voltage converter. SQUID magnetometers have unrivalled sensitivities of 10^{-9} emu. Considering a superconducting ring with two Josephson junctions. Each junction will contribute to the phase shift around the loop. The dc current passing through ring structure can be described by the following equation

$$I = I_c \sin \Delta\phi_2 + I_c \sin \left(\Delta\phi_1 - 2\pi \frac{\Phi}{\Phi_0} \right) \quad (3.19)$$

where ϕ_1 and ϕ_2 are the phase differences across the junctions. The maximum current is described by the following equation

$$I_{MAX} = 2I_c \left| \cos \left(\pi \frac{\Phi}{\Phi_0} \right) \right|. \quad (3.20)$$

The maximum current thus varies periodically with the change of flux, with a period equal to the flux quantum Φ_0 . In a magnetometer the flux to be measured is coupled to the SQUID via a flux transformer, allowing the sample to be remote from the device. A schematic of the setup is given below.

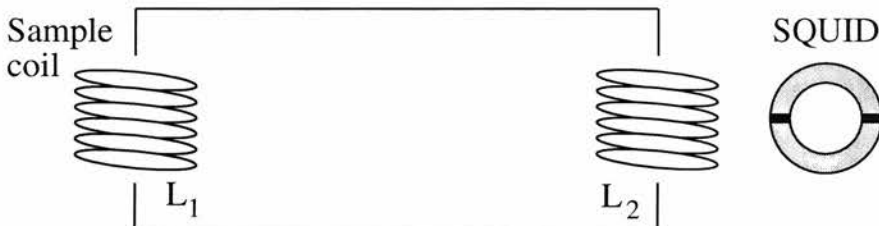


Figure 3.8: Schematic of SQUID magnetometer

Any change in the flux at the sample coil causes a current to flow in the second coil in order to maintain flux quantisation. This in turn causes a current to flow in the SQUID which is coupled to the second coil.

Although this technique has greater sensitivity than the VSM, it is limited in field range (± 5 T for St Andrews' SQUID and ± 1 T for that in Edinburgh) and all our high field work was performed using a VSM.

References

- [1] C. Namgung, Ph.D. thesis, University of St. Andrews, 1991.
- [2] J. R. Tolchard, Ph.D. thesis, University of St. Andrews, 2001.
- [3] W. R. Grove, *Philos Trans Faraday Soc* **87**, (1852).
- [4] M. von Laue, *Ann Physik* **41**, 989 (1912).
- [5] W. L. Bragg, *Proc. Cambridge Phil. Soc.* **17**, 43 (1913).
- [6] H. M. Rietveld, *Acta Cryst* **21**, A228 (1966).
- [7] A. C. Larson and R. B. V. Dreele, *GSAS: General Structure Analysis System*, 1994.
- [8] T. Ohta, F. Izumi, K. Oikawa, and T. Kamiyama, *Physica B* **234**, 1093 (1997).
- [9] J. Rodriguez-Carvajal, *An introduction to the program FullProf*, 1997.
- [10] H. Kiessig, *Ann Phys* **10**, 769 (1931).

Chapter 4

Investigation of T_c Suppression in Artificial Multilayers

4.1 Introduction

In recent years there has been an increased interest in multilayer systems composed of alternating magnetic (FM) and superconducting (SC) layers. These systems are of interest as they are model systems in which to investigate the interplay of the competing superconducting and magnetic order parameters. The superconducting proximity effect brings the superconducting electrons into contact with the strong exchange field of the ferromagnetic layers. This polarises the conduction electrons spins which penetrate into these layers, thus breaking Cooper pairs. One then expects the critical temperature to decrease monotonically with increasing FM thickness, reaching a minimum in T_c when the SC layers are decoupled. However, in 1986 Wong et al.[1] reported a nonmonotonic dependence of T_c as a function of Fe layer thickness in V/Fe superlattices of fixed V thickness.

4.2 Theoretical Review

There are several theories that attempt to describe the properties of superconducting multilayer systems and in doing so predict an oscillatory T_c dependence on the spacer layer thickness. The starting point is to consider the influence of the proximity effect on the superconducting electrons. This is well understood for the case of a SC/N interface, but not for the SC/FM case. At the boundary between a superconductor

and normal metal, Cooper pairs can diffuse into the metal with a penetration depth ξ_N . This is temperature dependent, contracting with decreasing temperature until the superconducting layers are decoupled. A similar coherence length ξ_F measures the penetration depth of a Cooper pair into the ferromagnet. Unlike in the case of a metal ξ_F is temperature independent and much smaller than the corresponding length ξ_N in a normal metal, of the order of 1nm.

Radović et al.[2, 3] developed a dirty-limit model in which the main magnetic influence on superconductivity was assumed to be through the exchange field I in the magnetic layers. This was applied in the strong pair breaking limit, assuming the exchange energy to be very large, $|I| \gg k_B T_{cS}$ where T_{cS} is the bulk transition temperature of the superconducting layers. They showed that the Cooper pair wavefunction in the FM layers exhibits an oscillatory behaviour damped by the usual exponential decay.

The most important result of this analysis is that the exchange field interacting on Cooper pairs results in a phase shift in the superconducting wavefunction. This phase shift is dependent on I and the time the Cooper pair spend crossing the magnetic layer. Therefore the coupling between neighbouring SC layers varies with the spacer layer thickness. For a specific FM layer thickness, Josephson coupling between two SC layers can lead to a junction with $\Delta\phi=\pi$ which can be energetically more favourable than the usual $\Delta\phi=0$. This $\pi \leftrightarrow 0$ switching then occurs periodically as a function of FM thickness resulting in an oscillation in T_c .

An example of the calculated dependence of T_c for the 0-phase and the π -phase states on d_M , the magnetic layer thickness, is shown in Figure 4.1. Interestingly, for $d_M \approx \xi_F$ to $3\xi_F$, the state with $\Delta\phi=\pi$ between neighbouring superconducting layers has a higher T_c than the ordinary state with $\Delta\phi=0$. Consequently as a function of d_M there will be oscillations in T_c as the ground state switches between these two phases.

More recently Aarts et al.[4] also investigated the behaviour of the superconducting transition temperature in SC/FM multilayers as a function of the different layer thicknesses. This concentrated on the interface transparency and predicted oscillations in V/Fe multilayers.

By far the most general approach to this problem has been adopted by Khusainov and Proshin [5]. In this theory the interface transparency is again included, being characterised by the parameter σ_s . The model also specifies the combination $2I\tau_f$

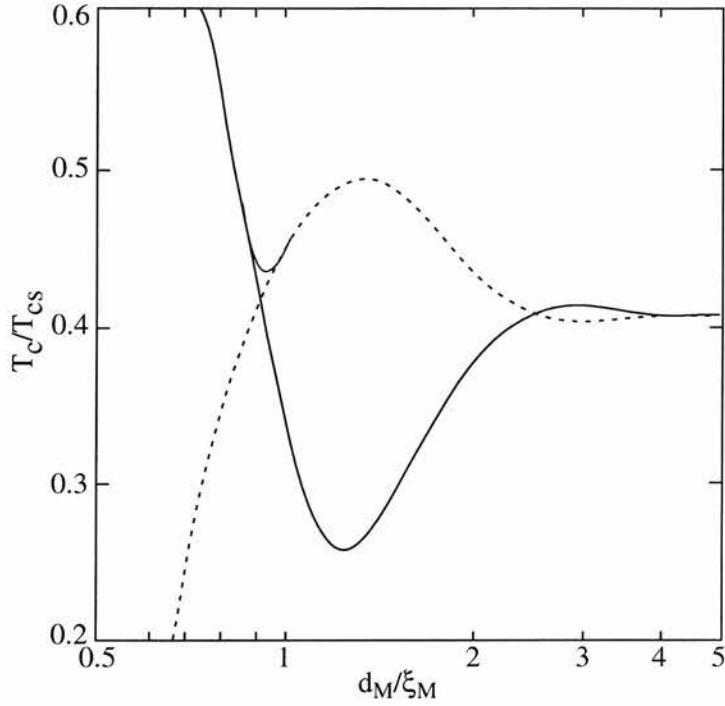


Figure 4.1: Theoretical dependence of T_c on d_{FM} as determined by Radović[2]. Presented are curves for the phase difference $\phi=0$ (solid line) and $\phi=\pi$ (dashed line).

where I is the exchange field and τ_f is the scattering time of electrons off non-magnetic impurities. Most importantly, this theory shows that the earlier model by Radović is a special case in which the transmissivity of the interface is very high and that oscillations can exist without the π -switching phenomenon.

From their theory they find that the quasiparticle motion in the ferromagnetic layer has a mixed diffusion-like and spin-wave-like character. As the clean limit is approached the spin-wave contribution dominates and the penetration depth of the pair amplitude into the ferromagnetic layer grows larger than the oscillation period. Even without considering phase switching, a periodic variation of $T_c(d_{FM})$ is possible in this model, due to the periodic compensation of the exchange field due to oscillations of the pair amplitude inside the magnetic layer (see Figure 4.2). A maximum in T_c occurs when the period of the Usadel function [6], describing the order parameter, matches the thickness of the ferromagnetic layer.

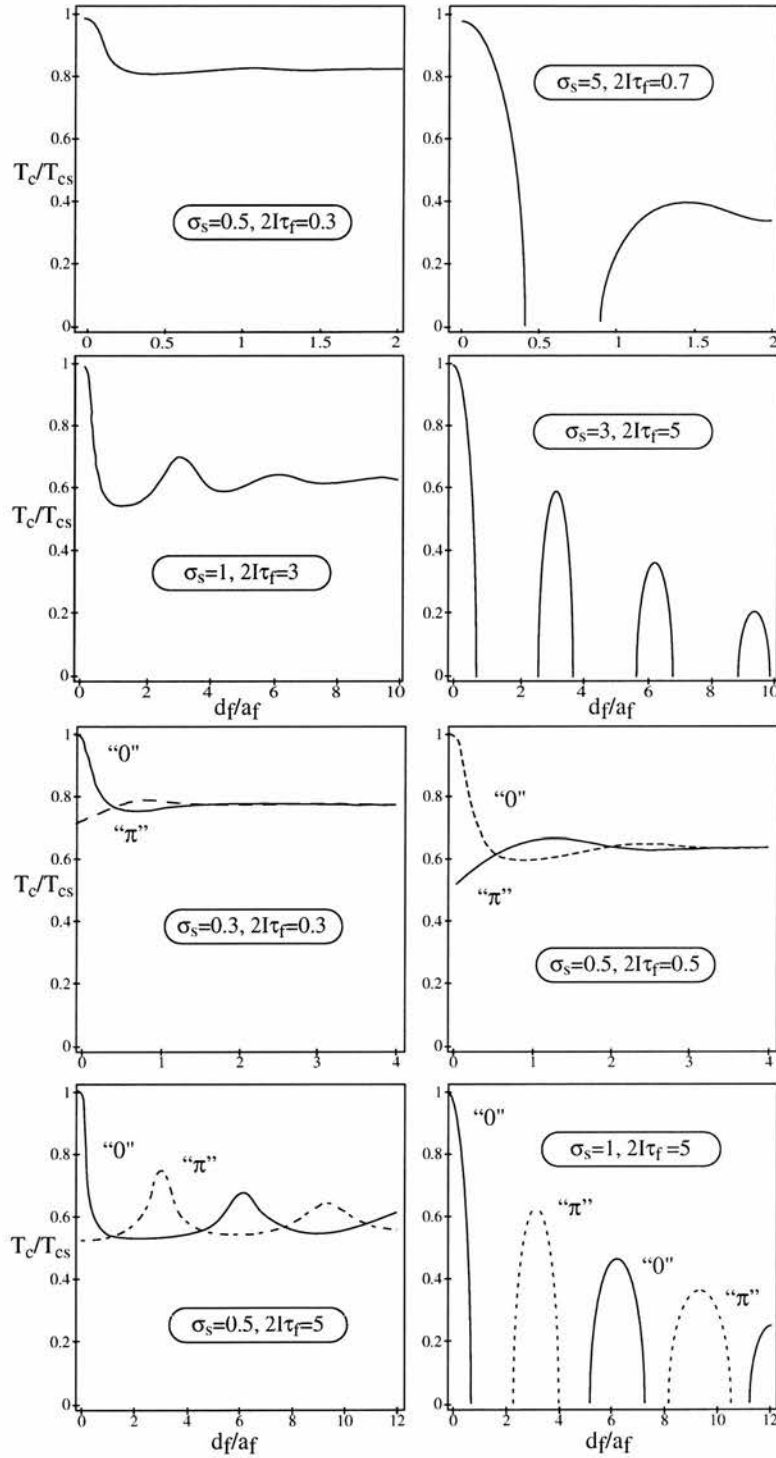


Figure 4.2: Example phase diagrams for SC/FM systems in different regimes of the theory by Khusainov and Proshin, as defined by the parameters σ_s , the interface transparency, and $2I\tau_f$, where τ_f is a non-magnetic scattering time for the electrons. The top 4 figures are obtained for a bilayer system and the bottom 4 figures for a multilayer system.

4.2.1 Previous Work

Experimental evidence of such oscillations has been sought in V/Fe, Nb/Fe, Nd/Gd and Nb/Co systems by several groups with varying success. In V/Fe[7], contrary to previous results, T_c oscillations as a function of d_M were not observed. Negative results have also been published for Nb/Fe multilayers[8]. In this case a decreasing T_c was observed with increasing d_{Fe} followed by a sharp drop upon the onset of ferromagnetism and a plateau. $T_c(d_{FM})$ curves have been reported by numerous authors [9, 10, 11] which exhibit a monotonic decrease or an initial decline followed by a plateau, showing no signs of oscillation.

Several experimental works have reported a single peak in T_c , which have been attributed to π -switching. The most notable is that of Jiang et al. in Nb/Gd superlattices. In both multilayer and trilayer (Nb/Gd/Nb) systems they observe a maximum in T_c showing qualitative agreement with the theory of Radović. However Mühge et al.[12] observed a T_c oscillation in Fe/Nb/Fe trilayers and Fe/Nb systems very similar to that of Jiang. These have only one superconducting layer therefore ruling out the possibility of π -switching. The oscillatory feature was reasoned to be due to magnetically dead regions in the Fe layer at low thicknesses. Similarly, Lazar et al.[13] reported oscillations in Fe/Pb/Fe trilayers.

Recently, more complex double oscillations have been reported in the Nb/Co system by Jiang et al.[14] They report a double minimum and identifying the second as being consistent with π -switching. Their first minimum is not predicted by Radović suggesting that modifications of this theory are required. Ogrin et al.[15] also observed a double oscillation and considered there to be good qualitative agreement with the predictions of Khusainov and Proshin [5] in the limit of strong exchange and approaching high transparency of the SC/FM boundary.

4.3 Characterisation

Nb/Co and Pb/Co multilayers and trilayers have been fabricated by dc magnetron sputtering on silicon substrates at room temperature using pure argon as the sputterer gas (see Chapter 3). The base pressure of the system was approximately 3×10^{-8} mbar after cooling with liquid N_2 . Pure target materials Nb, Pb, Co, Fe, Au and Mo were used. For a precise determination of the thickness dependence of the magnetic and superconducting properties on d_{FM} , it is essential that a complete series of samples is deposited under identical conditions. It is equally important that the layer thickness is well known.

In our experimental setup, series consisting of 13-15 samples with varying d_{FM} , or d_{SC} , were prepared within one run. The growth rates were determined from calibration samples for each target by low angle X-ray diffraction. As described earlier (see Chapter 3), the fringe positions are related to the film thickness by the simple relationship

$$\delta^2 = \delta_0^2 + \frac{\lambda^2}{4l^2}m \tag{4.1}$$

allowing determination of the deposition rate. A typical reflectivity profile is given in Figure 4.3, along with the extracted δ^2 and resultant fit in Figure 4.4. All growth rates were between 2-3 Å/s except that of Pb which was significantly higher (see Table 4.1).

Target	Nb	Pb	Co	Fe	Au	Mo
Deposition Rate (Å/s)	2.9	6.0	2.3	2.2	2.2	2.5

Table 4.1: Average deposition rates for relevant targets. These were obtained from X-ray reflectivity except in the case of Pb where the rate was inferred from PNR.

The strength of the reflected signal is a qualitative measure of the surface roughness. High reflectivities were obtained from all our calibration samples except that of Pb. The most probable reasons are surface roughness, due to softness of this material, and the fact that Pb is a good absorber of X-rays. However, recent PNR (polarised neutron reflectivity) experiments have shown similar samples to display strong interference fringes indicative of clean, sharp interfaces[16]. Like its X-ray equivalent, the fringe periodicity is related to the the film thickness and therefore the deposition rate.

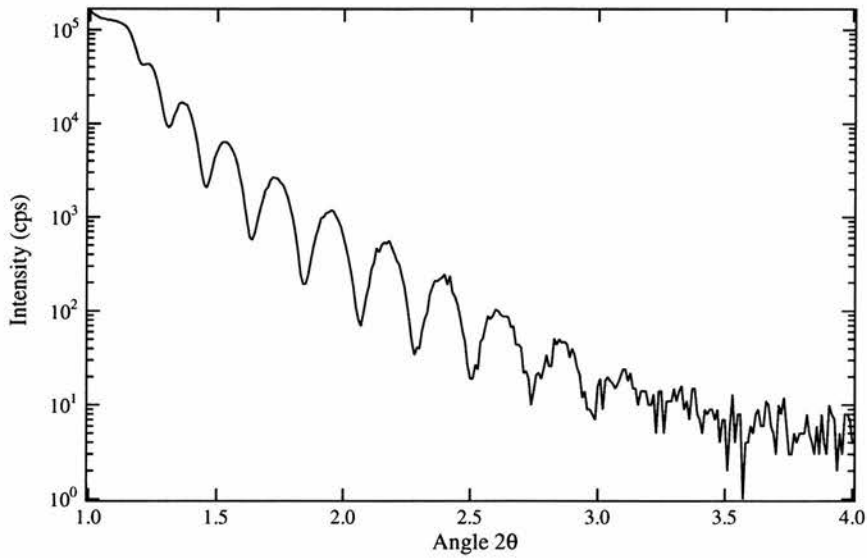


Figure 4.3: Low-angle X-ray diffraction profile for a thin Nb calibration sample, allowing determination of deposition rate.

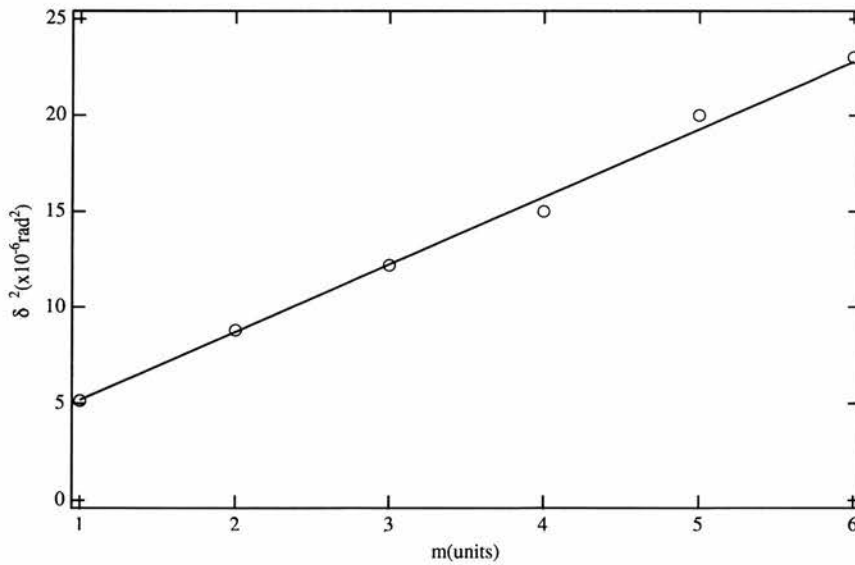


Figure 4.4: Example of fitting procedure used to obtain the deposition rate. From the gradient the layer thickness is calculated to be 290 \AA . The deposition time is known to be 100s giving a deposition rate of 2.9 \AA/s .

The problem of the Pb deposition rate was approached from a second direction by direct comparison of the transition temperatures of our samples with that of previous studies. Figure 4.5 shows the variation of T_c with Pb thickness and theoretical fit as determined by Lazar et al.[13] Superimposed onto this plot are the transition temperature and corresponding Pb thickness of two of our sample of known deposition time. At large thickness the T_c curve flattens making an accurate determination of the Pb thickness difficult. This, in conjunction with PNR measurements, allowed an accurate determination of the Pb deposition rate.

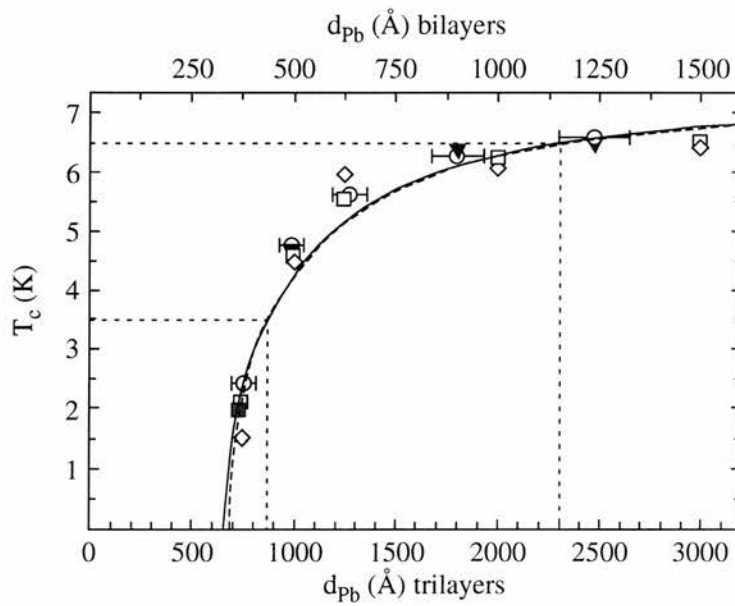


Figure 4.5: Dependence of the superconducting transition temperature on the thickness of the Pb-layer as determined by Lazar[13]. In their terminology, trilayer refers to a single Pb film sandwiched between two Fe layers of 30Å.

All the multilayers start and end with ferromagnetic layers to avoid surface superconductivity. In the case of the Pb-based multilayers, these were also covered by a protective Mo cap layer of about 40Å thickness; Lazar et al.[13] having previously reported that complete coverage could be achieved by Mo. This is necessary to prevent Pb degradation due to oxidation and moisture[17]. In addition a single multilayer series prepared by molecular beam epitaxy (mbe01) was also studied, the preparation details are given in ref[15]. A summary of the samples is given in the Table 4.2.

Our initial samples, mbe01 through sc11, were provided courtesy of Dr Chris Marrows and Dr T-H Shen of the University of Leeds. All other series were fabricated by our group in order to gain better understanding of the preparation process and for greater control. An additional advantage comes in the form of intimate knowledge of conditions under which each individual samples was fabricated. These were also prepared at the University of Leeds with the support and expert advice of Chris Marrows.

Table 4.2: Series number, description and layer thicknesses

No.	Sample type	d_{SC} (Å)	d_{FM} (Å)
mbe01	Nb/(Co/Nb) _{x5}	500	18 - 42
sc02	Si/Co/(Nb/Co) _{x10}	400	0 - 44
sc09	Si/Co/(Nb/Co) _{x5}	400	7.5 - 40
sc10	Si/Co/(Nb/Co) _{x5}	400	7.5 - 40
sc11	Si/Co/Nb/Co	400	0 - 40
sc13	Si/Co/(Nb/Co) _{x5}	400	0.5 - 22
sc14	Si/Co/(Nb/Co) _{x5}	400	1.0 - 22
sc15	Si/Co/(Nb/Co) _{x5}	400	1.0 - 22
sc16	Si/Co/(Nb/Co) _{x5}	400	14 - 40
sc17	Si/Co/(Nb/Co) _{x5}	400	14 - 40
sc20	Si/Fe/Pb/Fe/Pb/Fe/Mo	2400	4.5 - 45
sc21	Si/Co/Pb/Co/Mo	2400	8 - 45
sc22	Si/Co/Pb/Co/Pb/Co/Mo	2400	4.5 - 45
sc23	Si/Co/Pb/Co/Pb/Co/Mo	1200	4.5 - 45

4.4 Experimental

A computerised 4-point probe method was used to monitor the voltage across the multilayers, with a constant dc current, as a function of temperature. This gave a direct measurement of the superconducting transition temperature. Signal voltage was measured with a voltmeter with microvolt sensitivity. Contacts were attached to the sample surface with silver paint and were allowed to dry overnight before measurements were carried out.

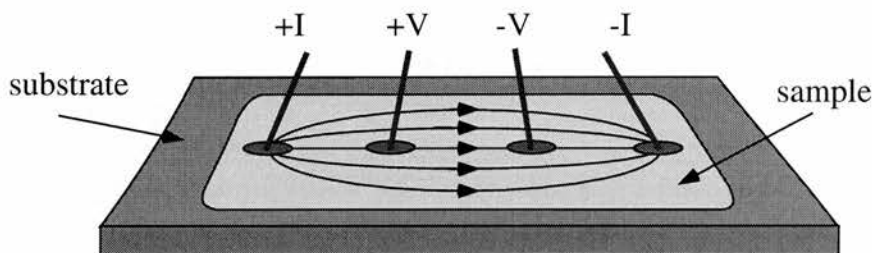


Figure 4.6: The four-probe geometry used for measuring sample resistivity. The resistivity of the region between the two voltage probes is measured.

This method proved quite effective, resulting in low contact resistances. During experiments the current was reduced to ensure that heating effects were minimised. Typically currents of approximately 7.5mA were used.

The sample environment was an Orange cryostat supplied by AS Scientific products ltd, Abingdon, Oxon. This cryostat was mounted on a rotation rig which allowed the sample to be rotated around a fixed field direction through scan angles of over 360°. Temperatures between 2 and 300K were regulated by a Lakeshore controller via computer with an accuracy of 0.01K. Magnetic fields of up to 1T were available with water cooled electromagnetic coils. The field strength was monitored by a small Hall sensor placed near the centre of the electromagnet coils. A schematic of the experimental set-up is given in Figure 4.7.

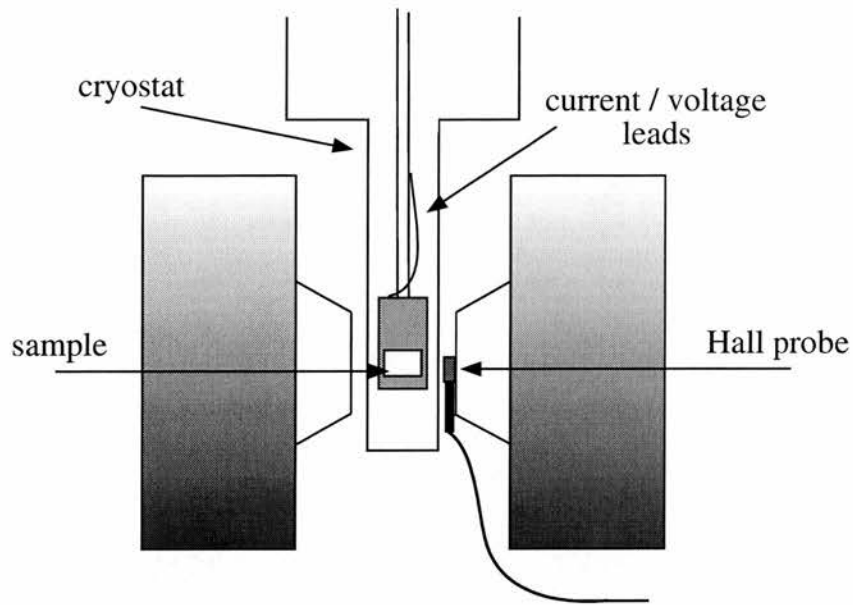


Figure 4.7: The low temperature resistance apparatus. The samples are inserted between the poles of a large electromagnet on the end of a stick.

Resistivity measurements on all series were measured in zero field, with the field direction parallel to the film surface, as described above. The superconducting transition temperature T_c was defined as 50% of the normal state resistance before the start of the transition. Errors in these values were generously estimated to be half the full transition width, from completely normal to fully superconducting.

4.5 Results

4.5.1 Nb-based multilayers

We began our study by repeating the measurements of Ogrin[15] in order to compare the results obtained by the torque method and direct measurement of the transition. The T_c dependence on d_{Co} obtained for the multilayer series mbe01 with fixed $d_{Nb}=500\text{\AA}$ is shown below.

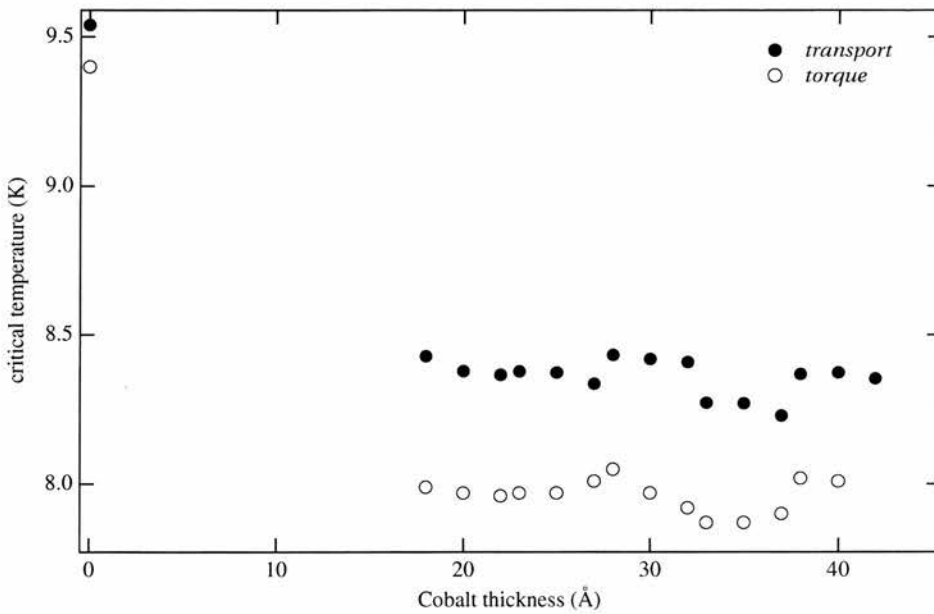


Figure 4.8: Transition temperature as a function of cobalt thickness in the MBE multilayer series mbe01. Both the transport results of the present study and those from torque are shown for comparison.

Examination of the figure shows similar trends in the data obtained by the two methods although there are some discrepancies. An initial T_c depression is observed and is attributed to the pair-breaking influence of the ferromagnetic layers. Following this fall there is an oscillation of T_c with increasing layer thickness. At higher d_{Co} both display two maxima at similar values.

The transport technique presented here is the more accurate method of characterising the superconducting transition, being a direct measurement. In torque magnetometry the torque in an applied magnetic field obeys the following relation-

ship

$$|\tau| = H\mu \sin \theta. \quad (4.2)$$

Multiple measurements in various fields allows extrapolation back to zero field and calculation of the critical temperature. The problem with this method lies in the direct proportionality between H and τ so that measurements are not possible close to zero field.

The sharp step-like features in our data are unexpected. An important point is that these samples were not made in a single run but in batches, under the same growth conditions. When considered with the oscillation profile it is apparent that this cannot be taken as conclusive evidence of a $T_c(d_{Co})$ oscillation.

It is evident that the superconducting layer in these samples is too thick and more impressive results, larger oscillations, would be obtained from thinner multilayers. The second series under investigation satisfied this condition having $d_{Nb}=400\text{\AA}$. Magnetisation measurements at 300K (see Figure 4.9) confirm all samples to be ferromagnetic and suggests that below $\approx 9\text{\AA}$ samples would not exhibit ferromagnetism. This is not unexpected since in the sputtering process layers are built up of connecting islands of sputtered material. If there is not sufficient material to cover the entire surface then one would expect to observe a superparamagnetic system of Co islands.

Figure 4.10 shows the critical temperature T_c as a function of Co thickness for this series. Following an initial depression a smooth increase of T_c is observed up to $d_{Co}=20\text{\AA}$ followed by a plateau. This increase coincides with the onset of ferromagnetism which has been previously reported by Mughe et al[12]. Unfortunately there are two striking data points that disrupt this trend. The width of the superconducting transition is largest for these two samples.

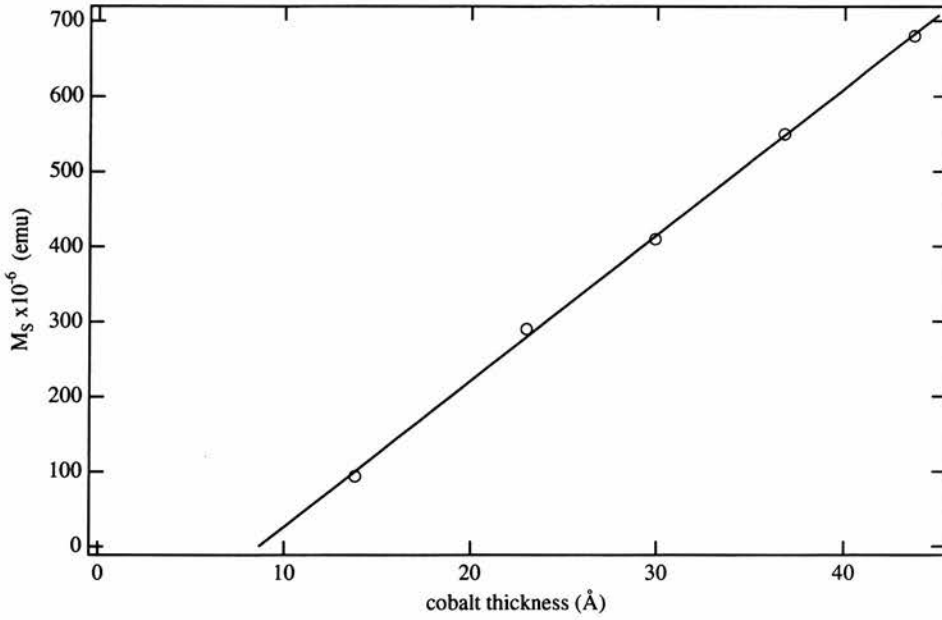


Figure 4.9: Saturation magnetisation obtained at 300K vs Co thickness for sc02. The solid line is a guide to the eye.

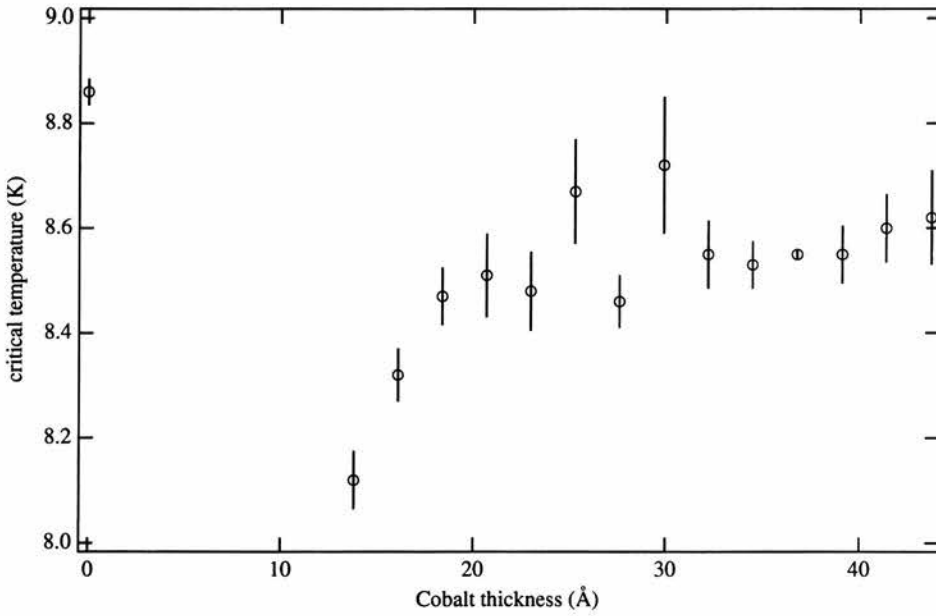


Figure 4.10: T_c vs d_{Co} as determined by dc resistivity measurements for series sc02 with fixed $d_{Nb}=400\text{Å}$.

Our study continued with two more multilayer systems consisting of $d_{\text{Nb}}=400\text{\AA}$ with varying d_{Co} , labelled sc09 and sc10. Unfortunately the former experienced problems with shutters during sputtering and we therefore expected non-systematic trends in the data. In addition to these, a trilayer series was fabricated consisting of a single superconducting Nb film sandwiched between two ferromagnetic Co layers. A comparison of the $T_c(d_{\text{Co}})$ curves of these systems should provide an insight into the role played by the coupling of the superconducting layers.

After preparation the samples were measured to ensure all displayed the expected ferromagnetism. Magnetisation data was collected for sc10 and sc11 but not for the sc09 series which was known to be of varying quality. The room temperature saturation magnetisation for sc10 is displayed in Figure 4.11. From this data the onset of ferromagnetism is seen to occur around $d_{\text{Co}}=5\text{\AA}$ and a similar value, $d_{\text{Co}}=6\text{\AA}$, is obtained for the sc11 series, although there is a greater scatter of the data, suggesting that the samples are of poorer quality.

Figure 4.12 shows examples for the superconducting transitions observed by electrical resistivity for 3 samples from the series sc10 with different d_{Co} . The resistances are normalised to the residual normal state values just above T_c . All samples displayed similar transition widths indicative of comparative sample quality.

The d_{Co} dependence of the transition temperature for the both multilayers is plotted in Figure 4.13. The sc09 data has been shown for comparison purposes only as there is no obvious trend. Additionally the large variation in error bars confirms the expected poor sample quality of this series.

The sc10 data is far more interesting. After an initial decrease of T_c we observe an oscillation showing three equally spaced maxima at 10\AA , 22\AA and 34\AA . This is unlike anything that has been previously reported and it is difficult to understand within the context of current theories. Unfortunately there exists the nominally pure Nb samples which exhibits a very low critical temperature (2.7K) casting doubts over the other samples in the series.

Similarly the $T_c(d_{\text{Co}})$ behaviour obtained for our trilayer system is displayed in Figure 4.14, with the error bars determining half the 0-100% transition. Although all values are suppressed in comparison to that of bulk T_c , it is clear that there is no trend in T_c . The other startling feature is the variation in the transition width, which is quite random.

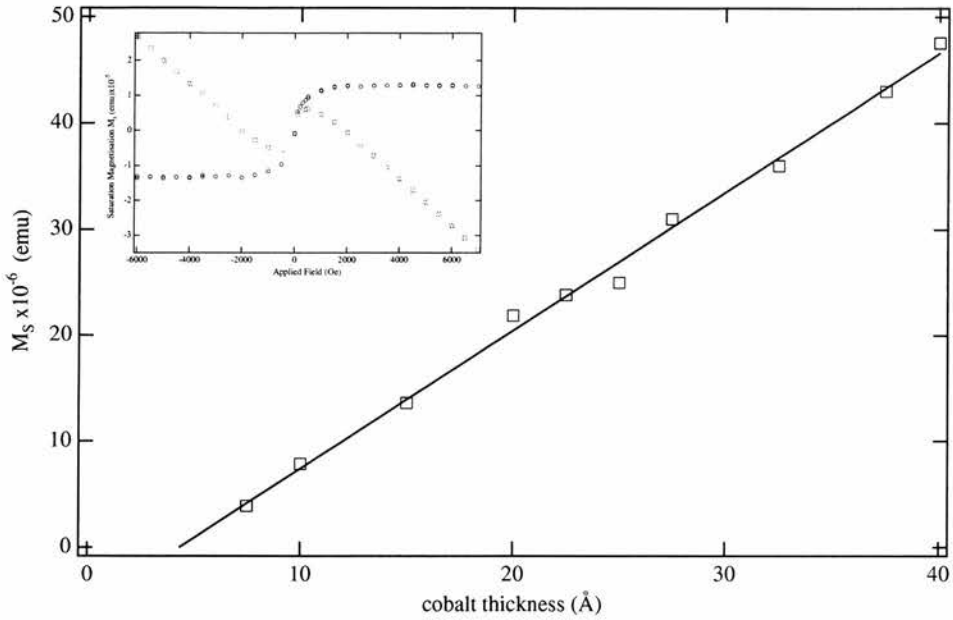


Figure 4.11: The spontaneous magnetisation M_s at room temperature as a function of Co layer thickness (series sc10). Inset shows the field loop obtained for the sample with $d_{Co}=15\text{\AA}$.

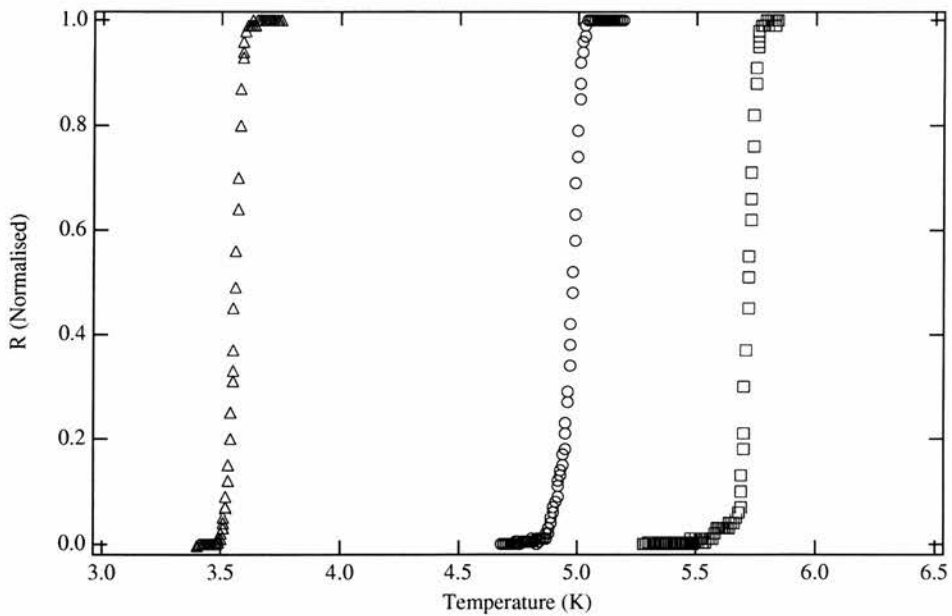


Figure 4.12: Superconducting transition curves measured by electrical resistivity for the multilayer series sc10 with $d_{Nb}=400\text{\AA}$ and $d_{Co}=11\text{\AA}$ (squares), 15\AA (circles) and 18\AA (triangles).

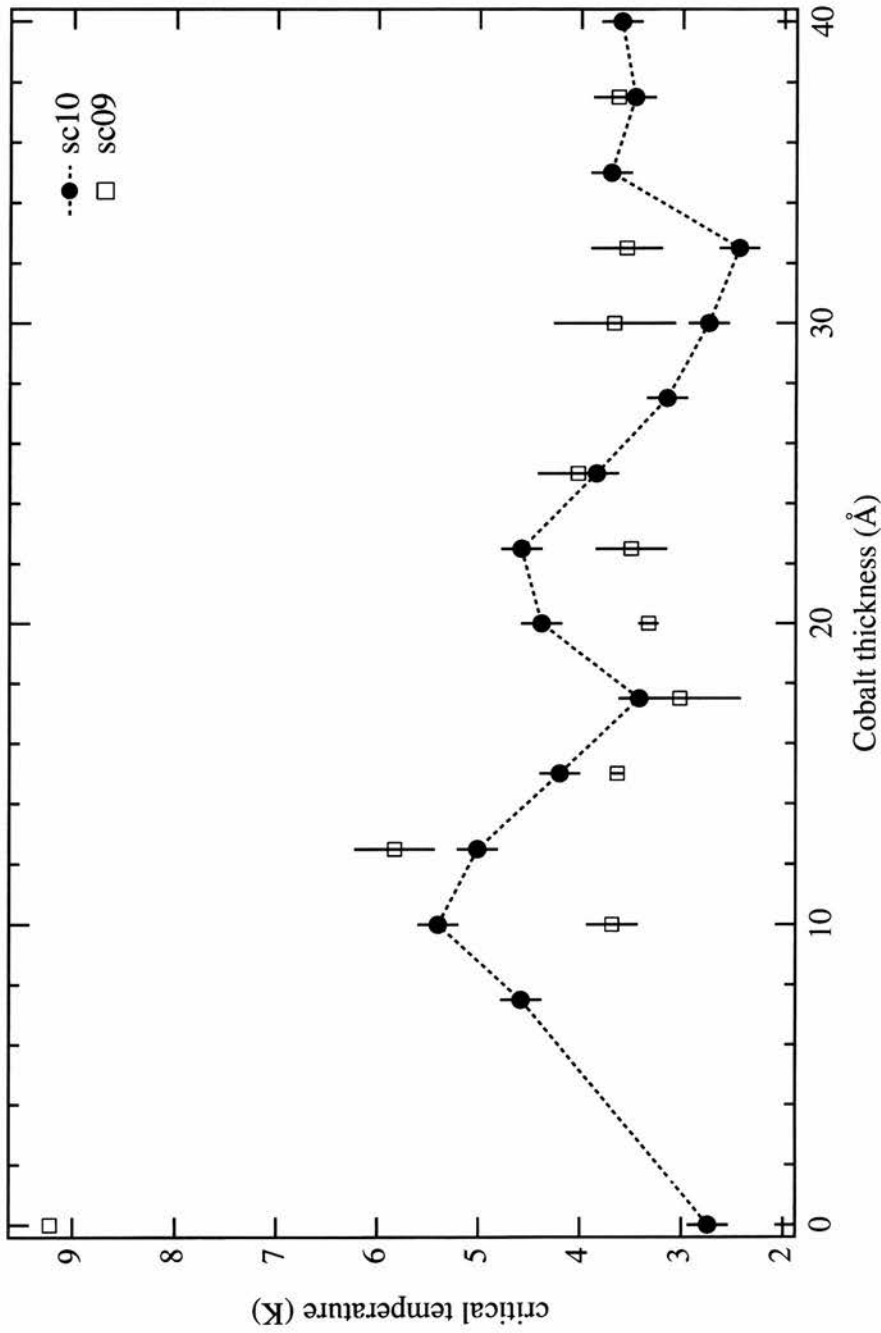


Figure 4.13: Dependence of the superconducting transition temperature on the thickness of the Co layer as determined by resistivity measurements (series sc09 and sc10). The line is a guide to the eye for sc10.

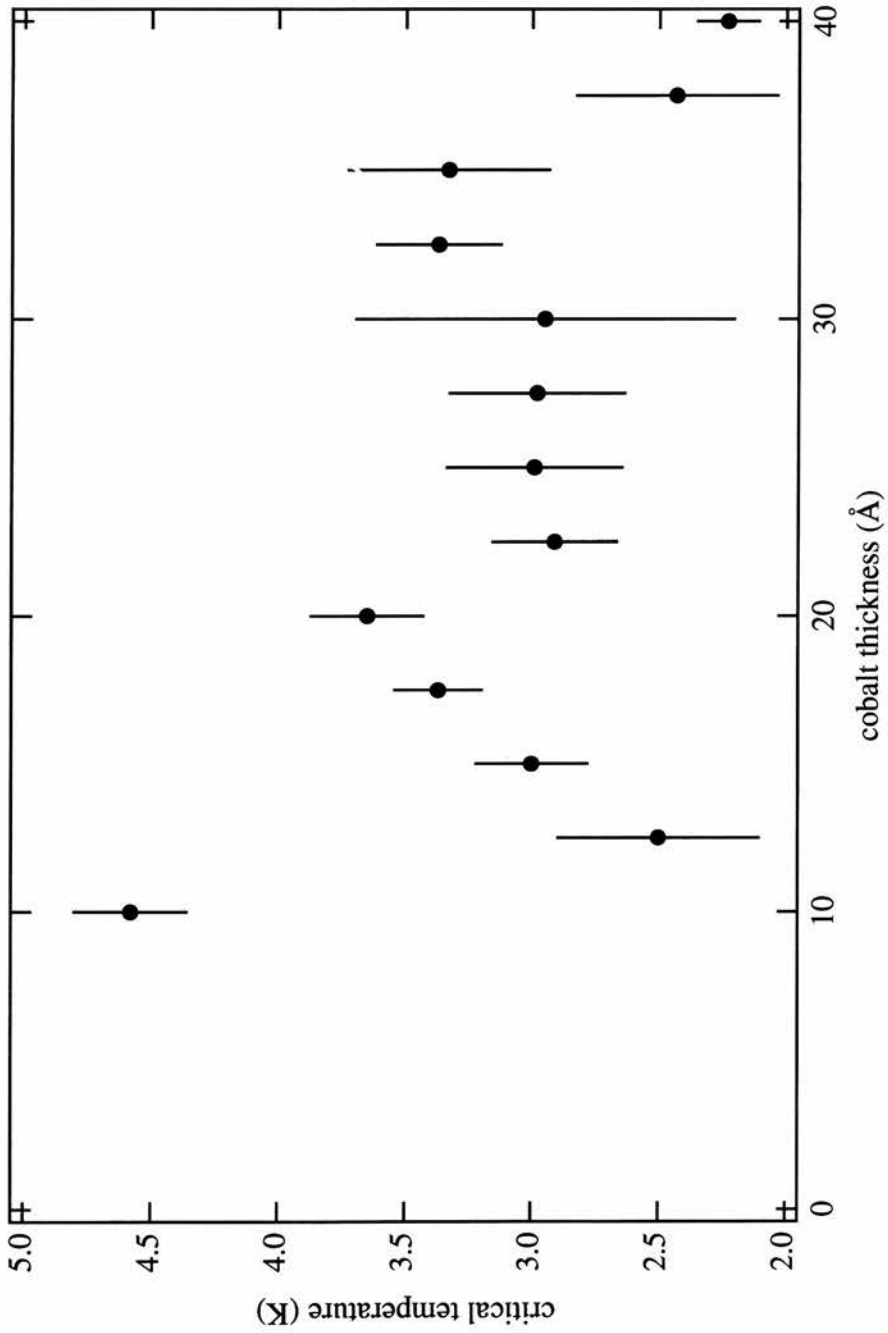


Figure 4.14: Dependence of the superconducting transition temperature on the thickness of the Co layer in Co/Nb/Co trilayers (series sc11) as determined by resistivity measurements.

It was at this point in our investigation that we became more involved in the sample preparation in order to gain better control and understanding of the process. Previously, we had only had general knowledge of any problems experienced during fabrication but for all following series we have sample specific details of problems.

Since the results of series sc10 had looked quite promising we decided to fabricate more series with similar parameters. The issue of sample quality was tackled in three ways. Firstly, each series of 15 samples was spread over a smaller range of d_{Co} giving a higher density of points and reducing the impact of a rogue data point. Secondly, series were made to overlap, producing a region where the inter-batch consistency could be directly assessed. Lastly, the samples in each series were sputtered in a random order, rather than increasing d_{Co} as with all previous batches. With this approach in mind series sc13 through sc17 were prepared.

An added advantage is the fabrication of samples with very thin Co layers which had not previously been examined. Figure 4.15 shows the magnetisation curves for two samples of differing Co thickness measured at 10K. The thicker film displays a typical ferromagnetic hysteresis loop while for the very short Co deposition, we observe a superparamagnetic signal. This is not unexpected since sputtered material initially nucleates into islands before growing into a film. If insufficient material is deposited then the spacer layer will consist of unconnected Co islands, an ideal situation for the existence of superparamagnetism.

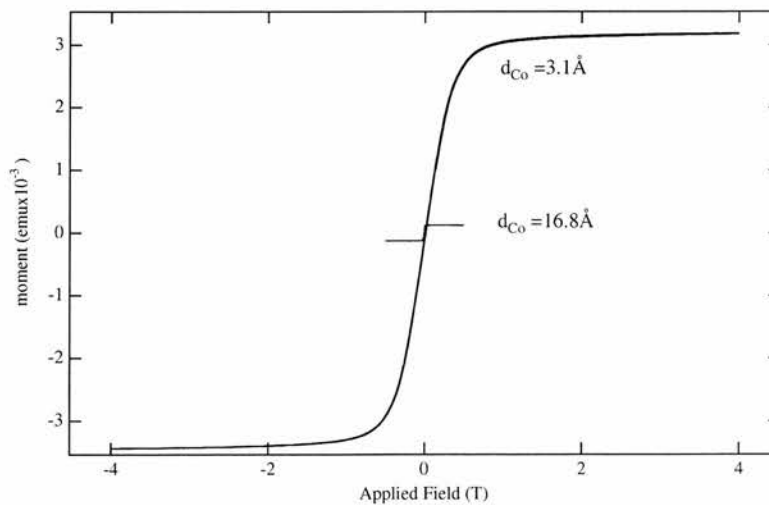


Figure 4.15: Magnetisation curves of two samples from the sc13 series obtained at 10K. The labels give the average layers thickness determined from the deposition time and rate.

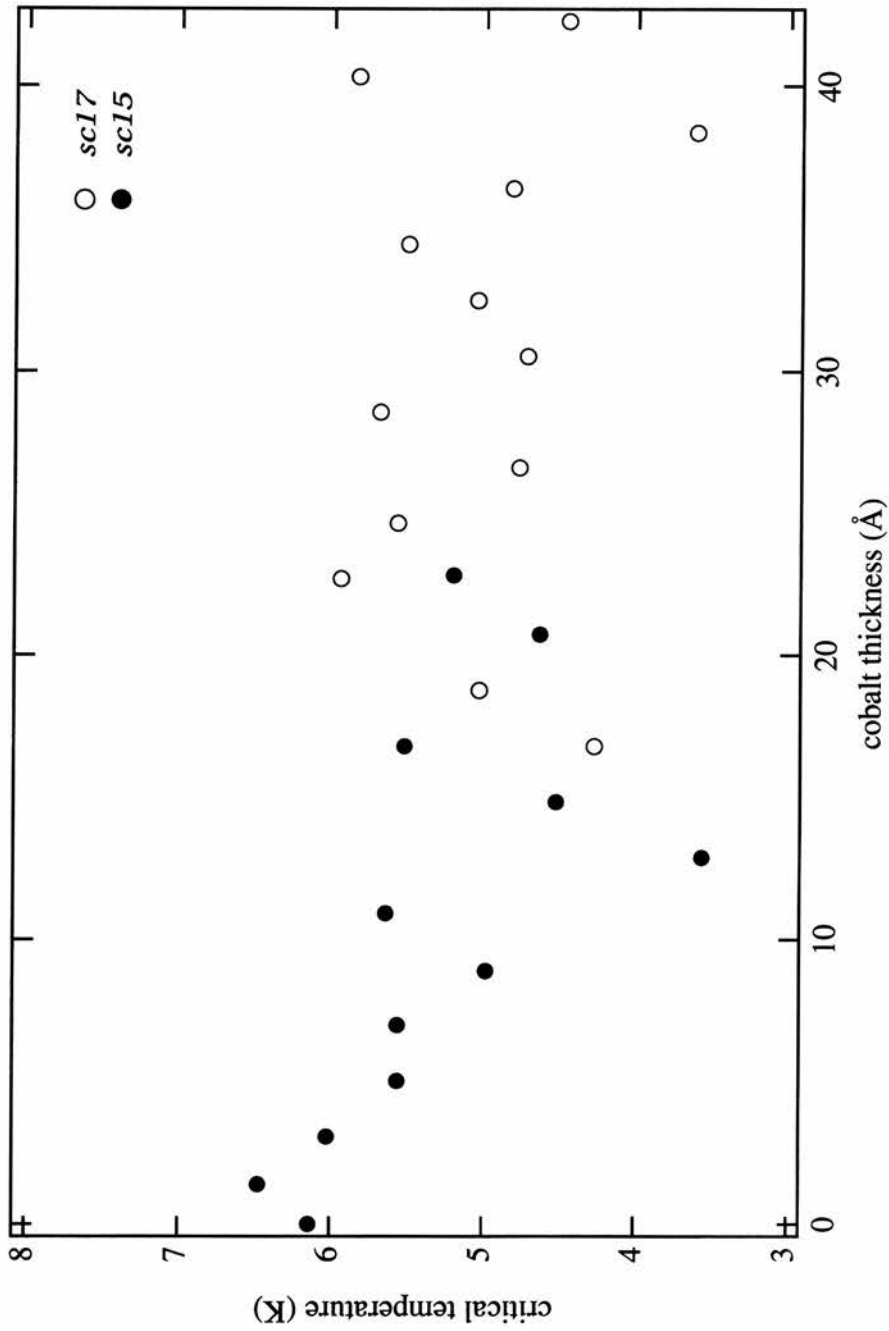


Figure 4.16: Dependence of the superconducting transition temperature on the thickness of the Co layer in two nominally identical Nb/Co multilayers as determined by resistivity measurements.

Figure 4.16 shows the composite of the transition temperatures obtained from sc15 and sc17. This displays no real trend and no consistency with the overlap of the two series yielding radically different T_c 's from samples of nominally equivalent parameters.

An additional problem with these samples (sc13-sc17) occurred in the actual fabrication process. Although counter measures were taken, it is mentioned here for completeness. Normally the temperature of the sputtering guns is controlled by a water cooling system, this was not functioning at full capacity during sample preparation. The current in each gun was monitored and after fabrication of 3 to 4 samples there was a noticeable rise from the desired value of the Nb gun, the others being used for far shorter times. This additional heating power increases the deposition rate reducing overall sample control. Therefore after every 3 samples the system was left to idle for approximately 1 hour, allowing the Nb gun to return to its normal operating temperature.

Discussion

In many respects the fundamental requirement for the success of this project, and the observation of a smooth nonmonotonic $T_c(d_{Co})$ curve, is good sample quality and in particular smooth, clean interfaces. In reality the main challenge in this project is to ensure samples are of sufficiently high quality.

All samples have been characterised by a variety of techniques and on the whole the quality determined to be excellent. When there have been problems during sputtering this has been highlighted in the transition temperature and breadth.

Figure 4.17 shows the Nb-Co phase diagram, with the hashed region highlighting the problematic area where a stable alloy exists. During the sputtering process it will be very difficult to avoid this region and alloying will result at the interface.

Although this interface alloying has a small influence, such that this system can be utilised for the observation of different physical phenomena, see Chapter 5, its presence is sufficient to destroy the subtle effect that we wish to study. It is very difficult to observe only the interaction of competing superconducting and magnetic mechanisms without the additional effects of interfacial alloying and roughness.

It is difficult to draw any conclusions from the data collected in this study. The most promising results have been shown by series sc02 and sc10 which display features reminiscent of previous work. In the former an increase in T_c is observed

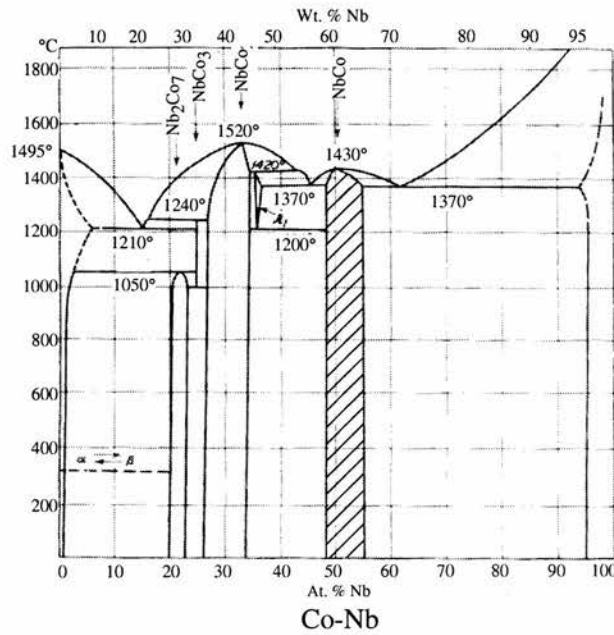


Figure 4.17: Nb-Co phase diagram[18]. The hashed area indicates the region of stable Nb-Co alloy.

following the onset of magnetic order in the spacer layer not dissimilar to that of Mughe et al., although the subsequent maximum and decreasing tail are not present. Similarly the multiple oscillations of series sc10 mimic previous studies.

It is evident that this system is not ideally suited to the elucidation of the mechanism of this phenomenon and a substitute to Nb as the superconducting layer is required.

4.5.2 Pb-based multilayers

At this point in our study it became apparent that the metallurgical character of the Nb-Co interface would hamper any chance of producing samples of consistently good quality, and therefore measuring these subtle effects, without considerable access to a sputterer to understand the systematics. Pb was chosen as our new superconductor layer due to its insolubility with Co or Fe. More details of the system suitability are given in the discussion at the end of this section.

Four batches of Pb-based multilayers were prepared for this study (see Table 4.2 for details). Figures 4.18 through 4.20 show the critical temperature T_c as a function of the magnetic layer thickness for these series. As with previous batches the room temperature saturation magnetisation has been measured to ensure that the samples indeed display ferromagnetism and that the expected linear increase with Co thickness is present. The data collected for sc21 and sc22 are shown in Figure 4.18; the inset indicating the onset of magnetic order to occur at $d_{Co}=7\text{\AA}$.

The temperature dependence on d_{Co} obtained for the two series of multilayers, sc21 and sc22 with fixed $d_{Pb}=1500\text{\AA}$, is shown in Figure 4.18. An initial T_c depression is observed up to $d_{Co}=10\text{\AA}$. For larger d_{Co} the T_c value saturates at $T_c=6.92\text{K}$. The width of the superconducting transitions for these series of samples does not exceed 0.05K . Therefore error bars in the determination of T_c are of the order of 25mK . There are two exceptions to this where the Mo cap is known to be defective and the transitions are broader, $\Delta T_c=0.15\text{K}$.

In Figure 4.19, the T_c dependence for the multilayer series sc20 is shown. Again the critical temperature drops quickly with increasing d_{Fe} , saturating at 6.84K . The measured lower critical temperature, than for similar d_{Co} , can be attributed to the stronger moment size of the Fe atoms. Following the initial fall in T_c there is a small oscillation reaching a maximum at $d_{Fe}=21\text{\AA}$, with a hint of a second oscillation for $d_{Fe} > 44\text{\AA}$. A single bad point stands out from the trend but this is associated to a lack of Mo cap and subsequent sample degradation. This is highlighted by the increased T_c and broader transition. The higher T_c is not entirely unexpected since Pb-oxide materials often exhibit enhanced superconductivity [17].

The T_c dependence on d_{Co} obtained for the sc23 series is given in Figure 4.20. Following the initial decrease, the critical temperature displays a maximum around $d_{Co}=12\text{\AA}$ before it flattens out remaining constant at 3.1K . This behaviour is very similar to that predicted by the Radović theory presented earlier.

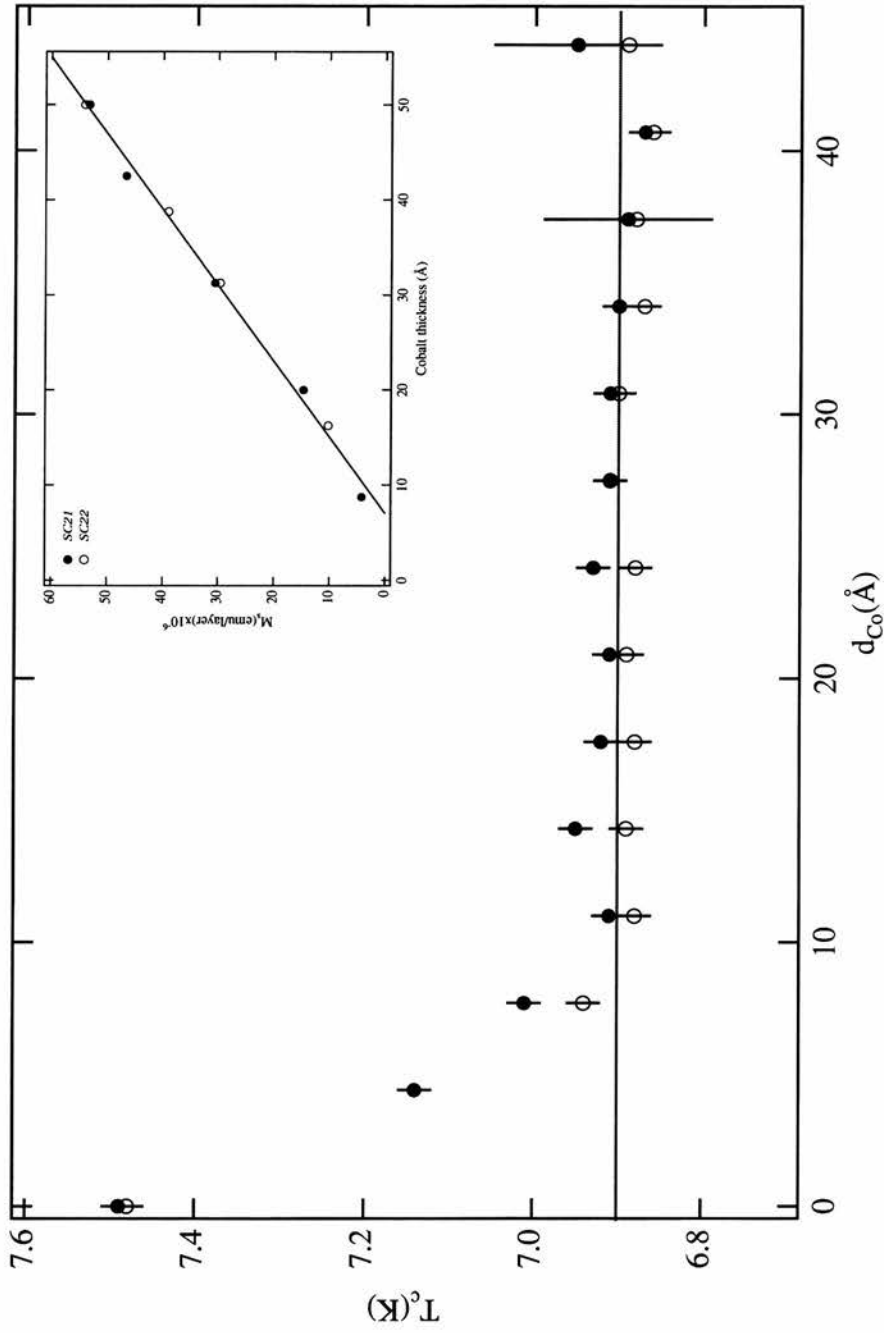


Figure 4.18: Superconducting transition temperature T_c as a function of d_{Co} for Pb/Co trilayer and multilayer series sc21 and sc22 as determined by resistivity measurements. Inset: Saturation magnetisation per layer showing ferromagnetism for $d_{Co} > 7\text{Å}$.

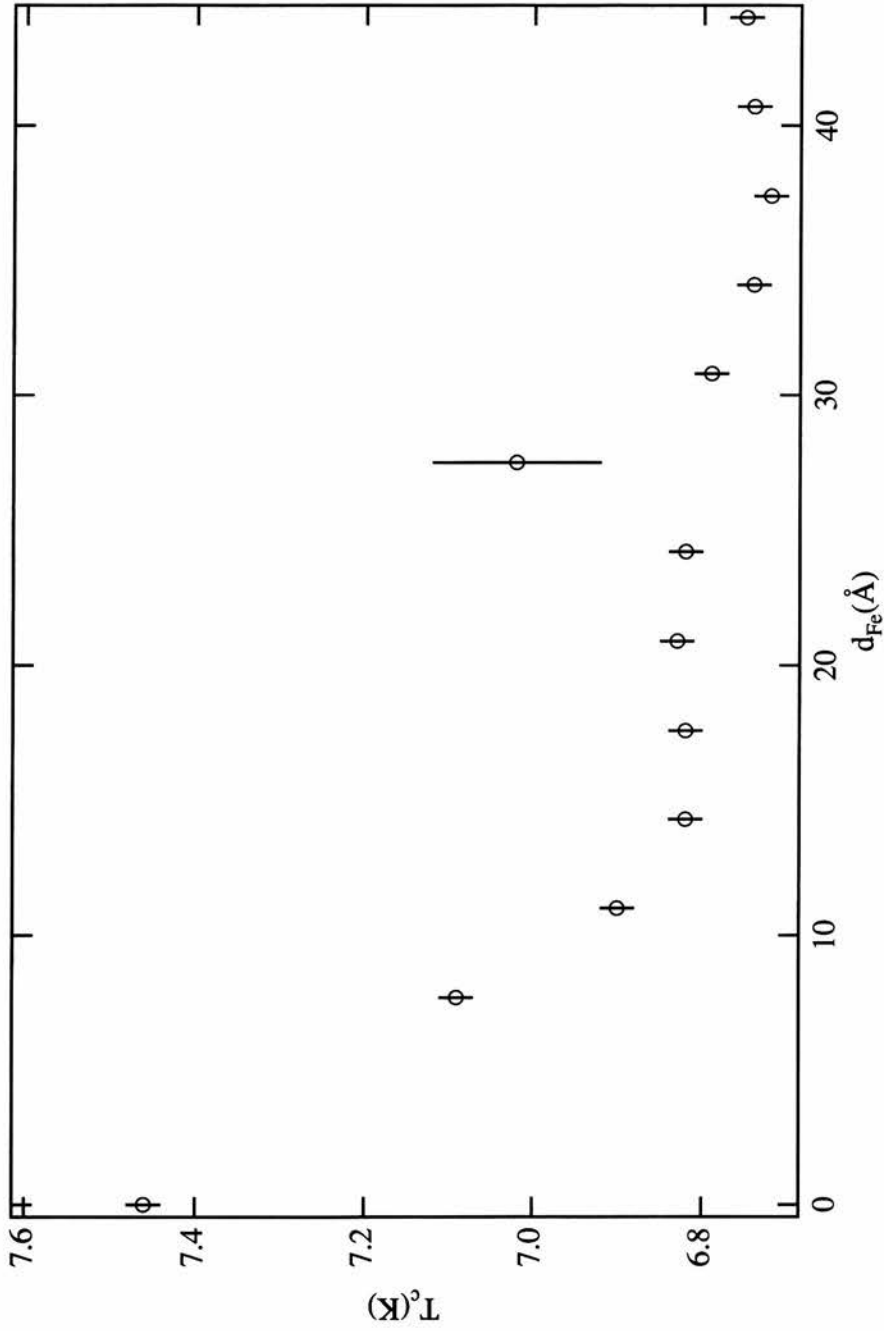


Figure 4.19: Superconducting transition temperature T_c as a function of d_{Fe} as determined by resistivity measurements for multilayer series sc20 (Si/Fe/Pb/Fe/Pb/Fe/Mo).

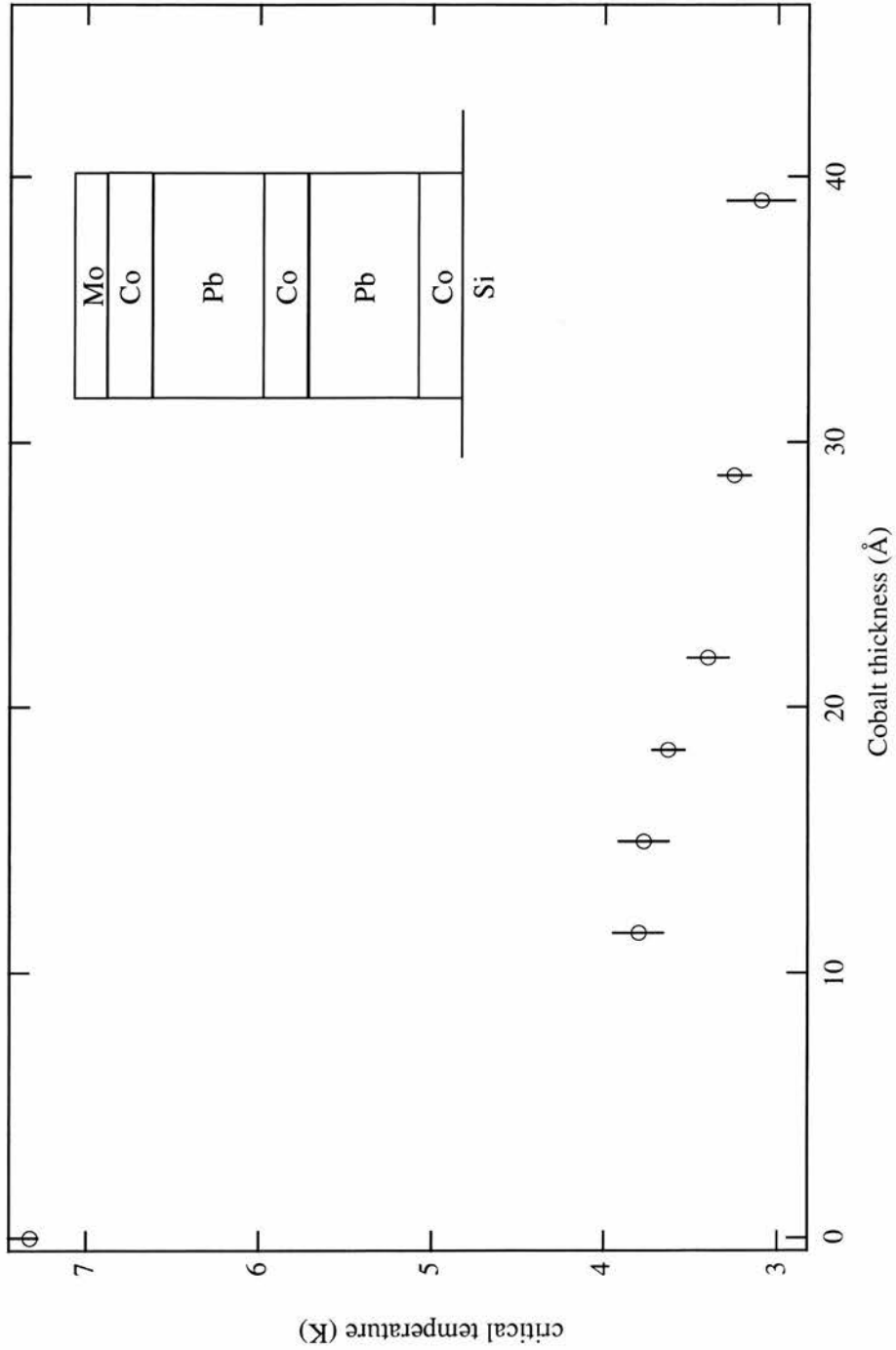


Figure 4.20: Superconducting transition temperature T_c as a function of d_{Co} as determined by resistivity measurements (series sc23).

Discussion

When deciding on an ideal system in which to investigate these effects, our prime concern was interface quality, with the aim of finding materials where no alloying would occur. Our second requirement was to find a superconducting material with a T_c similar to that of Nb which would have a suppressed T_c above 2K, under an applied field of 1T, the base temperature of our cryostat. This led us to examine several possible candidates, including NbTi and V, with Pb being the most suitable.

The figure below shows the phase (equilibria) diagrams for Pb-Co and Pb-Fe. Importantly in both cases the elements are completely immiscible so sputtering will produce sharp interfaces with minimal intermixing. Recent PNR studies have confirmed this to be the case.

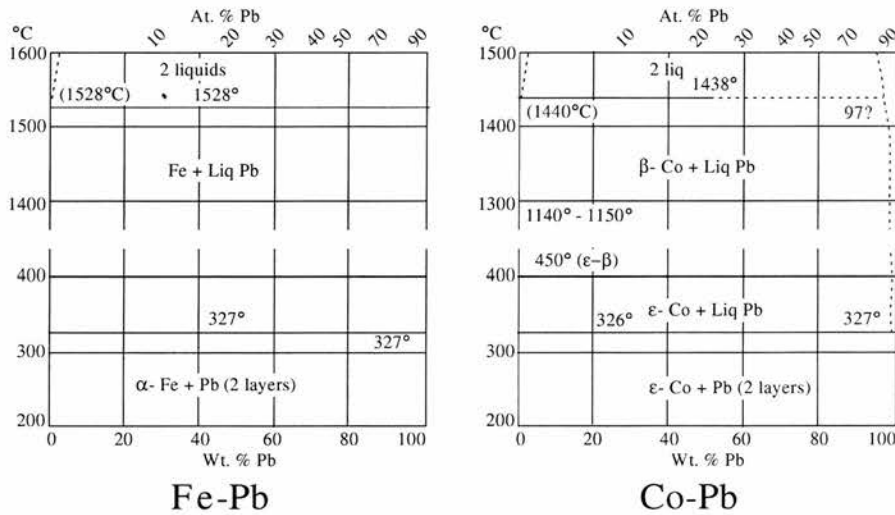


Figure 4.21: Phase diagram of Fe-Pb and Co-Pb[18]. There is no stable alloy present in either of these systems.

Similarly the measured T_c trends also confirm the sample quality with random points occurring only as a result of the Mo cap not being present. Otherwise all samples displayed similar resistivities and transition widths. Examination of these transitions shows that capping is a necessity, especially in the case of the Pb/Fe series where the transition is not only broadened but the critical temperature is also enhanced.

The region of interest with regards to the superconductor thickness is exemplified in Figure 4.5, where superconductivity begins around 700Å and saturates above a thickness of 2000Å. Observation of a large variation in the transition temperature requires the superconducting film thickness to be in the region of 60-70% of this saturation value.

It is apparent that our initial samples are too thick, only allowing observation of decoupling effects. This is due to the inability to calibrate the Pb deposition rate so that the yield was initially guessed at. These samples, however, are indicative of the good sample quality and reproducibility. The sc20 series displays a small oscillation in the $T_c(d_{Co})$ curve. The most interesting data is that of sc23 where a definite oscillatory behaviour is observed. These two series in which we observe the most promising results are those containing either Fe as the spacer layer, having a larger moment than Co and therefore greater magnetic influence, or the thinnest Pb films.

4.6 Conclusions and Further Work

Sputtered multilayers of Nb/Co were prepared and characterised by X-ray reflectometry and dc magnetisation techniques. This is further supported by the superconducting properties exhibited by the multilayers, eg anisotropy, as will be discussed in the following chapter.

Although the Nb/Co samples were determined to be of consistently good quality, the oscillation effect is very subtle and has been masked by interface mixing of the niobium and cobalt and the concomitant changes in transition temperature. As stated previously it is difficult to derive any solid conclusions from the data collected on the Nb-based multilayer, although promising results have been shown by series sc02 and sc10. The first of these displays a minimum in T_c coinciding with the onset of ferromagnetism in the cobalt layers. Similarly the multiple oscillations of series sc10 are not unusual with several authors having reported oscillations containing more than a single maximum. Given the inherent problems of the metallurgy of this system, it is impressive indeed that anyone has observed an oscillation in this system.

Additional multilayers consisting of Pb/Co and Pb/Fe were prepared and characterised by X-ray reflectometry and dc magnetisation techniques. They were found to exhibit good structural properties, having smooth surfaces and clean interfaces as evidenced by PNR and X-ray reflectometry. Any problems during fabrication that have directly influenced the sample's make-up are clearly visible in the critical temperature and transition breadth. The only problem experienced during the preparation of these multilayers was in the determination of the Pb layer thickness.

The initial samples consisted of superconducting layers which were too thick, allowing only the decoupling of the layers to be observed. The results from series sc20 (Pb/Fe) and sc23, thinner Pb, look far more promising. Both of these display oscillations, with that of sc23 showing a single broad maximum similar to that predicted by Radović. The region of interest in this system, see Figure 4.5, is small and unfortunately the time limitations of this project have only allowed us to isolate the range of sample parameters.

It is apparent that for such difficult measurements a large number of systematic measurements are required. Many of the problems encountered could be eliminated by either good access to sputtering facility or ideally to have your own. This opens up the opportunity to vary the sputtering parameter, including gun currents and

atmosphere pressure, to gain better knowledge and control of the sputtering environment and ultimately interface quality. At present the sputterer at the University of Leeds is one of a handful in the United Kingdom and as such is in great demand to the point of being oversubscribed. The facility also deals primarily with magnetic spin-valve systems so that it was a steep learning curve for all with regards to working with superconducting materials.

The experience and knowledge gained through this project is already being put to good use. At present our group is continuing to study these types of systems using a variety of techniques. Most notable is the slow- μ SR examination of Pb/Fe multilayers in which a direct observation of RKKY-type oscillation has recently been performed [19]. The problem of Pb deposition rate is yet to be completely resolved. Currently the calibration Pb films is being solved by PNR coupled with additional profilometry measurements performed by Chris Marrows. Additionally, the sample quality that we have shown to be available through sputtering has inspired other groups to consider using this technique.

References

- [1] H. K. Wong *et al.*, Journal of Low Temperature Physics **63**, 307 (1986).
- [2] Z. Radovic *et al.*, Physical Review B **44**, 759 (1991).
- [3] Z. Radovic, L. Dobrosavljevic-Grujic, A. I. Bazdin, and J. R. Clem, Physical Review B **38**, 2388 (1988).
- [4] J. Aarts *et al.*, Physical Review B **56**, 2779 (1997).
- [5] M. G. Khusainov and Y. N. Proshin, Physical Review B **56**, R14283 (1997).
- [6] K. Usadel, Physical Review Letters **25**, 507 (1970).
- [7] P. Koorevaar, Y. Suzuki, R. Coehoorn, and J. Aarts, Physical Review B **49**, 441 (1994).
- [8] G. Verbanck *et al.*, Physical Review B **57**, 6029 (1998).
- [9] C. Strunck, C. Surgers, U. Paschen, and H. v Lohneysen, Physical Review B **49**, 4053 (1994).
- [10] Y. Obi, M. Ikebe, H. Wakou, and H. Fujimori, Journal of the Physical Society of Japan **68**, 2750 (1999).
- [11] Y. Obi, H. Wanou, M. Ikebe, and H. Fujimori, Proceedings of the 21st International Conference on Low Temperature Physics **S2**, 721 (1996).
- [12] T. Muhge *et al.*, Physical Review Letters **77**, 1857 (1995).
- [13] L. Lazar *et al.*, Physical Review B **61**, 3711 (2000).
- [14] Y. Obi, M. Ikebe, T. Kubo, and H. Fujimori, Physica C **317-318**, 149 (1999).

- [15] F. Y. Ogrin, S. L. Lee, A. D. Hillier, and T.-H. Shen, *Physical Review B* **183**, 1659 (2000).
- [16] S. L. Lee, private communication.
- [17] J. J. Hauser, H. C. Theuerer, and N. R. Werthamer, *Physical Review* **142**, 118 (1966).
- [18] *Metals Reference Book*, edited by C. J. Smitthel (Butterworth, London, 1976).
- [19] S. L. Lee, private communication.

Chapter 5

Vortex Behaviour in Superconductor/Ferromagnet Multilayers

5.1 Introduction

Superconducting multilayers (ML) have unique physical properties that are quite different from those of both bulk superconductors and thin films. They are therefore interesting objects for fundamental science and have been intensively studied over the last decade, especially in connection with high- T_c superconductors (HTSC) [1]. The HTSC are well known to have a layered structure with superconductivity confined to the Cu-O layers and exhibit high anisotropy of their physical properties. These compounds behave as layered superconductors in the sense that they exhibit quasi-2D properties. An example of this crossover is the observation of 3D-2D transition in the vortex lattice, where the disintegration of the 3D vortex line and the appearance of a quasi-2D pancake vortices in individual layers is observed. For the understanding of HTSC properties caused by its layered structure, experiments on model low- T_c MLs with well defined parameters are of great importance.

5.2 Review

One of the peculiar properties of superconducting MLs is the three-to-two (3D-2D) dimensional crossover. In multilayers with strong interlayer coupling, the supercon-

ductivity is anisotropic three-dimensional (3D), while in the absence of coupling, the superconductivity is two-dimensional (2D). For weak interlayer coupling, the superconductivity is quasi-2D, showing a dimensional crossover.

The starting point to understanding the nature of the 3D-2D transition is the phenomenological Lawrence-Doniach model, based on the Ginzburg-Landau theory. In this model layered superconductors are viewed as stacked two dimensional superconductors, within each the G-L order parameter is a 2-D function, coupled together by Josephson tunneling between adjacent layers.

Close to T_c this model reduces to the anisotropic G-L theory with different coherence lengths parallel (ξ_{\parallel}) and perpendicular (ξ_{\perp}) to the plane of the layer. In this 3D regime the upper critical fields are given by the familiar equations

$$H_{c2\perp}(T) = \frac{\phi_0}{2\pi\xi_{\parallel}^2(T)} \quad (5.1)$$

and

$$H_{c2\parallel}(T) = \frac{\phi_0}{2\pi\xi_{\parallel}(T)\xi_{\perp}(T)}. \quad (5.2)$$

The angular dependence between these two extremes is governed by the following relationship

$$\left(\frac{H_{c2}(\theta)\sin(\theta)}{H_{c2\perp}}\right)^2 + \left(\frac{H_{c2}(\theta)\cos(\theta)}{H_{c2\parallel}}\right)^2 = 1 \quad (5.3)$$

where θ is the angle between the film surface and the field direction. A bell-like shape is displayed, with a smooth variation at $\theta=0^\circ$ (applied field parallel to layers), see Figure 5.1C.

With decreasing temperature $\xi_{\perp}(T)$ contracts and the layers eventually decouple. In this regime the upper critical fields are better described by the Tinkham model for isolated 2D superconducting films (see Chapter 1). The upper critical field perpendicular to the film has the same form as that described above

$$H_{c2\perp}(T) = \frac{\phi_0}{2\pi\xi_{\parallel}^2(T)}. \quad (5.4)$$

In a parallel field, the radius of the vortex perpendicular to the layer is restricted by the finite thickness of the superconducting film (D). The parallel critical field then shows a square-root dependence on temperature

$$H_{c2\parallel}(T) = \frac{\phi_0\sqrt{12}}{2\pi\xi_{\parallel}(T)D}. \quad (5.5)$$

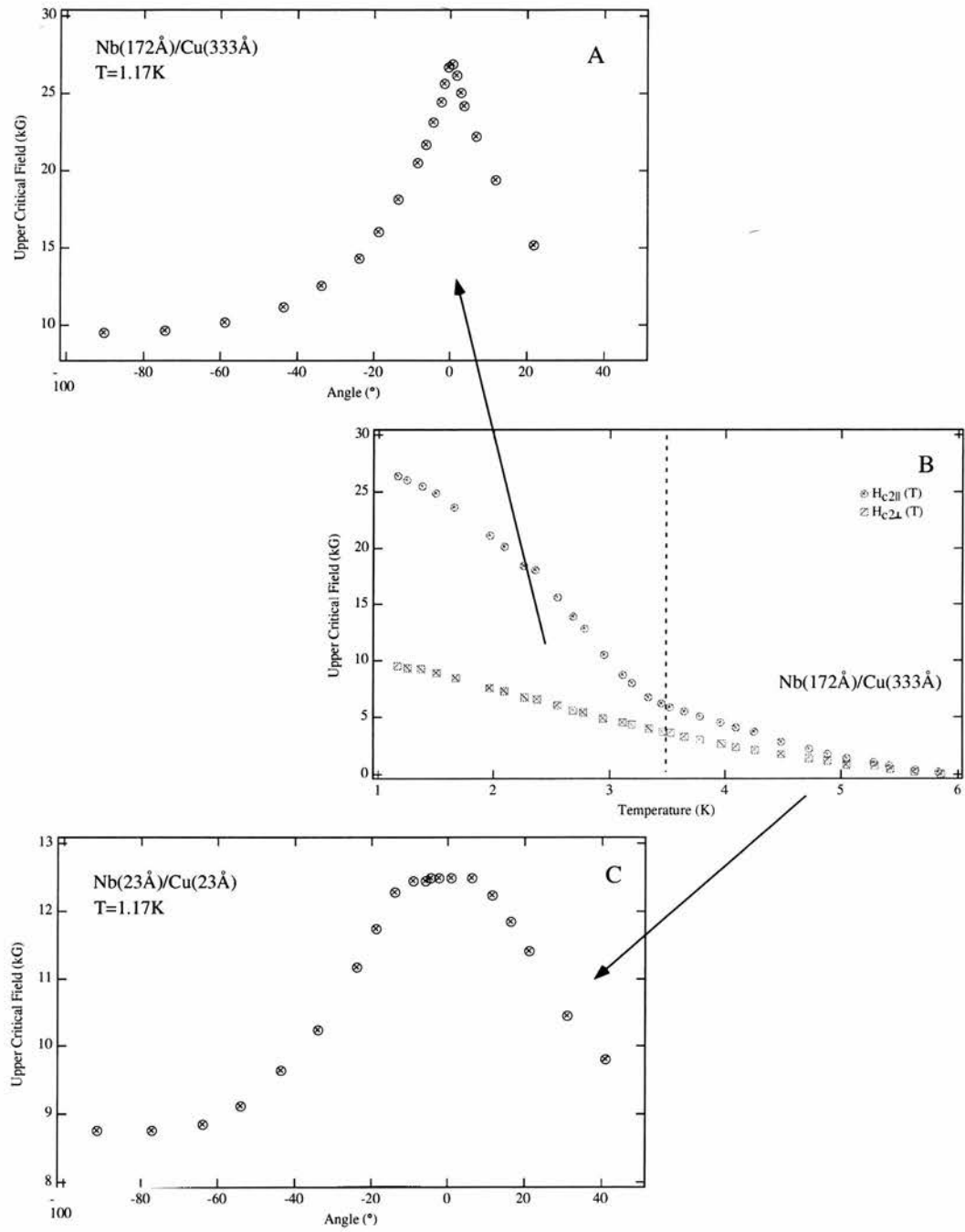


Figure 5.1: (A) Angular dependence of the critical field in the 2D state (B) Upper critical field for a Nb/Cu superlattice (C) Angular dependence of the critical field in the 3D state (all from ref[2]). The dimensional crossover is clearly observed in the temperature variation of the parallel critical field, as is the striking difference in the angular dependences.

For a 2D-thin-film Tinkham has obtained the following expression:

$$\left| \frac{H_{c2}(\theta) \sin(\theta)}{H_{c2\perp}} \right| + \left(\frac{H_{c2}(\theta) \cos(\theta)}{H_{c2\parallel}} \right)^2 = 1. \quad (5.6)$$

This shows similar behaviour to the angular dependence displayed in the 3D regime at high angles but differs in that it exhibits a cusp at $\theta=0^\circ$, see Figure 5.1A.

For the case of non-magnetic spacers the crossover to 2D behaviour occurs when ξ_\perp falls below some characteristic length which is of the order of D , the spacer layer thickness. The crossover is then observable through the following manifestations:

- (i) the transition from linear-to-square root dependence in the parallel upper critical field $H_{c2\parallel}(T)$
- (ii) the change of the angular dependence of the upper critical field $H_{c2}(\theta)$ from smoothly varying bell-like shape to being cusped when the field is parallel to the film.

The dimensional crossover phenomenon has been widely observed in various superconducting multilayers having different structures; superconductor-insulator-superconductor[3], superconductor-metal-superconductor[1, 2, 4, 5], superconductor-semiconductor-superconductor [6], superconductor-magnet-superconductor [7, 8, 9] and recently superconductor-spin glass-superconductor [10] systems.

In ML consisting of superconducting and non-magnetic (insulating or metallic) layers the crossover in behaviour is often observed as a function of temperature as the coherence length contracts with decreasing temperature.

In SC/FM multilayer systems similar crossover behaviour has been reported in the temperature dependence of $H_{c2\parallel}$. Obi et al. observed 3D behaviour in Nb/Co and V/Co multilayers for $d_{Co} < 12\text{\AA}$ and 24\AA respectively [7]. Similarly Verbanck et al. measured complete decoupling of the superconducting layers to occur for $d_{Fe} \geq 12\text{\AA}$ in Nb/Fe systems [8]. In these cases the 2D decoupled state was not observed to occur at the onset of ferromagnetism in the spacer layer but at larger FM thickness. However, an early study of the V/Fe system [11] showed decoupled 2D superconductivity to exist before the onset of ferromagnetism. At present there exists some ambiguity as to when the superconducting layers decouple, which is almost certainly related to the sample quality. It also seems worrying, given the relative moment sizes, that Obi observed 12\AA Co spacer layers to decouple Nb multilayers while 3D superconductivity exists in Nb/Fe of similar thickness.

5.3 Characterisation

The preparation and characterisation of these systems has already been described elsewhere (see Chapter 4) although a summary of the relevant samples is given in the table below.

Table 5.1: Characteristics of the 7 Nb/Co multilayer samples studied where d_{Co} is the average expected layer thickness.

No.	Sample type	d_{Nb} (Å)	d_{Co} (Å)	T_c (K)
sc02_02	Si/Co/(Nb/Co) _{x10}	400	13.8	7.66
sc02_05	Si/Co/(Nb/Co) _{x10}	400	20.7	8.15
sc02_08	Si/Co/(Nb/Co) _{x10}	400	27.6	8.08
sc02_14	Si/Co/(Nb/Co) _{x10}	400	41.4	8.27
sc13_04	Si/Co/(Nb/Co) _{x5}	400	3.08	7.69
sc13_05	Si/Co/(Nb/Co) _{x5}	400	5.04	7.48
sc13_06	Si/Co/(Nb/Co) _{x5}	400	7.00	7.41

5.4 Experimental

Samples were characterised by four-probe dc resistive transition measurements with field and current parallel as described elsewhere (see Chapter 4). High resolution H_{c2} angular measurements were performed at a variety of temperatures. The angle θ between the film surface and external field orientation was controlled via a step motor mechanism. This allowed an angular resolution equal to 0.02° .

The transition was observed using both field and angular swept methods with the value obtained at half the resistive transition characterising the latter. In the case of field swept measurements, the observed transition width was broad, often of the order of 0.5kOe, and a criteria of 90% was used to avoid underestimating the critical field.

Also presented are results from some preliminary magnetisation and flux flow experiments. In the latter, the sample was repositioned so that the applied magnetic field remained in plane under rotation.

5.5 Results

5.5.1 sc02 series

Angular Dependence

The angular dependence of the upper critical field obtained over a range of temperatures for sample sc02.08 is shown in Figure 5.2. At temperatures significantly lower than T_c , the range of fields available becomes limited but this does not seem to have affected our results. All the data show excellent agreement with the predicted Tinkham curve for a 2D superconducting film.

There seems to be some confusion regarding the upper critical fields defined by the different models presented earlier. At least one author[2] has defined the following quantity

$$\xi_{\perp}(T) = \left(\frac{\phi_0}{2\pi H_{c2\perp}} \right)^{1/2} \frac{H_{c2\perp}}{H_{c2\parallel}} \quad (5.7)$$

where $H_{c2\perp}$ and $H_{c2\parallel}$ are described by the anisotropic G-L theory. Although this does indeed describe the behaviour of $\xi_{\perp}(T)$ in the 3D regime they continued to use this formalism to define a coherence length in the decoupled regime, where the anisotropic Ginzburg-Landau is no longer valid.

Similarly, the above relationship was used to describe a temperature independent distance[9];

$$d_{\perp} = \xi_{\perp} = \left(\frac{\phi_0}{2\pi H_{c2\perp}} \right)^{1/2} \frac{H_{c2\perp}}{H_{c2\parallel}}. \quad (5.8)$$

This defined the effective length scale of the magnetic spacer layer which is larger than actual physical size due to its pair-breaking properties. Unfortunately this analysis is flawed for two important reasons. Firstly, as with the previous author, the G-L theory was applied in a situation where it is invalid. Secondly these equations all describe the properties of the superconducting layers and not those of the spacer.

In a similar manner to the relationships above we produce the following using equations 5.4 and 5.5

$$\frac{D}{\sqrt{12}} = \left(\frac{\phi_0}{2\pi H_{c2\perp}} \right)^{1/2} \frac{H_{c2\perp}}{H_{c2\parallel}} \quad (5.9)$$

where D is the superconductor film thickness. Whereas equation 5.7 is valid above the dimensional crossover, 3D superconductivity, our relationship is correct in the 2D decoupled regime.

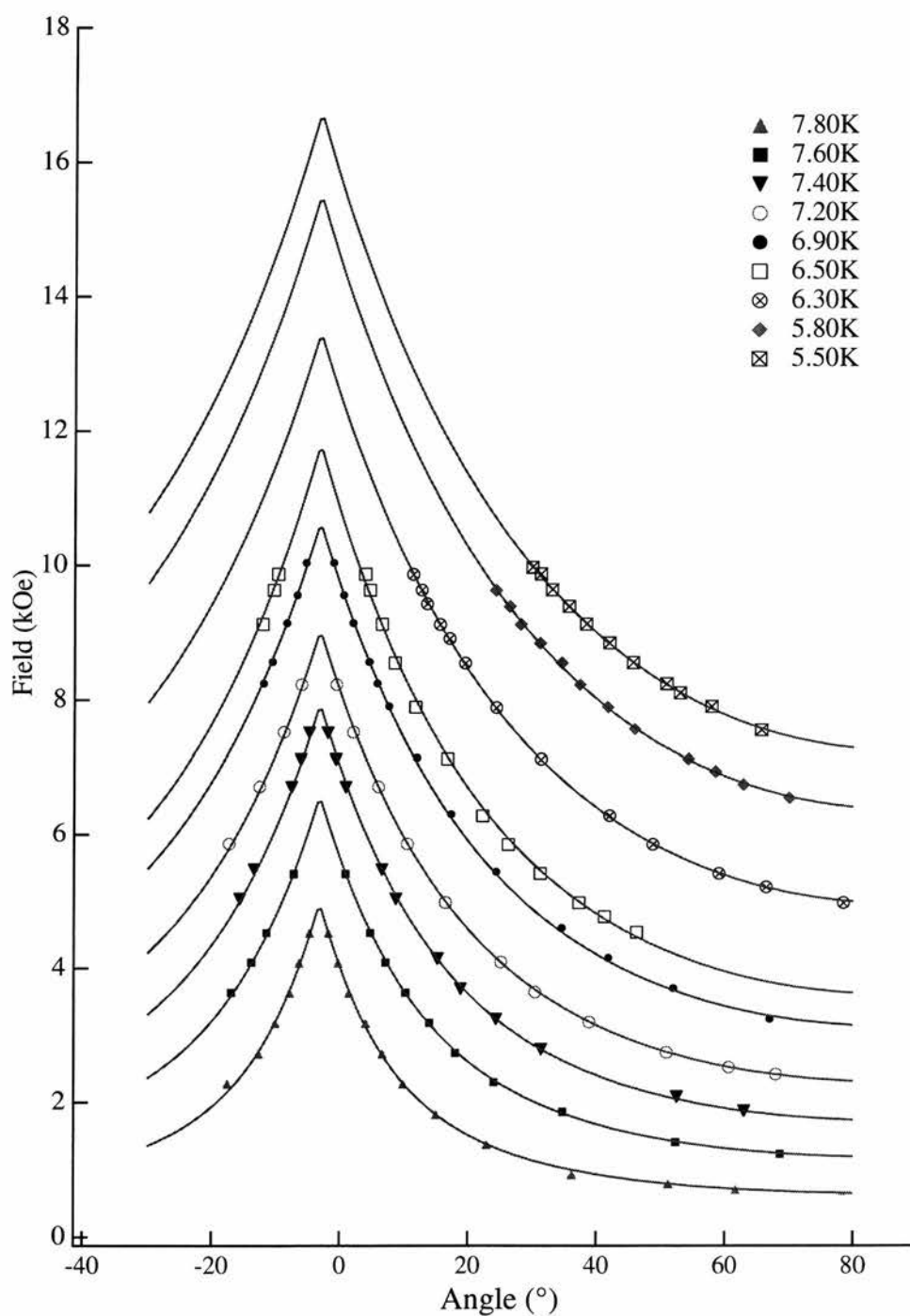


Figure 5.2: Angular dependence of the upper critical field for samples sc02_08 at various temperatures. Lines are fits to the experimental points with equation 5.6.

One problem when working with superconducting films is surface superconductivity. To counter this effect all films terminated in a Co layer. The existence of surface superconductivity would lead to the Tinkham behaviour displayed in the angular dependence of the upper critical field with the following ratio $H_{c2\parallel}/H_{c2\perp} = 1.70$ [12]. Analysis of our data shows that this is indeed not the case and our measurements are that of the bulk multilayer.

The temperature dependence of D , as defined in equation 5.9, is shown in Figure 5.3. As one would expect there is no variation of the predicted film thickness with temperature. The higher error bars at lower temperature reflect the reduced range of fields available for measurement.

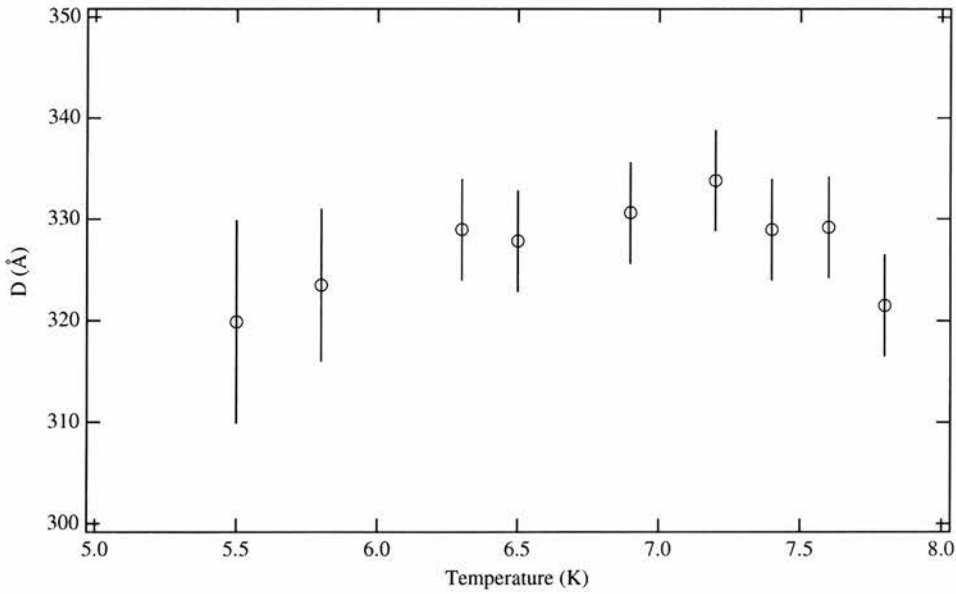


Figure 5.3: Temperature variation of D as determined from fits to angular dependence.

Scaling

Transport measurements were performed as a function of field and angle on four samples from series sc02 (see Table 5.1 for details). The data for sc02_08 is presented, along with the method analysis, followed by that obtained for the rest of the series studied.

In Figure 5.4 the temperature dependence of the upper critical fields, $H_{c2}(T)$, obtained at 50% of the resistive transition are shown for the magnetic field at a range of angles with respect to the film surface. The linear-to-square root transition, indicative of the 3D-2D crossover, is not observed in the $H_{c2||}$ dependence confirming that the sample is decoupled at all temperatures.

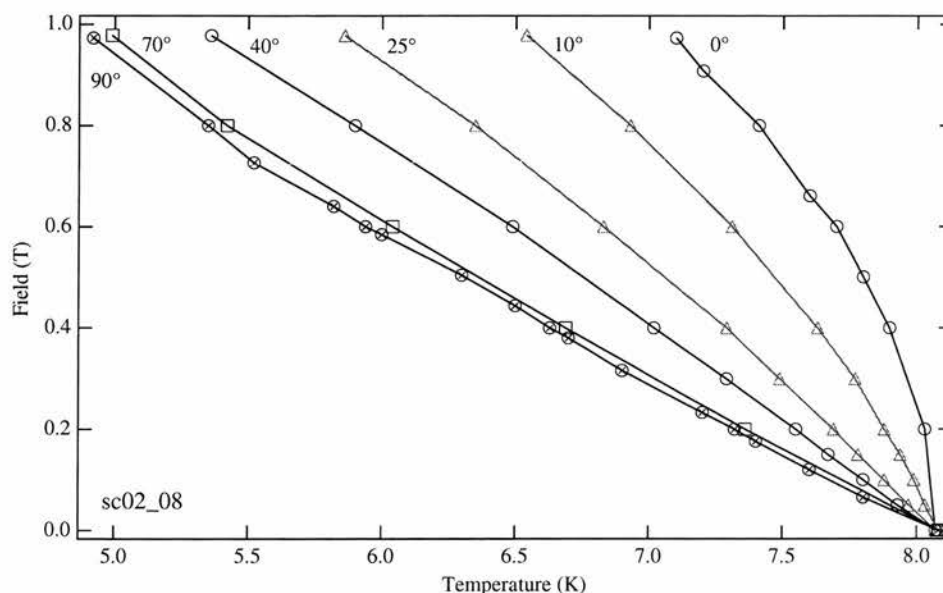


Figure 5.4: Overlay of the $H_{c2}(\theta, T)$ obtained for sample sc02_08 ($d_{Co}=27.6\text{\AA}$) at a range of angles. The lines are guides for the eye.

From Ginzburg-Landau theory we expect $H_{c2\perp}$ to display a linear temperature dependence close to T_c however, it is not unusual to observe a slight upward deviation from linearity at low temperatures [13]. Having already confirmed our sample to be in the decoupled 2D state, through the form of the angular dependence, we decided to verify whether the Tinkham theory extended to T_c or if, when sufficiently close to the transition temperature, the behaviour would be 3D.

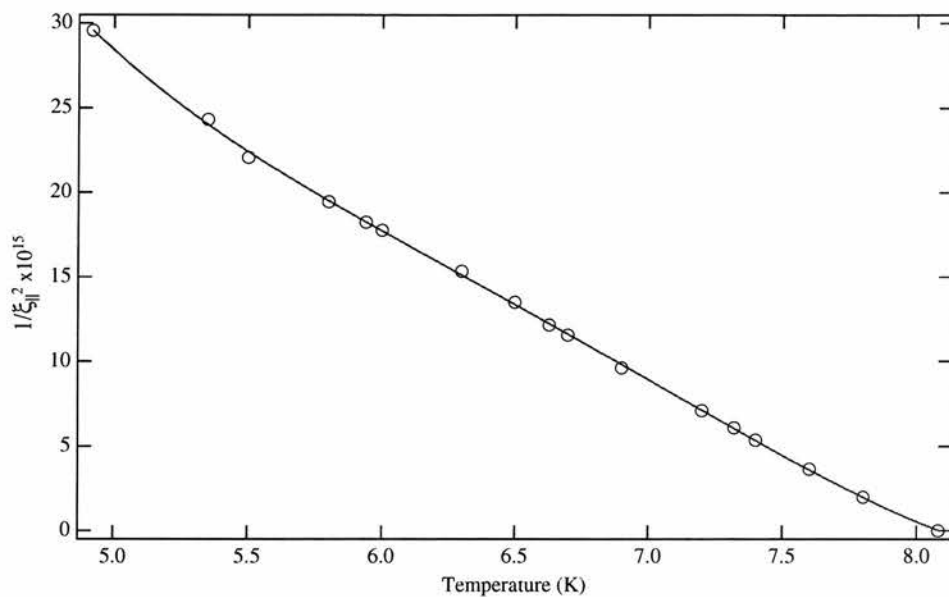


Figure 5.5: Polynomial fit to $1/\xi_{||}^2$ of sc02_08 to obtain a function describing the thermal dependence at all temperatures and not just close to T_c .

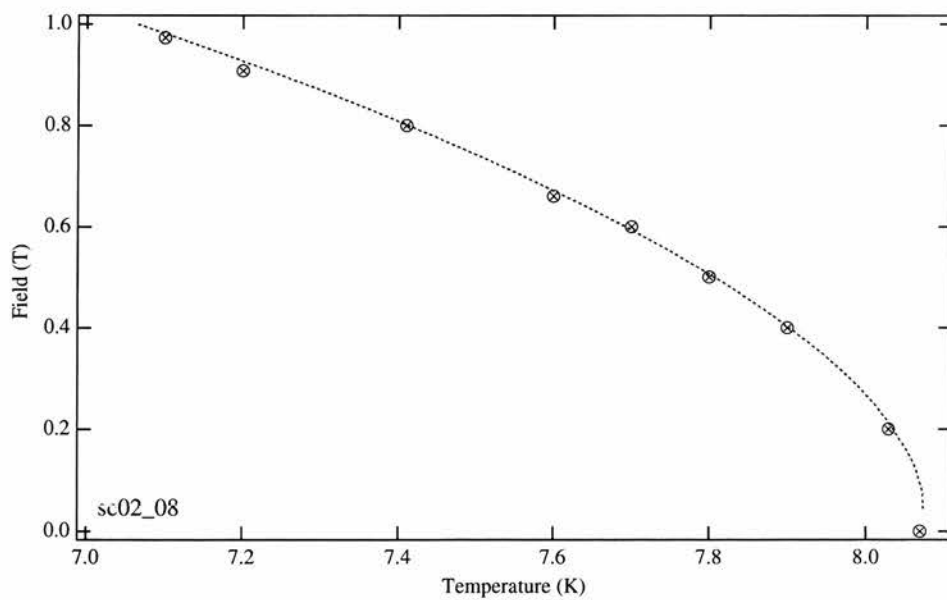


Figure 5.6: The upper critical field parallel to the film surface and the corresponding fit as described in the text.

The first step was to obtain a function to describe actual $\xi_{||}(T)$ measured for each sample. Typically this was achieved using a high order polynomial with no assumed no knowledge of the functional form. The data with fit to obtain $\xi_{||}(T)$ is shown in Figure 5.5.

Substituting into the equation below gives the dependence of $H_{c2||}(T)$

$$H_{c2||}(T) = \frac{\phi_0 \sqrt{12}}{2\pi \xi_{||}(T) D}. \quad (5.10)$$

The dashed line in Figure 5.6 represents this law fitted to the parallel field data. The best fit yields a value for the layer thickness $D \approx 336 \text{ \AA}$, which is close to the superconductor layer thickness, $d_{Nb} = 400 \text{ \AA}$.

Since our sample is in the 2D decoupled state we expect its behaviour to be governed by the Tinkham expression which can be re-written in the form

$$H_{c2\perp}^{Tink} = H_{c2}(\theta) |\sin(\theta)| \left(1 - (H_{c2}(\theta) \cos(\theta) \frac{2\pi \xi_{||} D}{\phi_0 \sqrt{12}})^2 \right)^{-1}. \quad (5.11)$$

In Figure 5.7 one can see that there is very good agreement of the data over the whole temperature range. Table 5.2 contains a selection of the scaling parameters, angle θ and D , obtained from comparison of the scaled angular data to the measured data.

Table 5.2: Tinkham fit parameters for sample sc02.08

Expt angle($^\circ$)	fit angle($^\circ$)	fit $D(\text{\AA})$
10	10.0	330
20	20.0	330
30	29.0	320
40	39.8	330
60	60.0	336
80	80.0	336
110	110.0	336

The fit parameters confirm that we have good knowledge of the angular orientation of our sample. There is also consistency in the value of the layer thickness $D \approx (331 \pm 10) \text{ \AA}$.

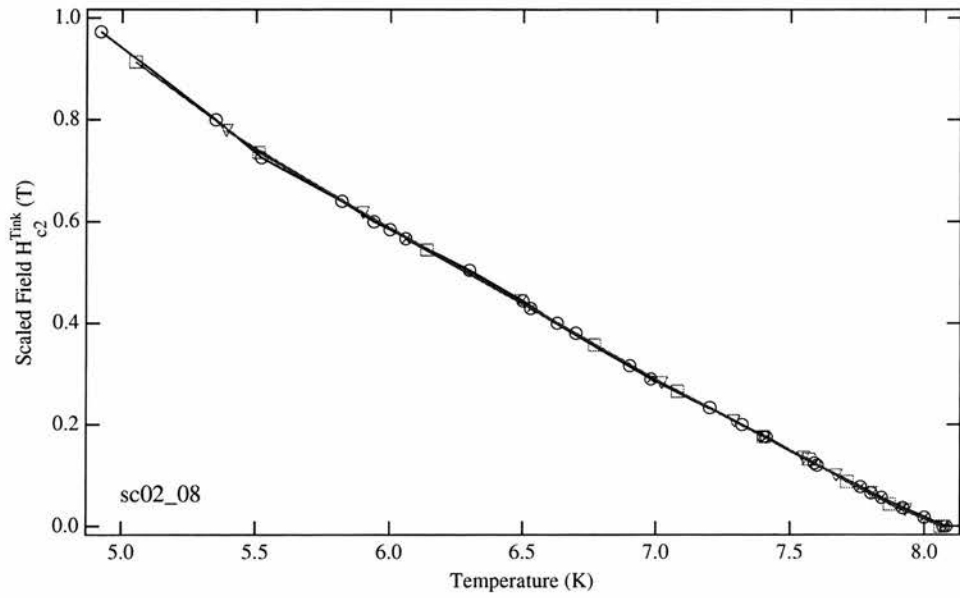


Figure 5.7: Tinkham scaling of angular field data, as described in the text, showing good agreement over the whole temperature range.

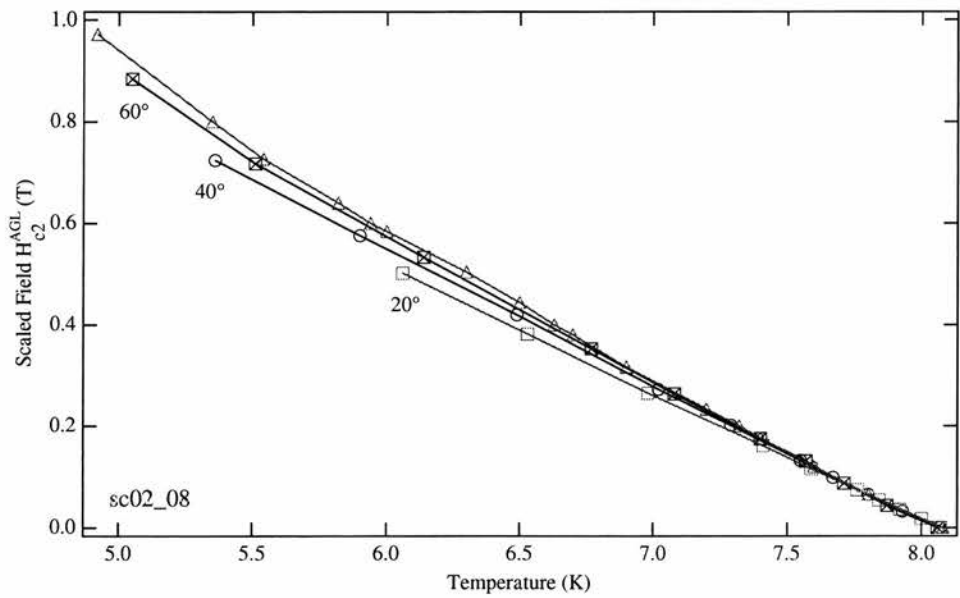


Figure 5.8: The expected $H_{c2\perp}(T)$ obtained from direct scaling of the angular $H_{c2}(\theta, T)$ data using the anisotropic Ginzburg-Landau theory.

A similar scaling was then performed using the anisotropic Ginzburg-Landau expression which can be expressed as follows

$$H_{c2\perp}^{AGL} = H_{c2}(\theta) \left(\sin^2(\theta) + \left(\frac{\xi_{\perp}}{\xi_{\parallel}} \right)^2 \cos^2(\theta) \right)^{1/2}. \quad (5.12)$$

The fit parameters obtained from the previous Tinkham fitting, with the substitution $\xi_{\perp} = D\sqrt{12}$, were used in anisotropic Ginzburg-Landau scaling to observe the applicability of each method. In Figure 5.8 the scaled $H_{c2\perp}^{AGL}$ for three angles mapped onto the measured $H_{c2\perp}$ are shown. The scaled data deviates from the expected behaviour with decreasing temperature and with increasing angle the deviation occurs at ever lower temperatures.

Close to T_c we observe that both scaling methods display good agreement with the measured data. This lack of a clear discontinuity between the scaling regimes demonstrates that the system does not cross from one regime, controlled by the anisotropic G-L theory, to a second, lower temperature regime, described by the Tinkham formalism. This suggests that the superconducting layers are probably decoupled until extremely close to T_c .

Similar studies were performed on three other samples in the sc02 series with the data being shown in the following figures. The table below provides a list of these figures as well as those for the sample already discussed (sc02_08).

Table 5.3: List of figures relating to the scaling.

Sample No.	sc02_02	sc02_05	sc02_08	sc02_14
Fit to $H_{c2\parallel}(T)$	Fig 5.10	Fig 5.14	Fig 5.6	Fig 5.18
Overlay of $H_{c2\parallel}(\theta, T)$	Fig 5.11	Fig 5.15	Fig 5.5	Fig 5.19
AGL scaling	Fig 5.12	Fig 5.16	Fig 5.8	Fig 5.20
Tinkham scaling	Fig 5.13	Fig 5.17	Fig 5.7	Fig 5.21

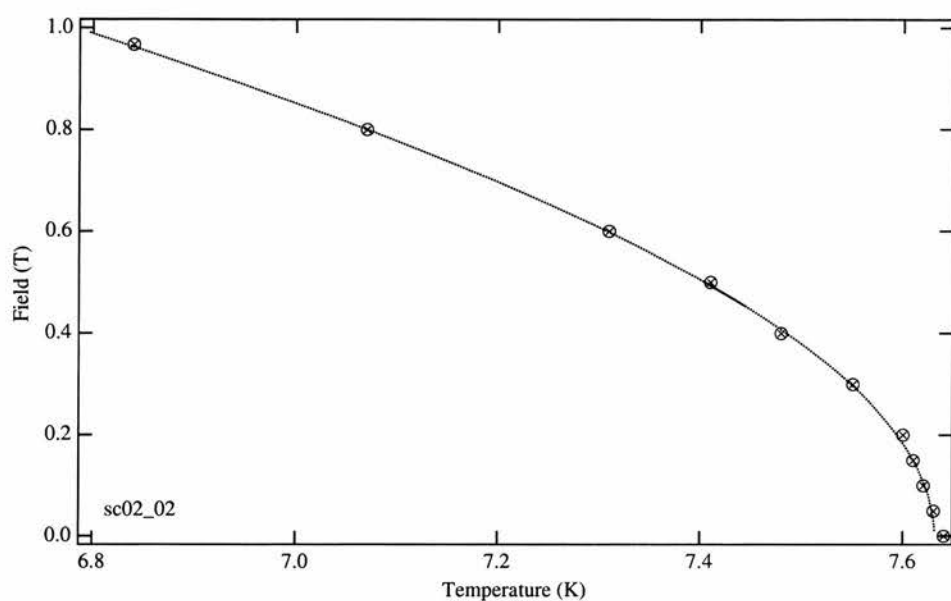


Figure 5.9: The upper critical field parallel to the film surface with corresponding fit as expected for 2D superconductivity.

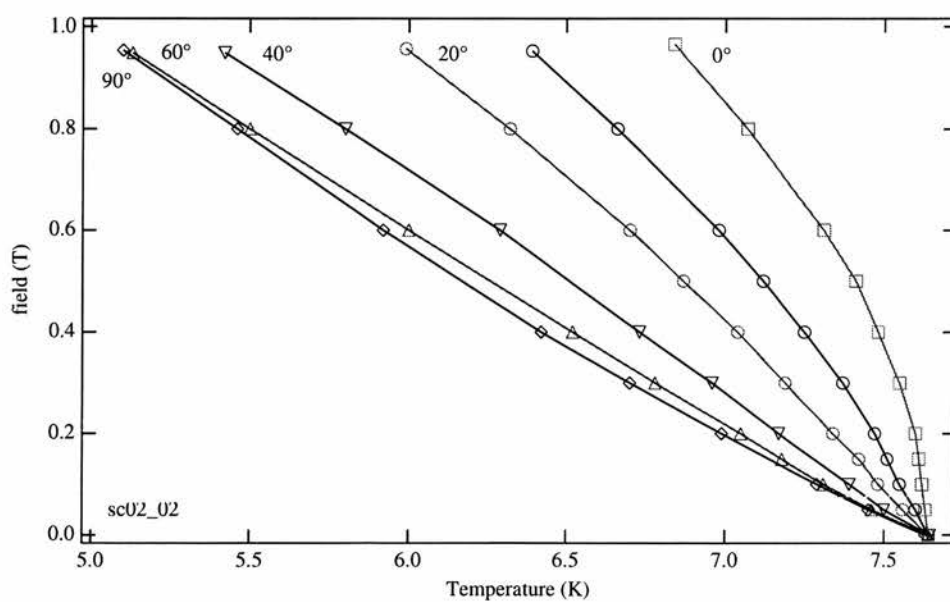


Figure 5.10: Overlay of the $H_{c2}(T, \theta)$ curves obtained for sample sc02_02 ($d_{Co}=13.8\text{\AA}$) at a range of angles. The lines are guides for the eye.

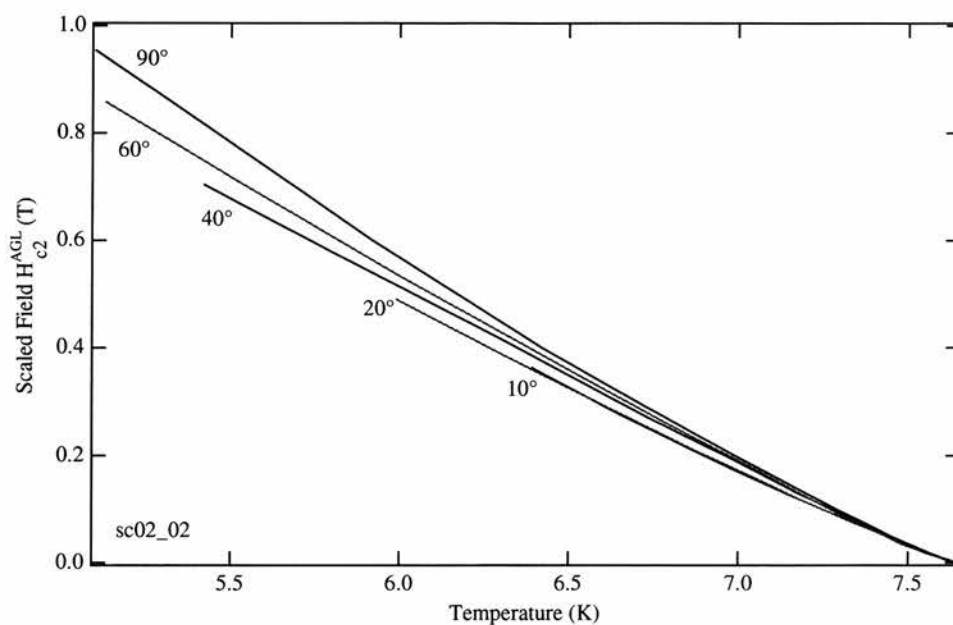


Figure 5.11: The expected $H_{c2\perp}(T)$ obtained from direct scaling of the angular $H_{c2}(T, \theta)$ data using the anisotropic Ginzburg-Landau theory.

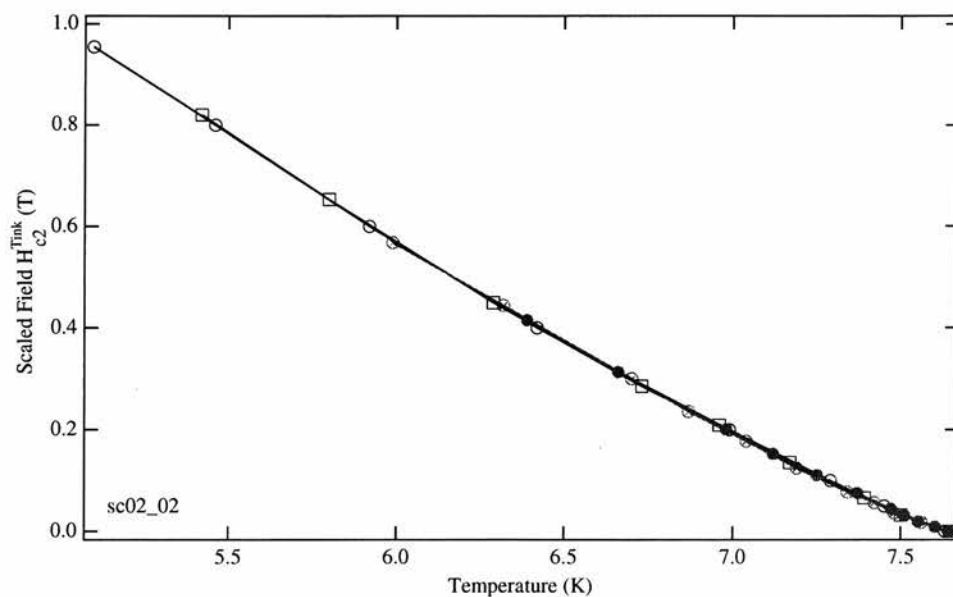


Figure 5.12: $H_{c2\perp}(T)$ obtained from Tinkham scaling of the measured $H_{c2}(\theta, T)$ data.

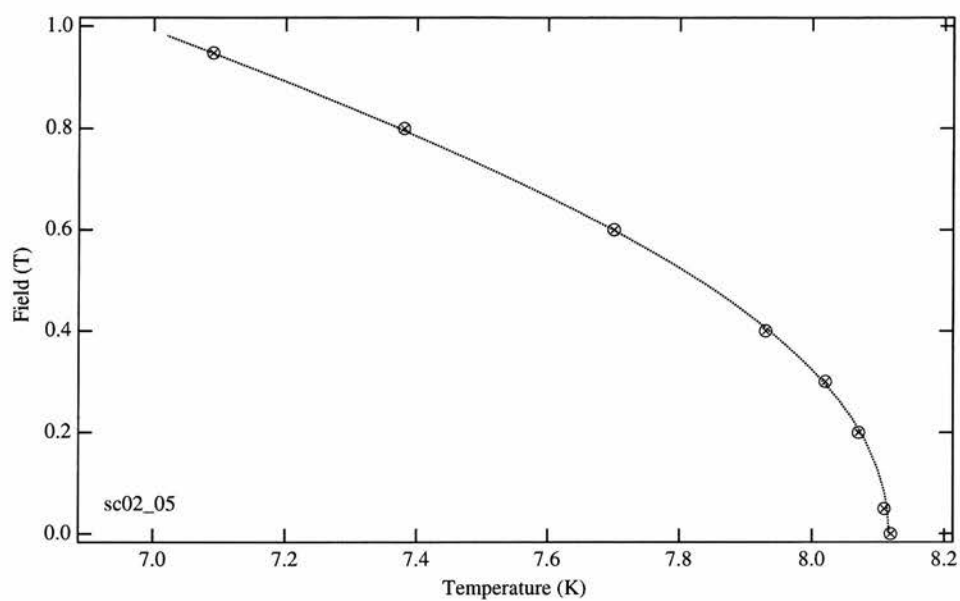


Figure 5.13: The upper critical field parallel to the film surface with corresponding fit as expected for 2D superconductivity.

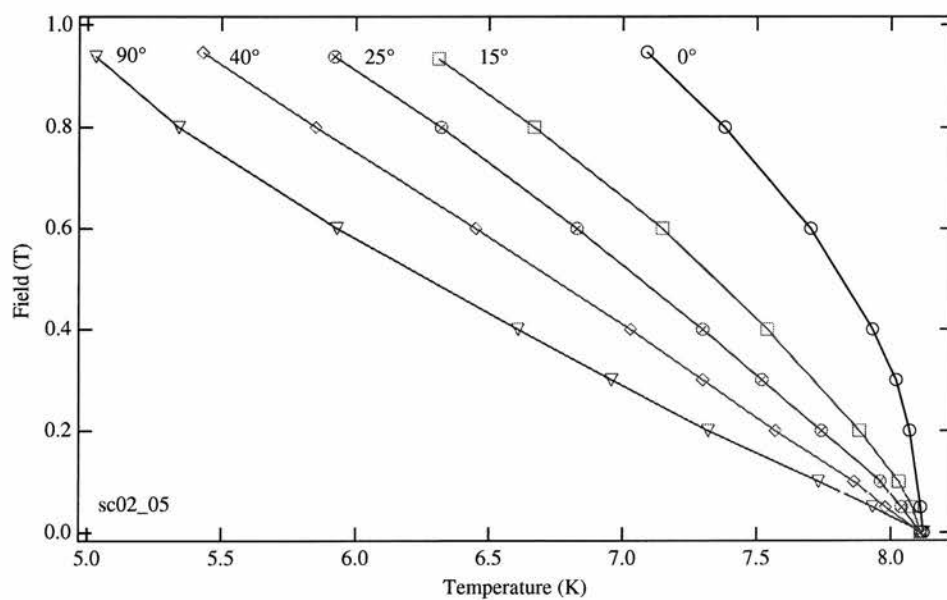


Figure 5.14: Overlay of the $H_{c2}(T, \theta)$ curves obtained for sample sc02_05 ($d_{Co}=20.7\text{\AA}$) at a range of angles. The lines are guides for the eye.

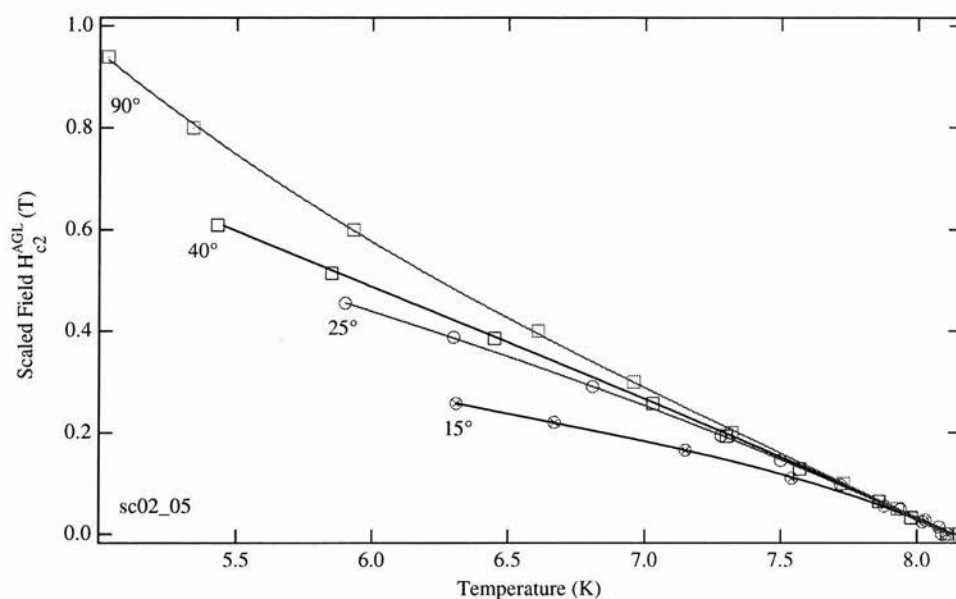


Figure 5.15: The expected $H_{c2\perp}(T)$ obtained from direct scaling of the angular $H_{c2}(T,\theta)$ data using the anisotropic Ginzburg-Landau theory.

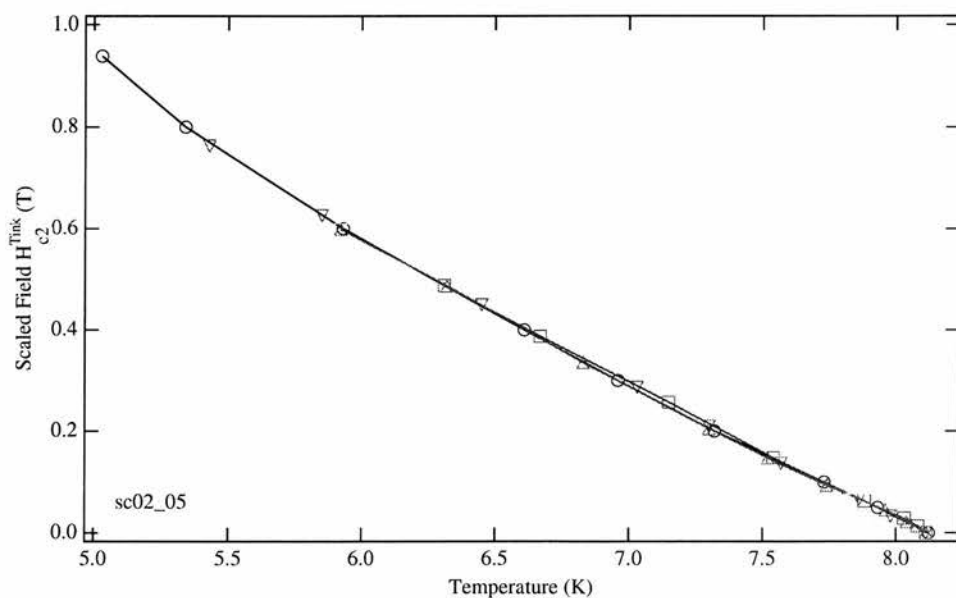


Figure 5.16: $H_{c2\perp}(T)$ obtained from Tinkham scaling of the measured $H_{c2}(\theta,T)$ data.

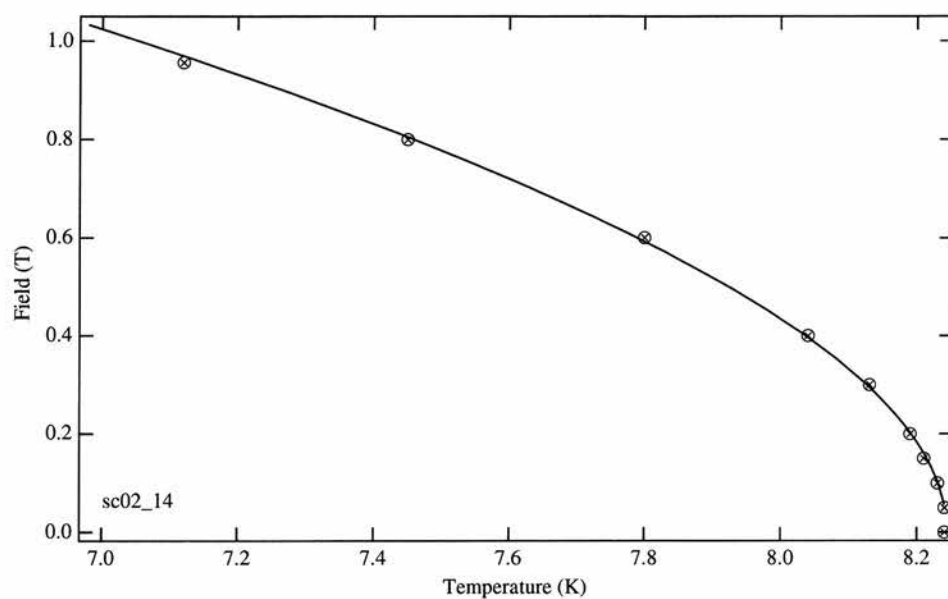


Figure 5.17: The upper critical field parallel to the film surface with corresponding fit as expected for 2D superconductivity.

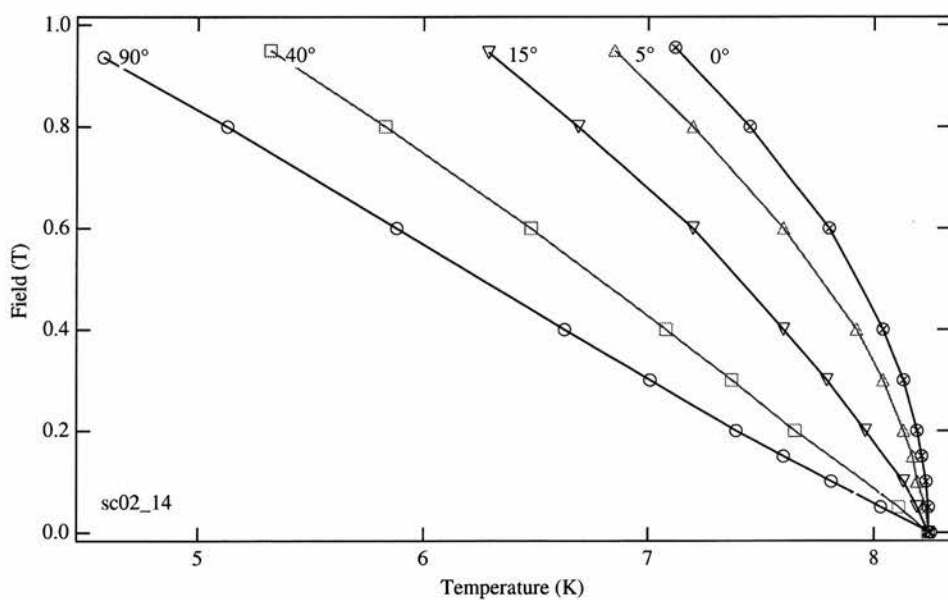


Figure 5.18: Overlay of the $H_{c2}(T, \theta)$ curves obtained for sample sc02_14 ($d_{Co}=41.4\text{\AA}$) at a range of angles. The lines are guides for the eye.

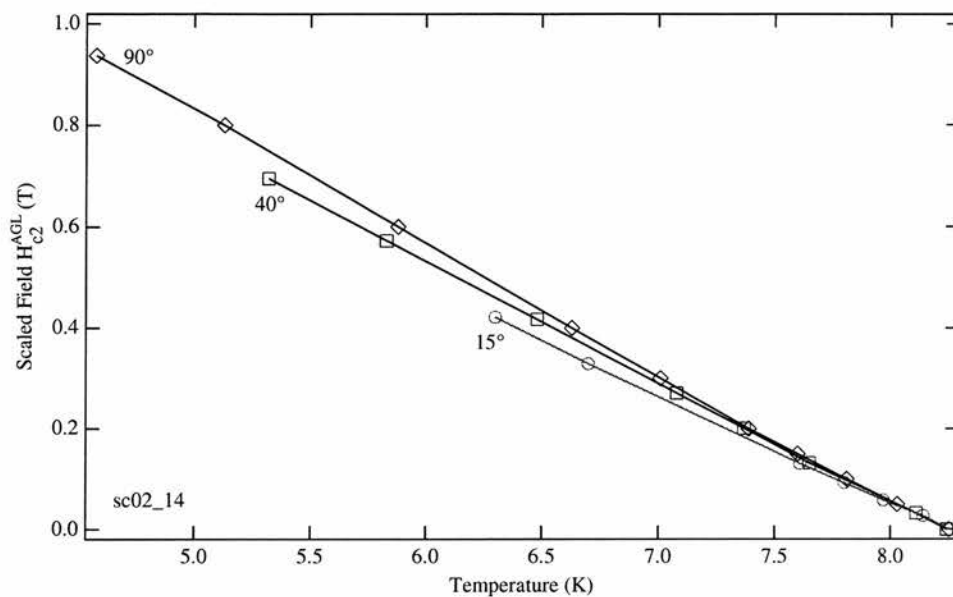


Figure 5.19: The expected $H_{c2\perp}(T)$ obtained from direct scaling of the angular $H_{c2}(T, \theta)$ data using the anisotropic Ginzburg-Landau theory.

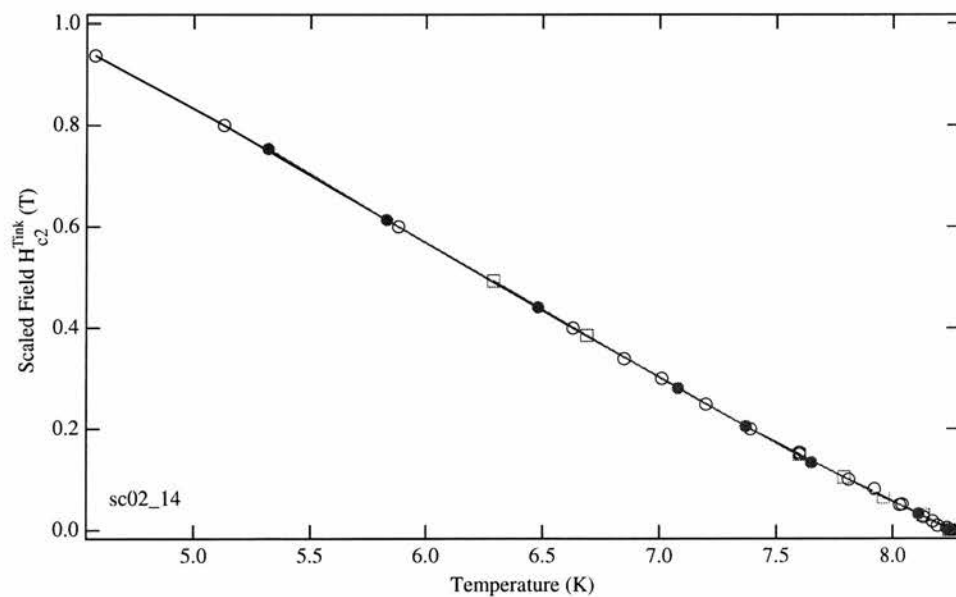


Figure 5.20: $H_{c2\perp}(T)$ obtained from Tinkham scaling of the measured $H_{c2}(\theta, T)$ data.

All our samples examined here do not appear to display a dimensional crossover, being in the 2D decoupled regime at all temperatures. The average D values obtained from fitting and scaling are given in Table 5.4 for each sample. We can see that there is no relationship between the spacer size and the measured layer thickness.

Table 5.4: Comparison of D-value from fitting with spacer thickness.

sample	$d_{Co}(\text{\AA})$	$D(\text{\AA})$
sc02_02	13.8	330
sc02_05	20.7	343
sc02_08	27.6	331
sc02_14	41.4	338

The estimated D value is slightly smaller than that expected for a single Nb layer, 400 \AA . We attribute this to the pair breaking effects of the magnetic layer which will inhibit superconductivity some way into the superconducting layer. Assuming $d_{Nb}=400\text{\AA}$, this would suggest that the magnetic effects extend 30-35 \AA into the Nb layers.

Analysis of the data obtained by Ogrin et al. [9] shows that their $d_{Co}=18\text{\AA}$ samples predicts a D of approximately 416 \AA . When compared to the expected individual layer thickness, 500 \AA , we see that the ferromagnetism extends into the superconductor layer by 42 \AA which is close to that measured here.

In the case of non-magnetic layers, the D value is measured to be slightly greater than the actual superconductor thickness. This is due to superconductivity expanding into the metal [14].

5.5.2 sc13 series

Our study continued with an investigation of ML systems containing very thin magnetic layers. However, instead of producing thin sheets, very short deposition times resulted in partially complete Co layers and clustering of large islands. This is confirmed by the observed superparamagnetic behaviour in these multilayers (see Figure 4.15) and the onset of ferromagnetism, indicative of complete coverage.

Figure 5.22 shows the temperature dependence of both $H_{c2\parallel}$ and $H_{c2\perp}$ for the Nb/Co multilayer sc13_04. The angular dependence of the upper critical field is shown in Figure 5.21. At all temperatures, the behaviour matches the Tinkham curve expected for a 2D superconductor, confirming that $H_{c2\parallel}(T)$ is indeed described by equation 5.5.

While $H_{c2\perp}$ can be described by the expected 3D behaviour $H_{c2\parallel}$ displays a change in behaviour at $T^*\approx 7.40\text{K}$. Normally this would indicate the 3D-2D crossover but the angular dependence follows the Tinkham dependence above and below T^* indicating that the ML is never in the 3D region.

$H_{c2\parallel}(T)$ was fitted in these two regions using the Tinkham equation:

$$H_{c2\parallel} = \frac{\phi_0\sqrt{12}}{2\pi\xi_{\parallel}D} \quad (5.13)$$

using the $\xi_{\parallel}(T)$ dependence obtained from $H_{c2\perp}(T)$. At lower temperatures this function was modified to determine the offset from T_c which we call T_{2D}^* . In this decoupled region $D \approx 370\text{\AA}$ which is close to the superconductor layer thickness, $d_{\text{Nb}}=400\text{\AA}$. The best fit yields a crossover temperature $T_{2D}^*=7.49\text{K}$. Close to T_c the fit gave $D \approx 780\text{\AA}$ which is twice the superconductor layer thickness.

The temperature dependence of the upper critical field for samples sc13_05 and sc13_06 are shown in Figures 5.23 and 5.24. This transition is again observed in the sc13_05 $H_{c2\parallel}(T)$ data although not in sc13_06. With increasing Co deposition the transition moves closer to T_c until, as shown in sc13_06 data, a single function describes the observed behaviour. This occurs, unsurprisingly, at the onset of ferromagnetism, at approximately 6\AA indicative of complete coverage of the film surface with Co.

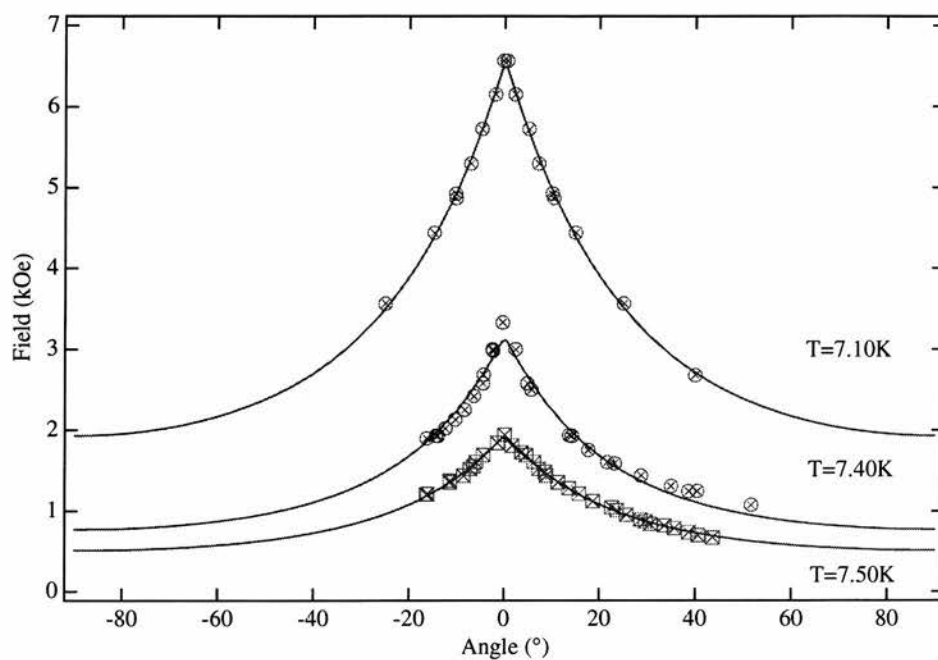


Figure 5.21: Angular dependence of sc13_04 above and below the transition.

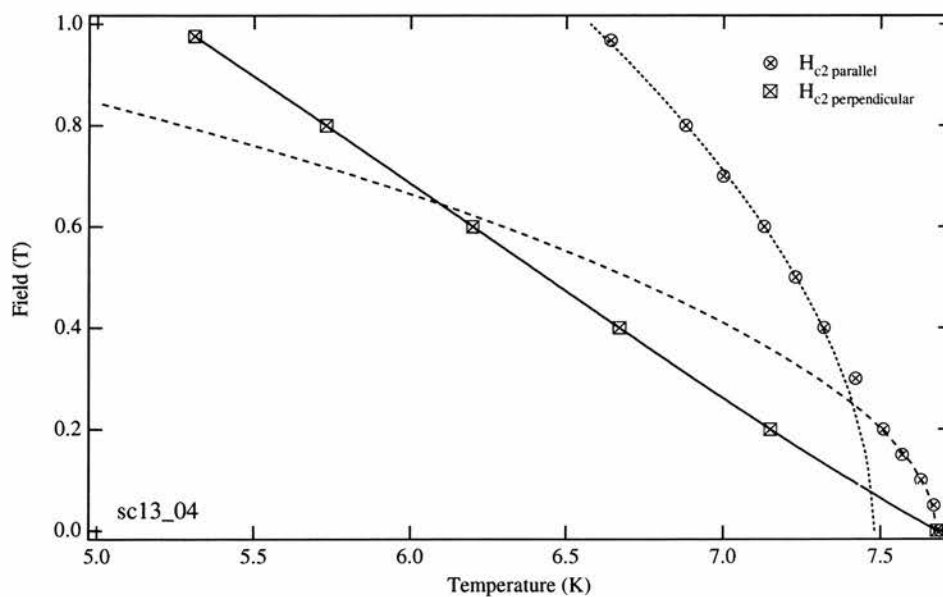


Figure 5.22: Temperature dependence of the upper critical field parallel and perpendicular to the film surface. The lines are fits to the data as described in the text.

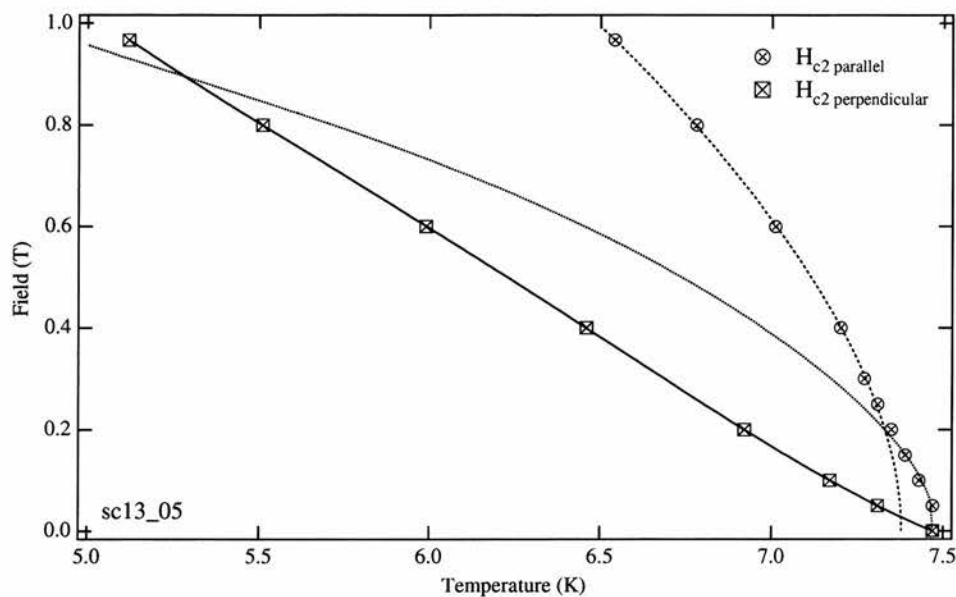


Figure 5.23: Temperature dependence of the upper critical field parallel and perpendicular to the film surface.

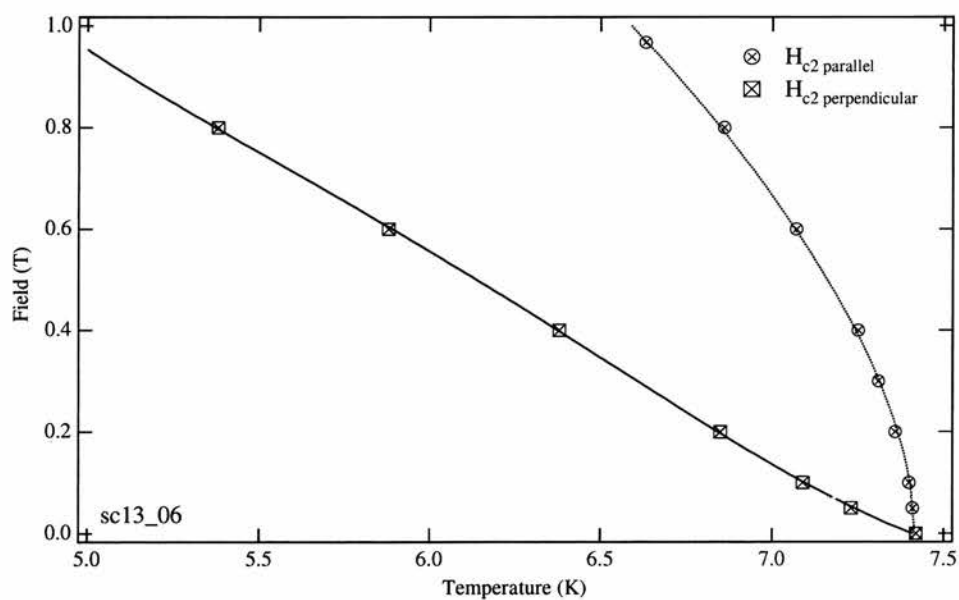


Figure 5.24: Temperature dependence of the upper critical field parallel and perpendicular to the film surface.

A summary of the D thickness determined for each sample is given in Table 5.5.

Table 5.5: Comparison of D-value from fitting with spacer thickness and crossover temperature.

sample	$d_{\text{Co}}(\text{\AA})$	$D^{\text{low}}(\text{\AA})$	$D^{\text{high}}(\text{\AA})$	$T_{2\text{D}}^*(\text{K})$
sc13_04	3.08	374	783	7.49
sc13_05	5.04	374	762	7.37
sc13_06	7.00	341	-	-

In this series we have observed two regions of decoupled superconductivity which is not in keeping with previous work where 3D behaviour is observed for very thin magnetic layers and crossover to 2D with decreasing temperature. Close to T_c the size of the superconducting layer is twice that expected. With decreasing temperature there is a transition to a 2D region of smaller superconducting layer thickness.

Below $T_{2\text{D}}^*$ superconductivity is *locked* into single decoupled layers. Closer to T_c the effective superconductor layer thickness is twice that of the actual layer size. At present we are unsure as to the why we observe this behaviour. One possibility is that the vortex core sits on the Co partial layer between the Nb sheets, thus reducing its energy. With regards to the crossover it is uncertain as to whether it results from a contraction of the coherence length imposed by a change in the magnetism in the spacer layer or an intrinsic property of the superconductor.

With increasing spacer material, increasing coverage, this transition temperature approaches T_c , the two coinciding when the spacer layer is complete. We therefore observed decoupling of the superconducting layers at the onset of ferromagnetism and not after as has been reported by previous studies. Comparison of the measured d_{Nb} with the expected value shows again that the pair breaking influence of the magnetic layer extends about 30\AA into the sc-layer, which is comparable with the previous series, sc02.

5.5.3 Magnetisation

Magnetisation data were collected with a SQUID at the University of Edinburgh and VSM at the University of St Andrews. The main purpose of these measurements was to characterise the samples, in particular to monitor the increase of the layer moment with Co thickness. These data have already been presented (see Chapter 4).

The magnetic response obtained from sc02.02 ($T_c=7.66\text{K}$) at 5K, with applied field parallel to the plane, is shown in Figure 5.25. The hysteresis loop is interesting, exhibiting a superposition of the ferromagnetic signal of the Co layer and that of the superconducting Nb.

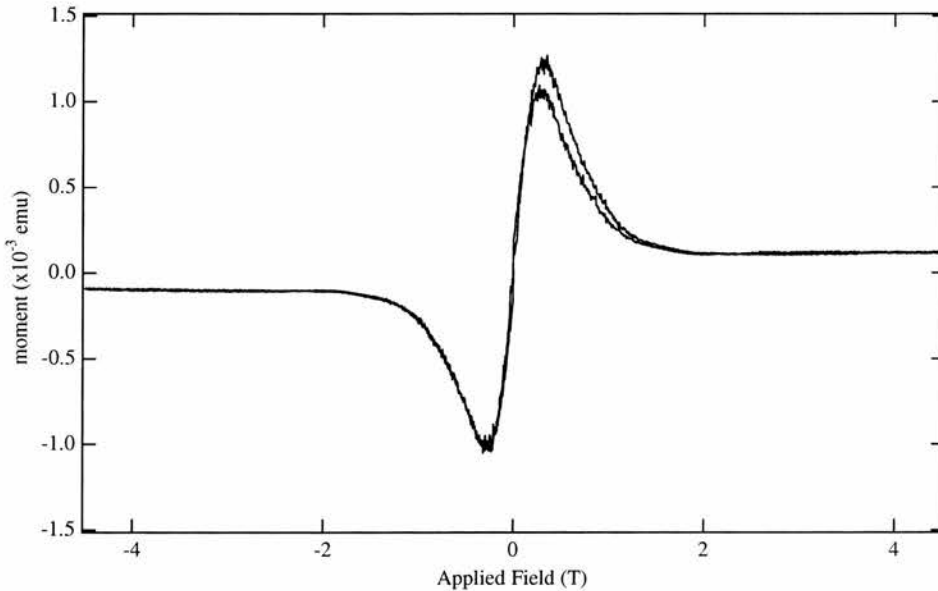


Figure 5.25: The hysteresis loop obtained below T_c for sample $\text{Co}14\text{\AA}/(\text{Nb}400\text{\AA}/\text{Co}14\text{\AA})_{\times 10}$. At high fields the ferromagnetism of the Co is observed.

We do not observe the expected diamagnetic signal but rather a paramagnetic one. This exists until the applied field is approximately 0.25T at which point the magnetisation begins to decrease. The magnetisation continues to decrease with increasing external field, reaching a plateau, offset due to the ferromagnetism of the Co layer, at 1.9T. Another peculiarity is the reversibility displayed in the loop which may indicate very weak pinning in this direction.

Previous measurements on these systems have investigated only the crossover

from purely ferromagnetic to completely superconducting, not displaying any unusual behaviour. These measurements, however, were performed in trilayer systems consisting of SC/FM/SC[15] and FM/SC/FM[16] which may account for the difference in our data.

Two scenarios arise which may describe the observed magnetic behaviour. If indeed the superconductor is in the Meissner state before reaching the down turn then the paramagnetic signal could result from a Meissner effect reacting to the return field of the cobalt. This contribution, although diamagnetic with respect to the return fields, is in the same direction as the applied field resulting in a paramagnetic signal.

Alternatively, flux may penetrate the superconductor at all times. In this case the paramagnetic signal can be explained by the fluxlines preferentially entering the center of sample and with increasing field spreading to the edges. The flux density profile is therefore the opposite of a normal superconducting slab and the resultant magnetisation also displays a change in sign or direction.

5.5.4 Flux Flow

Additional transport measurements were performed on sc02_14 after adjustment of the sample position as shown in Figure 5.26. This configuration allows investigation of vortex pinning within layers, in particular with respect to motion perpendicular to the planes.

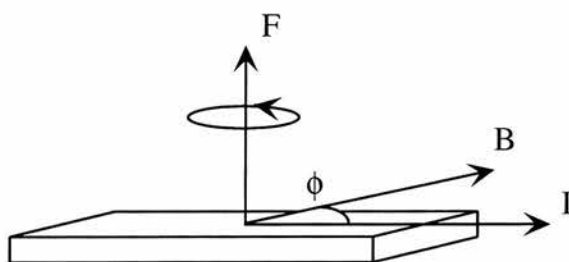


Figure 5.26: Schematic of the flux flow geometry with the force applied perpendicular to the layer interfaces.

In the previous orientation the applied field and current were always parallel, producing no force on the vortices. In the new arrangement the external magnetic field is always within the plane of the film. Under rotation the angle between the current and magnetic field is increased and will produce a Lorentz force on the vortices as

defined below

$$\mathbf{F} = \mathbf{I} \times \mathbf{B} = |\mathbf{I}||\mathbf{B}| \sin \phi \hat{\mathbf{z}}. \quad (5.14)$$

The vortex motion is expected to be hampered by the interlayer boundaries.

Measurements were performed at a range of angles and the transition monitored by field sweeping at fixed temperature. Figure 5.27 shows a selection of the transitions obtained by field sweeping at a rate of 0.31G/s at 7.50K. All transitions display step-like features, this is a result of the measurements being close to the resolution of our equipment and is reflected in this digitisation effect.

With increasing angle, and therefore force acting on the vortices, we observe the onset of the transition to the normal state occurring at decreasing critical field. There is no change in the actual H_{c2} value with all orientations displaying the same closing point. The onset field variation with angle is shown in Figure 5.28. As one would expect, the maximum onset field occurs when \mathbf{B} and \mathbf{I} are parallel and the minimum when $\phi=90^\circ$. The data has been fitted using the following function

$$H_{onset}(\phi) = H_{onset}(0) - \kappa |\sin(\phi - \phi_0)| \quad (5.15)$$

reflecting the dependence of the force on $\sin\phi$. ϕ_0 is an offset angle due to experimental inaccuracies.

From Figure 5.28 the broadening of the transition indicates that the system is in the flux flow regime and that vortices are moving perpendicular to planes. This is quite a surprising observation. The current used for these measurements is relatively small, only 7.5mA, implying that the applied force is also small. Since vortex motion is observed when the applied force is greater than the pinning force, the pinning in this orientation must be weak. This is contrary to the expected strong pinning at the SC/FM interface.

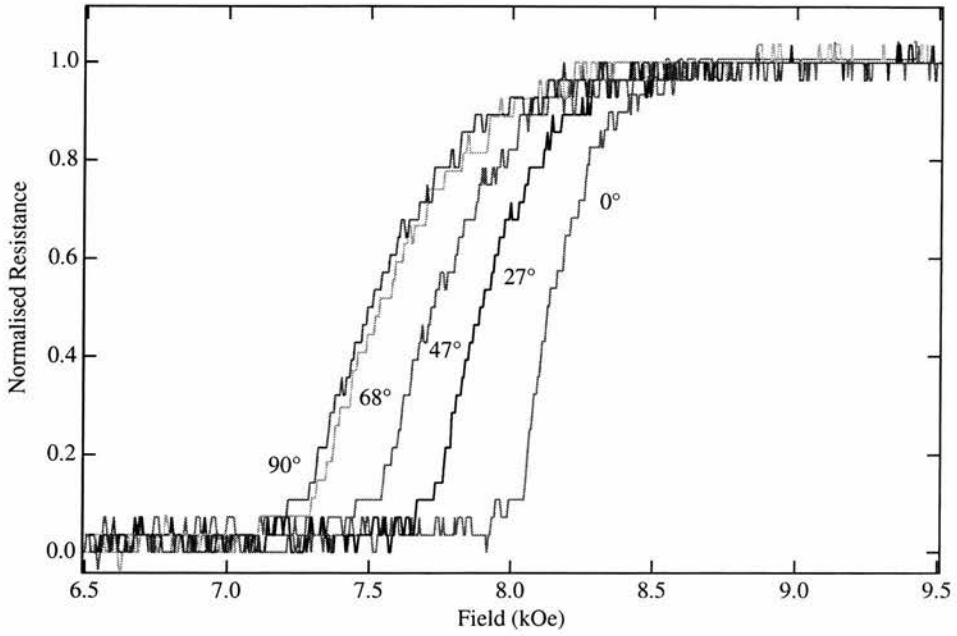


Figure 5.27: Typical resistive transitions for our sample with increasing angle between \mathbf{B} and \mathbf{I} .

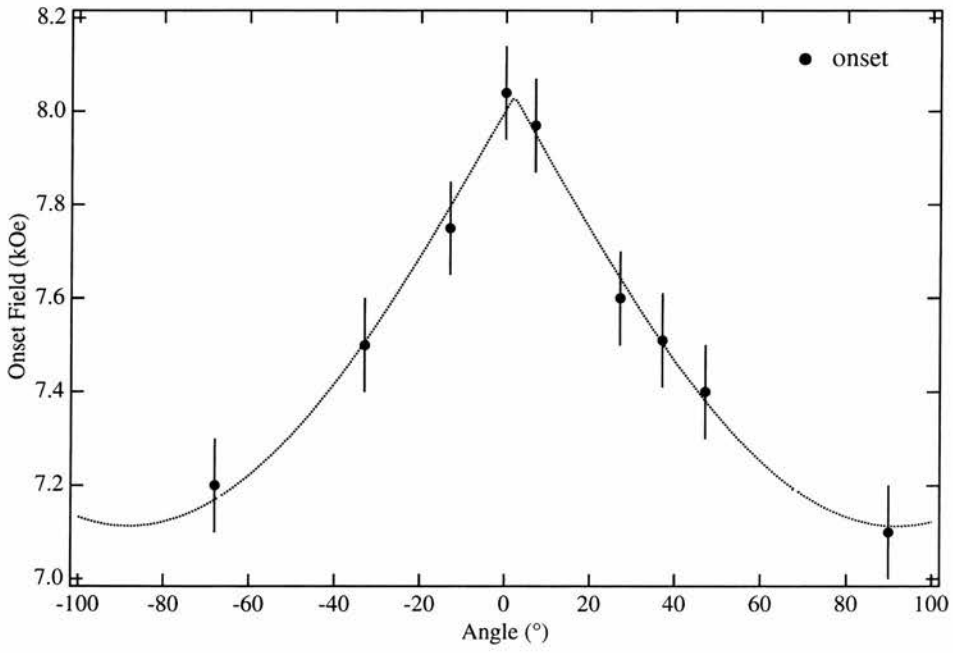


Figure 5.28: Angular variation of the onset of vortex motion. The line is the fit to data as described in the text.

5.6 Conclusions and Further Work

Sputtered multilayers of Nb/Co were prepared and characterised as described in the previous chapter. As already discussed these exhibit consistently high quality structural and superconducting properties. It should be noted that the interface alloying is such a small effect that it is not expected to impact on the measurements described in this chapter.

The sc02 series samples studied all displayed ferromagnetic ordering of the Co layer indicative of complete coverage of the Nb surface and therefore complete separation of the Nb films. With decreasing temperature we observe no dimensional crossover, the samples being in the 2D decoupled regime at all temperatures. This is confirmed by the angular dependence of the critical field which show excellent agreement with the predicted Tinkham curve for a 2D superconducting film.

From the fits to the data, the estimated D value is found to be slightly smaller than that expected for a single Nb layer. We attribute this to the pair breaking effects of the magnetic layer inhibiting superconductivity some distance into the superconducting layer. Comparison with the physical size, 400\AA , suggests that the magnetic effects extend $30\text{-}35\text{\AA}$ into the Nb layer at each boundary.

The study continued with an investigation of MLs containing very thin magnetic layers. Due to the nature of sputtering this produced partially complete Co layers and clustering of large islands with full coverage occurring at 6\AA for this system. When incomplete, a 2D'-2D crossover is observed with decreasing temperature. The crossover temperature, T_{2D}^* , rises progressively towards T_c as the Co layer becomes complete.

Close to T_c the predicted superconductor thickness is twice that expected ie twice a single Nb layer. This may result from vortex cores lying between the superconductor layers; on the Co clusters. Below the crossover temperature the system displays 2D behaviour predicted for a single thin film with $D \approx 360\text{\AA}$. At present we are uncertain as to the cause of the crossover; whether there is a magnetic transition in the spacer layers or a lower energy configuration within the superconductor.

The experimental D values are again smaller than expected with the pair breaking influence of the magnetic layer extending into the superconductor by 20\AA , close to that measured in the sc02 series. When one considers the errors associated with the determination d_{SC} , $\pm 10\text{\AA}$, this leads to an error in this penetration depth of a similar value. We therefore conclude that at the SC/FM boundary the pair breaking

influence travels $\approx 30\text{\AA}$ into the superconducting film.

We have also examined our fully decoupled samples with regards to current theories. All samples displayed 2D behaviour as described by Tinkham for a 2D superconducting film. Close to T_c the coherence length diverges and the anisotropic G-L theory is expected to be valid while at low temperature decoupling of the layers results in 2D behaviour. From our scaling we observe no clear discontinuity between these two regimes, observing the Tinkham formalism to show good agreement with the experimental data at all temperatures.

A limited study of the magnetism below T_c revealed some interesting behaviour. Similar to previous experiments we observe a superposition of the magnetic and superconducting signals. However the hysteresis loop is not that typical of a type-II superconductor and shows paramagnetic rather than diamagnetic behaviour.

Preliminary flux flow experiments have similarly produced unexpected results. We have shown that a weak force produces flux flow perpendicular to the interface boundary where strong pinning had been expected. At present only these experiments have been performed with other orientations not possible due to contact geometry. We are endeavouring to fabricate MLs with contacts above and below the allowing current flow perpendicular to the film surface. This requires a different sputtering mask and are slightly more complicated to prepare.

Continuation of this work could proceed along a couple of directions. A study of the Nb/ferromagnetic multilayers of similar dimensions but with differing magnetic materials would show quantitatively how the suppression of superconducting into the layer changes with moment size. Presumably the influence of Fe extends further into a superconducting film than Co since it carries a larger moment. This can also be examined by varying the superconducting material. To fully understand the properties of the s13 series, those with partial Co layers, a systematic study of identical systems, but with additional magnetic measurements, is necessary.

References

- [1] V. M. Krasnov, A. E. Kovalev, V. A. Oboznov, and N. F. Pedersen, *Physical Review B* **54**, 15448 (1996).
- [2] C. S. L. Chun, G.-G. Zheng, J. L. Vicent, and I. K. Schuller, *Physical Review B* **29**, 4915 (1984).
- [3] J. P. Locquet, D. Neerink, and H. V. der Straaten, *Japanese Journal of Applied Physics* **26**, 1431 (1987).
- [4] I. Banerjee, Q. S. Yang, C. M. Falco, and I. K. Schuller, *Physical Review B* **28**, 5037 (1983).
- [5] V. I. Dediou, V. V. Kabanov, and A. S. Sidorenko, *Physical Review B* **49**, 4027 (1994).
- [6] S. T. Ruggiero, T. W. Barbee, and M. R. Beasley, *Physical Review B* **26**, 4894 (1982).
- [7] Y. Obi, M. Ikebe, H. Wakou, and H. Fujimori, *Journal of the Physical Society of Japan* **68**, 2750 (1999).
- [8] G. Verbanck *et al.*, *Physical Review B* **57**, 6029 (1998).
- [9] F. Y. Ogrin *et al.*, *Physical Review B* **62**, 6021 (2000).
- [10] C. Attanasio *et al.*, *Physical Review B* **57**, 6056 (1998).
- [11] H. K. Wong *et al.*, *Journal of Low Temperature Physics* **63**, 307 (1986).
- [12] P. G. deGennes, *Superconductivity of Metals and Alloys* (Benjamin, New York, 1966).

- [13] M. Ikebe *et al.*, *Physica C* **317**, 142 (1999).
- [14] V. M. Krasnov, A. E. Kovalev, V. A. Oboznov, and V. V. Ryazanov, *Physica C* **215**, 265 (1993).
- [15] S. F. Lee *et al.*, *Journal of Applied Physics* **87**, 5564 (2000).
- [16] S. F. Lee, C. Yu, W. T. Shih, and Y. D. Yao, *Journal of Magnetism and Magnetism Materials* **209**, 231 (2000).

Chapter 6

Studies on the LiTi_2O_4 ramsdellite

6.1 Introduction

The lithium titanate is well known as the first oxide superconductor discovered, having a transition temperature of about 13K[1]. Its cubic, spinel structure is well characterised as are its magnetic properties, revealing a straightforward d-band metallic material. Lithium titanate has also been observed to exist in a high temperature second phase, exhibiting the ramsdellite structure. Unfortunately this phase is an unstable material, being known to degrade if exposed to air for even a short period of time.

This chapter represents the results of an extensive investigation into the properties of the ramsdellite phase of this material. Polycrystalline samples made by a solid state reaction were initially characterised using X-ray diffraction. Investigations were then made into the properties below room temperature using ^7Li NMR, variable temperature X-ray and neutron diffraction, dc magnetisation and muon spin relaxation techniques. The conclusions of these studies are given in a summary at the end of this chapter.

6.2 Previous Work

The ramsdellite structure was first observed by Bystrom[2] in $\gamma\text{-MnO}_2$. It consists of distorted MO_6 octahedra which link with adjacent octahedra by sharing opposite edges therefore forming columns. Adjacent pairs of columns share edges to form double columns, giving rise to an open framework type structure. In between these

columns are tetrahedral channel sites into which smaller ions such as H^+ and Li^+ can reside. Johnston[1] first reported the existence of this phase, after observation of a ramsdellite type structure upon heating LiTi_2O_4 but was unable to confirm the stoichiometry. It was not until 1994 that Akimoto et al.[3] succeeded in preparing single crystals and confirmed both the stoichiometry and the structure of the phase. The structure and channel sites as described by Akimoto are shown in Figure 6.1 below.

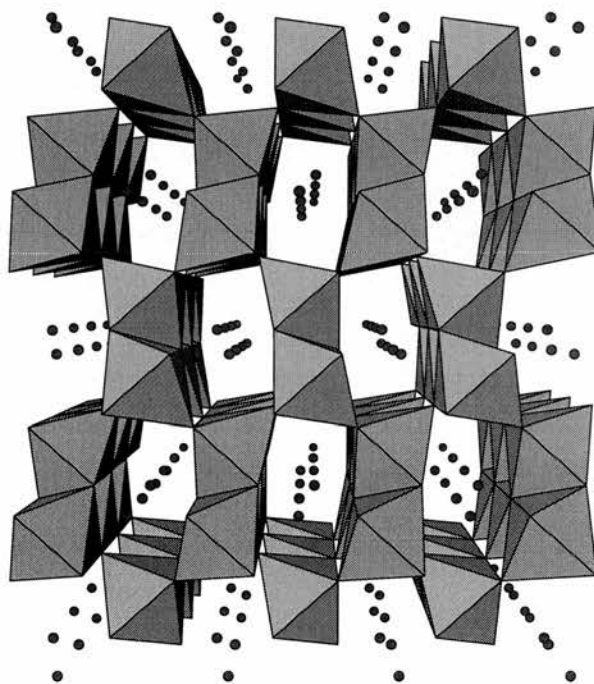


Figure 6.1: Ramsdellite structure of LiTi_2O_4 viewed down \mathbf{b} , showing the location of the occupied Li sites.

High temperature neutron diffraction, carried out by Gover et al.[4], again confirmed this stoichiometry, placing the spinel-ramsdellite transition as occurring between 875°C and 925°C . In addition it was shown that no intermediate phase is involved in the transition. This is consistent with a recent ^6Li MAS NMR study by Kartha et al.[5] in which the quenching temperature during preparation was varied to produce a series of compounds from pure spinel to mainly ramsdellite. By assigning different room temperature ^6Li NMR responses to possible sites they concluded

that the spinel-ramsdellite transformation occurs via the creation of a lithium-rich spinel and a lithium-deficient ramsdellite.

The principal ^6Li resonance signal observed for the pure spinel lithium titanate in the experiments of Kartha et al. occurs close to zero shift ($-2.1\text{ppm} \pm 0.2\text{ppm}$). A narrow peak ($\approx 1\text{ppm}$) this has a spin-lattice relaxation time of around 85s, not unexpected for a metallic material. Ramsdellite LiTi_2O_4 however, gives a dominant broad (4ppm) NMR resonance at +11.4ppm. This peak was also observed to relax very quickly, $T_1 = (600 \pm 100)\text{ms}$. The large shift, in comparison to those observed in insulating lithium materials, and short spin-lattice relaxation time are indicative of a metallic compound. However, Gover et al.[4] has intimated that ceramic pellets of ramsdellite phase show no sign of metallic character. When the large MAS linewidth is also considered the NMR was analysed as due to a weak magnetic phase with antiferromagnetic tendencies.

Several groups have undertaken magnetic measurements on ramsdellite to further identify this magnetic phase. The first reported data is that of Johnston et al.[6], who noted only that superconductivity was not observed above 1.5K, although no magnetic susceptibility data was published. More recently Akimoto et al. presented magnetic susceptibility measurements between 4.3 and 300K on a small single crystal. Their data remained flat between 300 and 100K, below which it exhibits a sharp upturn. This was interpreted as resulting from paramagnetism due to localised electrons or an impurity.

Gover also performed magnetic measurements on two powdered samples, one between 1.8 and 25K the other from 1.8 to 100K. The data was described by a Curie-Weiss law involving 10% of the susceptibility expected if all the lithium electrons were to reside on the titanium sites and carry a single Bohr magneton of magnetic moment per formula unit. The inferred ordering temperature, $\approx 2\text{K}$, indicates that the moments are weakly coupled by an antiferromagnetic interaction.

There are significant differences in these studies, most notably in the magnitude of the measured susceptibilities. One notable feature is the poor quality of any Curie-Weiss fit to the higher temperature data. After removal this leaves a residual susceptibility that increases with temperature eventually reaching a plateau. This behaviour has been compared to that expected from a spin ladder with only the Akimoto data showing good agreement (see Figure 6.2).

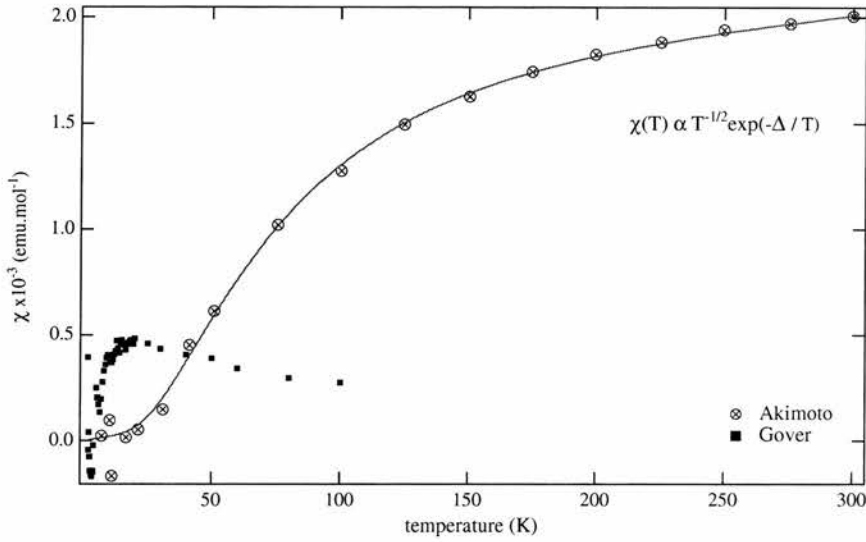


Figure 6.2: Residual magnetic susceptibility of LiTi_2O_4 as obtained by Gover and Akimoto. The line is a fit to the susceptibility expected from a two-leg spin ladder.

Additional investigations have been performed using ESR at 110K[7]. This found a broad resonance with a g-value of approximately 2, and an intensity indicative of 11% spins per mole of sample, in agreement with the susceptibility measurements.

Further to their susceptibility measurements, Gover et al.[8] undertook zero field muon spin relaxation measurements, between 2 and 150K. This data was described by the following relaxation function

$$a_0 G_z(t) = a_0 G_z^{DKT}(\Delta, \nu, t) \exp[-(\lambda t)^\beta] + a_{bg} \quad (6.1)$$

in which $G_z^{DKT}(\Delta, \nu, t)$ is the dynamic Kubo-Toyabe function described in Chapter 2. The main finding of this study is a similarity of the temperature dependence of the asymmetry with that of earlier work by Matsuda et al.[9] on the spin-ladder material SrCuO_2 . This explanation is also used to account for the residual susceptibility observed.

Below 10K, a second decay mechanism, due to a second muon site, becomes noticeable. This showed a divergence in the atomic relaxation rate, λ , with decreasing temperature while β , the power exponent, decreased sharply. This is indicative of moments starting to freeze and experience some frustration. They were unable to identify the magnetic phase any further. This interpretation is however quite spec-

ulative due to the quality of the low temperature data collected. Further analysis, including comparison with our data, is provided in Section 6.6.2.

6.3 Characterisation

Polycrystalline samples were made using the method detailed in chapter 3, courtesy of Mr Julian Tolchard of chemistry department of the University of St Andrews. Carbon wrapping during the final stages of preparation allowed higher sintering temperatures and therefore improved formation of the ramsdellite phase. A number of samples were prepared in this fashion with different cooling rates, again to aid ramsdellite formation. These were studied by a variety of techniques with a summary of relevant details provided in the table below.

Table 6.1: List of samples prepared for this study, the preparation method along with the delay before measurement.

Sample	Cooling	Techniques	Delay
0041R	rapid	NMR	2 weeks
0041S	slow	NMR	1 week
		SQUID	3 weeks
		X-Ray	4 weeks
0057	rapid	Neutron diffraction	2 weeks
0079	rapid	SQUID	8 weeks
		μSR	1 week

The cooling method is also listed, with slow referring to the normal rate of the muffle furnace. To rapidly cool the samples, the last heating cycle was performed in a quench furnace, and the sample allowed to cool naturally, which is faster than in a muffle furnace, to reduce the spinel formation in the 700-900°C range during cooling. Typical cooling rates were 8°C/min (muffle) and 15°C/min (quench) in the region of the phase transition.

Phase identification and purity was established using two diffractometers: a Philips PW3810 reflection mode machine and a high resolution Stoe StadiP diffractometer. A typical X-ray diffraction pattern is shown in Figure 6.3. They were found to have the previously reported Pbnm structure with typical lattice parameters being $a=9.6384\text{\AA}$, $b=2.9482\text{\AA}$ and $c=5.0356\text{\AA}$.

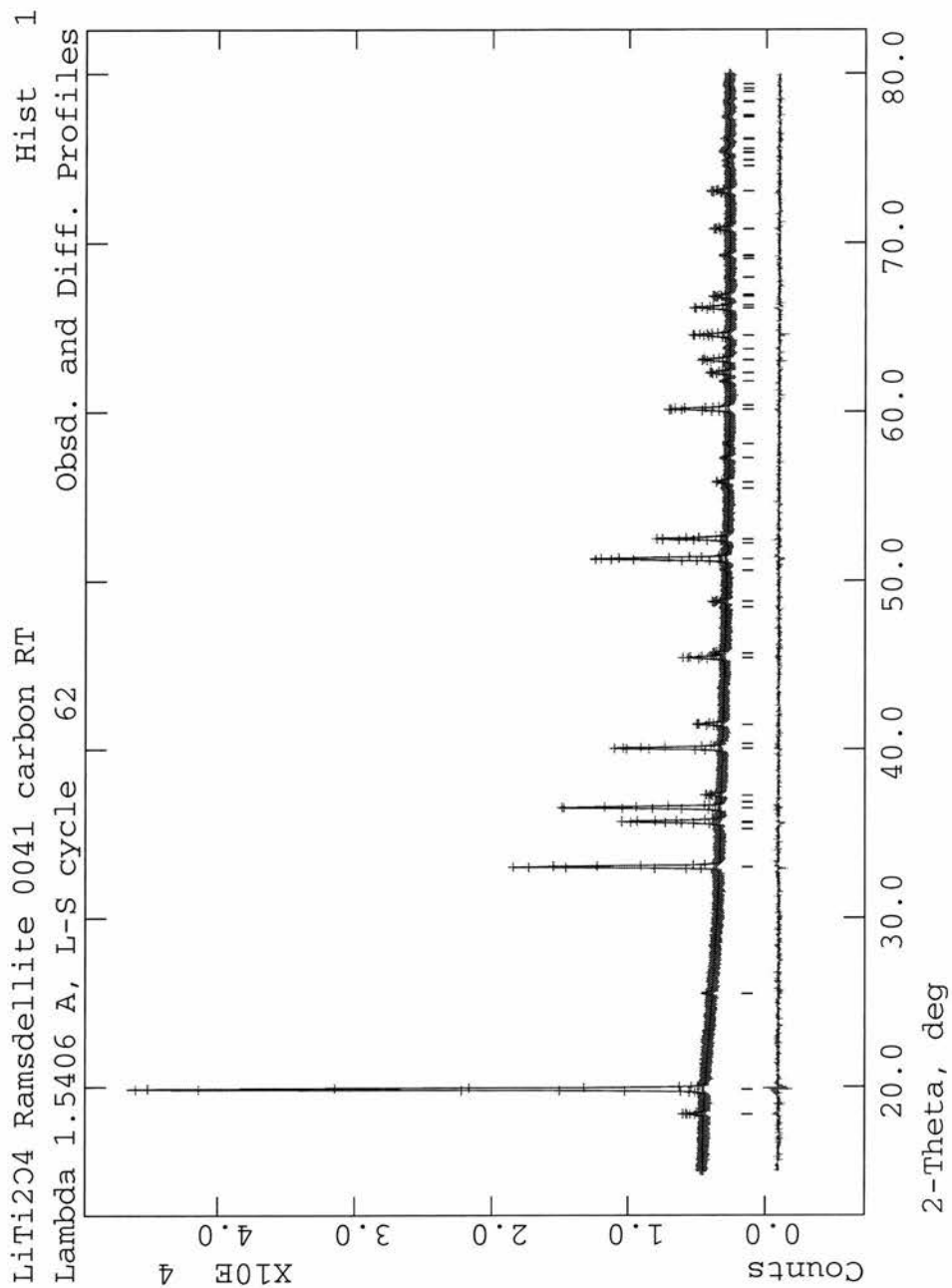


Figure 6.3: X-ray powder diffraction pattern with Rietveld refinement of LiTi_2O_4 obtained using GSAS. Also shown is the difference line.

6.4 ^7Li MAS NMR Study

6.4.1 Experimental

An extensive study using nuclear magnetic resonance has been made at the lithium site for the LiTi_2O_4 system. In this study the ^7Li isotope was used since the ^6Li isotope resonance was outside the frequency range of the MAS spectrometer. ^7Li nucleus is spin-3/2 and has a natural abundance of 92.6%. The Li occupy the channel sites although the number of these is not fully known. ^7Li NMR study will therefore shed some light on this. Spectra were obtained using a Bruker MSL 500 spectrometer, with a static field of 11.75T and were referenced using solid $\text{Li}_4\text{Ti}_5\text{O}_{12}$ as a secondary reference to 0ppm in LiCl solution. All experiments were carried out under a dry nitrogen atmosphere that was used to achieve spinning. This reduced the sample contact with air and especially moisture to a minimum, helping to prevent sample degradation[3].

MAS spectra were obtained between 350K and 160K below which it is difficult to maintain spinning without damage to, or freezing of, the sample rotor. The saturation recovery technique was used with varying delays between pulses to measure the spin-lattice relaxation time. Spinning rates of approximately 6kHz were maintained over the whole temperature range studied. As a function of temperature we measured the resonance peak shift and linewidths of all observable peaks.

Temperature calibration of the various probes used had been undertaken earlier by other workers using the relaxation time of aluminium nuclei in aluminium metal as a secondary reference ($T_1T=1850\text{msK}$).

6.4.2 Results

Magic angle spinning ^7Li NMR spectra were obtained for two samples produced by the carbon wrapped technique, one being slowly cooled (0041S) and the other more rapidly (0041R). At high temperatures the spectra display the same features. Figure 6.4 shows the full spectrum obtained at room temperature along with the reduced central region. The reduced spectra were fitted using a pseudo-Voigt function for each peak

$$pV(x) = \eta L(x) + (1 - \eta)G(x) \quad 0 \leq \eta \leq 1 \quad (6.2)$$

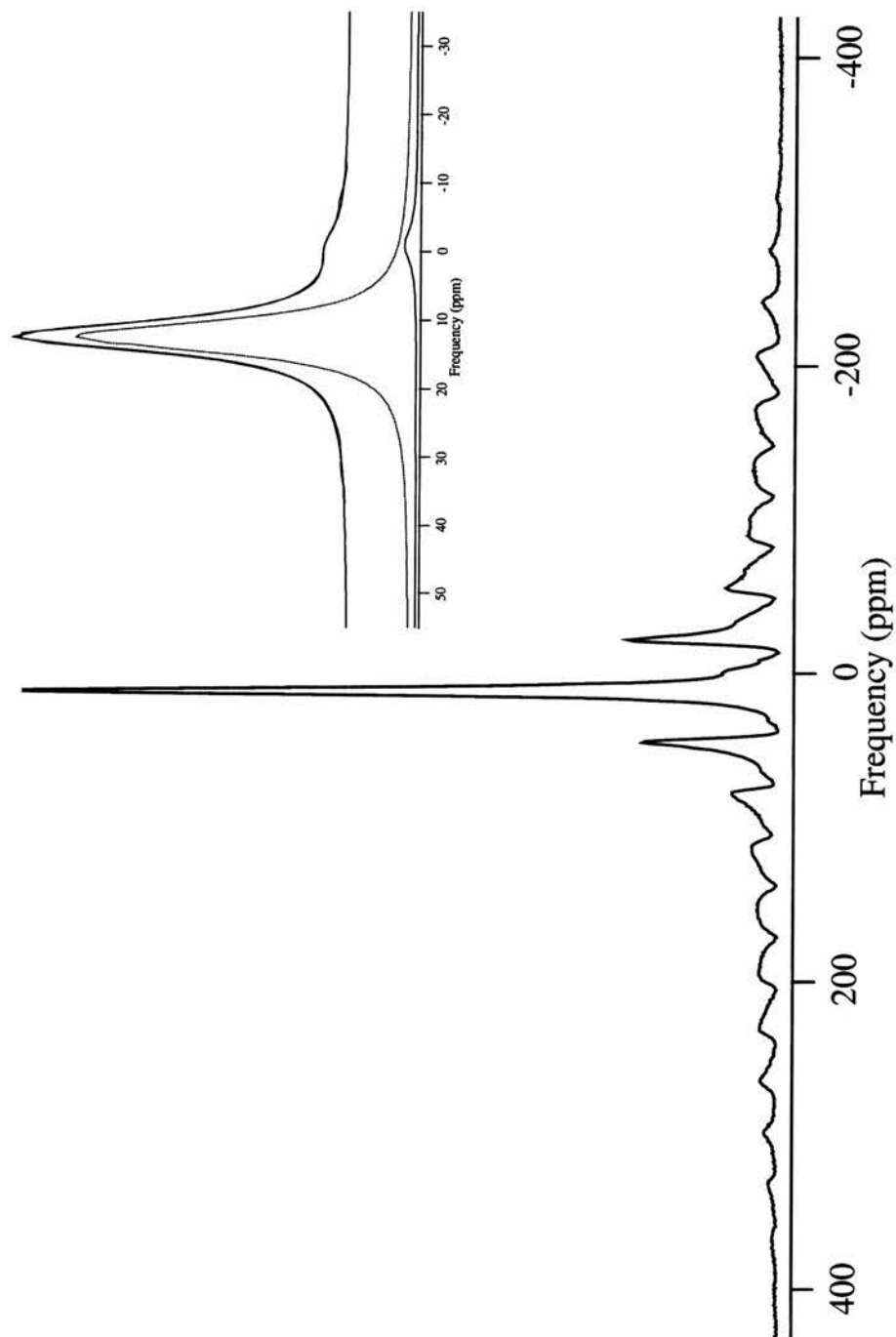


Figure 6.4: ^7Li MAS NMR LiTi_2O_4 spectrum obtained at room temperature. The inset shows reduced region of spectrum consisting of central peaks, each fitted using a pseudo-Voigt function.

The pseudo-Voigt is a linear combination of a Lorentzian $L(x)$ and a Gaussian $G(x)$ function of the same peak position and width. The function is normalised to area allowing easy determination of the signal intensity and therefore direct knowledge of the number of participating nuclei. Analysis of all the observed spectra is provided in Appendix A.

The data collected is broad containing considerable sideband structure spanning ≈ 800 ppm (160kHz). This is quite typical of 1st order quadrupolar broadening of the satellite transitions in ^7Li , which can typically span many tens of kHz.

It can be seen from Figure 6.4 that the MAS ^7Li NMR spectra obtained at room temperature display similar features to that observed by Kartha[5]. There is a dominant broad peak of width about 4.5 ppm at large shift, +12.3 ppm. In addition there is a second smaller resonance at almost no shift, with a broader width of about 7.7 ppm. This second signal is close to that expected from spinel impurity, however slower cooled samples show an additional third feature at -6 ppm which does not appear in rapidly cooled samples indicative of spinel impurity. This would seem to suggest 2 different Li sites within the channel structure.

At this point it is important to mention a study by Tunstall et al.[10] in which the ^7Li NMR resonance is monitored as a function of temperature down to 160K. At room temperature they observe a broad peak (≈ 6 ppm) at high shift +8ppm along with a spinel impurity peak at -2.4ppm. With decreasing temperature the ramsdellite signal gains a small peak at 1ppm which then grows at the expense of the original resonance. The spinel signal is observed to be static over the whole temperature range. Above the transition the relaxation time is constant at 120ms, then with decreasing temperature T_1 jumps sharply only to fall abruptly to ≈ 100 ms at the lowest temperature of 160K.

Figure 6.5 shows regions of the MAS spectra obtained at temperatures between 330 and 170K. High temperature spectra consisted of a nearly lorentzian principal peak with the lower intensity signal being described by a mainly gaussian lineshape. The spectra obtained at low temperature, below 210K, were broad with peaks from different orders overlapping and therefore difficult to analyse. With decreasing temperature the lineshape of the main peak also changes, being fully described by a gaussian at 190K and below.

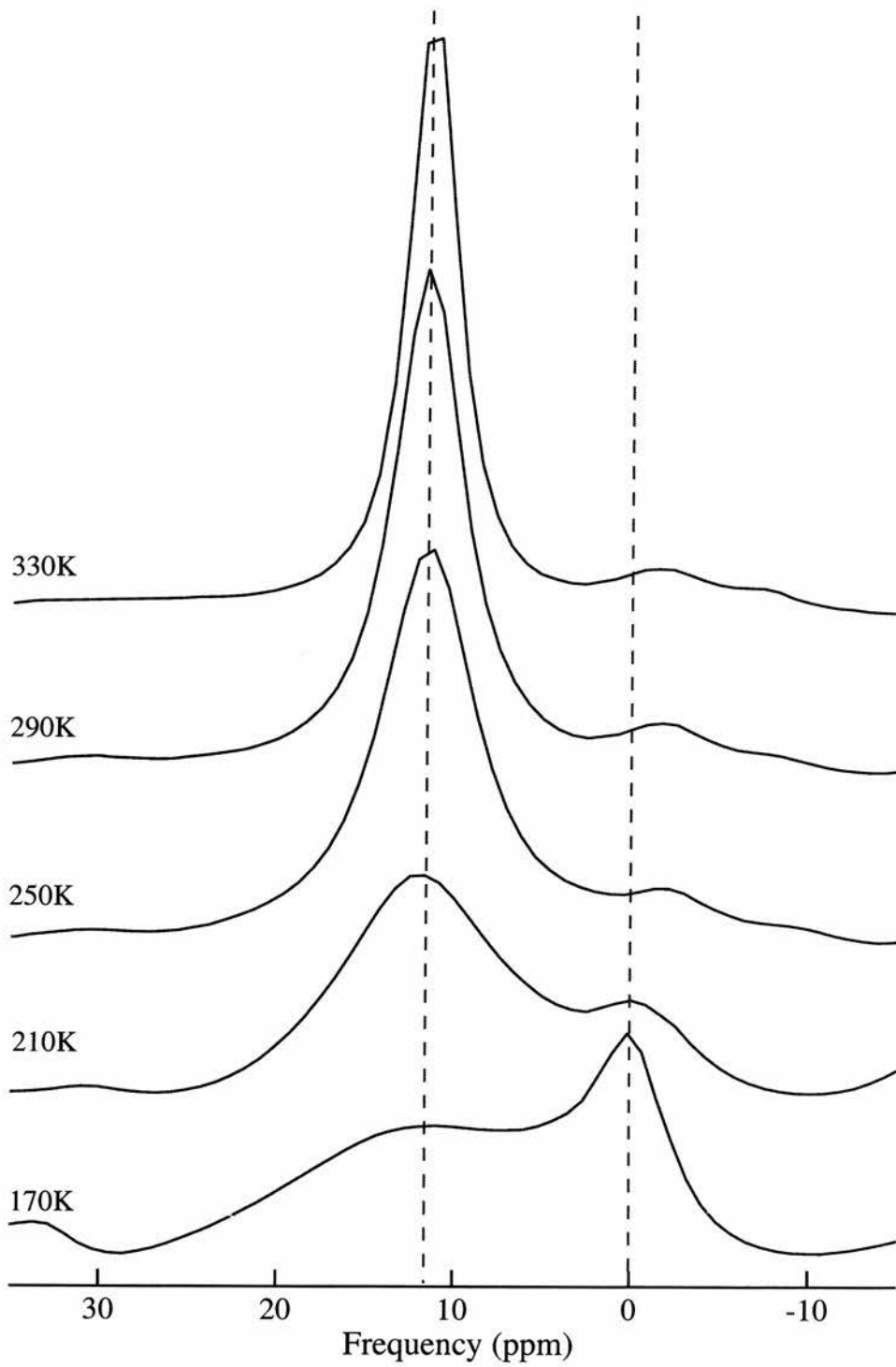


Figure 6.5: ^7Li NMR LiTi_2O_4 spectra obtained between 340K and 160K.

The intensity of each peak was extracted from the fitting procedure. The total intensity is expected to be constant and is directly related to the number of nuclei involved in the resonance. Slight variations occurred in the calculated total intensity calculated but these were within experimental error. Figure 6.6 shows the temperature dependence of the fractional intensities of both peaks. The temperature dependence of the peak intensities obtained from fits is constant at high temperature. Below $\approx 200\text{K}$ the low shift resonance grows at the expense of the high shift peak.

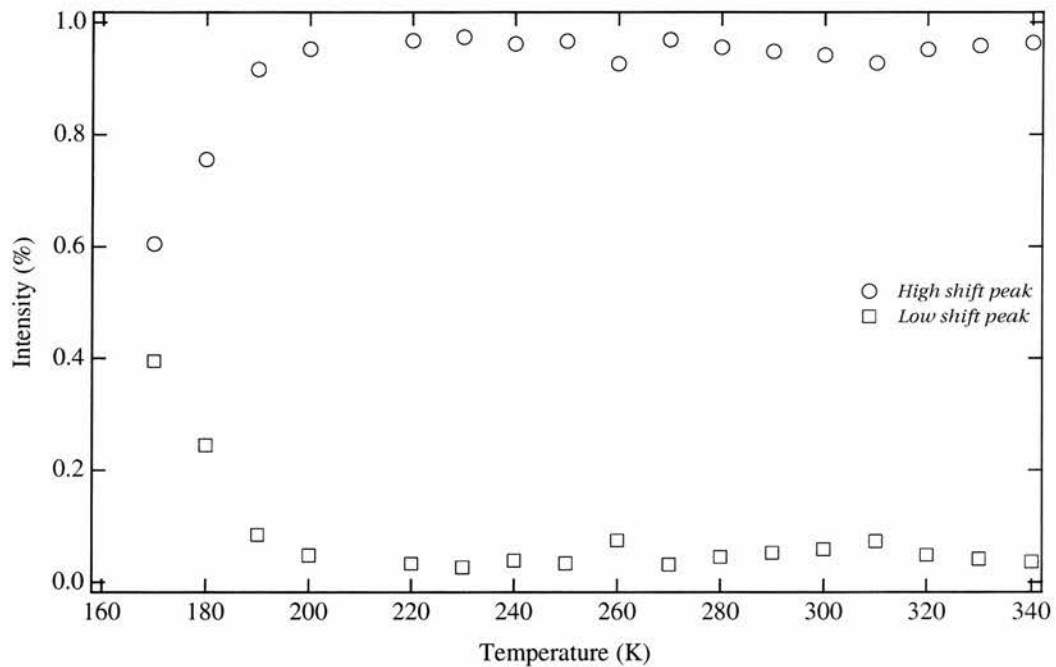


Figure 6.6: Temperature dependence of the resonance intensities as determined from fits to spectra

The temperature dependence of the linewidth and shift obtained from the fitting procedure are presented in Figures 6.7 and 6.8 respectively. In the temperature region examined the linewidths of the low shift resonance is nearly temperature independent at approximately 1200Hz. The main peak broadens with decreasing temperature displaying a Curie-Weiss-like behaviour. Fitting the main resonance signal to this formalism gives the following θ values 160K(0041R) and 130K(0041S).

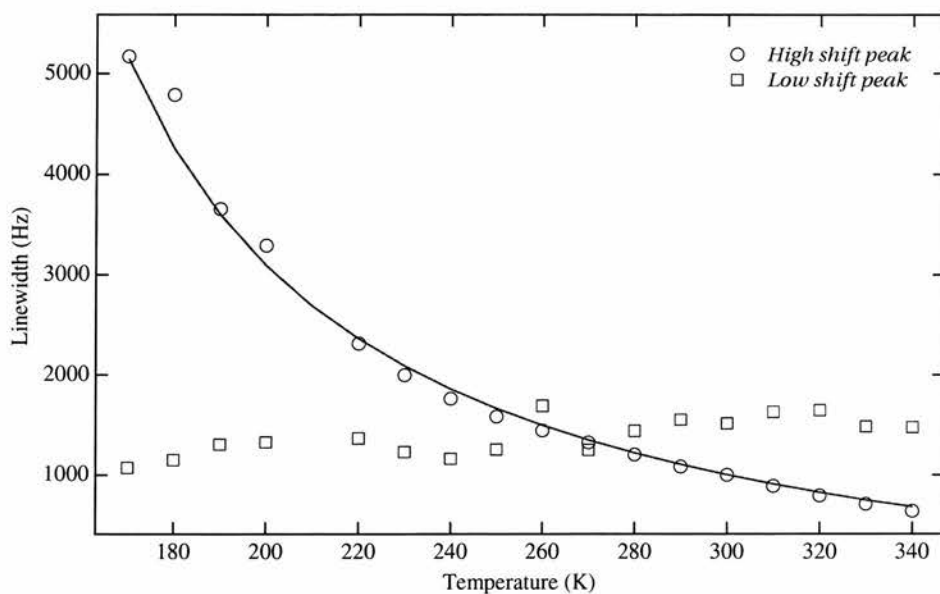


Figure 6.7: Temperature dependence of linewidths from fits to data. The large shift displays a Curie-Weiss-like broadening with decreasing temperature, while the low shift linewidth is approximately temperature independent.

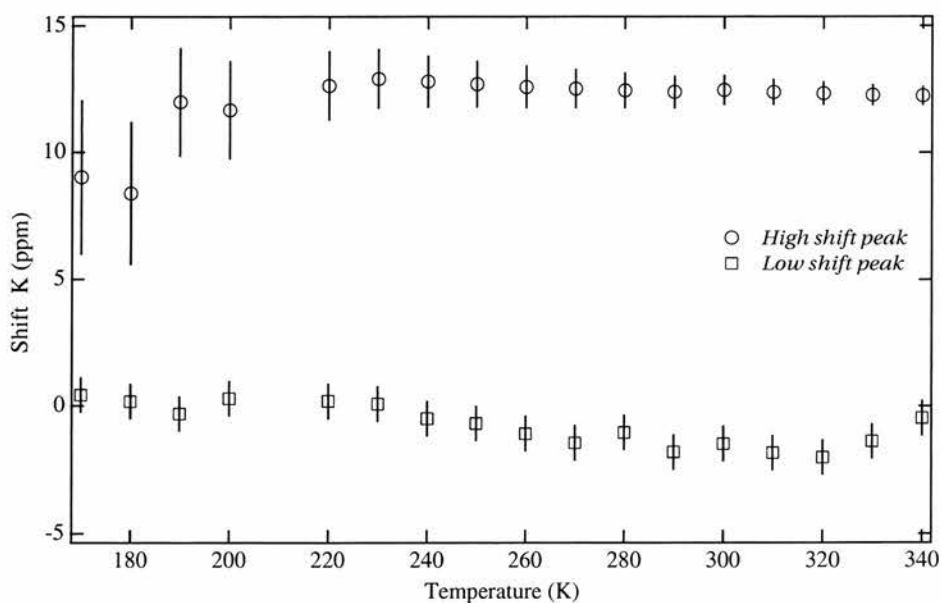


Figure 6.8: ${}^7\text{Li}$ NMR shift obtained from fits to data, showing nearly temperature independent behaviour.

The resonance shifts obtained from the data were temperature independent, remaining at ≈ 0 ppm and +12ppm respectively. Near the base temperature of our experiment the high shift peak is broad making it difficult to determine its exact position.

Figures 6.9 and 6.10 show the evolution of the signal intensity with time and the spin-lattice relaxation temperature of the main peak respectively. The spin-lattice relaxation measurements followed single exponential dependences on the delay-times. The value $T_1 = (125 \pm 0.5)$ ms was obtained for the main peak at room temperature, which is less than that measured previously (600ms). With decreasing temperature the relaxation time decreases monotonically from 150ms at 340K to 60ms at 160K, further supporting previous evidence of non-metallic behaviour.

Due to the low intensity of the second signal it was difficult to evaluate the spin-lattice relaxation time at high temperatures as can be seen in Figure 6.9. At lower temperatures this becomes measurable and exhibits similar values to the high shift peak. It is therefore not possible to know if the the two signals share the same relaxation mechanism.

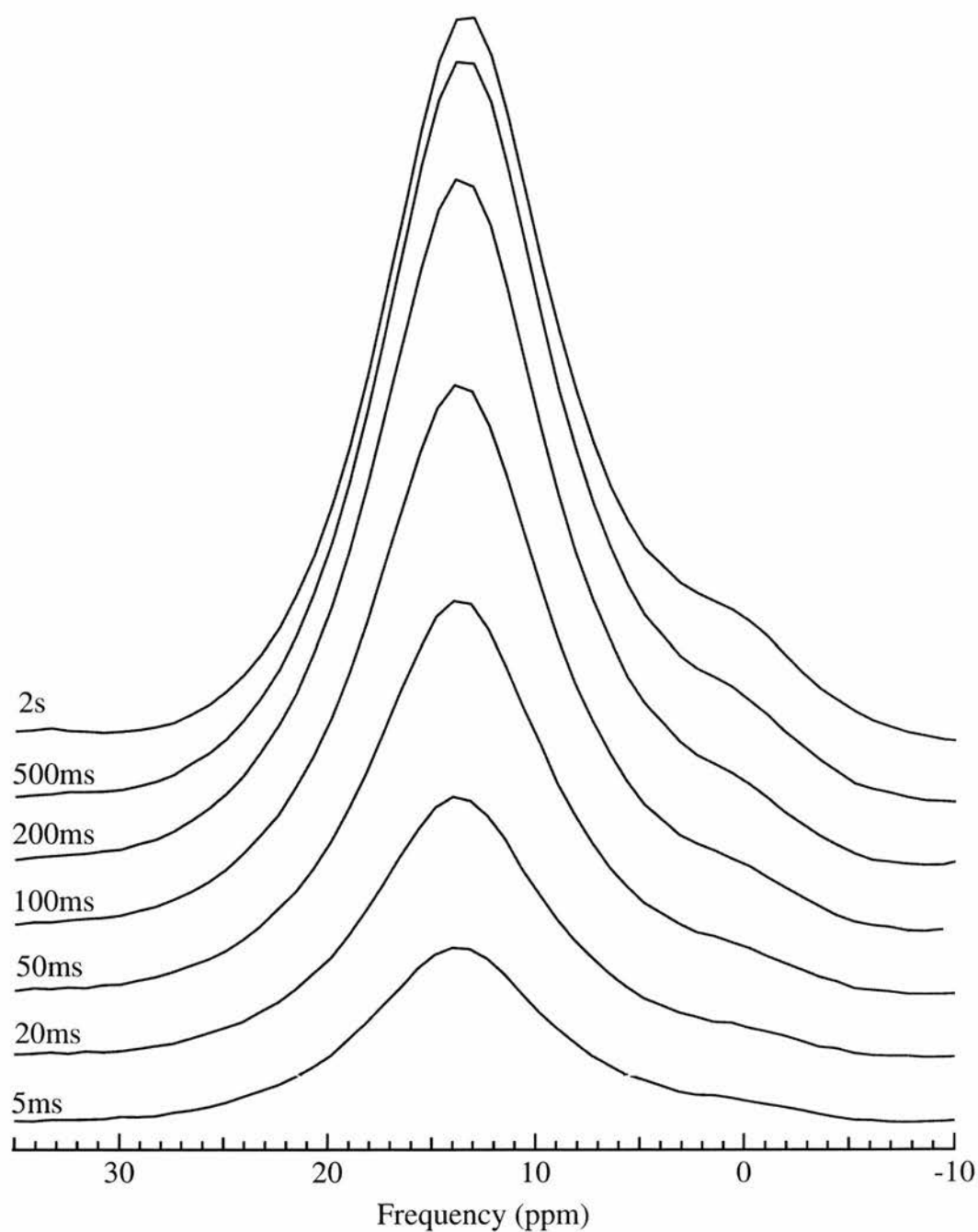


Figure 6.9: Example of the progression of the spectrum with delay for LiTi_2O_4 at 230K.

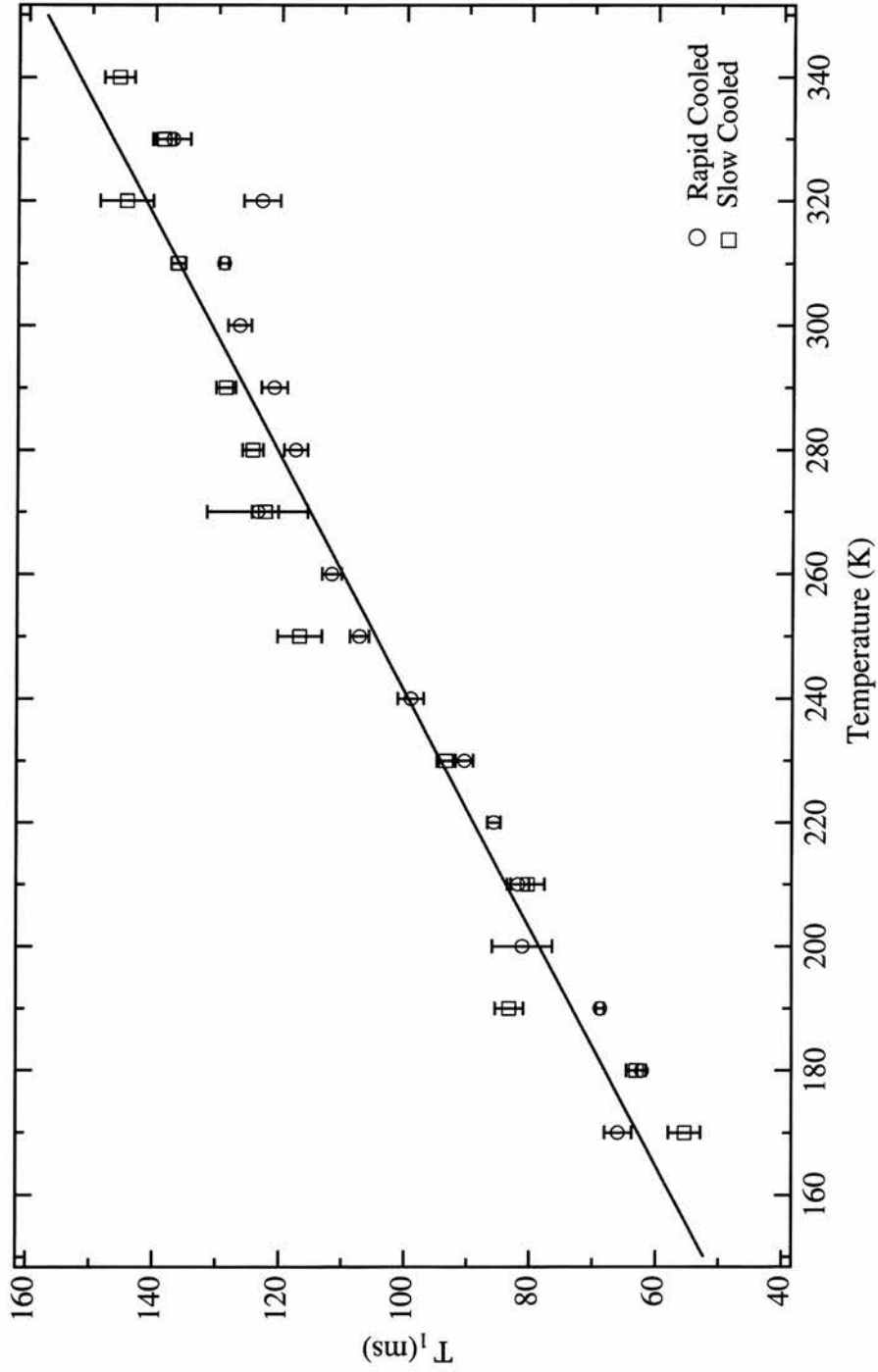


Figure 6.10: The temperature dependence of the ^7Li NMR spin-lattice relaxation time. The line is a least squares fit to the data.

6.5 Low Temperature Diffraction

6.5.1 Introduction

The NMR study presented in the previous section shows a transition which would seem to involve the Li atoms. To help understand and determine the nature of this phase change, low temperature diffraction studies were performed. Both neutron and X-ray techniques were utilised due to their differing sensitivities, providing a complementary analysis. X-ray scattering involves the extra-nuclear electrons resulting in highest sensitivity to Ti atoms and lowest to Li atoms. In fact Li atoms can be assumed to be invisible to X-ray diffraction. Neutrons, however, interact with the atomic nucleus making this technique far more sensitive to the presence of Li.

6.5.2 Neutron Diffraction

Low temperature neutron diffraction data were collected on a polycrystalline sample of LiTi_2O_4 (sample 0057) using the VEGA spectrometer at KENS-KEK Japan, courtesy of Professor Ryoji Kaino. Measurements were performed at 100K, 200K and 300K to observe structural changes and possible re-ordering of the lithium atoms. Data were fitted using the Rietan Reitveld refinement software[11].

A typical diffraction pattern with fit is given in Figure 6.11. At all temperatures the structure was refined using the ramsdellite model with a single unindexed peak. This anomaly, which occurs at $d=2.41\text{\AA}$ in all spectra, has been associated with the instrumentation and does not represent an impurity.

Figure 6.12 presents the lattice parameters from Rietveld refinements to data. The only noticeable feature is the negative thermal expansion for the \mathbf{a} -axis.

If there were a re-ordering of the Li atoms to a different site then we would expect additional peaks to appear. From our neutron study there is no evidence of a second phase or a re-ordering of the lithium atoms.

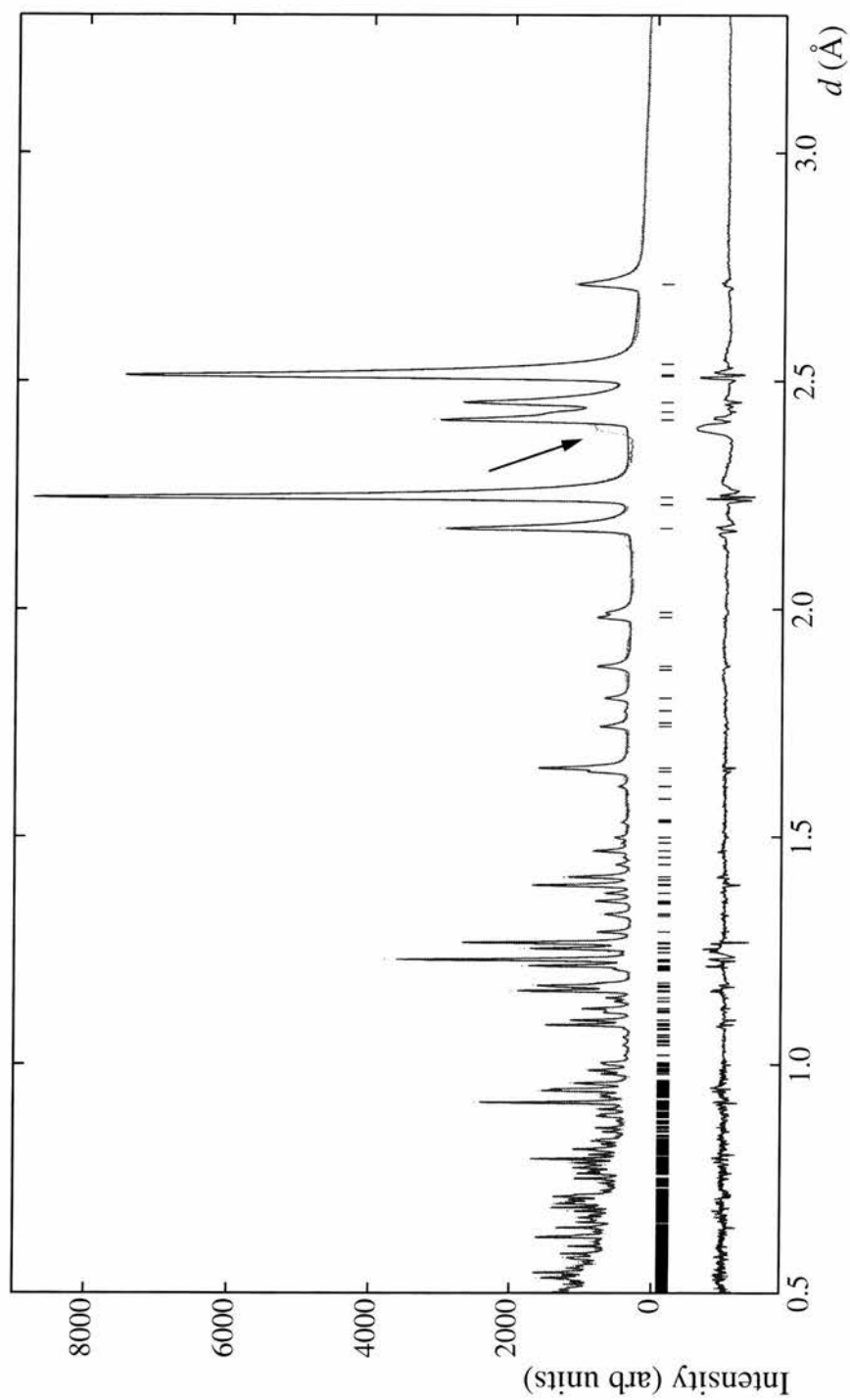


Figure 6.11: Neutron powder diffraction pattern and Rietveld refinement of LiTi_2O_4 at 100K. The unindexed peak (highlighted by arrow) is present at all temperatures studied.

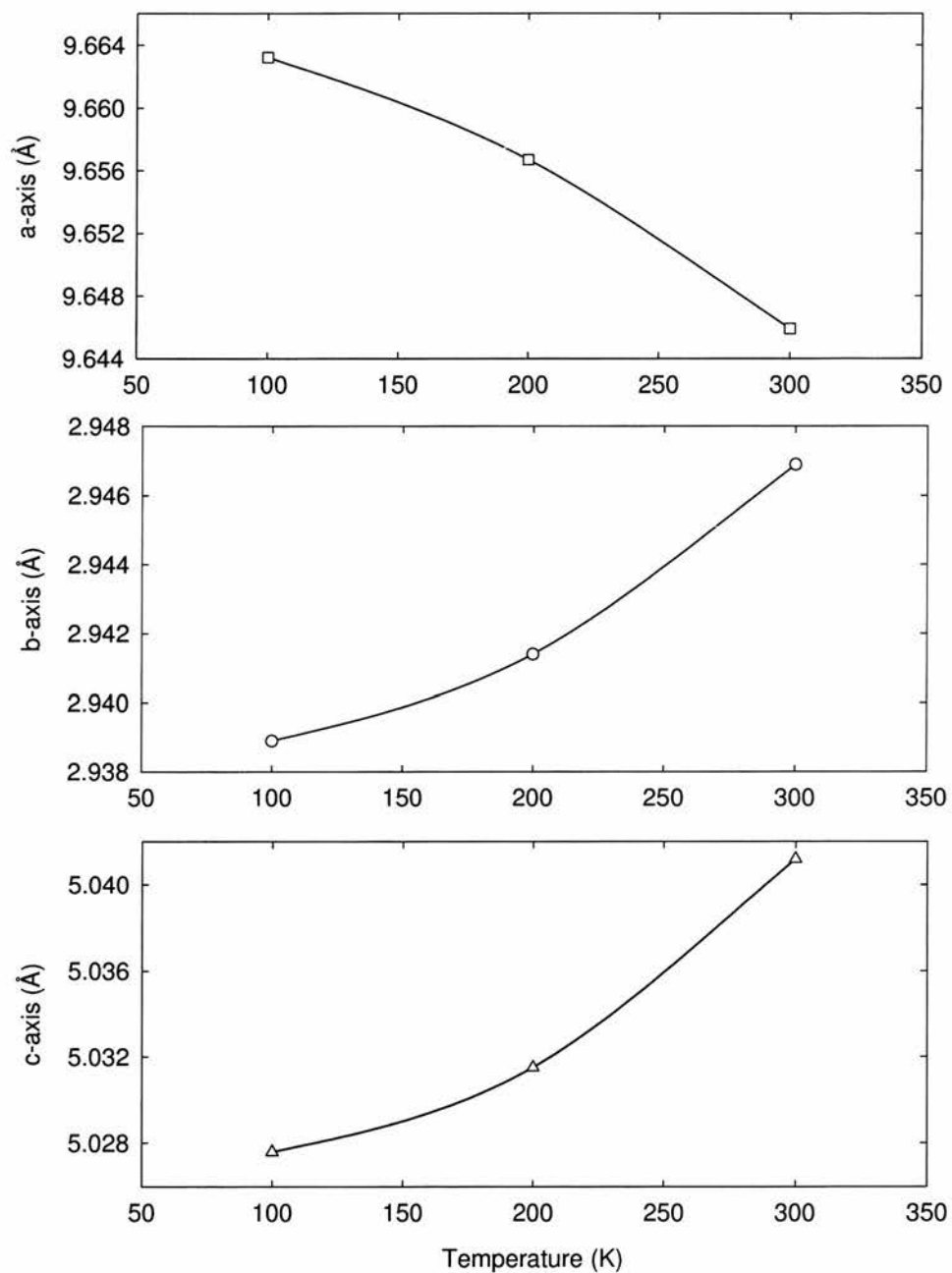


Figure 6.12: Variation of lattice parameters with temperature from Rietveld refinements to low temperature neutron diffraction data. The lines are guides to the eye.

6.5.3 X-ray Diffraction

Additional variable temperature XRD data were collected using a Bruker D8 diffractometer, courtesy of Dr John Evans at Durham University. These were performed using sample 0041S described in section 6.3. At each temperature the sample was allowed to equilibrate before a 26 minute 2θ scan was performed between 10° and 90° . Reitveld refinements of the data were carried out using GSAS.

The data collected is presented in its raw form. A sample spectrum, $T=350\text{K}$, is given in Figure 6.13. With decreasing temperature several peaks are observed to split. The most intense and obvious of these is the (130) peak, the temperature variation of which is given below in Figure 6.14. With decreasing temperature this can be seen to split indicating a change in crystal symmetry.

From these figures it can be seen that the sample undergoes a subtle structural transition in the 220-260K range. From the peak splittings observed, a change in symmetry from orthorhombic to monoclinic has been suggested but as yet no space group has been accurately assigned.

Fitting the low temperature data to the high temperature ramsdellite structural model we observe unusual behaviour in the unit cell lattice parameters, see Figure 6.15. These display similar trends to that of the neutron diffraction data presented earlier, although exhibiting slightly different lattice magnitudes. This disparity can be attributed to differences in the samples studied. For all three axes there is a change in behaviour in the visually observed transition region, 220-260K. The **a**-axis displays a peculiar steady contraction above $\approx 210\text{K}$ which flattens out at towards 350K.

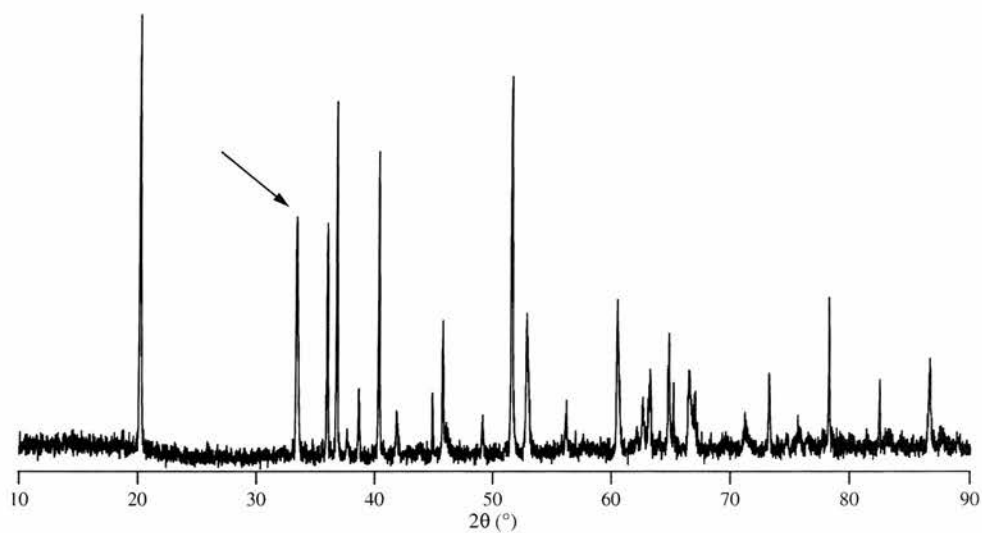


Figure 6.13: X-ray powder diffractogram of raw data at 350K. The (130) peak has been highlighted by arrow.

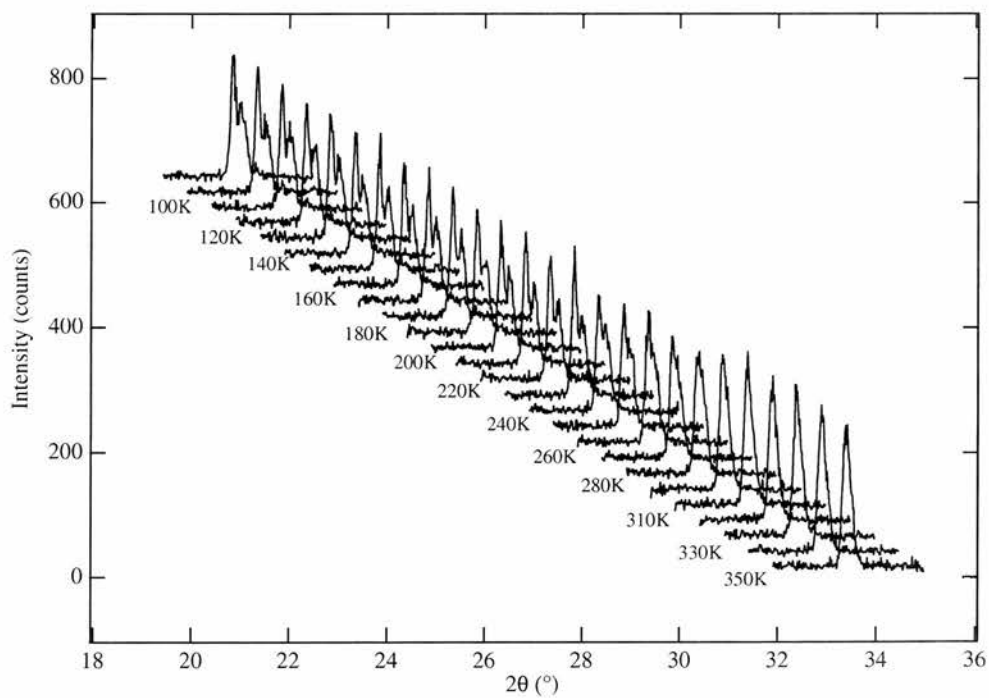


Figure 6.14: The splitting of the (130) peak of LiTi_2O_4 with temperature. The intensities and diffraction angles are offset for clarity.

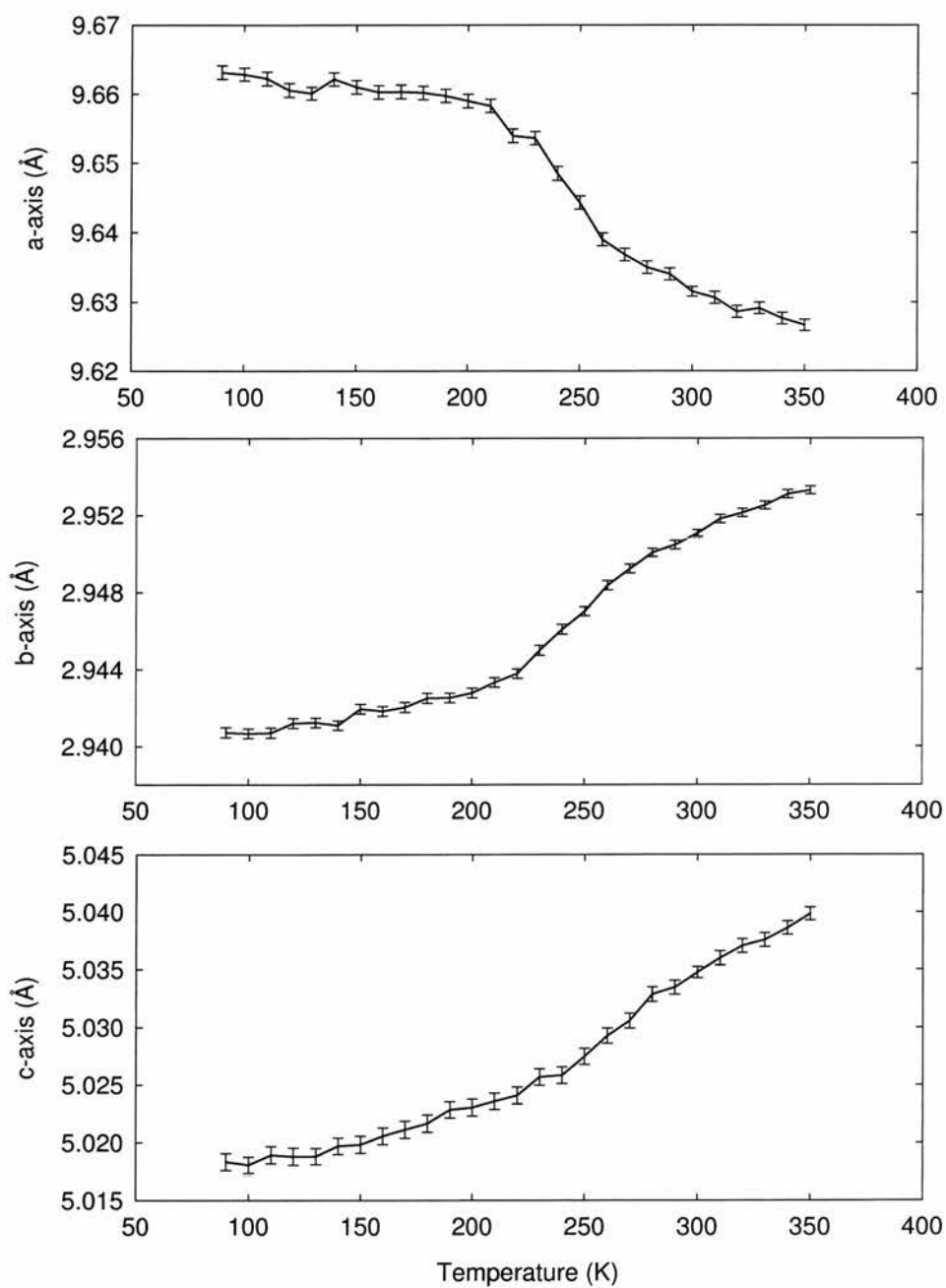


Figure 6.15: Variation of lattice parameters with temperature from Rietveld refinements to low temperature XRD patterns.

6.6 Magnetic Characterisation

6.6.1 dc magnetisation

Magnetisation measurements were performed with a commercial superconducting quantum interference device (SQUID) magnetometer at the University of Edinburgh as a function of applied field H ($0 \leq H \leq 10\text{kG}$) and temperature T ($2 \leq T \leq 300\text{K}$). Data was collected for the two samples labelled 0041S and 0079, the characterisation described earlier. One important point to note is that there was a significant time delay, ≈ 8 weeks, between the preparation of 0079 and the measurements being taken, therefore the sample may have aged. Sample 0041S, however, was measured shortly after preparation (4 weeks).

The results of zero-field cooled susceptibility measurements as a function of temperature for both samples are shown in Figures 6.16 and 6.18. For each data set the low temperature region was fitted to the Curie-Weiss expression for paramagnetism

$$\chi_{measured} = \chi_0 + \frac{C_M}{T - \theta} \quad (6.3)$$

where χ_0 represents the contribution from sample container and background. The resultant parameters are given in table 6.2 along with those of previous investigations. A comparison of the Curie constant and ordering temperature of the various investigations shows some agreement with our data and that of Gover.

Table 6.2: Results of low temperature fitting of the measured susceptibility for various experimentals on LiTi_2O_4 ramsdellite.

Sample	0041S	0079	Gover8[8]	Gover9[8]	Akimoto[3]
C(emu.K/mol.g)	0.035	0.130	0.035	0.051	0.058
θ (K)	3.6	5.0	1.3	1.3	8.8

The small values of θ indicate that the moments are coupled by a weak antiferromagnetic interaction and may not even order except at exceptionally low temperatures. From the Curie constant for each sample, the moment per unit cell can be calculated by the following

$$\mu_{\text{eff}} = g[S(S+1)]^{1/2} = \left(\frac{3Ck_B}{\mu_B^2} \right)^{1/2} \quad (6.4)$$

The effective moments for 0041 and 0079 are $0.53\mu_B$ and $1.02\mu_B$ respectively, corresponding to 9.4% and 34.8% of that expected from a single Ti^{3+} , $\mu_{\text{eff}} = 1.73\mu_B$.

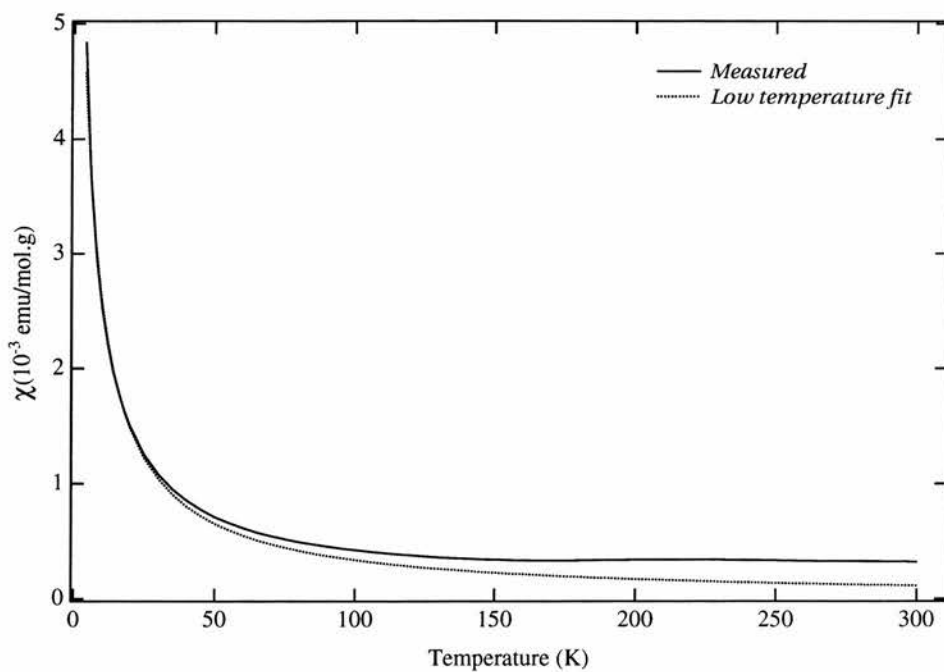


Figure 6.16: Temperature dependence of the ZFC susceptibility of sample 0041S in an applied field of 10kG.

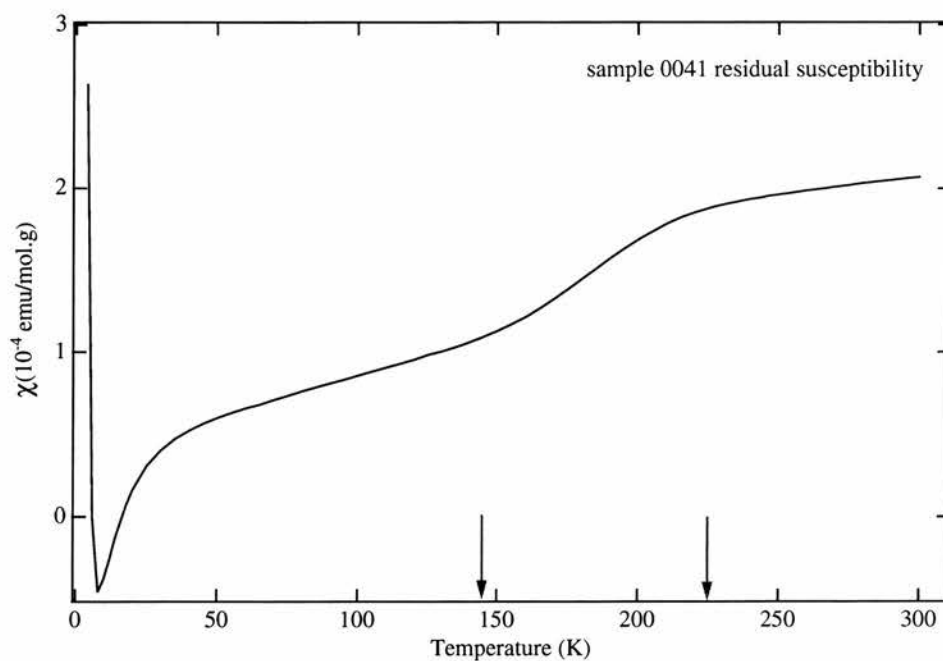


Figure 6.17: Variation of the residual susceptibility, obtained after subtraction of Curie term, with temperature.

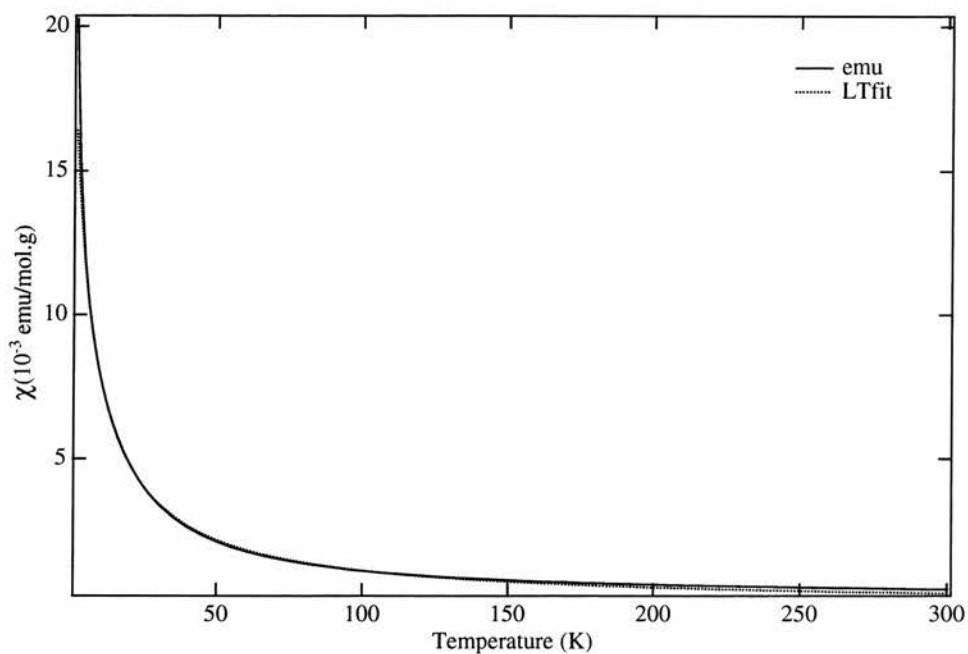


Figure 6.18: Temperature dependence of the ZFC susceptibility of sample 0079 in an applied field of 1kG.

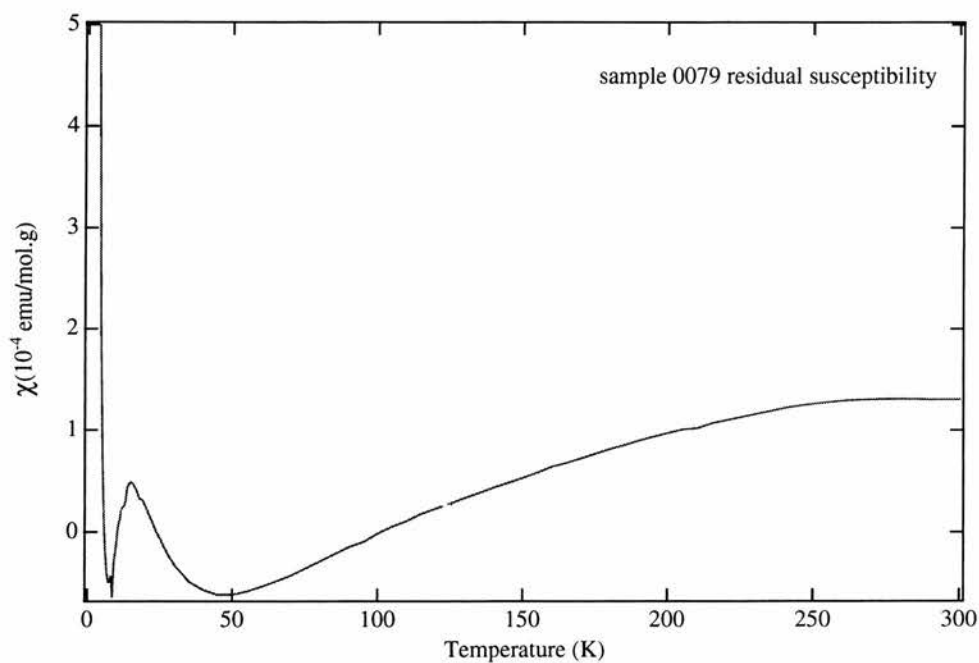


Figure 6.19: Variation of the magnetic susceptibility with temperature, after subtraction of a Curie term.

It is apparent from the fits that the Curie-Weiss description is only adequate at low temperature for 0041, $T < 40\text{K}$. Above this temperature there exists a residual magnetism which grows with increasing temperature. A similar situation is observed in the 0079 data. Although the 0079 data displays no deviation this is a result of the scale and the deviation is clear in the residual susceptibility plot. Plots of this residual susceptibility are shown in Figures 6.17 and 6.19. That of 0041S shows an interesting feature between 140K and 220K where the susceptibility gradient is sharper in this range. In sample 0079, the larger paramagnetism and the lack of any characteristic trends in the residual susceptibility may result from ageing of the sample before measurement.

In addition to the ZF measurements described earlier, field cooled experiments have been performed on sample 0079. When the data sets are compared there is no observable difference and this is confirmed qualitatively by the results of the fits which show that C_M and θ are sufficiently close. One other point of interest is the deviation from the C-W behaviour for temperatures below 5K.

Remanence measurements obtained after cooling in a field of 1000Oe are presented in Figure 6.20. There are two interesting features in this data. Firstly at $T=11\text{K}$ there is a small dip in the susceptibility. Since the ramsdellite is a polymorph of the superconducting phase, $T_c \approx 13\text{K}$, this is evidence of a small amount of spinel being present.

The second, more interesting feature, occurs at 4.7K where the susceptibility diverges. This transition is reminiscent of that reported by Gover through μSR , where they hinted at a spin-glass formation below 10K. From our data it is difficult to identify this state, further measurements at higher fields and lower temperatures are required. It is uncertain if this low temperature transition exists in the 0041S sample since measurements were performed only down to 5K.

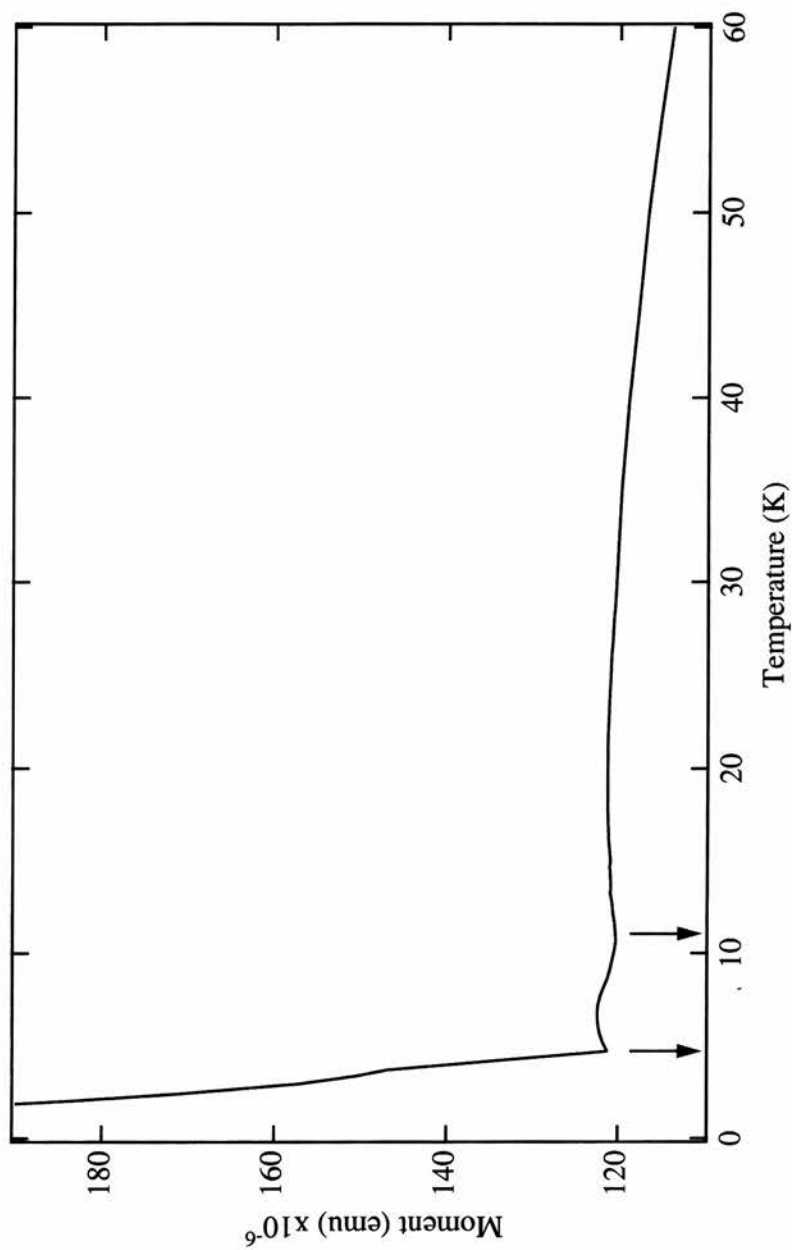


Figure 6.20: Temperature dependence of remanence from cooling in an applied field of 1000Oe (Sample 0079). For clarity only data below 60K are shown.

6.6.2 Muon Spin Relaxation

Muon spin relaxation experiments were performed on powdered single-phase polycrystalline samples of LiTi_2O_4 (sample 0079) with the help of Dr Adrian Hillier. The ARGUS spectrometer at RIKEN-RAL facility at ISIS was used with a continuous flow minicryostat allowing temperatures between 4 and 330K. μSR data was obtained between 100 and 300K, typical muon spectra being shown in Figure 6.21 and 6.22. The data is well described by the following relaxation function:

$$a_0 G_z(t) = a_0 G_z^{DKT}(\Delta, \nu, t) \exp[-(\lambda t)^\beta] + a_{bg} \quad (6.5)$$

in which $G_z^{DKT}(\Delta, \nu, t)$ is the dynamic Kubo-Toyabe function described in Chapter 2, associated with a Gaussian distribution of local magnetic fields at the muon site arising from neighbouring nuclear spins. $G_{MAG}(t) = \exp[-(\lambda t)^\beta]$ represents the magnetic spin relaxation arising from dynamic magnetic fields associated with the fluctuating atomic spins. The combination of nuclear and atomic relaxation functions in equation 6.5 assumes that these are two independent channels for muon depolarisation. Whereas the Kubo-Toyabe function, $G_z^{DKT}(t)$, provides direct information on the interstitial site occupancy of the muon, $G_{MAG}(t)$ provides an insight into the spin fluctuations and electron moment localisation.

Our lowest temperature data was used to obtain the initial and background asymmetries. At each temperature the data in an applied field was analysed giving λ and β . These parameters were then held during analysis of the the zero-field data to obtain Δ and ν .

In order to measure these two mechanisms reliably, experiments have been performed with longitudinal fields sufficiently large, ie above 3mT, to quench the nuclear depolarisation. The field dependence of the spectra obtained at 100K is given in Figure 6.22.

Our μSR data is very different from that of Gover[8] although both sets of results are described by a Gaussian K-T function and stretched exponential. At low temperatures the data was reported to consist of two components resulting from two different muon sites in the sample. Also reported was a possible magnetic transition between 2 and 10K, characterised by an increase in λ and a similar decrease in β for one of the muon sites. Gover suggests this a possible spin glass transition but that further measurements are required. This low temperature ordering is not investigated in the present study due to time restrictions on equipment.

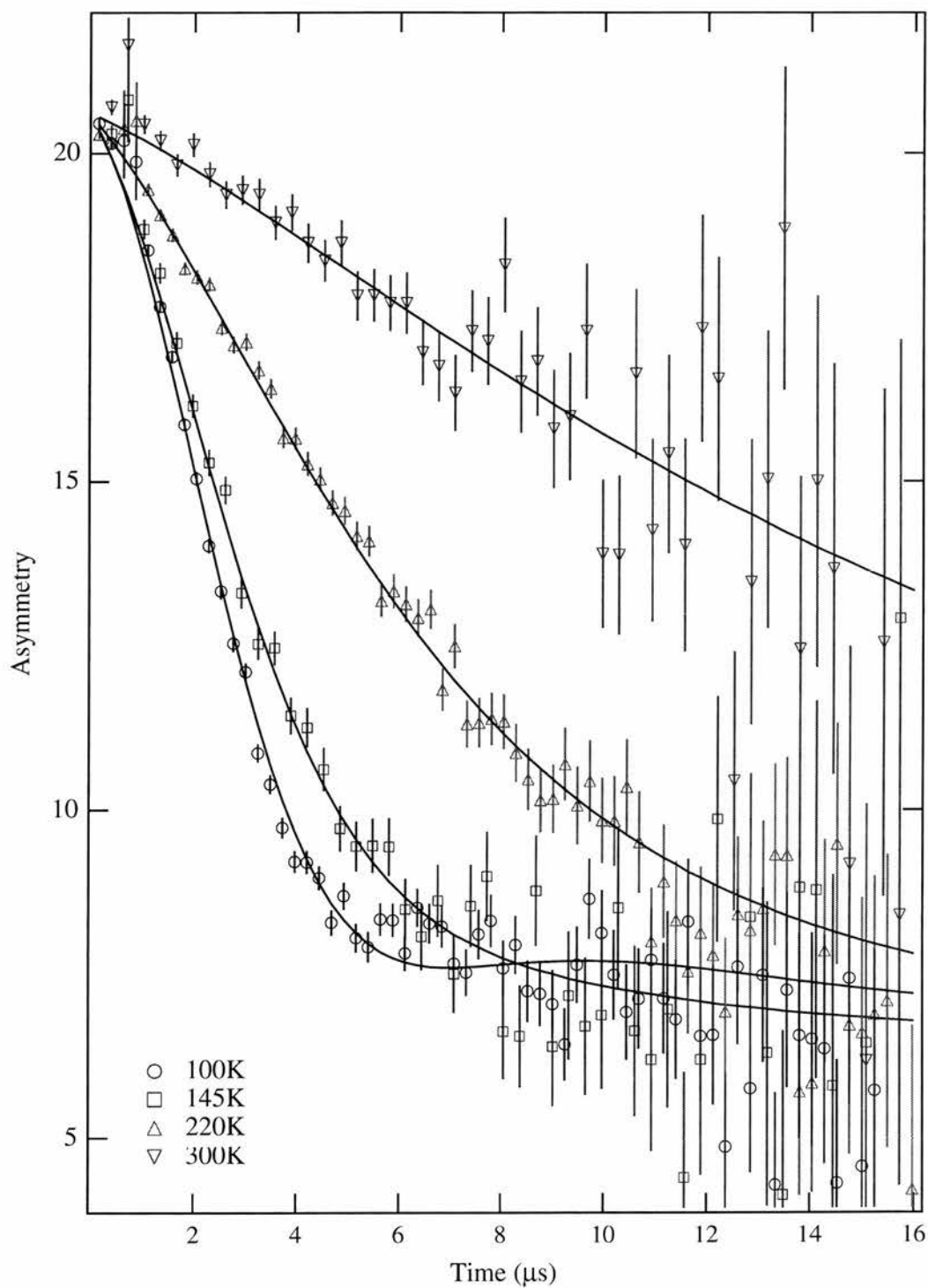


Figure 6.21: μSR spectra of LiTi_2O_4 measured in zero field at several temperatures. The lines are least squares fits to the data as described in the text.

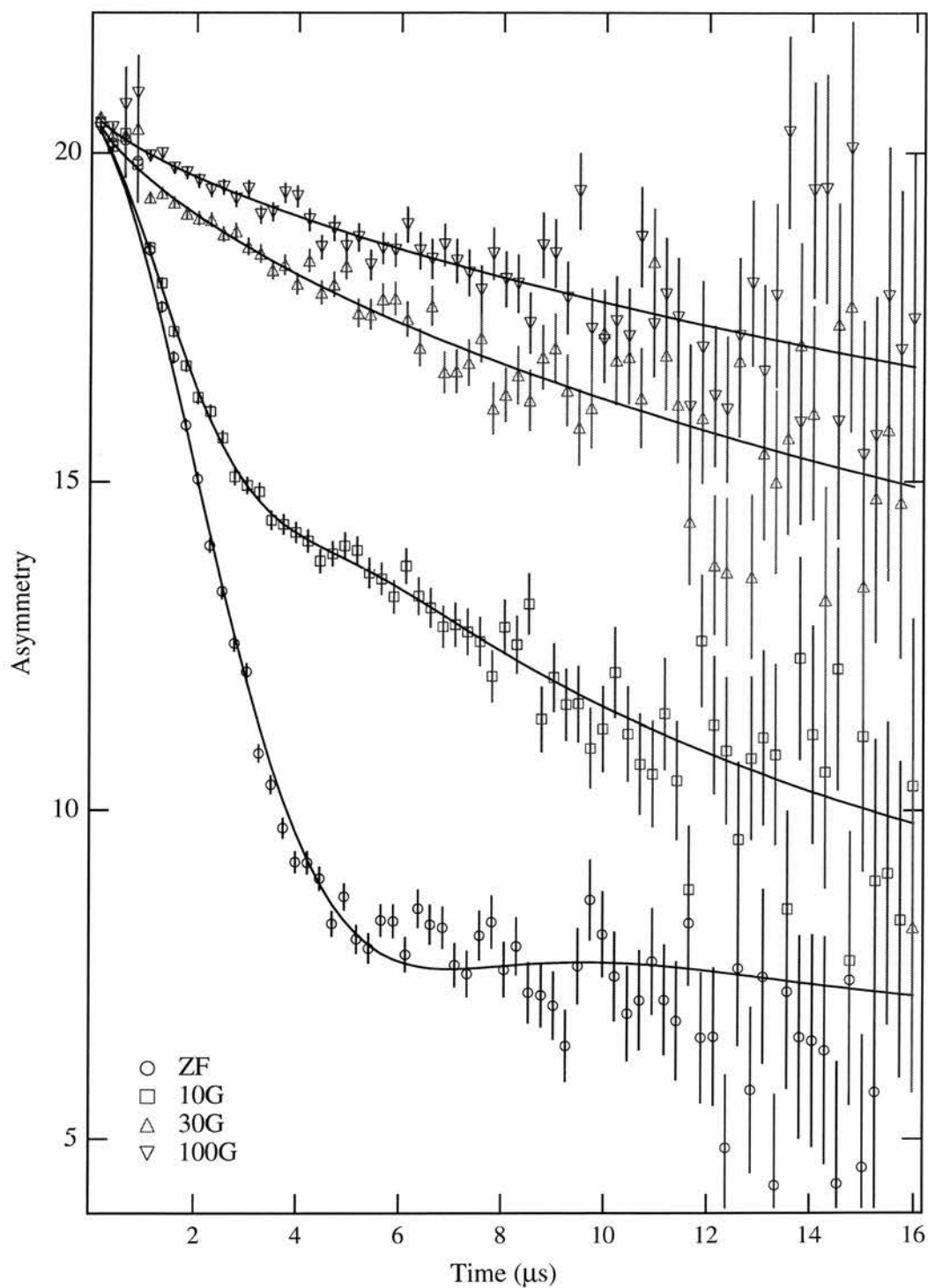


Figure 6.22: Field dependence of μSR spectra of LiTi_2O_4 obtained at 100K. The lines are least squares fits to the data as described in the text.

In Figure 6.21 we compare the μSR spectra recorded between 100 and 300K in zero field. The first feature of these spectra is the temperature independence of the initial asymmetry. A sudden drop of this parameter is indicative of a magnetic transition. Since no decrease is observed there is no transition. We also observe a stronger depolarisation rate at lower temperature. This is confirmed by the values of the field width Δ extracted from the fits to the spectra as shown in Figure 6.23. A decrease of Δ is observed between 140 and 260K. Either side of this behaviour Δ displays two plateau regions.

The temperature dependence of ν can be seen in Figure 6.23. At high temperatures it is flat ($\approx 0.13\text{MHz}$). With decreasing temperature ν increases up to a maximum value of 0.38MHz at 190K below which it falls off gently.

Since this behaviour can describe the hopping of either the muon or the Li^+ , it is instructive to examine the muon residence time, which is related to the thermal dependence by the following $\tau = 1/\nu$. If this is comparable to, or longer than, the precession time of the muon in the local field at the trapping site then the muon can be assumed to be quasi-static [12]. In other words ν should be less than or comparable to Δ . Examination of Figure 6.24 shows that this is the case and that the muon is indeed quasi-static in the whole temperature range investigated and the system displays Li motion. This view point is further supported when the sample stoichiometry is also considered as it is not uncommon to observe static muons in materials containing oxygen, due to the large electronegativity of the p electron shells [13].

The parameters describing the dynamic behaviour at the muon site are shown in Figure 6.24. The extracted values of λ are small inferring a weak interaction between the atomic moments. λ displays a broad maximum at $\approx 200\text{K}$. Near a magnetic transition λ experiences a critical divergence due to the onset of ordering. This behaviour is not observed here.

The dynamic behaviour is well described by the stretched exponential function, meaning a distribution of relaxation rates. As the temperature is lowered, the exponent β saturates to ≈ 0.7 below 175K. This decrease is indicative of a trend towards a broader distribution of atomic dipoles.

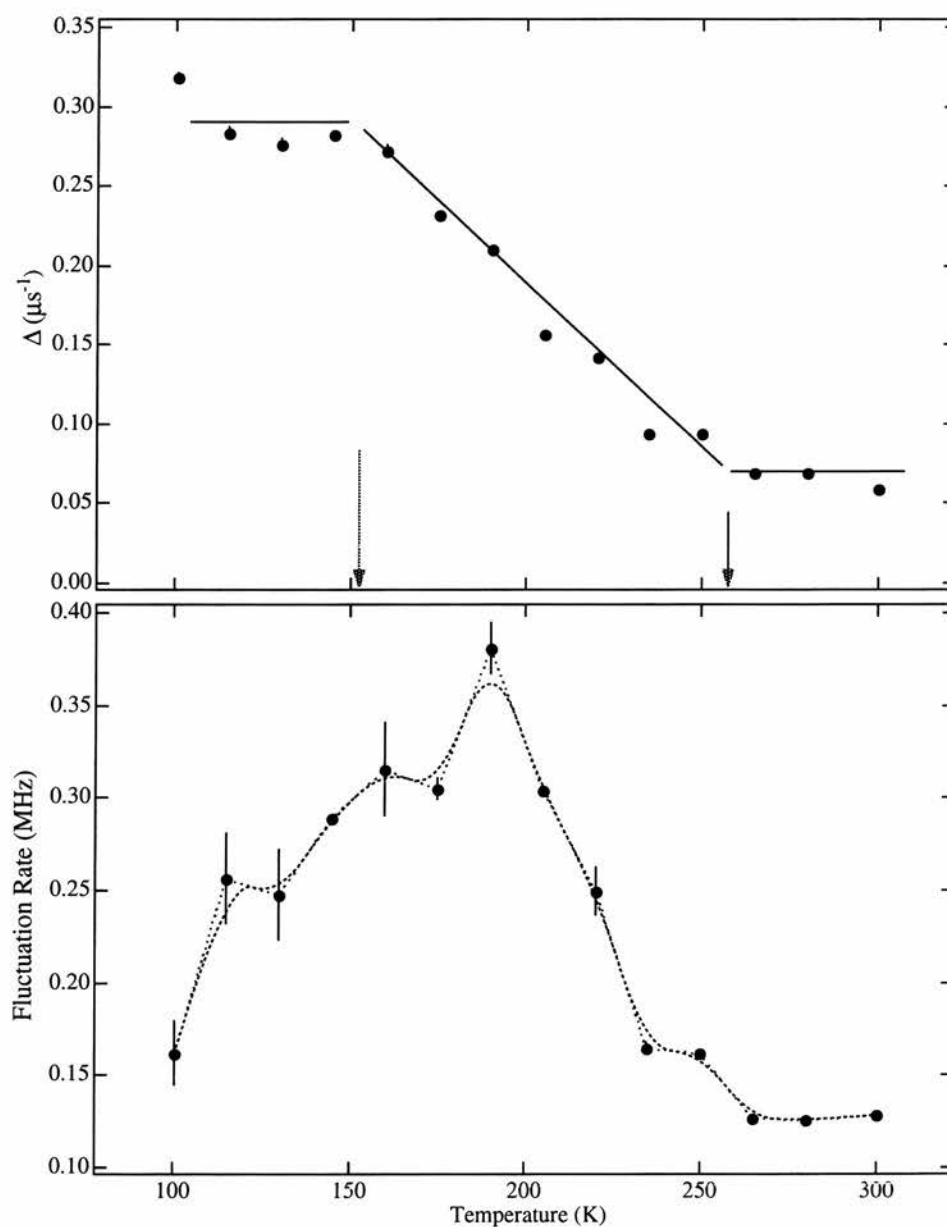


Figure 6.23: Kubo-Toyabe linewidth Δ and fluctuation rate ν measured between 100 and 300K. The solid lines are a guide to the eye.

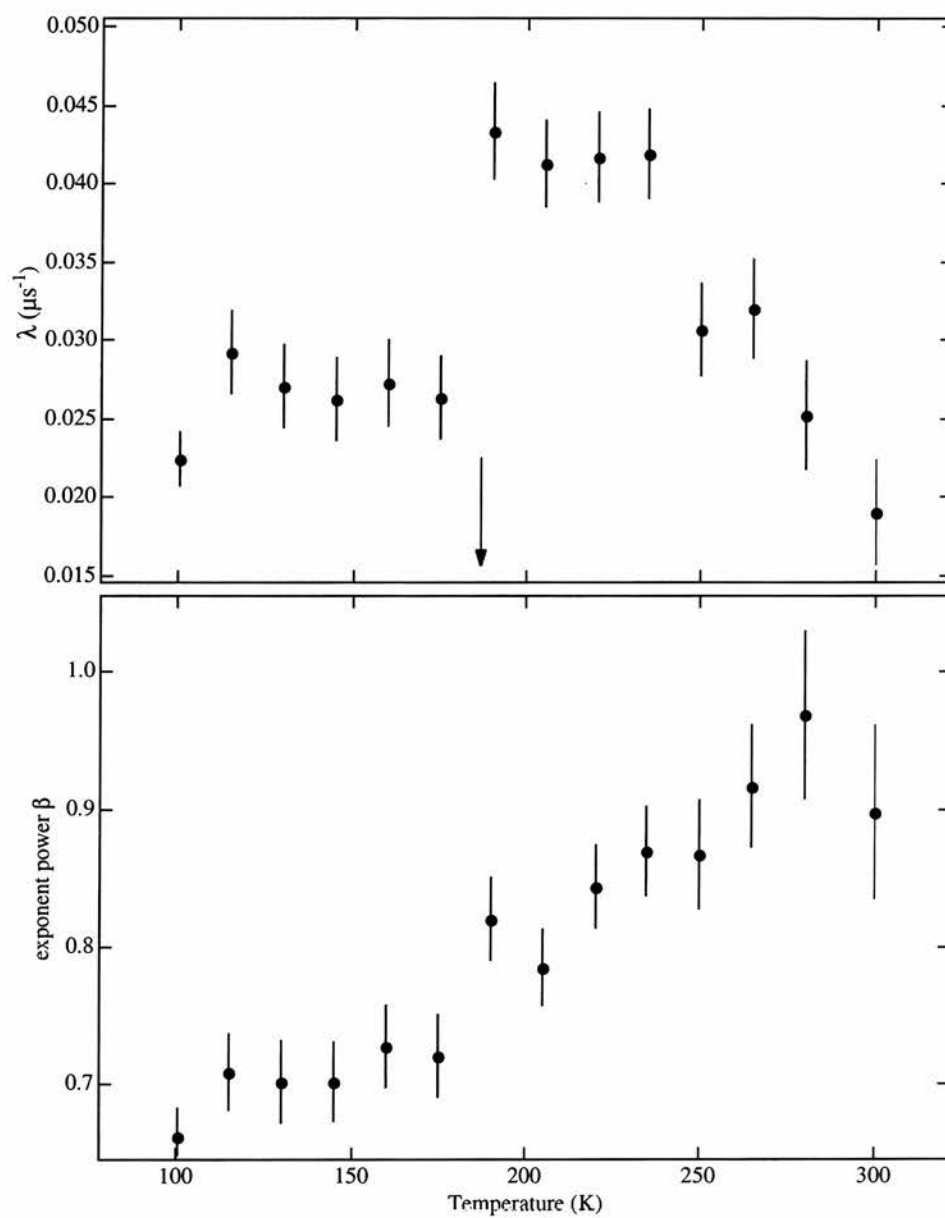


Figure 6.24: The power exponent β obtained from fitting LF- μ SR with stretched exponential relaxation function. Temperature dependence of the atomic relaxation rate λ as determined from applied field data.

6.7 Conclusions and Further Work

Polycrystalline samples of LiTi_2O_4 were prepared and characterised by X-ray diffraction. They were found to be phase pure, exhibiting the same structure as predicted by Akimoto and previously observed by Gover and Tolchard. As mentioned earlier, this is an unstable material, being well known to degrade if exposed to air for even a short period of time. During the course of this project we found that even storage under vacuum is insufficient to preserve ramsdellite LiTi_2O_4 for more than a couple of weeks.

Low temperature structural studies using X-ray diffraction suggest a subtle structural change between 220-260K. A more limited study using neutron diffraction did not display this peak splitting. This discrepancy can be accounted for by the differences in the scattering cross-sections for the two probes and we therefore attribute the peak splitting to positional changes in the Ti atoms. At present the transition is not fully understood. One possibility is that the system undergoes an orthorhombic to monoclinic transformation although further experiments and analysis are required.

Low temperature magnetic investigations have shown this system to be a paramagnetic system with very weakly antiferromagnetically coupled moments. The SQUID signal corresponds to 10% of that expected due to a single magnetic Ti^{3+} per unit cell. We observe unusual behaviour between 140K and 220K due to an additional magnetic component. A broad maximum is also displayed in the temperature dependence of λ at 210K. At present this second component is not fully understood although it may arise from short range antiferromagnetic coupled clustering of the Ti.

A low temperature transition has been observed in the remanent magnetisation at 4.7K. This is not inconsistent with the μSR work of Gover which suggested a spin-glass type transition between 2K and 10K. At present, sufficient data does not exist to identify this phase absolutely, except to comment that it is a cooperative phenomenon at work.

One thing is certain from our measurements; this is not a spin-ladder material as was predicted by Gover. We observe different μSR data to that of Matsuda et al.[9] and our SQUID magnetisation data does not display the behaviour expected for a zig-zag ladder material. Moreover it seems unlikely that the structure of this material could support such a complex magnetic state [14].

The ^7Li NMR data is the most interesting of all. Here we observe two distinct Li resonance signals, at high and low shifts, indicative of two distinct environments, close to and far from a magnetic moment. Since the Li occupy sites in the channel structure we expect them to be in close proximity of each other. This is confirmed by the relatively small difference in their shifts and identical relaxation rates, indicative of spin-spin coupling so that both share the fast relaxing mechanism provided by the magnetic species. This fast relaxation rate increases with decreasing temperature indicative of non-metallic, magnetic interactions. Our analysis is in contrast with previous measurements by Kartha who observed a larger relaxation time, $T_1=600\text{ms}$, and so concluded that the system was metallic.

The proximity of a magnetic moment close to the high shift is further evidenced by the Curie-Wiess-like behaviour of the linewidth. This displays an ordering temperature close to 150K although such a long-range ordering is not observed in our dc magnetisation measurements. It is a difficult task to reconcile the conflicting information supplied by these complementary techniques. One possible scenario is that the moments do indeed order ferromagnetically but only over short distances.

The most interesting feature of the ^7Li NMR spectra is the progressive transfer of the signal intensity from the high to low shift site with decreasing temperature. Initially it was uncertain if this behaviour was the result of lithium motion or changing environment. When considered in conjunction with our μSR data it is apparent that the lithium are indeed in motion although these techniques show this to be occurring over different temperature ranges. We attribute this discrepancy to the slight differences in the samples used for each measurement. Overall, the interpretation of this data has been problematic and the analysis of this data is ongoing.

Clearly this is quite a complex system which can be thought of as TiO_2 cage structure with Li occupying the channel sites. With decreasing temperature the surrounding structure undergoes a transition most probably due to a shear within the a-c plane due to motion of the titanium. This is then followed by a magnetic transition the origin of which is not fully understood at present. A change in the lithium site occurs in a similar temperature range. It would seem that these phenomena are related but systematic measurements on a single sample are required to determine if this is the case and indeed if the temperature ranges described herein are separate or overlap.

One of the fundamental problems which has to be overcome is that of sample

reproducibility or to be able to use multiple techniques on a single specimen. The latter option is not available to us at present. Since samples are effectively useless once exposed to air, a huge amount would have to be prepared in a single batch and this in itself creates new problems.

A repeat of the ⁷Li NMR measurements coupled with additional ⁴⁹Ti NMR data would be most beneficial to understanding this system. This was not attempted here due to the complicated spectra that result from two Ti nuclei resonances overlapping and is a major piece of research in itself. Continuation of ⁷Li NMR measurements to lower temperatures to observe the full transition is obviously the next step forward. These measurements will have to be performed using static techniques as sample spinning is difficult at 160K and becomes even more problematic below 100K.

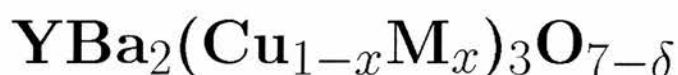
Additional measurements are also required to fully characterise the subtle structural transition observed in this system. Since neutrons are quite insensitive to the titanium atoms that are central to this transition, the logical step is to probe the temperature region of interest with a synchrotron source of X-rays of single wavelength and higher intensity than is possible in a normal laboratory.

Lastly more magnetic measurements, SQUID or μ SR, would help to define the low temperature magnetic transition. Our results suggest that this is possibly a spin-glass state and so a μ SR study would most beneficial in elucidating the magnetic structure.

References

- [1] D. C. Johnston, H. Prakash, W. H. Zacharisen, and R. Viswanthan, *Mater. Res. Bull.* **8**, 777 (1973).
- [2] A. M. Bystrom, *Acta. Chem. Scand.* **3**, 163 (1949).
- [3] J. Akimoto, Y. Gotoh, and Y. Oosawa, *Journal of Solid State Chemistry* **110**, 150 (1994).
- [4] R. K. B. Gover, J. T. S. Irvine, and A. A. Finch, *Journal of Solid State Chemistry* **132**, 382 (1997).
- [5] J. P. Kartha, D. P. Tunstall, and J. T. S. Irvine, *Journal of Solid State Chemistry* **152**, 397 (2000).
- [6] D. C. Johnston, *Journal of Low Temperature Physics* **96**, 446 (1976).
- [7] J. P. Kartha, private communication.
- [8] R. K. B. Gover, Ph.D. thesis, University of St. Andrews, 1997.
- [9] M. Matsuda *et al.*, *Physical Review B* **55**, 11953 (1997).
- [10] D. P. Tunstall, private communication.
- [11] T. Ohta, F. Izumi, K. Oikawa, and T. Kamiyama, *Physica B* **234**, 1093 (1997).
- [12] C. T. Kaiser *et al.*, *Physical Review B* **62**, R9236 (2000).
- [13] A. D. Hillier, private communication.
- [14] D. P. Tunstall, private communication.

Chapter 7



7.1 High temperature Superconductivity (HTSC)

Named after their unexpectedly high transition temperatures, the high- T_c cuprates have been a source of fascination since their discovery in 1986. It is now experimentally well-established that the CuO_2 planes are responsible for the magnetic and superconducting properties of the cuprates. The interconnection between these two is still unanswered and an understanding of the normal state is still a prerequisite for any theoretical approach to the microscopic origin of HTSC.

This chapter describes our attempts to use NMR to identify and characterise the moments induced on the CuO_2 planes in YBCO by doping with zinc and lithium; in particular we focus on fully oxygenated samples where the moments are known to be very small.

7.1.1 Structure of YBCO

$\text{YBa}_2\text{Cu}_3\text{O}_{7-\delta}$ (YBCO) is an oxygen deficient triple perovskite structure with two crystallographically and chemically inequivalent copper sites (Figure 7.1). The structure of the high temperature superconducting cuprates can be viewed as alternating stacks of electronically active metallic CuO_2 layers and insulating layers which act as charge reservoirs. This complicated system also gives rise to a variety of magnetic states. The system undergoes a phase transition from a tetragonal to an orthorhombic structure which is controlled by the oxygen content.

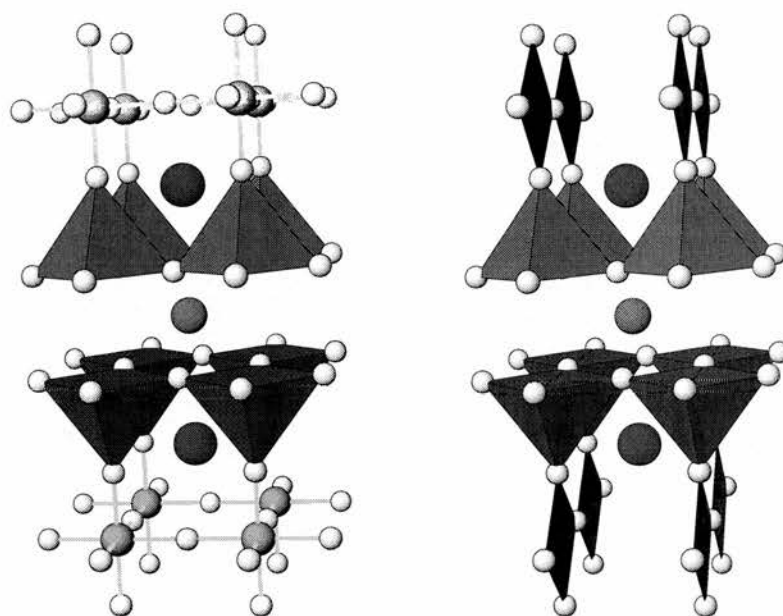


Figure 7.1: Tetragonal and Orthorhombic structures of YBCO-123 system

The tetragonal phase is an anti-ferromagnetic (AF) insulator. The undoped parent compound has composition $\text{YBa}_2\text{Cu}_3\text{O}_6$ in which the planar copper ions have electronic configuration $3d^9$ (2^+ valence) and those on the chain $3d^{10}$ (1^+ valence). These oxidation states imply magnetic $\text{Cu}(2)$ and non-magnetic $\text{Cu}(1)$. The moments align in the basal plane of the unit cell and within the plane there is simple Néel ordering. A schematic of the ordering is given in Figure 7.2 where the black and white spin sites represent opposite spins perpendicular to the c -axis.

Between nearest neighbour A-C layers dipolar effects act to give AF ordering of the moments and connecting next nn layers are oxygen atoms which allow superexchange to align these moments also in an AF configuration. The resulting magnetic unit cell has twice the volume of the chemical one. As oxygen is added the B layer $\text{Cu } 1^+$ are converted to 2^+ oxidation state with an associated magnetic moment. The presence of extra moments tends to frustrate AF pairing of its two neighbours and forces ferromagnetic ordering of the three. This leads to fluctuations in the local order and a decrease in the Néel temperature. As the oxygen content increases T_N changes slowly until the tetragonal-to-orthorhombic transition is approached, at which point it quickly falls to zero.

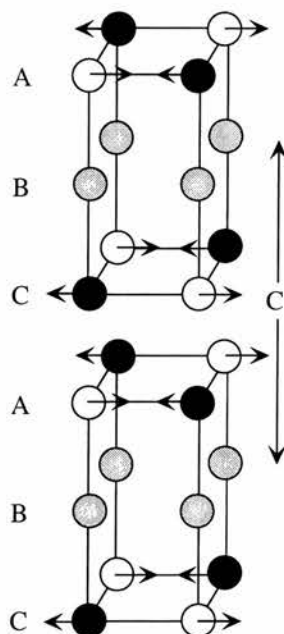


Figure 7.2: The AF structure of $\text{YBa}_2\text{Cu}_3\text{O}_6$. The black and white sites represent the magnetic Cu^{2+} ions, black being of opposite spin to white. The non-magnetic Cu^{1+} ions are shown in grey.

For values of δ between 0 and 0.6 the system is an orthorhombic superconducting metal with a maximum transition temperature of about 94K. The Cu(2) sites form two conducting nearest neighbour parallel planes which support superconductivity. The Cu(1) form Cu-O chains along the b-axis which have been found to act as a reservoir of conduction holes for superconductivity in the planes. The observed decrease in T_c is associated with disorder in the chains implying that they play a major role in the mechanism of the high temperature superconductors. There is a variation of transition temperature with hole concentration with a plateau being observed. The superconducting phase diagram is split into three segments dependent on the transition temperature. The region around $\delta=0.06$ where $T_c=93\text{K}$ is referred to as optimally doped. Above this is the overdoped region and below the underdoped. In the very underdoped region there exists a plateau of roughly constant $T_c=60\text{K}$. The magnetic phase diagram for this system is shown in Figure 7.3.

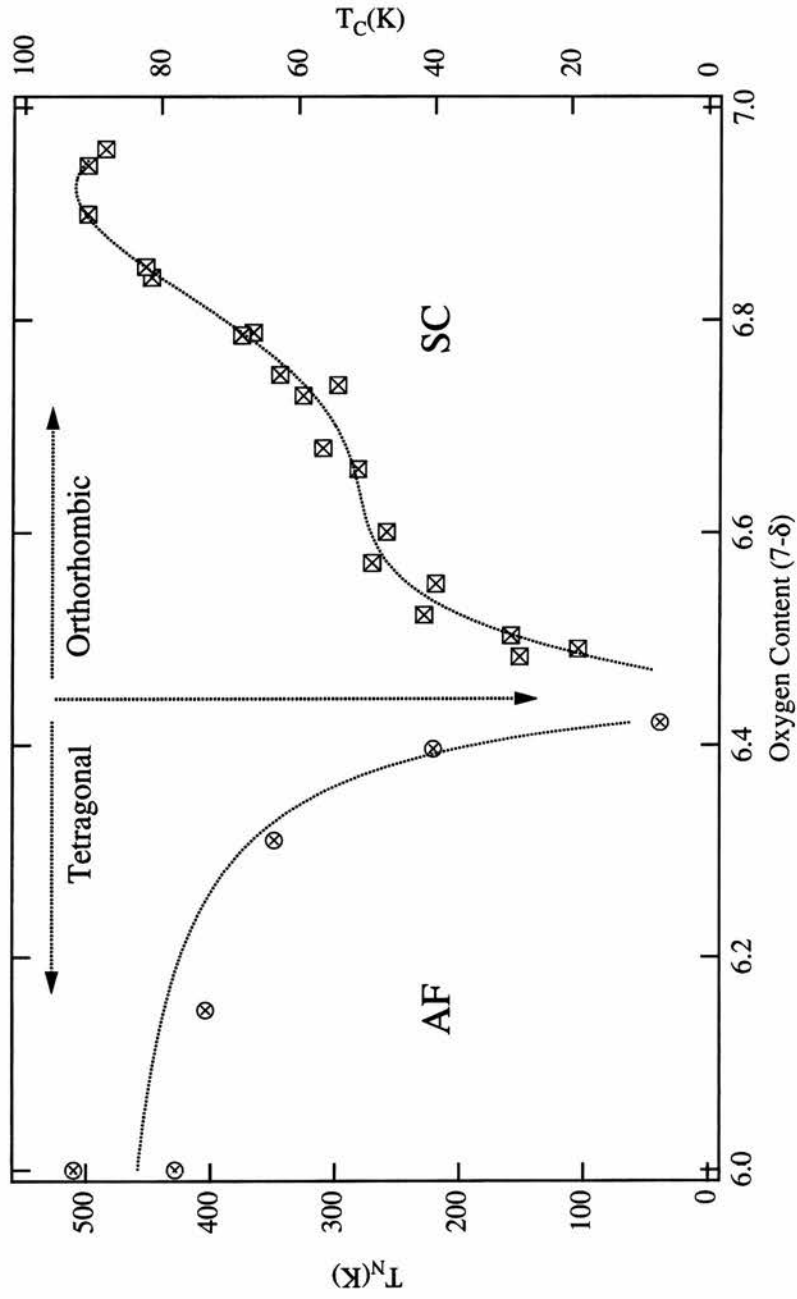


Figure 7.3: Phase diagram with varying oxygen content[1]. Lines are guides to the eye.

7.1.2 Superconducting YBCO

Normal State

It is the normal state, which exhibits the most exotic behaviour and has been the subject of the greatest experimental attention [1]. A description of the metallic behaviour yet alone the other exotic properties is still to be reached. Simple empirical laws such as the Korringa relationship which are predicted by a Fermi liquid approach no longer apply.

There are two noteworthy properties of the normal state that should be mentioned. These are the opening of a spin pseudogap and the persistence of AF fluctuations into the metallic state.

Pseudogap

Occurring only in the under and optimally doped materials, the pseudogap is their most outstanding feature. The pseudogap appears at low temperatures, in the normal state, as a partial gap in the spin excitation spectrum. First observed in NMR experiments of the bulk susceptibility [2], it has now been observed by NMR Knight shift, relaxation rates of ^{63}Cu , inelastic neutron scattering and ARPES. In the nuclear magnetic resonance studies the appearance of the gap is manifested by a sharp decrease in the above mentioned properties. This property is hole dependent, occurring at ever decreasing temperature until appearing just above T_c in the optimally doped compound. The microscopic mechanism is unknown but it might be a signature of pre-forming of pairs, analogous to a Bose-Einstein condensate, which is predicted by several theories.

Recent experiments would seem to suggest this is not the case [3]. The magnetic field dependence of the onset of pseudogap has been measured through the ^{63}Cu spin-lattice relaxation rate in near optimally doped sample. Although the application of a magnetic field shifts T_c the pseudogap remains unaffected. If related to superconductivity one would expect the onset temperature to scale with the superconducting transition. This insensitivity of the spin gap to an applied magnetic field demonstrates the weakness of the relationship between the two and suggests it is not representative of pre-formation of pairs.

Antiferromagnetic Fluctuations

The close proximity of the AF and superconducting phases has always drawn great attention. It has been observed that magnetic fluctuations continue into the metallic state [4]. The coexistence of magnetic ordering with superconductivity is evidence for a strong electron-electron correlation starting point for a description of the normal state. The nearly antiferromagnetic Fermi liquid approach to the normal state of Pines and Monthoux [5] is one of many different theories describing a superconducting mechanism which is magnetic in origin.

Superconducting state

All the high temperature superconductors exhibit the main properties of the elemental superconductors, ie those predicted by BCS theory. These are zero resistance, Meissner effect, flux quantisation and the Josephson effect. In addition they also possess more exotic properties, the most obvious being the extremely high transition temperatures. This is related to the energy gap that separates the normal and superconducting states by

$$\frac{2\Delta(0)}{k_{\text{B}}T_c} \approx 8 \rightarrow 10 \quad (7.1)$$

compared with a value of 3.52 for conventional BCS type superconductivity. These also have an anisotropic d-wave symmetry of the order parameter. This itself has consequences on the pairing mechanism. Another strange property of these materials concerns the isotope effect, which is the signature of electron-phonon interaction. In YBCO this is found to be very weak and at first was not detectable.

7.2 Review of Doping experiments

Controlled study of dopant effects is a common method of elucidating the properties of a material. This technique has been employed on the high temperature superconducting cuprates ever since their discovery, with the hope of understanding the superconducting pairing mechanism. Since superconductivity is known to reside on the CuO_2 planes, substitution of copper with metallic elements should produce substantial changes in the superconducting properties.

The most interesting dopant is Zn. It is diamagnetic and has a similar ionic radius to copper resulting in a preference to occupy the $\text{Cu}(2)$ site, retaining the orthorhombic structure. The intriguing result of substitution is the drastic depression of the transition temperature with T_c less than 3K for 10% replacement [6]. This is not the only consequence of Zn doping, which strongly modifies the whole phase diagram (see Figure 7.4) showing suppression of both AF and SC states along with a large intermediate region of spin-glass like behaviour [7].

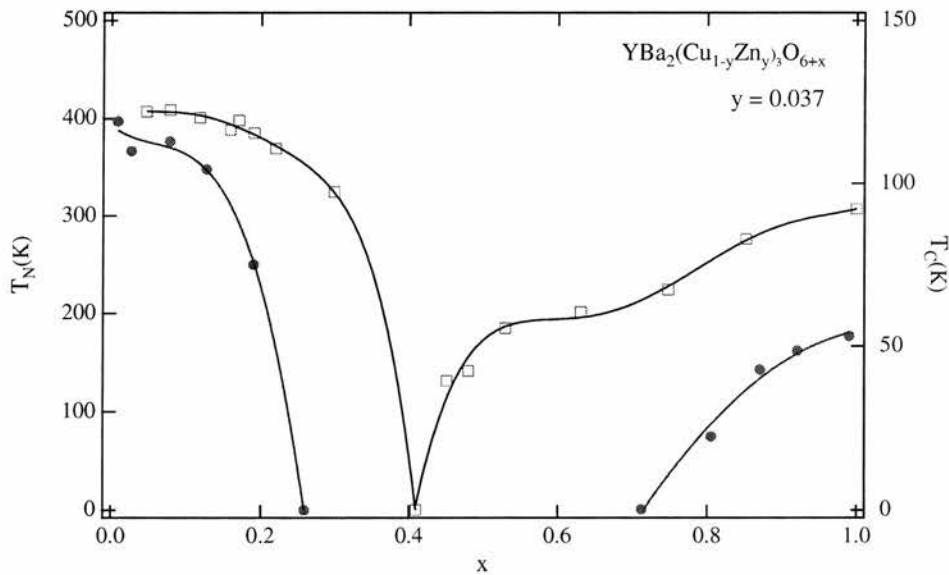


Figure 7.4: Phase diagram of Zn-substituted (solid symbols) and pure $\text{YBa}_2\text{Cu}_3\text{O}_{6+x}$ (open symbols)[7]. The line are guides for the eyes.

A consensus on the reason for the destruction of superconductivity has not yet been reached. It is generally accepted that Zn impurities lead to the creation of local moments on the planes lying predominantly on the $\text{Cu}(d_{x^2-y^2})\text{-O}(2p_\sigma)$ orbitals. The role of these moments, if any, in the suppression of T_c is still under

debate and several other explanations of non-magnetic nature have also been suggested. Initially the moments were observed via the broadening of the ^{89}Y NMR linewidth [7]. This is the narrowest in the cuprate family and shows a temperature dependent broadening which can be described by the Curie law, evidence of the existence of paramagnetic moments. More recently these moments were characterised in the underdoped material via observation of nearest neighbour resonances in ^{89}Y NMR spectrum by Alloul et al. [8] (See Figure 7.5). By considering a simple RKKY analysis of the long distance spin polarisation and the Abrikosov-Gor'kov pair breaking formulation they calculated the strength of interaction between these induced moments and the conduction electrons. The result of their experiments is the conclusion that the coupling is sufficiently large to play a role in the suppression of superconductivity.

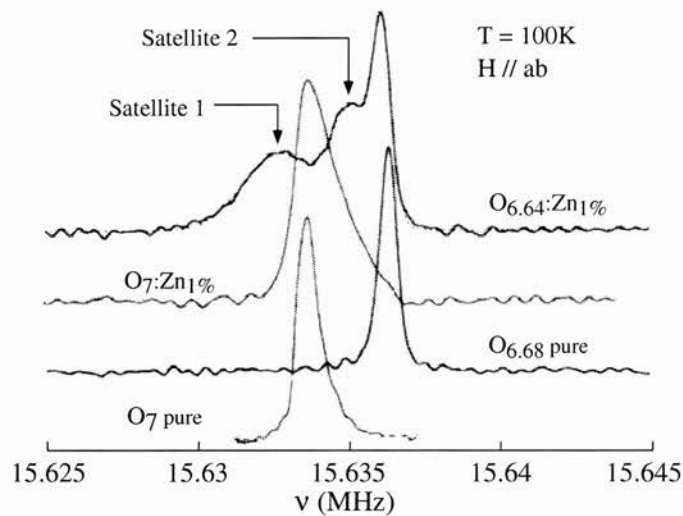


Figure 7.5: Spectra for YBCO:Zn showing the nearest and next nearest resonances[8] due to Zn induced moments.

In their analysis Alloul et al. also concluded that observation of similar satellites in fully oxygenated material would be difficult; (1) because of the reduced size of the moments and (2) because of the inherent linewidth of ^{89}Y resonance due to oxygen inhomogeneity. This is exemplified in Figure 7.5 where there are no discernable additional peaks in the $\text{YBCO}_7:\text{Zn}1\%$ resonance spectrum.

Several other authors have refuted this interpretation. A ^{63}Cu NMR study by Walstedt et al. [9] found that the measured Curie term would produce a theoretical depression of T_c 300 times smaller than the observed effect. This led them to the

conclusion that magnetic pair-breaking is definitely not at work but that potential scattering may be strong enough to account for the observations.

Another group has carried out an ^{89}Y NMR study of Zn doping of the $\text{YBa}_2\text{Cu}_4\text{O}_8$ system [10]. Unlike in the $\text{YBa}_2\text{Cu}_3\text{O}_{7-\delta}$ material, hole doping is varied by controlled substitution of Ba for La. The chemical formula for this compound with Zn doping is therefore $\text{Y}(\text{Ba}_{1-y}\text{La}_y)_2(\text{Cu}_{1-x}\text{Zn}_x)_4\text{O}_8$. These experiments found that the strength of the local moments is dependent on the hole concentration, increasing slightly with the number of holes. As samples become more underdoped, magnetic pair breaking is increasingly unable to account for the decline of T_c . The conclusions of these experiments support the NAFL approach to the normal state which predicts a magnetic pairing mechanism. In this formulation substitution by Zn onto the plane drastically reduces T_c as it disrupts the magnetic structure over a lengthscale that is similar to the correlation length [11]. Furthermore the substitution of a magnetic impurity should have less impact since it maintains the magnetic structure. This is observed in Ni doping which replaces on the Cu(2) site and causes only a slight decrease in T_c , eg 63K at 10% doping [6].

7.3 Characterisation

Ceramic samples of both zinc and lithium doped YBCO were prepared in-house by a standard solid-state method (see Chapter 3). Since our interest in these materials is primarily with the influence of doped impurities, knowledge of the site occupied and exact concentration is paramount. X-ray and time of flight neutron diffraction were used to confirm sample purity and structure. Oxygen content was determined by thermogravimetric analysis and is also inferred through lattice parameters from XRD studies.

7.3.1 Structural Analysis

X-Ray Analysis

Analysis by x-ray powder diffraction was carried out on the materials after removal from the furnace using a Philips PW1049 spectrometer $\text{CuK}_{\alpha 1}$ source ($\lambda=1.5405\text{\AA}$). Data once obtained were fitted using the FULLPROF Rietveld refinement software [12]. Generally overnight runs, lasting about 12 hours, were used as this gave a better indication of the sample purity.

All samples were described by the expected orthorhombic Pmmm structure except for the 5% Zn-doped sample which contained unindexed peaks indicative of a spurious phase. A typical x-ray diffraction pattern is shown in Figure 7.6. The splitting of the [013] and [110/103] peaks are particularly indicative of the orthorhombic structure.

Neutron Diffraction

Neutron diffraction data were collected using the POLARIS diffractometer at ISIS, RAL courtesy of Martin Smith. Room temperature neutron time of flight powder diffraction data were obtained on various samples in order to ascertain the concentration and site occupied by the dopants. Data once obtained were fitted using the GSAS Rietveld refinement software [13]. A typical diffraction pattern and refinement are shown in Figure 7.7.

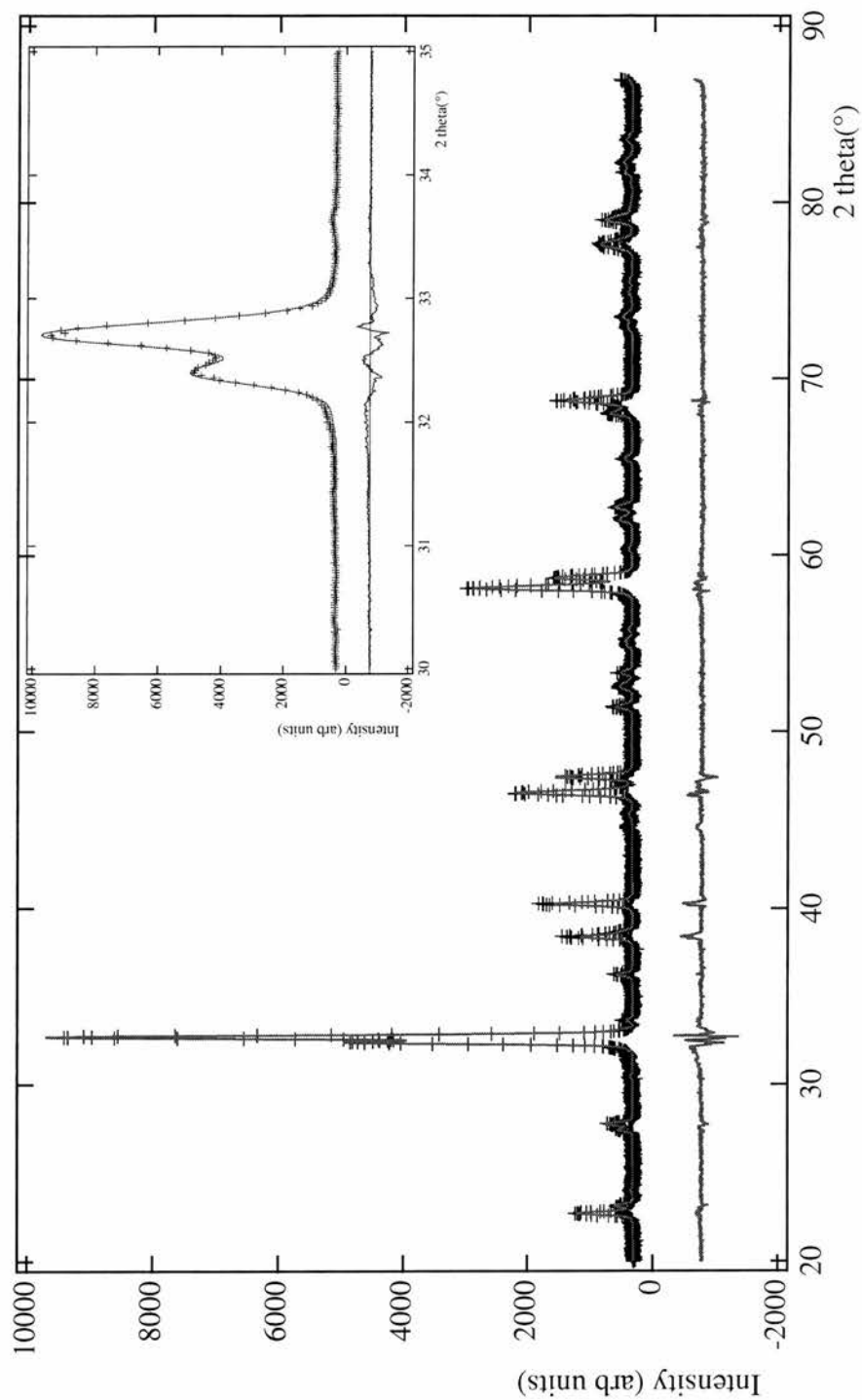


Figure 7.6: X-ray powder diffraction pattern and full profile refinement for $\text{YBa}_2(\text{Cu}_{1-x}\text{Zn}_x)_3\text{O}_{7-\delta}$ $x=0.01$ obtained at room temperature. Inset: expanded fit to the main peaks indicative of orthorhombic structure.

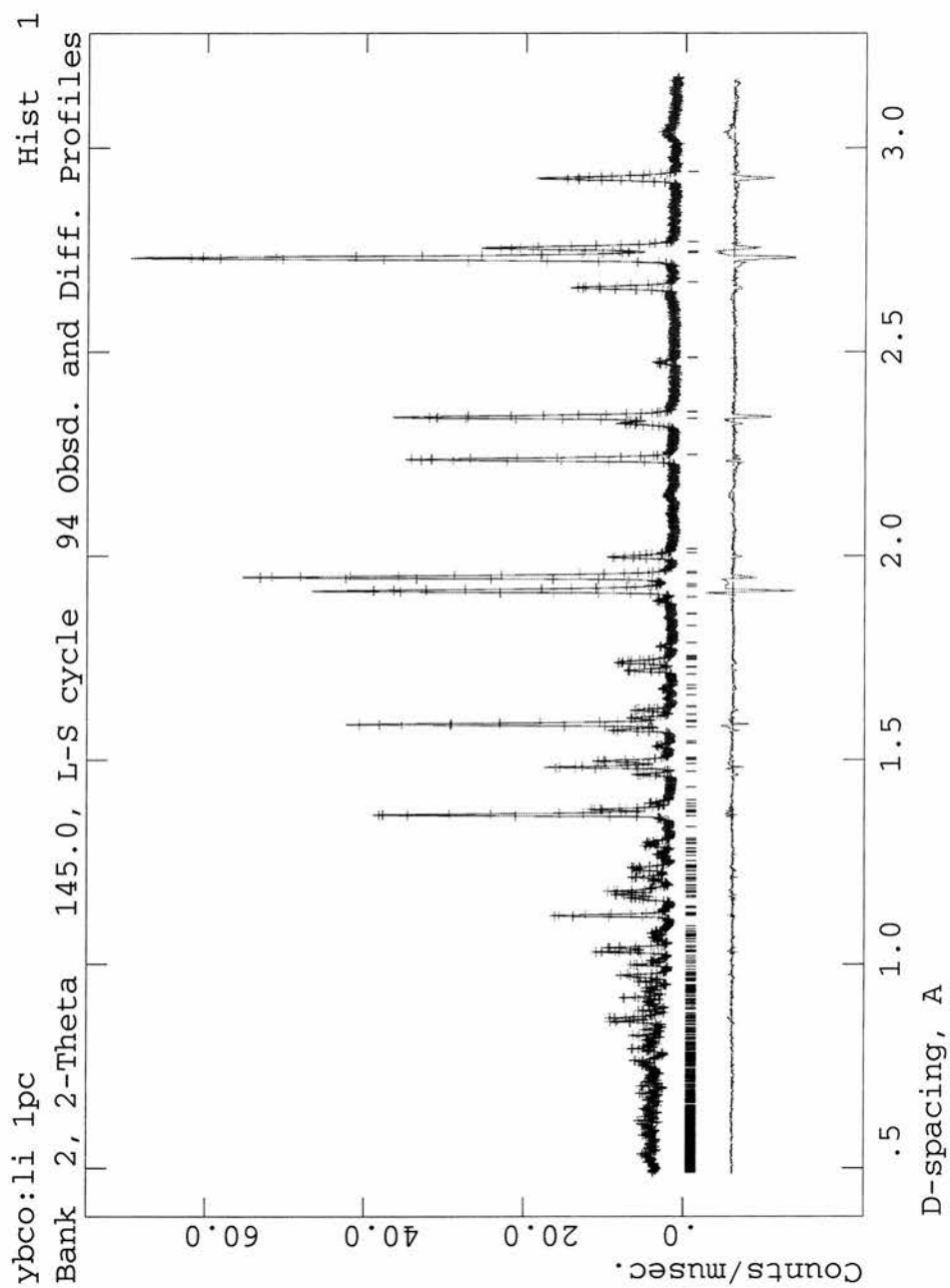


Figure 7.7: Neutron powder diffraction pattern and GSAS refinement for $\text{YBa}_2(\text{Cu}_{1-x}\text{Li}_x)_3\text{O}_{7-\delta}$ $x=0.01$ obtained at room temperature on POLARIS.

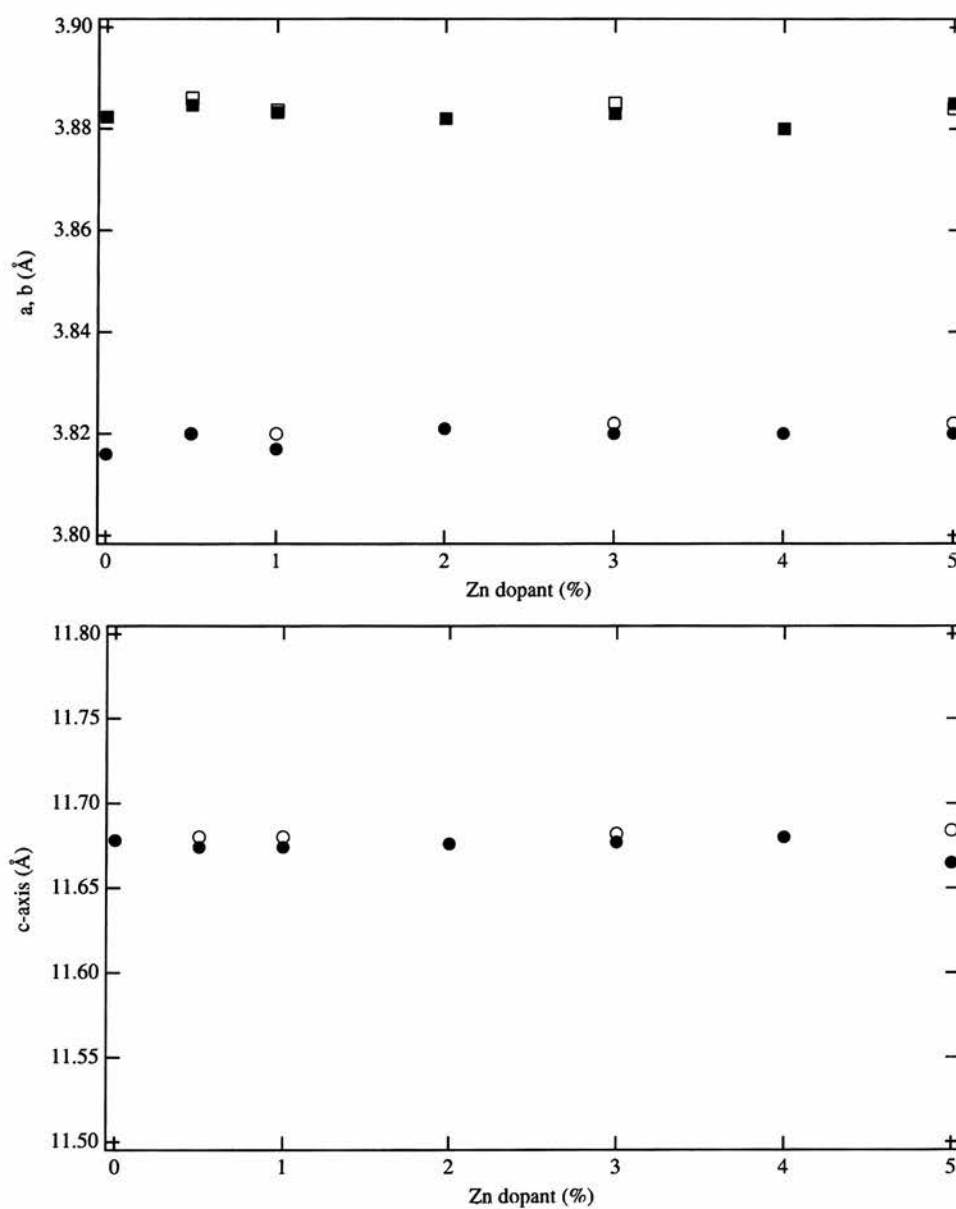


Figure 7.8: Structural parameters as a function of the Zn content. The closed markers represent data from the refinement of X-ray diffraction and the open that from neutron.

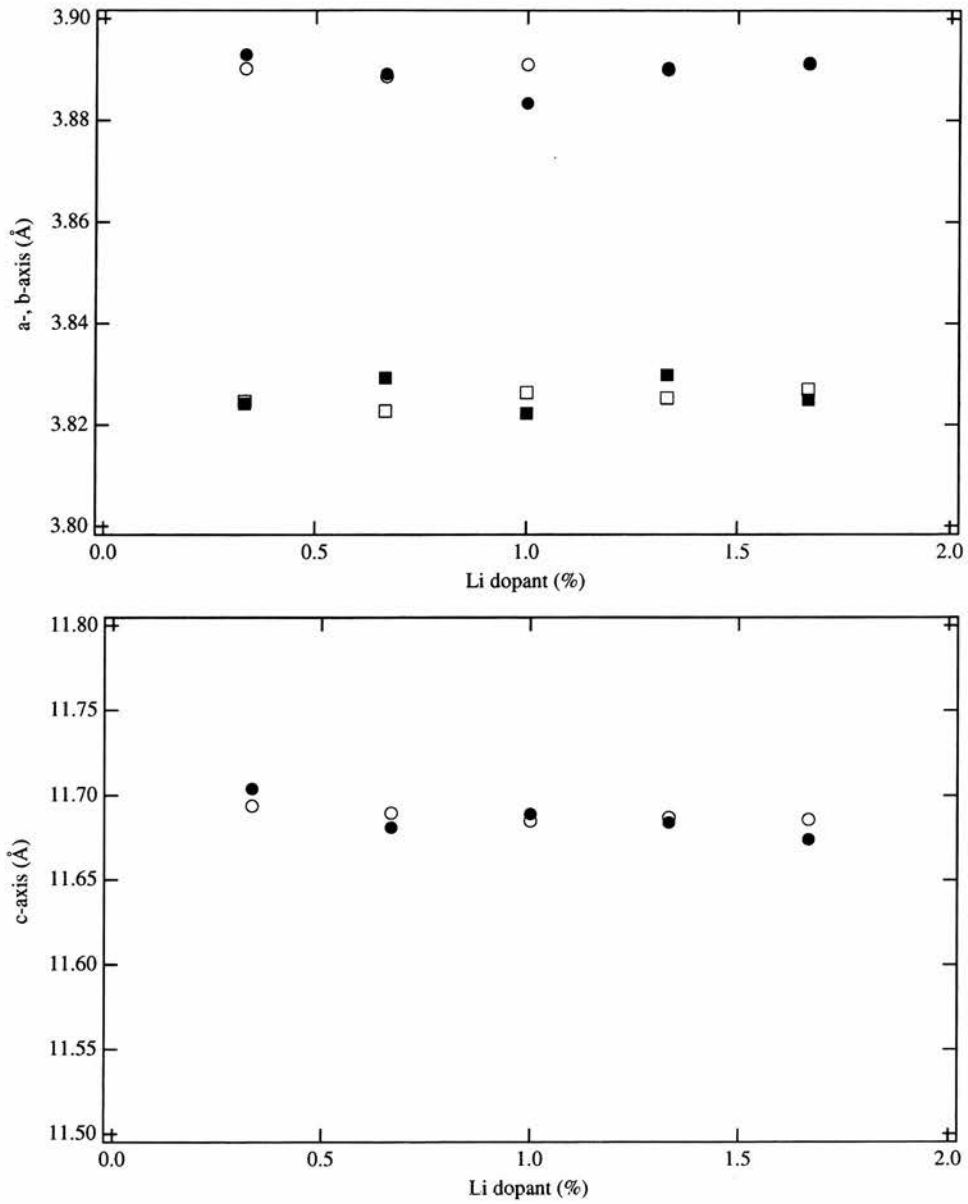


Figure 7.9: Structural parameters as a function of the Li content. The closed markers represent data from the refinement of X-ray diffraction and the open that from neutron.

Since the dopant concentration is small, determination of the dopant site and occupancy proved to be difficult, producing unstable minima in the model. This method does have higher resolution than XRD and so confirmed our samples to be single phase. It also gives similar values for the lattice parameters to those determined by XRD.

In Figure 7.8 we can see that the Zn-doped samples are orthorhombic with constant lattice parameters and good agreement between the neutron and x-ray diffraction data. The lack of variation in the c lattice parameter over the entire range studied implies only a slight variation in the oxygen content. This also indicates that the Zn is substituting onto the planar Cu site rather than the chain site which would result in a contraction of the c -axis. Comparison of these values with those obtained by other groups suggests an oxygen content of between 7 and 6.9 for all samples.

The lattice parameters extracted for the Li-doped samples are given in Figure 7.9. This displays similar orthorhombicity of all samples but with variations being observable. The c -lattice shows a constant decrease with increasing Li content indicative of at least some substitution onto the chain sites.

7.3.2 T_c measurements

The superconducting transition temperature was determined from SQUID susceptibility measurements. The derivative of the susceptibility data was taken to measure the transition width and onset used to define the critical temperature.

Figure 7.10 shows the variation of the superconducting transition temperature T_c of $\text{YBa}_2(\text{Cu}_{1-x}\text{Zn}_x)_3\text{O}_{7-\delta}$ as a function of Zn concentration. The transition temperature decreases rapidly with increasing Zn content with only the 5% doped sample standing out from this trend. The slope of the decrease is found to be $-11.89\text{K}/\text{Zn}\%$, which is consistent with published data [1]. For high Zn contents the transition width broadens as a result of increasing inhomogeneity due to the Zn substitution.

Similarly, the T_c dependence on Li% is given in Figure 7.11. From previous studies we expect a decrease of $6\text{K}/\%\text{Li}$ [14], about half that experienced by Zn substitution, this is shown in the figure. It is evident that three of our samples display the predicted behaviour. The others have both broad transitions and critical temperatures lower than expected, indicative of poor sample quality.

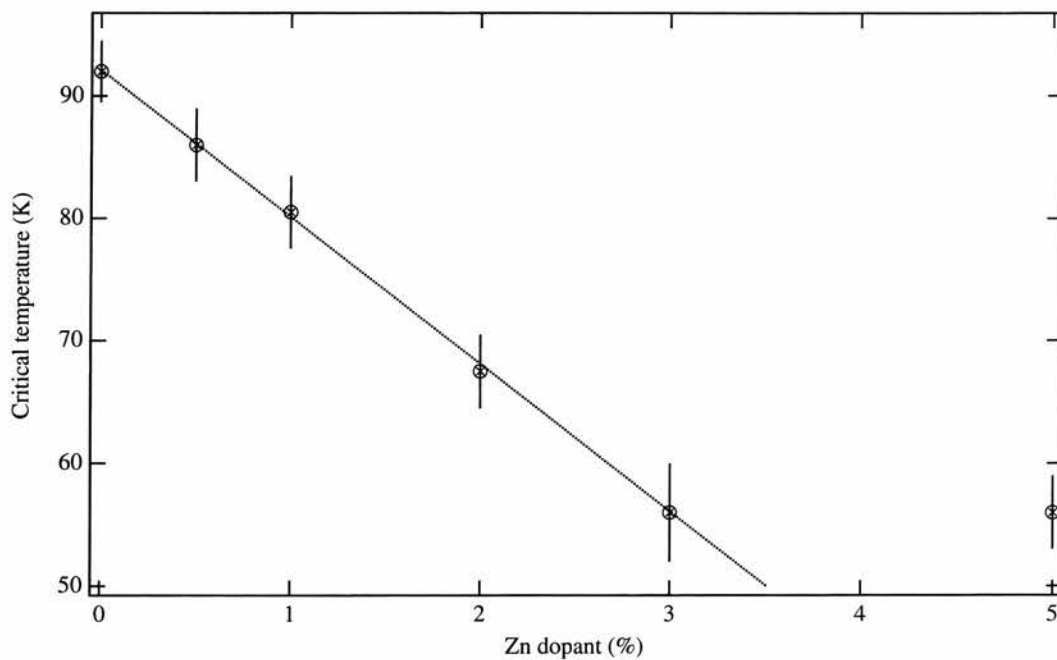


Figure 7.10: The superconducting transition temperature vs Zn concentration. The vertical lines represent transition widths and the dashed line the best fit through the data excluding that of 5%Zn.

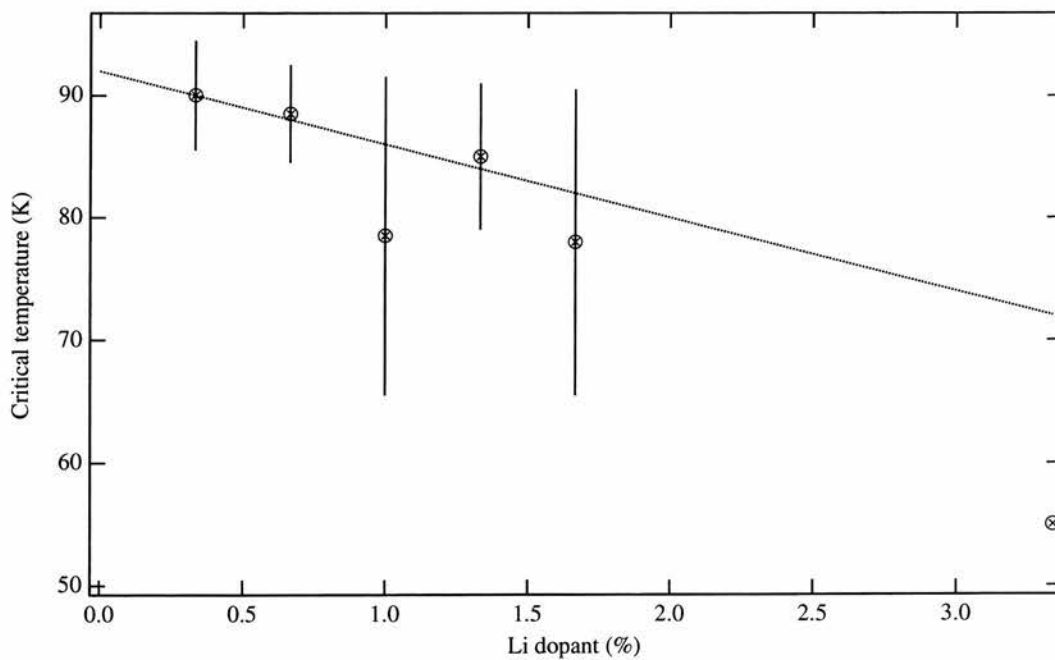


Figure 7.11: Variation of T_c with Li concentration. The line shows the expected trend as described in the text [14].

7.3.3 Thermogravimetric Analysis

A typical run is shown in Figure 7.12. In this run the temperature has been increased constantly up to 900°C where it was held for 60 minutes before cooling. Upon cooling the sample returns to approximately its initial weight corresponding to a similar uptake of oxygen and indicating that the specimen is close to fully oxygenated.

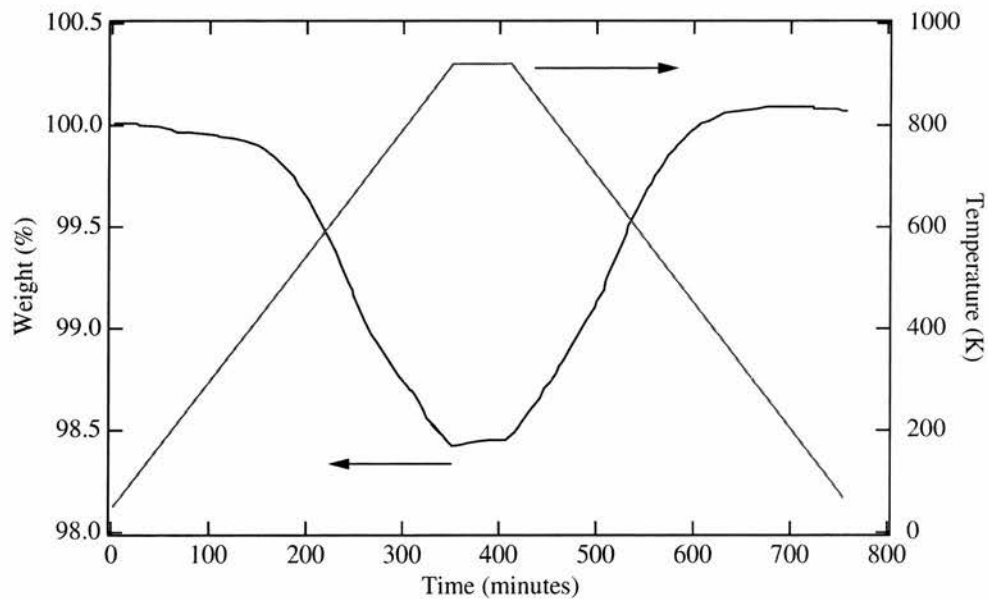


Figure 7.12: A typical TGA data plot showing both the temperature profile of the sample environment and variation of the sample weight throughout.

All samples examined in this way, including those with Zn impurities, proved to be optimally doped, having very similar oxygen contents in agreement to those calculated from diffraction measurements (see Table 7.1).

Table 7.1: Oxygen content determined by TGA.

Zn conc (%)	0.0	1.0	2.0	4.0
oxygen content	6.93	6.95	6.94	6.92

7.3.4 Discussion

The necessity for samples of high quality cannot be over-emphasised. We therefore take time to discuss the information gathered so far. In the case of Zn doping, the Zn is well known to substitute preferentially onto the planar Cu site. Although site identification was not possible directly with our characterisation techniques, sufficient data exists to ascertain the site of substitution.

From the diffraction spectra, we observe no change in the crystal structure, remaining orthorhombic throughout. Similarly the c-axis showed no variation, being constant at 11.67Å. Cross over to a tetragonal structure and a reduction in the c-axis are both well known indicators of chain-site substitution[1]. The lack of these effects is indicative that the zinc is indicates planar-site substitution.

The thermogravimetric analysis reports all samples examined to have similar oxygen contents, therefore the observed decrease in transition temperature can be attributed to dopant effects. All these factors point to well oxygenated, homogeneous samples with the dopant occupying the desired site.

The question of the lithium site is a more crucial problem since various possibilities can exist, including interstitial occupation [15]. The crystal structure was obtained using the Rietveld refinement data treatment although the goodness of fit being worse than for the Zn-doped specimens. Neutron diffraction spectra were also collected in an effort to identify the Li site but the data quality was such that this was impossible. The most damning evidence is that of the transition temperature variation with Li content. There is no clear trend and it is difficult interpret the cause of the decrease, whether due to changing lithium or oxygen content.

From our studies here, and those of other authors [14], it is difficult to control the placement of the Li within the crystal structure without a systematic examination of the sample preparation conditions. With this in mind, and the time constraints of this project, we decided to discontinue the lithium doped series and concentrate on a reduced set of zinc doped samples.

7.4 ^{89}Y MAS NMR study

7.4.1 Experimental

NMR measurements were performed on our reduced samples series, undoped, 1% and 2% Zn, by standard pulsed NMR techniques. Static and magic angle spinning (MAS) spectra techniques were utilised to obtain spectra. Typically the decay following either a single pulse or a spin echo after a $\pi/2 - \pi$ sequence was monitored and the corresponding spectrum obtained after Fourier transform. Spectra were obtained using Bruker MSL 500 and Varian Infinity Plus spectrometers with a static field of 11.75T corresponding Larmor frequency of 24.506MHz. The ^{89}Y shift was measured with respect to a standard YCl_3 solution.

Yttrium is a 100% naturally abundant spin-1/2 nucleus; the absence of quadrupole interactions makes it attractive both experimentally and for ease in interpretation of the data. Furthermore occupying a site between the two Cu-O planes, the yttrium is ideally placed to monitor the planar properties.

Previous experiments have failed to use the added sensitivity of magic angle spinning to monitor the behaviour of satellites resulting from induced moments, preferring to use traditional techniques. We believe that this additional sensitivity will allow direct observation of these satellite resonances in fully oxygenated YBCO which, as of now, have eluded detection.

7.4.2 Results

The room temperature ^{89}Y NMR spectra obtained for a range of samples with different dopant concentrations can be seen in Figure 7.13. The resonance from the undoped sample displays an asymmetric lineshape containing a high frequency, more positive shift, shoulder. This is not unusual, having been previously reported as resulting from regions of the sample which are not fully oxidized [16]. The spectra of the doped samples show an additional broad shoulder which increases with the dopant concentration.

Magnetisation data previously obtained on zinc doped YBCO [17] shows that the Curie constant for $\text{YBCO}_7:\text{Zn}$ is approximately one-sixth that of $\text{YBCO}_{6.64}:\text{Zn}$. Assuming the same hyperfine couplings, Alloul calculated the expected position of the first nn line using the following expression;

$$\Delta K_1 = (5/8)K_s + K_c + \delta_1 \quad (7.2)$$

where K_s is the spin shift of the main line, K_c ($=2C_s/T$) is the Curie contribution to the spin shift due to its two first nn Cu with a moment and δ_1 is the chemical shift. Here, the first nn Y sites are assumed to have five Cu nn which are nearly unaffected by Zn, two Cu nn which exhibit Zn induced Curie magnetism and the nonmagnetic Zn neighbour.

This theory predicts a positive shift of 31ppm with respect to the main line resonance and is shown in Figure 7.13 by the arrow. Although attached to the mainline, the approximate position of this component agrees with that predicted for a satellite in fully oxygenated YBCO [16].

Unfortunately there is also a small resonance in the pure sample signal that occurs at a similar frequency. It is therefore difficult to determine whether this shoulder is a direct result of resonances close to zinc induced moments. However, if this signal were due to an impurity, increasing as a result of increased inhomogeneity with larger dopant concentration, there would be a corresponding increase in impurity peaks in the X-ray diffraction pattern. This is not the case and we therefore attribute the shoulder in the doped samples to a satellite resonance.

In Figure 7.14 the spectra obtained between 323K and 135K for $\text{YBCO}_7:\text{Zn}_1\%$ are shown. With decreasing temperature the signal broadens and moves towards higher shifts. At the lowest temperatures, the high frequency shoulder becomes more pronounced. The shift behaviour can be seen more clearly in Figure 7.15 where the temperature dependence of the mainline shift (ΔK) for each sample is shown. An increase in shift is observed as temperature decreases, in keeping with previous studies [16], although it is unknown if our data will display the normal broad cusp at 130K.

Figure 7.16 shows the variation of the mainline linewidth with temperature. In previous studies this has displayed a Curie-like behaviour [16] while our data has a more linear temperature dependence.

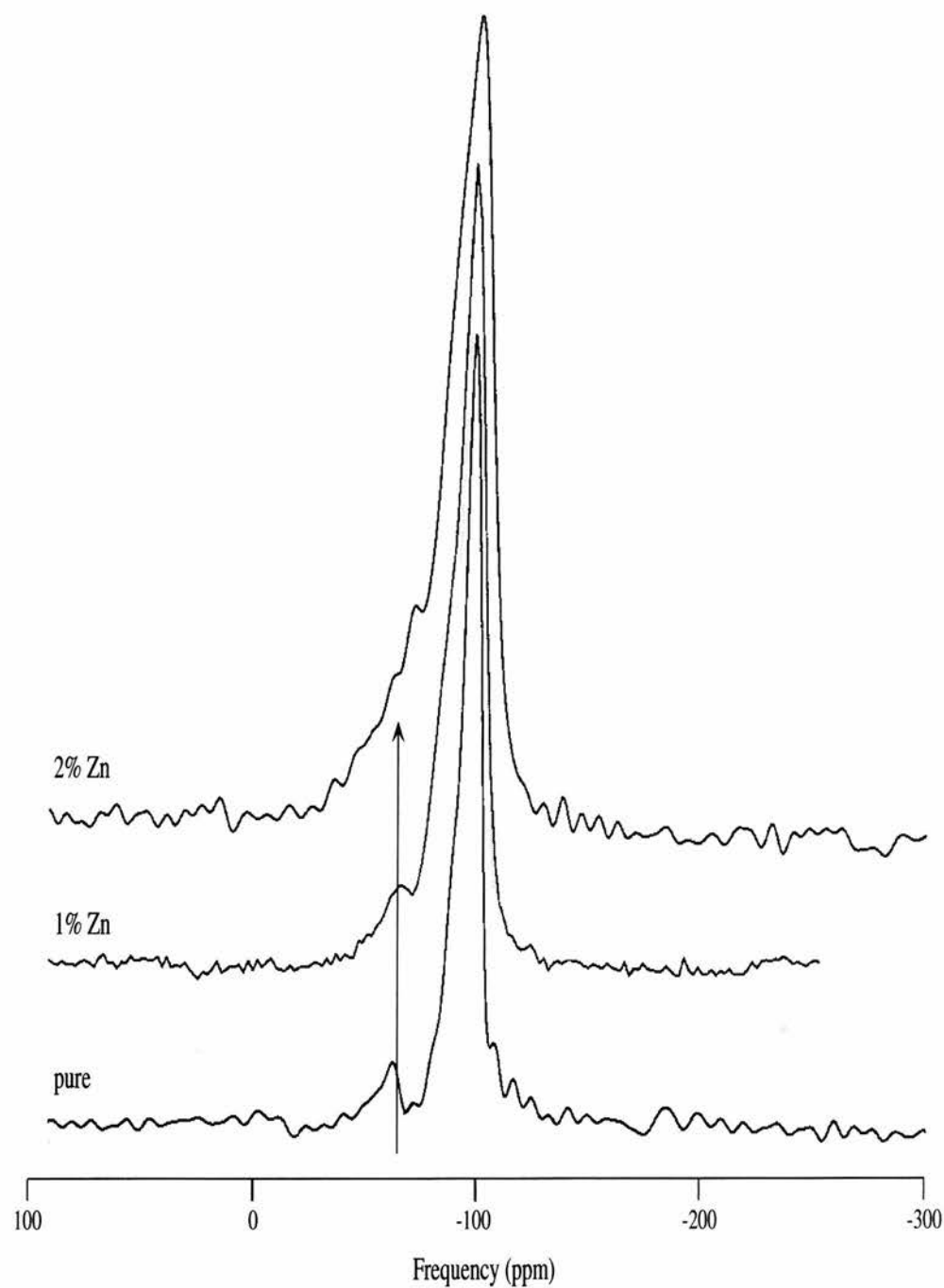


Figure 7.13: ^{89}Y NMR lineshape at room temperature in $\text{YBCO}_7:\text{Zn}_y\%$ showing an additional high frequency component which increases with zinc concentration. The arrow indicates the expected position of 1st nn satellite resonance.

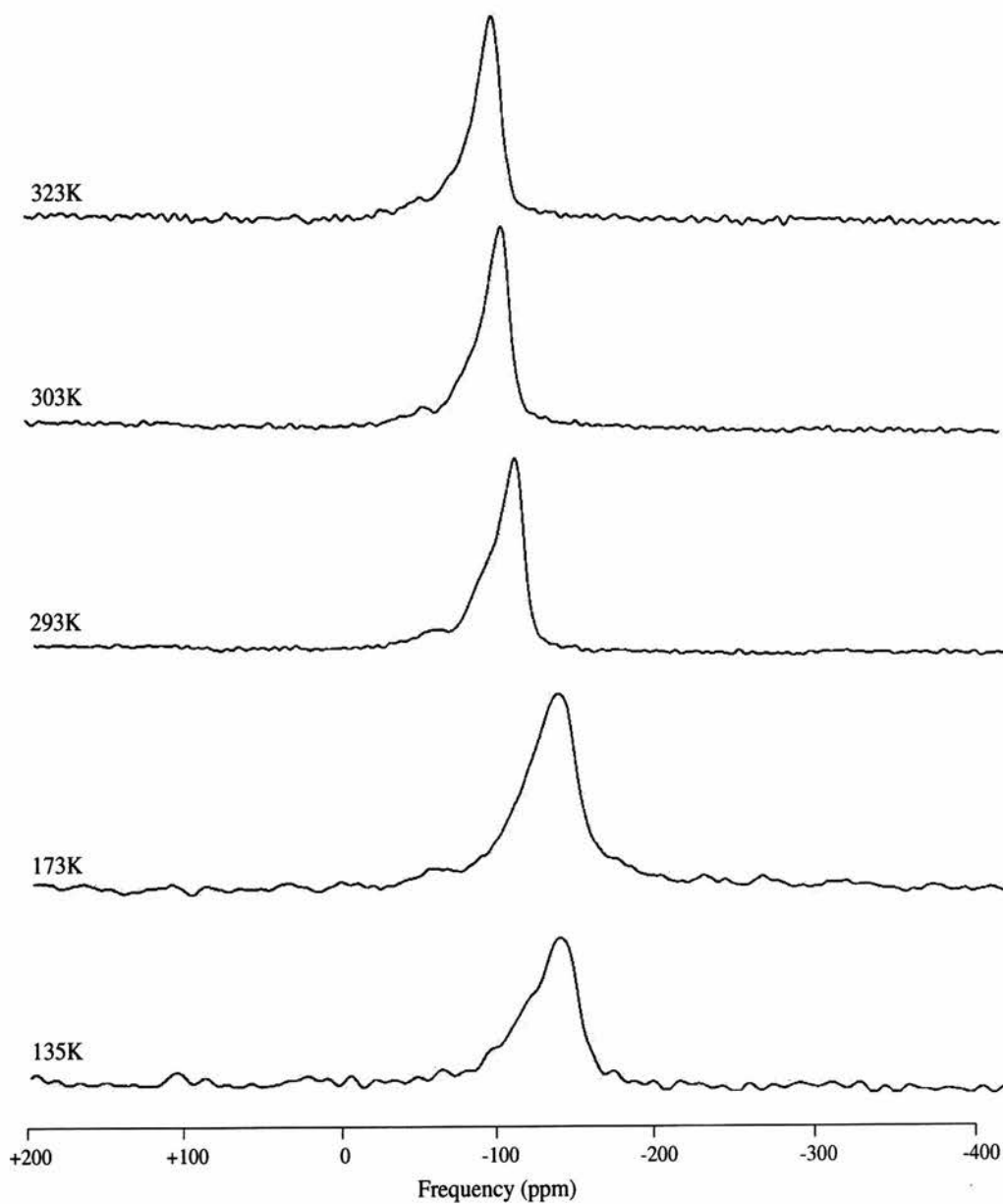


Figure 7.14: ^{89}Y NMR $\text{YBCO}_7:\text{Zn}_1\%$ spectra obtained between 323K and 135K. With decreasing temperature the signal broadens and progresses towards larger shifts.

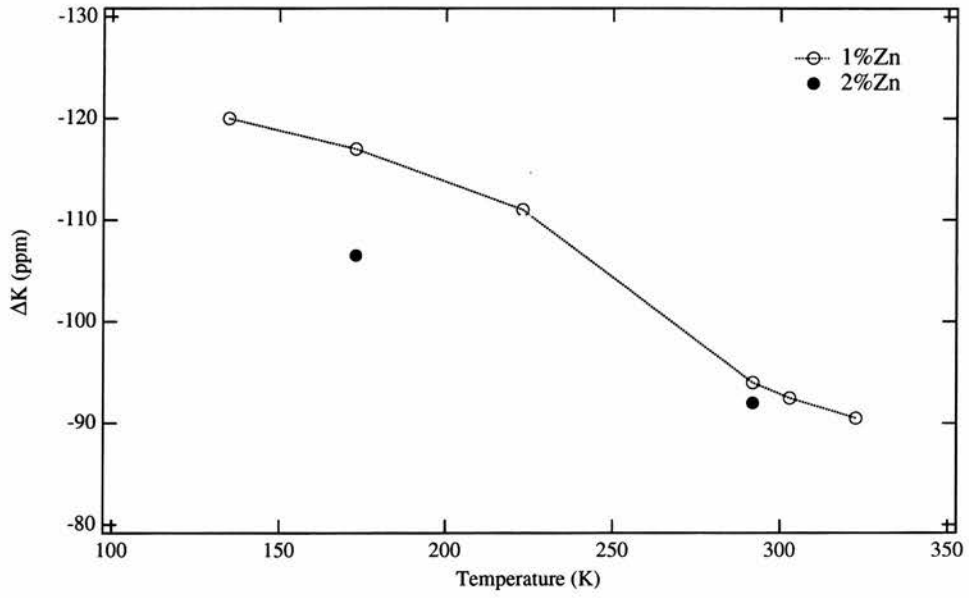


Figure 7.15: ^{89}Y NMR mainline shift K versus temperature T for doped $\text{YBCO}_7:\text{Zn}$. The line is a guide for the eye.

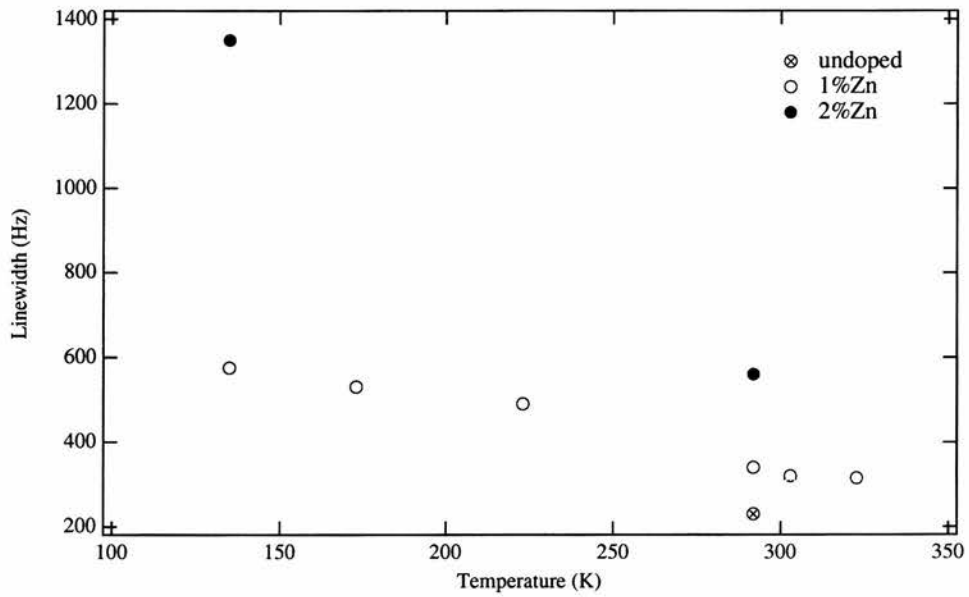


Figure 7.16: ^{89}Y NMR linewidth of the mainline resonance versus temperature for $\text{YBCO}_7:\text{Zn}$.

7.5 Conclusions and Further Work

Ceramic samples of both zinc and lithium doped YBCO were prepared in-house by standard solid-state techniques. Although the preparation of these compounds requires minimal equipment, extreme care has to be used in order to produce fully oxygenated, highly homogeneous, good quality samples. NMR is such a highly sensitive technique that samples of exceptional quality are necessary, especially if the aim of the experiments is to study the effects of a small amount of controlled dopant.

A substantial amount of the time dedicated to this project was therefore spent on sample characterisation and refinement of the preparation method, especially the oxygenation treatment. X-ray and time of flight neutron diffraction were used to confirm sample purity and structure. The oxygen content was determined by thermogravimetric analysis and inferred indirectly through lattice parameters from the XRD studies.

All of these methods confirmed that zinc substituted preferentially onto the desired planar copper site producing well oxygenated, homogeneous samples. The lithium doped samples proved to be more problematic as various crystallographic sites are available for occupation including interstitial sites. The neutron diffraction data did not allow identification of the lithium site. Similarly there was no clear trend in the transition temperature variation with Li content. It was difficult to ascertain the position of the lithium within the crystal structure without a systematic examination of the sample preparation conditions. This was outwith both the remit and timescale of the project resulting in the discontinuation of the lithium doped series.

The ^{89}Y NMR measurements performed on our reduced sample set confirmed them to be of high quality and close to fully oxygenated displaying linewidths close to 400Hz. Although showing no prominent features, ie additional resonances, our spectra do contain high frequency shoulders that grow with dopant concentration. The position of these also shows good agreement with the calculations of Alloul. Overall our data shows tentative evidence that satellites are indeed resolvable from the mainline resonance.

The properties of the mainline show good agreement with those previously reported using standard techniques. There is however a discrepancy in the temperature dependence of the linewidth which displays a more linear behaviour in contrast

to the expected Curie-Weiss behaviour. Unlike previous studies, where the satellites have merged completely with the mainline, in our data the 1st nn satellite is clearly an appendage. These have not been clearly resolved in the study presented here and this may well account for this disparity.

I feel it is necessary to mention some of the problems that disrupted and ultimately halted the progress of this project. During the course of our research, a new NMR spectrometer was purchased and installed in our laboratory. Although this should have been of major benefit to the project, due to its increased sensitivity, computing power and decreased down time, the opposite was true. The combination of decommission time of the first spectrometer and delayed installation of its replacement to full capacity, coupled with limited sample shelf-life conspired to turn these difficult experiments into a Herculean task.

The results presented here are preliminary and experimental work is still ongoing. Further work on this system should include a repeat of the work presented here with an extension to higher zinc dopant concentrations. It would also be beneficial to perform a similar set of experiments on lithium doped $\text{YBa}_2(\text{Cu}_{1-x}\text{Li}_x)_3\text{O}_{7-\delta}$ over a comparable range of dopant concentrations. This is quite a daunting task, involving considerable time during which an extensive, systematic examination of the sample preparation conditions would be paramount.

These difficult experiments are only possible using magic angle spinning and would benefit greatly from the increased resolution that a larger static field would provide.

References

- [1] D. M. Ginsberg, *Properties of High Temperature Superconductors II* (World Science Publishing, Singapore, 1990).
- [2] H. Alloul, *Physica B* **169**, 51 (1991).
- [3] K. Gorny *et al.*, *Physical Review Letters* **82**, 177 (1999).
- [4] H. Alloul, *Journal of Applied Physics* **69**, 4513 (1991).
- [5] P. Monthoux and D. Pines, *Physical Review B* **50**, 16015 (1994).
- [6] G. Xiao *et al.*, *Physical Review B* **35**, 8782 (1987).
- [7] H. Alloul *et al.*, *Physical Review Letters* **67**, 3140 (1991).
- [8] A. V. Mahajan, H. Alloul, and G. C. J. F. Marucco, *Physical Review Letters* **72**, 3100 (1994).
- [9] R. E. Walstedt, R. F. Bell, L. F. Schneemeyer, and J. V. Waszczak, *Physical Review B* **48**, 10646 (1993).
- [10] G. V. M. Williams, J. L. Tallon, and R. Meinhold, *Physical Review B* **52**, R7035 (1995).
- [11] P. Monthoux and D. Pines, *Physical Review B* **49**, 4261 (1994).
- [12] J. Rodriguez-Carvajal, *An introduction to the program FullProf*, 1997.
- [13] A. C. Larson and R. B. V. Dreele, *GSAS: General Structure Analysis System*, 1994.
- [14] K. Sauv, J. Conard, M. Nicolas-Francillon, and F. Bouree, *Physica C* **273**, 49 (1999).

- [15] M. S. Islam and C. Ananthamohan, *Journal of Solid State Chemistry* **100**, 371 (1992).
- [16] A. V. Mahajan, H. Alloul, G. Collins, and J. F. Marucco, *The European Physical Journal* **13**, 457 (2000).
- [17] J. H. B. P. Mendels, H. Alloul and G. D. Morris, *Physical Review B* **49**, 10035 (1994).

Chapter 8

Summary and Conclusions

8.1 Summary

This thesis is an investigation of a variety of phenomena existing in condensed matter materials. All the work presented here is a continuation of previous studies in an effort to add to the body of knowledge and elucidate the underlying physics. The investigations have used a variety of approaches including magnetisation measurements, diffraction methods, nuclear magnetic resonance and muon spin relaxation as well as direct transport measurements. The results presented in this thesis are summarised below for the various systems investigated. Much interesting work is still to be performed on these samples, and some of the results presented here have opened up many more avenues of research.

8.2 Superconductor/Ferromagnet Multilayers

Sputtered multilayers of Nb/Co, Pb/Co and Pb/Fe materials were prepared and characterised by a variety of techniques including reflectometry and dc magnetisation techniques. Simple dc transport measurements provided a direct method of characterising the superconducting transition of artificial multilayers and therefore identifying the critical temperature. Initially the critical temperature was monitored as a function of the magnetic spacer layer thickness in order to confirm the existence of an oscillation phenomenon. In a series of follow-up experiments the upper critical field was measured as a function of temperature for a selection of samples. The main difficulty with this project rested with preparing samples of sufficiently high

quality, in particular, achieving exceptionally clean surface interfaces with nearly no intermixing.

8.2.1 T_c Oscillations

Although the Nb/Co samples were determined to be of consistently good quality, the oscillation effect is very subtle and has been masked by interface mixing of the niobium and cobalt and the concomitant changes in transition temperature. However, promising results have been shown by series sc02, Si/Co/(Nb/Co)_{x10}, and sc10, Si/Co/(Nb/Co)_{x5}, where $Nb \approx 400 \text{ \AA}$.

Initial samples of Pb/Co and Pb/Fe contained superconducting lead layers that were too thick. This allowed only the decoupling of the lead layers to be observed, showing a characteristic decrease in critical temperature followed by a plateau with increasing spacer thickness. The results from sc20 (Pb/Fe) and sc23 (thinner Pb) were far more promising. Both of these display oscillations, with that of series sc23 exhibiting a single broad maximum.

The time constraints of this project have only allowed us to isolate the range of sample parameters which satisfy the requirements for our measurements. There are therefore a range of possible experiments still to be carried out.

8.2.2 Vortex Behaviour

The upper critical field has been measured as a function of angle and temperature in order to study the dimensionality of the vortex properties of Nb/Co multilayer films. These measurements have shown there to be an effective decrease in the superconductor layer thickness by 30 \AA when the cobalt spacer layers are ferromagnetic. In this case the superconducting layers are decoupled and act as individual thin films.

For the case of very thin magnetic layers, sputtering results in partial layers of cobalt islands which display superparamagnetic behaviour. Instead of the expected 3D-2D dimensional crossover with decreasing temperature and increasing spacer thickness, we observe a 2D'-2D transition from coupled bilayers to individual superconducting layers.

The fully decoupled samples also displayed 2D behaviour consistent with the Tinkham theory for 2D superconducting films. Close to the critical temperature, the coherence length diverges and the anisotropic G-L theory is expected to be valid.

From our scaling measurements we observe no clear discontinuity between these two regimes, the Tinkham formalism showing good agreement with the experimental data at all temperatures.

Preliminary flux flow experiments have shown that vortices are not strongly pinned when a force is applied perpendicular to the interface boundary whereas very strong pinning had been expected. Similarly hysteresis loops from magnetisation measurements revealed a response uncharacteristic of a conventional type-II superconductor displaying paramagnetic rather than diamagnetic behaviour. Overall these materials have proven to be extremely interesting, exhibiting a variety of unexpected behaviour. Continuation of this work could proceed along a couple of directions including a more extensive set of measurements performed on the sc13 series and using different materials to monitor the change in the suppression depth due magnetic effects.

8.3 LiTi_2O_4 Ramsdellite

Polycrystalline samples of LiTi_2O_4 were prepared and characterised by X-ray diffraction. They were found to be phase pure, exhibiting the same structure as had previously been reported for samples of this composition. Interpretation of the data has been problematic due to the use of different samples, and therefore sample variation, for different experiments.

The low temperature structural and magnetic behaviour have been characterised by a variety of techniques. X-ray diffraction revealed a subtle structural transition between 220K-260K due to titanium movement. This has been tentatively described as an orthorhombic to monoclinic transformation although further experiments and analysis are required.

Low temperature magnetic investigations by SQUID and μSR have revealed this material to be a paramagnetic system with very weakly antiferromagnetically coupled moments. This signal results from 10% of the expected magnetism due to a single Ti^{3+} situated in each unit cell. A second magnetic phase was also observed, displaying a broad maximum at 180K. At present this additional component is not fully understood although it may arise from short range antiferromagnetic coupled clustering of the Ti.

With decreasing temperature this material undergoes another magnetic transi-

tion at 4.7K. This was only observed using standard dc magnetisation techniques and identification of the phase is incomplete at present although it is a cooperative phenomenon and may well be a spin glass state.

The most interesting feature of this material were discovered through variable temperature NMR and μ SR. These indicate that the lithium atoms are in motion although the temperature range is not known exactly.

This is a fascinating material exhibiting a variety of phenomena, and although we have added to the body of knowledge there are still areas which require further investigation. Future work should include a repeat of the ^7Li NMR measurements, with an extension to lower temperatures, coupled with additional ^{49}Ti NMR data.

8.4 $\text{YBa}_2(\text{Cu}_{1-x}\text{M}_x)_3\text{O}_{7-\delta}$

Ceramic samples of both zinc and lithium doped YBCO were prepared in-house by standard solid-state techniques. X-ray and time of flight neutron diffraction were used to confirm sample purity and structure. The oxygen content was determined by thermogravimetric analysis and inferred indirectly through lattice parameters from the XRD studies.

All of these methods confirmed that zinc substituted preferentially onto the desired planar copper site producing well oxygenated, homogeneous samples. The lithium doped samples proved to be more problematic as various crystallographic sites are available for occupation including interstitial sites. The quality of these samples was dubious and this resulted in the discontinuation of the lithium doped series.

The ^{89}Y NMR measurements performed on our reduced sample set confirmed them to be of high quality and, although showing no additional resonances, the spectra do contain high frequency shoulders that grow with dopant concentration. The position of these shoulders also agrees with that predicted theoretically.

Further work on this system should include a repeat of the work presented here with an extension to higher zinc dopant concentrations. It would also be beneficial to perform a similar set of experiments on lithium doped $\text{YBa}_2(\text{Cu}_{1-x}\text{Li}_x)_3\text{O}_{7-\delta}$ over a comparable range of dopant concentrations. This is quite a daunting task, involving considerable time during which an extensive, systematic examination of the sample preparation conditions would be paramount.

Appendix A

${}^7\text{Li}$ NMR Spectra of LiTi_2O_4

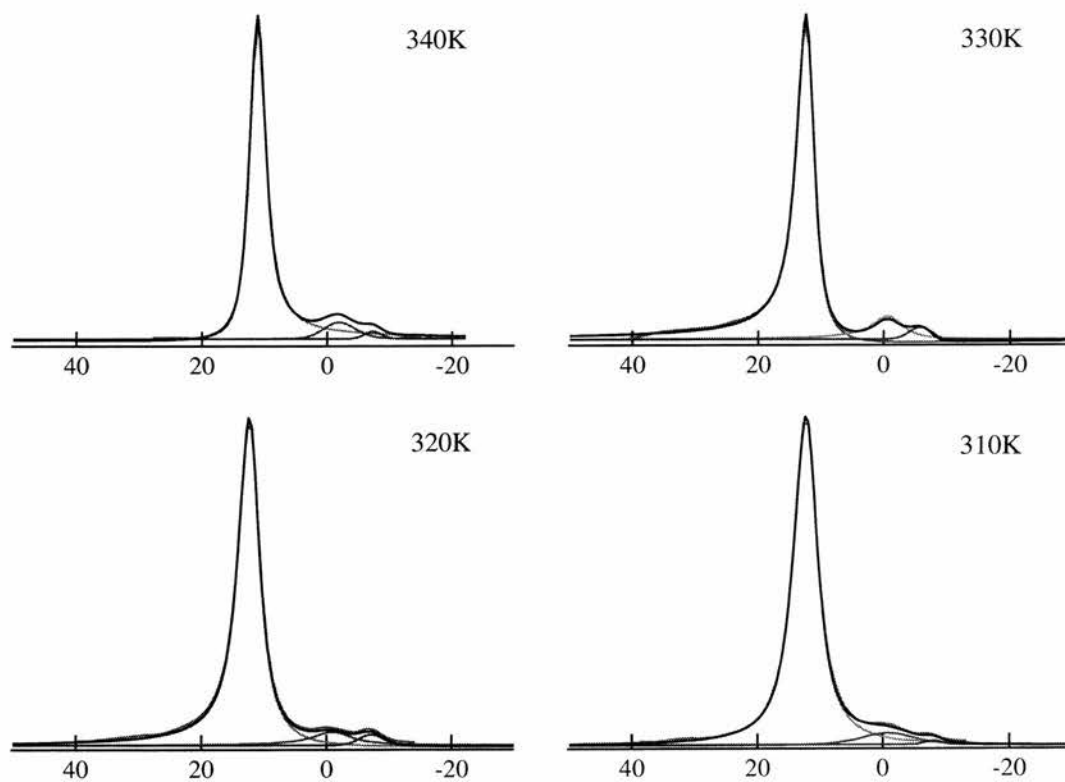


Figure A.1: Temperature dependence of the ${}^7\text{Li}$ NMR spectra for polycrystalline LiTi_2O_4 (slow cooled). Each spectra has been fitted to a pseudo-Voigt function as described in Chapter 6.

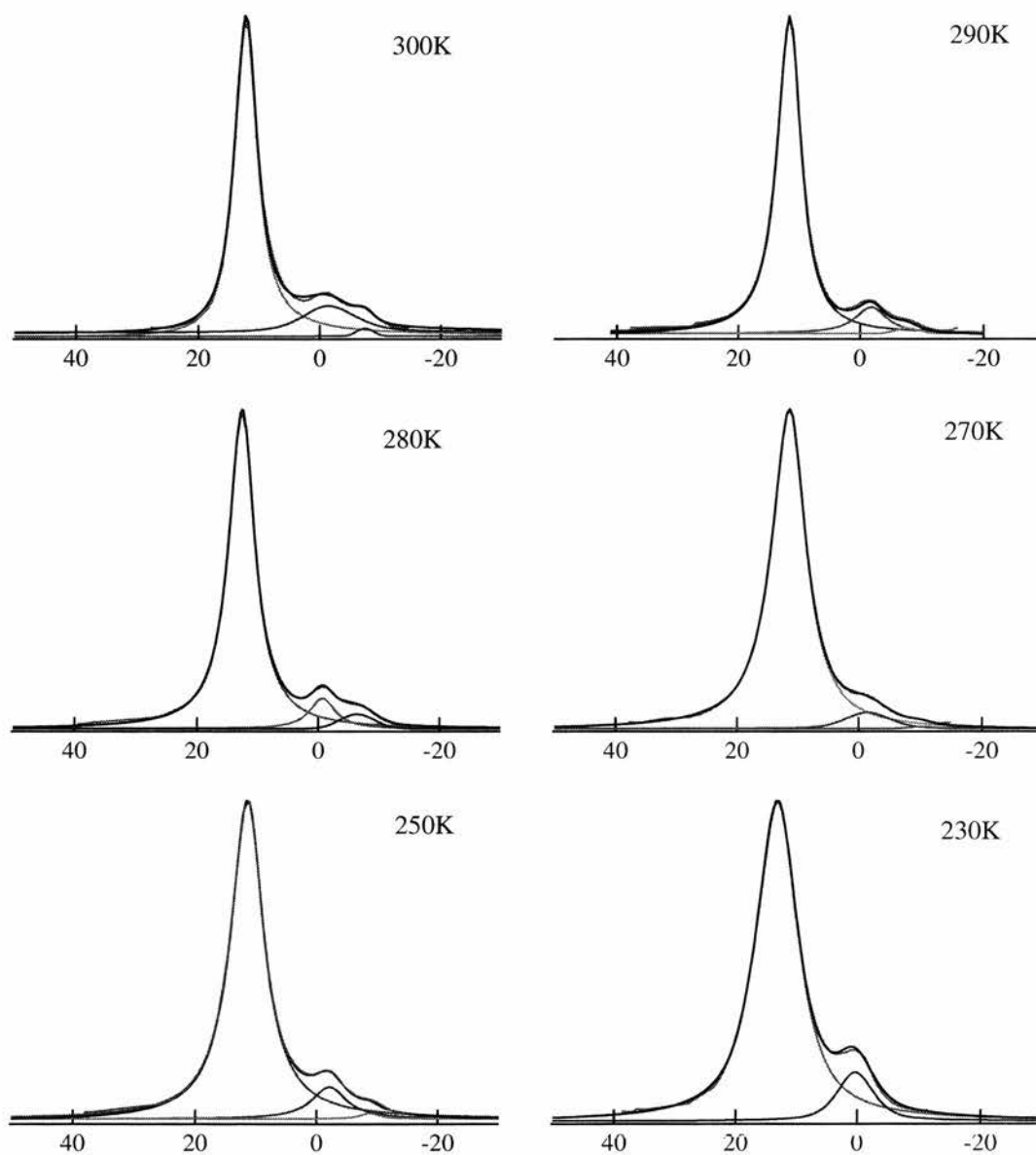


Figure A.2: Continued from Figure A.1. Temperature dependence of the ^7Li NMR spectra for polycrystalline LiTi_2O_4 (slow cooled). Each spectra has been fitted to a pseudo-Voigt function as described in Chapter 6.

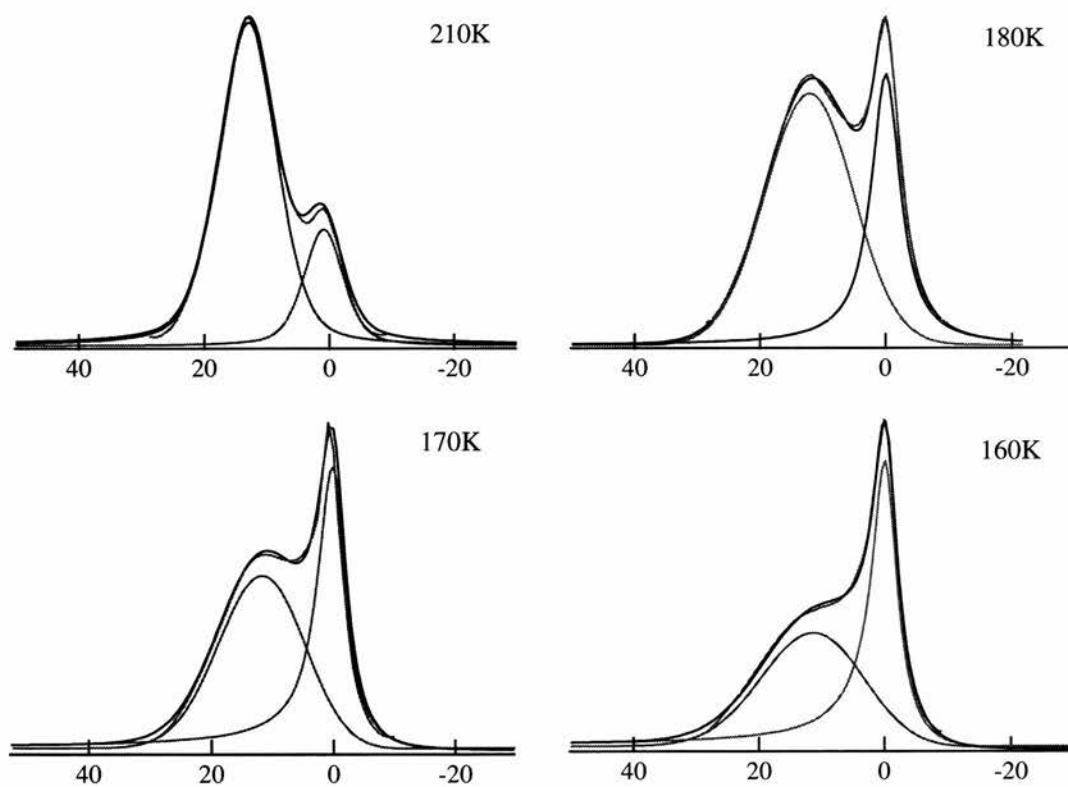


Figure A.3: Continued from Figure A.2. Temperature dependence of the ^7Li NMR spectra for polycrystalline LiTi_2O_4 (slow cooled). Each spectra has been fitted to a pseudo-Voigt function as described in Chapter 6.

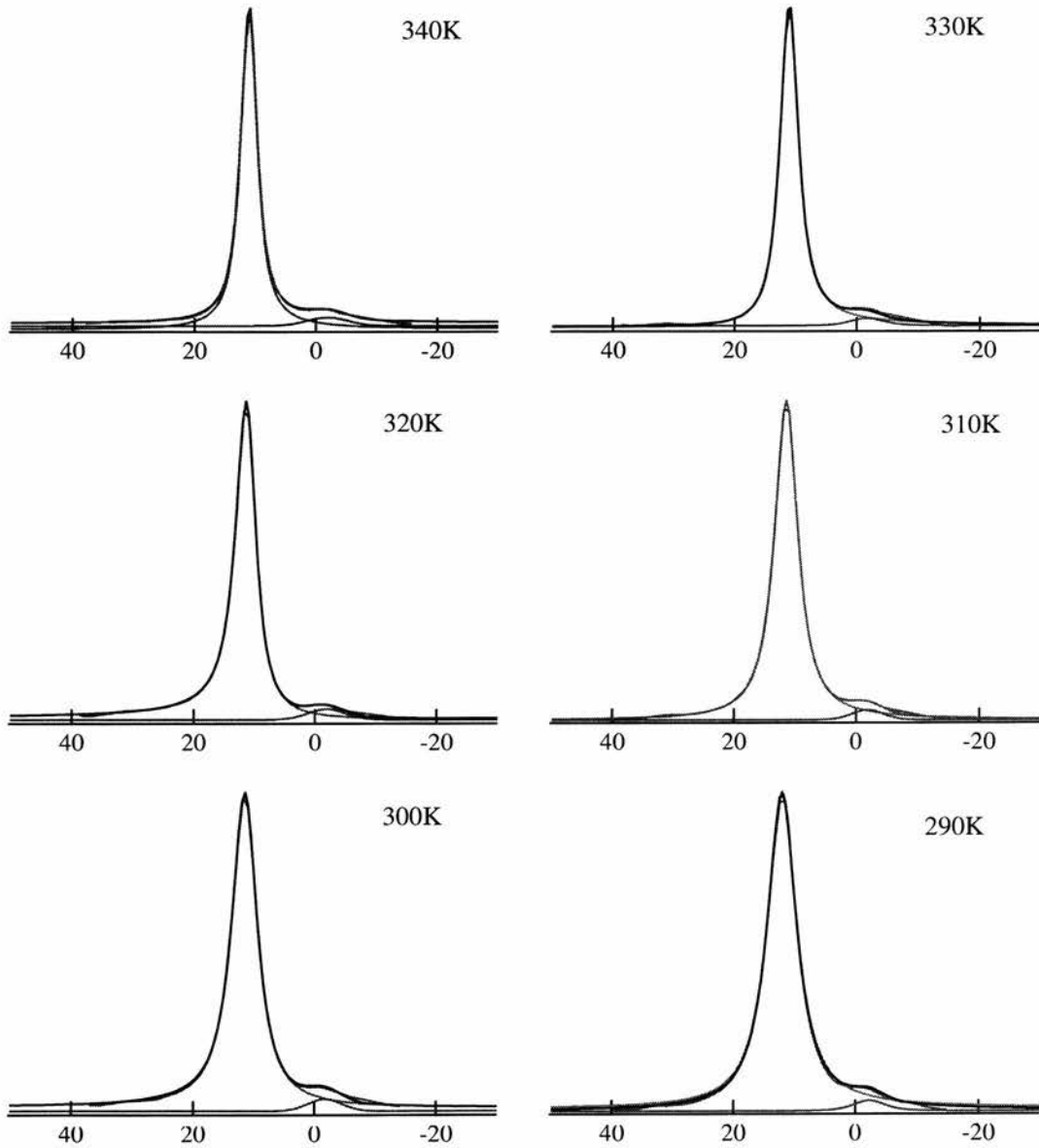


Figure A.4: Temperature dependence of the ^7Li NMR spectra for polycrystalline LiTi_2O_4 (rapid cooled). Each spectra has been fitted to a pseudo-Voigt function as described in Chapter 6.

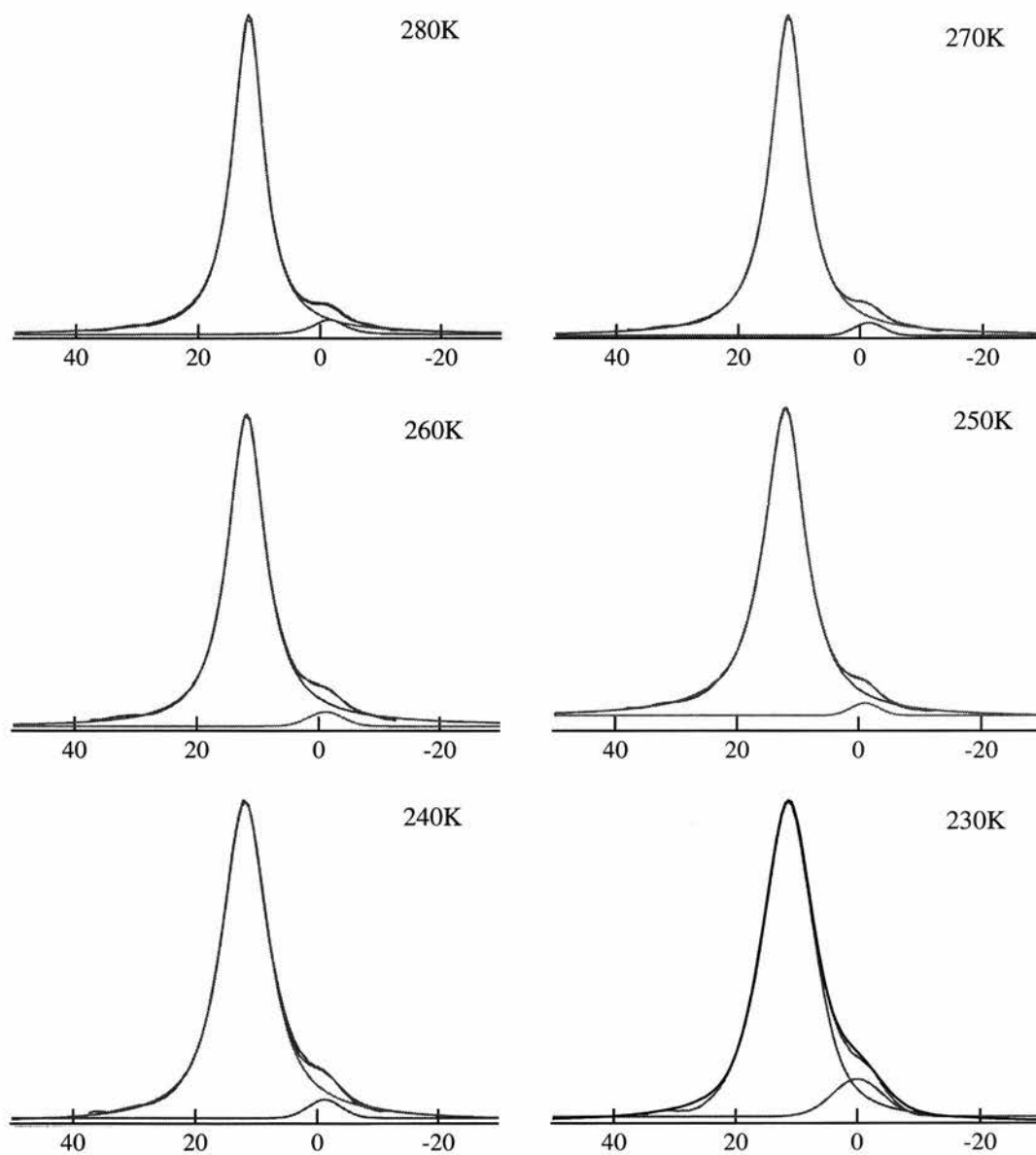


Figure A.5: Continued from Figure A.4. Temperature dependence of the ^7Li NMR spectra for polycrystalline LiTi_2O_4 (rapid cooled). Each spectra has been fitted to a pseudo-Voigt function as described in Chapter 6.

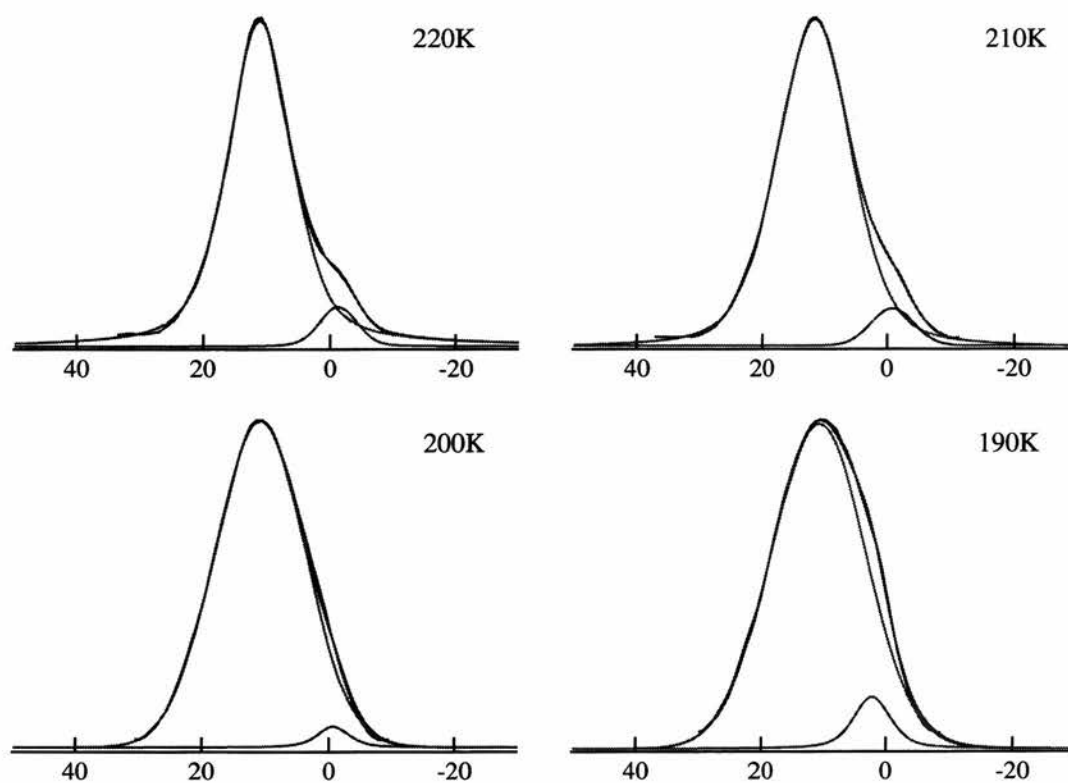


Figure A.6: Continued from Figure A.5. Temperature dependence of the ^7Li NMR spectra for polycrystalline LiTi_2O_4 (rapid cooled). Each spectra has been fitted to a pseudo-Voigt function as described in Chapter 6.